ANALYSIS, MODELING AND SIMULATION OF MACHINE TOOL PARTS DYNAMICS FOR ACTIVE CONTROL OF TOOL VIBRATION

Tatiana Smirnova

Blekinge Institute of Technology
Doctoral Dissertation Series No. 2010:08

School of Engineering

Analysis, Modeling and Simulation of Machine Tool Parts Dynamics for Active Control of Tool Vibration

Tatiana Smirnova

Blekinge Institute of Technology Doctoral Dissertation Series
No 2010:08

Analysis, Modeling and Simulation of Machine Tool Parts Dynamics for Active Control of Tool Vibration

Tatiana Smirnova

Department of Electrical Engineering
School of Engineering
Blekinge Institute of Technology
SWEDEN

© 2010 Tatiana Smirnova
Department of Electrical Engineering
School of Engineering
Publisher: Blekinge Institute of Technology
Printed by Printfabriken, Karlskrona, Sweden 2010
ISBN: 978-91-7295-187-7
Blekinge Institute of Technology Doctoral Dissertation Series
ISSN 1653-2090
urn:nbn:se:bth-00472

Abstract

Boring bar vibration in machine tools during internal turning operations is a pronounced problem in the manufacturing industry. Due to the often slender geometry of the boring bar, vibration may easily be induced by the material deformation process. One approach to overcome such vibration problems is to use active control of boring bar vibration. The design time of an active boring bar depends to a great extent on the knowledge of its dynamic properties when clamped in a lathe for different actuator positions and sizes, crucial for its performance. This thesis focuses on the development of accurate dynamic models of active boring bars with the purpose of providing qualitative information on suitable actuator position for a certain boring bar.

The first part of the thesis considers the problem of building an accurate "3-D" finite element (FE) model of a standard boring bar used in industry. Results from experimental modal analysis of the actual boring bar are the reference. The second and the third parts discuss analytical and experimental methods for modeling the dynamic properties of a boring bar clamped in a machine tool. For this purpose, the Euler-Bernoulli and Timoshenko beam theories are used to produce both distributed-parameter system models and corresponding "1-D" FE models. A more complete "3-D" FE model of the system boring bar - clamping house is also developed. Spatial dynamic properties of these models are discussed and compared with adequate experimental modal analysis results from the actual boring bar clamped in a machine tool. The third part also investigates the sensitivity of the spatial dynamic properties of the derived boring bar models to variation in the structural parameters' values.

The fourth part focuses on the development of a "3-D" FE model of the system boring bar - actuator - clamping house. Two models are discussed: a linear model and a model enabling variable contact between the clamping house and the boring bar with and without Coulomb friction in the contact surfaces. Based on these FE models fundamental bending modes and control path frequency response functions are discussed in conjunction with the corresponding quantities estimated for the actual active boring bar.

In the fifth part, a method based on FE modeling and artificial neural networks for selecting a suitable actuator position inside an active boring bar is presented. Objective functions for selecting an actuator position are suggested. An active boring bar with an actuator position suggested by the method was manufactured and it displays fairly good correlation with the corresponding FE model.

The final part focuses on modeling of an active boring bar vibration control system. A simple "1-D" FE model of a boring bar is utilized to simulate the dynamic response and an adaptive digital feedback controller realized by the feedback filtered-x LMS algorithm is used.

Preface

This thesis summarizes my work at the Department of Electrical Engineering at Blekinge Institute of Technology. The thesis comprises an introduction followed by six parts:

Part	
I	On Accurate FE-modeling of a Boring Bar with "Free-Free" Boundary Condition.
II	Dynamic Modeling of a Boring Bar Using Theoretical and Experimental Engineering Methods Part 1: Distributed-Parameter System Modeling and Experimental Modal Analysis.
III	Dynamic Modeling of a Boring Bar Using Theoretical and Experimental Engineering Methods Part 2: Finite Element Modeling and Sensitivity Analysis.
IV	Modeling of an Active Boring Bar.
V	Initial Development of an Actuator Positioning Method for Active Boring Bars.
VI	Simulation of Active Suppression of Boring Bar Vibrations by Means of a Boring Bar "1-D" Finite Element Model.

Acknowledgments

I would like to express my sincere gratitude to all the people who have influenced my life and my studies, inspired me to pursue the field of science and helped me during the years towards PhD studies as well as while writing this thesis.

First of all, I would like to express my deep gratitude to Professor Ingvar Claesson for giving me the opportunity to conduct research in the form of a PhD position at the Blekinge Institute of Technology. I would also like to thank my research supervisor and friend Professor Lars Håkansson for his constant guidance, his support while writing this thesis, and also for his continuous care. His profound knowledge and experience in the fields of applied signal processing and mechanical engineering, his enthusiasm in conducting research, his persistent will for constant improvement both in carrying out measurements and writing journal articles, and his overall positive attitude to life make him a great mentor. I am grateful to all my colleagues at Acticut International AB for their industrial guidance, help and constructive collaboration.

Special thanks go to my dear friends Associate Professor Nedelko Grbic and his wife Marina for their warmth, inspiration, encouragement and all their help during my stay in Sweden.

I would like to thank all my present and former colleagues at the department of Electrical Engineering for being so helpful, friendly and cheerful, creating a great working environment. Especially, I am indebted to my colleague and friend Dr. Henrik Åkesson for all his help and support, patience and many fruitful discussions.

I am most grateful to my parents Nadezhda and Aleksandr and my sister Anastasiya for always believing in me and being there for me. I appreciate your endless love, support and care given to me daily no matter where I am. Finally, I would like to thank my husband Sergey for his acceptance of my choices, his patience, understanding and all his love.

Tatiana Smirnova
Karlskrona, September 1, 2010

Contents

Preface vii

Acknowledgments ix

Publication list xiii

Introduction 1

Part

I On Accurate FE-modeling of a Boring Bar with "Free-Free" Boundary Condition. 21

II Dynamic Modeling of a Boring Bar Using Theoretical and Experimental Engineering Methods Part 1: Distributed-Parameter System Modeling and Experimental Modal Analysis. 33

III Dynamic Modeling of a Boring Bar Using Theoretical and Experimental Engineering Methods Part 2: Finite Element Modeling and Sensitivity Analysis. 55

IV Modeling of an Active Boring Bar 77

V Initial Development of an Actuator Positioning Method for Active Boring Bars 123

VI Simulation of Active Suppression of Boring Bar Vibrations by Means of a Boring Bar "1-D" Finite Element Model 161

Publication List

Part I is based on the publication:

T. Smirnova, H. Åkesson, L. Håkansson, I. Claesson, and T. Lagö, *Accurate FE-modeling of a Boring Bar Correlated with Experimental Modal Analysis*, In proceedings of the IMAC-XXV A Conference and Exposition on Structural Dynamics, February 19-22, 2007, Orlando, Florida USA.

Part II is published as:

T. Smirnova, H. Åkesson and L. Håkansson, Dynamic Modeling of a Boring Bar Using Theoretical and Experimental Engineering Methods Part 1: Distributed-Parameter System Modeling and Experimental Modal Analysis, *IJAV-International Journal of Acoustics and Vibration*, 14(3), (pp. 124-133), 2009.

Part III is published as:

T. Smirnova, H. Åkesson and L. Håkansson, Dynamic Modeling of a Boring Bar Using Theoretical and Experimental Engineering Methods Part 2: Finite Element Modeling and Sensitivity Analysis, *IJAV-International Journal of Acoustics and Vibration*, 14(3), (pp. 134-142), 2009.

Part IV is based on the publications:

T. Smirnova, H. Åkesson and L. Håkansson *Modeling of an Active Boring Bar*, Research Report No 2007:14, Blekinge Institute of Technology, ISSN: 1103-1581 December 2007.

T. Smirnova, H. Åkesson, L. Håkansson, I. Claesson and T. Lagö, *Initial Experiments with a Finite Element Model of an Active Boring Bar*, ICSV14 - The Fourteenth International Congress on Sound and Vibration, Cairns, Australia, 9 - 12 July, 2007.

Part V is published as:

T. Smirnova, H. Åkesson, L. Håkansson, I. Claesson and T. Lagö, *Initial Development of an Actuator Positioning Method for Active Boring Bars*, submitted for publication in *Journal of Mechanical Systems & Signal Processing*, September, 2010.

Part VI is based on the publication:

T. Smirnova, H. Åkesson, L. Håkansson, I. Claesson and T. Lagö, *Simulation of Active Suppression of Boring Bar Vibrations by Means of Boring Bar's "1-D" Finite Element Model*, In proceedings of ACTIVE 2009 the 2009 International Symposium

on Active Control of Sound and Vibration, August 20-22, 2009, Ottawa, Canada.

Other Publications

H. Åkesson, T. Smirnova, L. Håkansson, and T. Lagö, *Analysis of Dynamic Properties of Boring Bars Concerning Different Clamping Conditions* Research Report No 2007:6, ISSN: 1101-1581.

H. Åkesson, T. Smirnova, I. Claesson and L. Håkansson, "On the Development of a Simple and Robust Active Control System for Boring Bar Vibration in Industry", *IJAV-International Journal of Acoustics and Vibration*, 12(4), pp. 139-152, 2007.

T. Smirnova "Dynamic Analysis and Modeling of Machine Tool Parts", Technology Licentiate Dissertation, ISSN 1650-2140, 2008.

H. Åkesson, T. Smirnova and L. Håkansson, "Analysis of Dynamic Properties of Boring Bars Concerning Different Clamping Conditions", *Journal of Mechanical Systems & Signal Processing*, 23(8), pp. 2629-2647, 2009.

H. Åkesson, T. Smirnova, I. Claesson, T. Lagö and L. Håkansson, "Estimation and Simulation of Nonlinear Dynamic Properties of a Boring Bar", submitted for publication in *IJAV-International Journal of Acoustics and Vibration*, August 2009.

H. Åkesson, T. Smirnova, T. Lagö, L. Håkansson and I. Claesson, *Investigation of the Dynamic Properties of a Milling Tool Holder*, Research Report No 2009:14, ISSN: 1103-1581.

H. Åkesson, T. Smirnova, L. Håkansson, T. Lagö, I. Claesson, *Analog and Digital Approaches of Attenuation Boring Bar Vibrations During Metal Cutting Operations*, ICSV12 - The Twelfth International Congress on Sound and Vibration, Lisbon, Portugal, 11 - 14 July, 2005.

H. Åkesson, T. Smirnova, L. Håkansson, I. Claesson and T. Lagö, *Analog versus Digital Control of Boring Bar Vibration*, Accepted for publication in proceedings of the SAE World Aerospace Congress, WAC, Dallas, Texas, USA, October 3-6, 2005.

H. Åkesson, T. Smirnova, L. Håkansson, I. Cleasson, A. Sigfridsson, T. Svensson and T. Lagö, *Active Boring Bar Prototype Tested in Industry*, Adaptronic Congress 2006, 03-04 May, Göttingen, Germany.

H. Åkesson, T. Smirnova, L. Håkansson, I. Claesson, A. Sigfridsson, T. Svensson and T. Lagö, *A First Prototype of an Active Boring Bar Tested in Industry*, ICSV13 - The Thirteenth International Congress on Sound and Vibration, Vienna, Austria, 2 - 6 July, 2006.

T. Smirnova, H. Åkesson, L. Håkansson, I. Claesson and T. Lagö, *Identification of Spatial Dynamic Properties of the Boring Bar By Means of Finite Element Model: Comparison with Experimental Modal Analysis and Euler-Bernoulli Model*, ICSV13 - The Thirteenth International Congress on Sound and Vibration, Vienna, Austria, 2 - 6 July, 2006.

H. Åkesson, T. Smirnova, L. Håkansson, I. Claesson and T. Lagö, *Comparison of different controllers in the active control of tool vibration; including abrupt changes in the engagement of metal cutting*, Sixth International Symposium on Active Noise and Vibration Control, ACTIVE, Adelaide, Australia, 18-20 September, 2006.

T. Smirnova, H. Åkesson, L. Håkansson, I. Claesson and T. Lagö, *Investigation of Boring Bar Mode Shape Rotation by Experimental Modal Analysis in Correlation with Finite Element Modeling*, Noise and Vibration Engineering Conference, ISMA2006, Leuven, Belgium, 18 - 20 September 2006.

H. Åkesson, T. Smirnova, L. Håkansson, I. Claesson and T. Lagö, *Vibration in Turning and the Active Control of Tool Vibration*, Second World Congress on Engineering Asset Management and the Forth International Conference on Condition Monitoring, Harrogate, 11 - 14 June, 2007.

H. Åkesson, T. Smirnova, L. Håkansson, I. Claesson and T. Lagö, *Investigation of the Dynamic Properties of a Boring Bar Concerning Different Boundary Conditions*, ICSV14 - The Fourteenth International Congress on Sound and Vibration, Cairns, Australia, 9 - 12 July, 2007.

H. Åkesson, T. Smirnova, L. Håkansson, I. Claesson and T. Lagö, *Investigation of the Dynamic Properties of a Passive Damped Boring Bar*, In proceedings of Adaptronic Congress 2008, Berlin, Germany, 20-21 May, 2008.

T. Smirnova, H. Åkesson, L. Håkansson, I. Claesson and T. Lagö, *Modeling a Clamped Boring Bar using Euler-Bernoulli Beam Models with Various Boundary Conditions*, MMWP08 - The third International Conference on Mathematical Modelling of Wave Phenomena, Växjö, v1106, pp 149-156, Sweden, 9-13 June, 2008.

H. Åkesson, T. Smirnova, L. Håkansson, I. Claesson and T. Lagö, *Advantages and Drawbacks Using Different Sensors in Feedback Control in Active Boring Bar Applications*, ICSV15 - The Fifteenth International Congress on Sound and Vibration, Daejeon, Korea, 6-10 July, 2008.

T. Smirnova, H. Åkesson, L. Håkansson, I. Claesson and T. Lagö, *Investigation Concerning Actuator Position in an Active Boring Bar Regarding Its Performance by Means of "3-D" Finite Element Models*, ICSV15 - The Fifteenth International Congress on Sound and Vibration, Daejeon, Korea, 6-10 July, 2008.

H. Åkesson, T. Smirnova, L. Håkansson, I. Claesson and T. Lagö, *Dynamic Properties of Tooling Structure: Hydraulic Clamping versus Standard Screw Clamping in the Lathe Application*, CST2008 - The Ninth International Conference on Computa-

tional Structures Technology, Athens, Greece, 2-5 September, 2008.

T. Smirnova, H. Åkesson, L. Håkansson, I. Claesson and T. Lagö, *Estimation of an active boring bar's control path FRF:s by means of a "3-D" FE model of the system "boring bar - actuator - clamping house" with Coulomb friction*, CST2008 - The Ninth International Conference on Computational Structures Technology, Athens, Greece, 2-5 September, 2008.

H. Åkesson, T. Smirnova, L. Håkansson, I. Claesson and T. Lagö, *Developments Steps of an Active Boring Bar for Industrial Application*, In Proceedings of the 37th International Congress and Exposition on Noise Control Enginering, Internoise 2008, Shanghai, China, 26-29 October, 2008.

H. Åkesson, T. Smirnova, L. Håkansson, I. Claesson and T. Lagö, *Investigation of the Dynamic Properties of a Milling Structure; Using a Tool Holder with Moderate Overhang*, IMAC-XXVII , Orlando, Florida USA, 9-12 February, 2009.

T. Smirnova, H. Åkesson, L. Håkansson, I. Claesson and T. Lagö, *Investigations of Possibilities of Improvement of a Finite Element Model of an Active Boring Bar*, IMAC-XXVII, Orlando, Florida USA, 9-12 February, 2009.

T. Smirnova, H. Åkesson, L. Håkansson, I. Claesson and T. Lagö, *Investigations Concerning Dynamic Properties of an Active Boring Bar Regarding Its Performance by Means of "1-D" Finite Element Models*, ICSV16 - The Sixteenth International Congress on Sound and Vibration, Krakow, Poland, 5-9 July, 2009.

H. Åkesson, T. Smirnova, L. Håkansson, I. Claesson and T. Lagö, *Preliminary investigation of active control of a milling tool holder*, ACTIVE 2009 - The 2009 International Symposium on Active Control of Sound and Vibration, Ottawa, Canada, 20 - 22 August, 2009.

T. Smirnova, M. Larsson, I. Gertsovich, S. Johansson, I. Claesson, and L. Håkansson, *"Initial Investigations Concerning Modelling of Sound Propagation in Ducts with ANC by Means of Two-Port Theory and FEM"*, ICSV17 - The Seventeenth International Congress on Sound and Vibration, Cairo, Eqypt, 18-22 July, 2010.

Introduction

Vibration is a common phenomenon in all physical objects possessing mass and elasticity. There are some vibrations that are useful and desired, e.g. vibrations of parts of musical instruments, vibrations of a cone of a loudspeaker transducer. In engineering, however, vibrations are often considered to be harmful and unwanted, some examples are: the large vibration amplitudes of buildings and bridges excited by e.g. wind, the flutter of an airplane's wings or vibrations that lead to damage or reduced efficiency in machines. Vibration or oscillation is generally referred to as a repetitive motion of a system in time around its position of equilibrium [1, 2], e.g. see Fig. 1. In order to predict the dynamic behavior of mechanical structures, dynamic analysis is often utilized. Dynamic analysis comprises e.g. the calculation of spatial dynamic properties, natural frequencies, mode shapes, etc., of mechanical systems and is based on models of these systems.

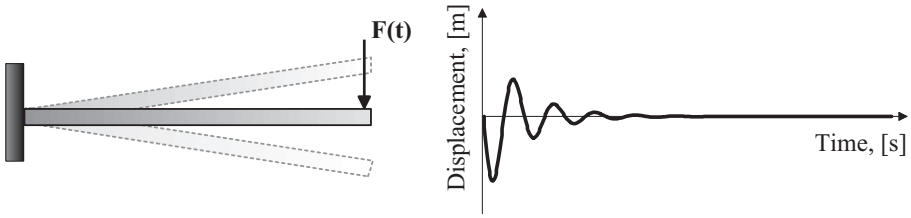

Figure 1: An example of the decaying vibration of a cantilever beam.

Vibration is a common problem in the manufacturing industry especially in relation to metal cutting (e.g., during turning, milling and grinding operations). Internal turning involves machining cavities inside workpiece materials to pre-defined geometries by means of a tool holder usually referred to as a boring bar (see Fig. 2). Traditionally, the interface between the cutting insert and the machine tool, i.e., the tooling structure, is considered to be the weakest link in the machining system [3, 4]. With respect to internal turning, the critical component in the tooling structure is usually the boring bar, which may be clamped inside the clamping house by means of screws, hydraulic pressure, spring-clamps, etc. The tooling structure may exhibit vibrations of different kinds: free and forced vibrations as well as self-excited chatter [3–6]. Vibrations such as these may result in a failure to maintain machining tolerances resulting in unsatisfactory surface finish, excessive tool wear and thus decreased productivity of the lathe.

Active Control of Boring Bar Vibrations

Different methods may be utilized to reduce degrading vibration problems in internal turning and improve both productivity and the working environment. There are basically two general directions for controlling boring bar vibrations. The first direction refers to manual control of cutting data in a structured manner in order to maintain stable cutting [3, 7, 8]. The second direction concerns structural modifications of the boring bar with the purpose of increasing its dynamic stiffness to resist the machine tool chatter [3, 9–11]. Generally, the boring bar vibration control methods that modify the dynamic stiffness are divided into two groups: passive and active control. When utilizing passive boring bar vibration control, the increase in dynamic

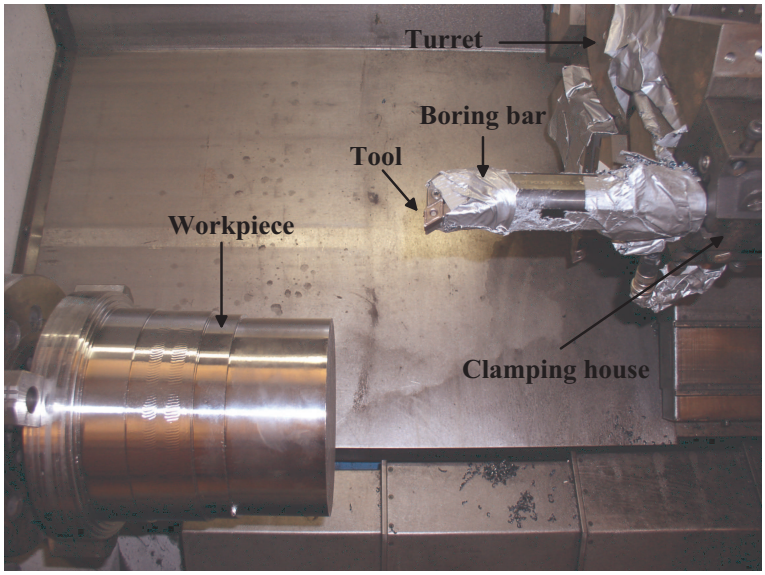

Figure 2: The part of the lathe Mazak SUPER QUICK TURN - 250M CNC where machining is carried out.

stiffness is achieved by changing the structural stiffness or/and the damping of the bar [3, 9].

The general idea behind active vibration control is to attenuate structural vibration induced through primary excitation by introducing controlled secondary "anti vibration" induced via an actuator (see Fig. 3).

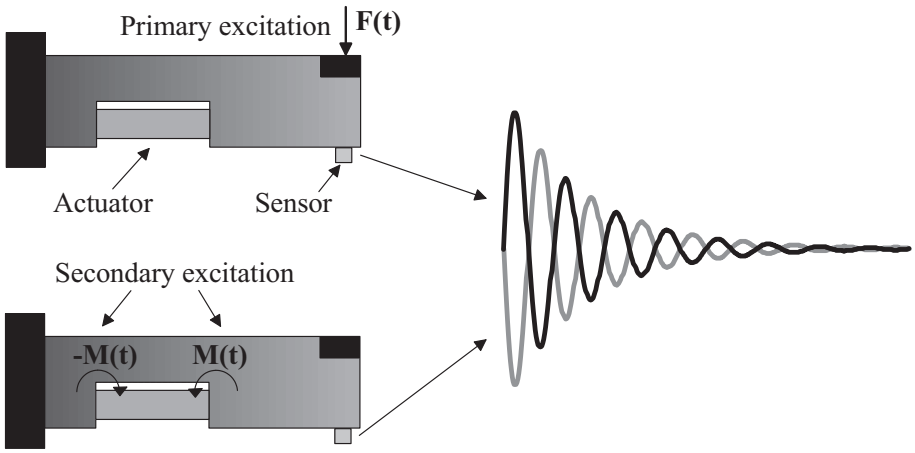

Figure 3: A scheme of active vibration control in internal turning.

One way to implement active control in the internal turning operation is to use an active boring bar based on a standard industry boring bar in combination with a feedback controller and a suitable amplifier, etc. The active boring bar may be

equipped with an error accelerometer to measure the boring bar vibrations and an embedded piezoelectric actuator to introduce the secondary "anti vibration" based on the control signal produced by the feedback controller [11]. The feedback controller may be either analog or digital. In this thesis, an adaptive digital feedback controller based on the filtered-x LMS algorithm is utilized in the simulation of the active control of boring bar vibration [11].

The active control of boring bar vibration implemented by utilizing an active boring bar results in the selective increase of the dynamic stiffness of the boring bar at the frequency of its fundamental bending mode. This is thus a flexible solution.

The feedback filtered-x LMS algorithm

For the active control of boring bar vibration in internal turning, a feedback controller is appropriate since the primary excitation force signal is impossible to measure separately, which means that a feedforward reference signal cannot be produced [11]. An adaptive digital controller based on the feedback filtered-x LMS algorithm can be used to control boring bar vibration [11, 12]. The feedback filtered-x LMS algorithm is based on a gradient search method which in its turn relies on an optimization technique known as the method of steepest descent [13]. The objective of the control is to minimize the mean square value of the error signal. In this case, the error signal is the output signal of a vibration sensor sensing the boring bar vibration, i.e., the sum of the primary boring bar vibration originating from the material deformation process and the secondary "anti vibration" induced by the actuator embedded in the boring bar [12]. A block diagram of the feedback filtered-x LMS algorithm is shown in Fig. 4 and it is described by Eqs. (1-4) [11, 13].

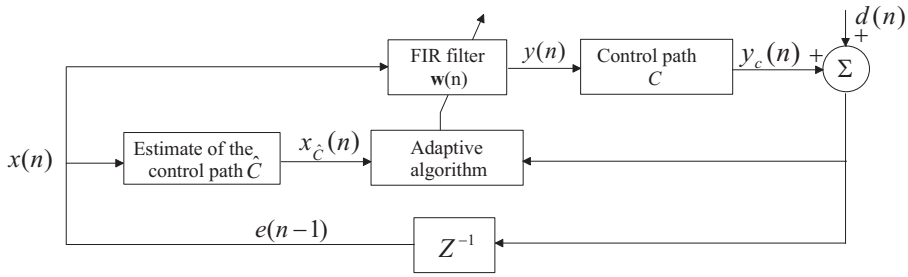

Figure 4: Block diagram of an active feedback control system based on the feedback filtered-x LMS algorithm.

$$
\begin{aligned}
y(n) &= \mathbf{w}^T(n)\mathbf{x}(n), && (1)\\
e(n) &= d(n) + y_c(n), && (2)\\
\mathbf{w}(n+1) &= \mathbf{w}(n) - \mu \mathbf{x}_{\hat{\mathbf{C}}}(n) e(n), && (3)\\
\mathbf{x}_{\hat{\mathbf{C}}}(n) &= \left[\sum_{i=0}^{I-1} \hat{c}_i x(n-i), \ldots, \sum_{i=0}^{I-1} \hat{c}_i x(n-i-P+1) \right]^T . && (4)
\end{aligned}
$$

Here, $\mathbf{w}(n)$ is the adaptive FIR filter coefficient vector with the length P; $\mathbf{x}(n) = [x(n), x(n-1), \ldots, x(n-P+1)]^T$ is the reference signal vector; $y(n)$ is the output

signal from the adaptive FIR filter; $d(n)$ is the primary disturbance signal and $e(n)$ is the error signal. The reference signal is related to the error signal as $x(n) = e(n-1)$ [11, 13]. Furthermore, $\mathbf{x}_{\hat{\mathbf{C}}}(n)$ is the filtered reference signal vector that is usually produced e.g., by filtering the reference signal with an I -coefficients FIR filter estimate of the control path, $\hat{c}_i$, $i \in 0, 1, \ldots, I-1$. $y_C(n)$ is the secondary "anti vibration"; $\hat{C}$ is an estimate of the control path and μ is the step size [11–13].

By utilizing the filtered reference signal vector to form the direct gradient estimate in the coefficient adjustment algorithm in Eq. (3), it will on average adjust the adaptive filter coefficients in the direction of steepest descent of the mean square error as a function of the filter coefficients. This, of course, requires that the estimate of the control path is fairly well correlated with the actual control path in the frequency range of interest for active control.

The rule of thumb, when selecting the step size μ for convergence in the mean-square of the filtered-x LMS algorithm, is expressed by

$$0 < \mu \leq \frac{2}{(P+\delta)E[x^2_{\hat{C}}(n)]}, \tag{5}$$

where δ is the overall delay (in samples) in the control path [13, 14].

The LMS algorithm

The control path present in the active control of boring bar vibration in internal turning is usually comprised of a signal conditioning filter, an actuator amplifier, the transfer path between the actuator input and the boring bar's response measured by the error accelerometer [12]. The control path C can be estimated by means of the LMS algorithm [15]. A block diagram of the control path estimation using the LMS algorithm is shown in Fig. 5.

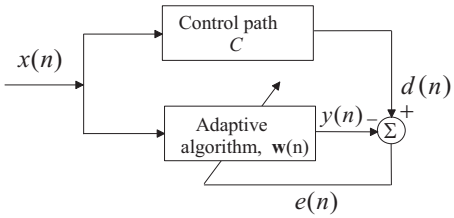

Figure 5: Block diagram of the control path estimation using the LMS algorithm.

The LMS algorithm steers the filter coefficients in $\mathbf{w}(n)$ to minimize the error signal $e(n)$ in the mean-square sense. The algorithm can be summarized as follows:

$$\begin{aligned} y(n) &= \mathbf{w}^T(n)\mathbf{x}(n), & (6)\\ e(n) &= d(n) - y(n), & (7)\\ \mathbf{w}(n+1) &= \mathbf{w}(n) + \mu e(n)\mathbf{x}(n), & (8) \end{aligned}$$

where $\mathbf{x}(n)$ is the input signal vector to the adaptive filter; $\mathbf{w}(n)$ is the adaptive FIR filter coefficient vector; $y(n)$ is the output signal of the adaptive filter; $e(n)$ is the error signal; $d(n)$ is the desired signal and μ is the step size.

In order for the LMS algorithm to converge in the mean square, it is recommended that the step size should be selected according to [15]:

$$0 < \mu \leq \frac{2}{IE[x^2(n)]}, \tag{9}$$

where I is the length of the adaptive FIR filter coefficient vector $\mathbf{w}(n)$.

Methods of the Dynamic Modeling of a Boring Bar

Design of the active boring bar implies structural modification of the original boring bar, e.g. embedment of the actuator. These modifications result in the alteration of the dynamic stiffness of the boring bar and its spatial dynamic properties. Therefore, the level of success of utilizing active control for the reduction of tool vibration is closely related to the engineer's knowledge of the dynamic properties of the tooling structure [3, 16].

The dynamic properties of boring bars may be estimated using a number of different approaches. Simple models of the boring bar can be created using Euler-Bernoulli or Timoshenko beam theory. However, these distributed-parameter system models are not capable of accurately describing the actual boring bar's geometry and boundary conditions (such as interfaces and joints between machine tool parts, e.g., the screw clamping of the boring bar inside the clamping house). Assuming rigid boundary conditions while utilizing such distributed-parameter system models leads to oversimplification of the real structure and rough estimates of the dynamic properties. Thus, the influence of joints should not be underestimated because they not only introduce damping in the structure, they may also contribute to nonlinearity in the structure's response [17, 18]. More accurate models of machine tool parts together with joints and contact interfaces can be developed using numerical methods, e.g., finite element analysis [18]. In order to verify and update models of dynamic systems, modal testing techniques or experimental modal analysis is generally used to provide information regarding the actual dynamic behavior of a system [17].

Experimental Modal Analysis

Experimental Modal Analysis (EMA) is usually referred to as the process of identifying a system's dynamic properties (such as natural frequencies, relative damping ratios and mode shapes) based on the experimental vibration measurements of the time-varying excitation and system's response signals [19].

Experimental modal analysis is built on the following assumptions: that the system is linear and time invariant, that the system is observable, and that Maxwell's reciprocity principle holds [20]. The experimental modal analysis procedure basically consists of three stages: measurement planning, frequency response measurements, modal data extraction [21]. The concept of experimental modal analysis will be described in the subsequent text based on an example structure, a simple "clamped-free" beam or cantilever beam, see Fig. 6. The first three bending modes of the cantilever beam provided as an example will be considered in the experimental modal analysis description.

Measurement planning In order to extract estimates for the first three natural frequencies, damping ratios and mode shapes of the cantilever beam, it is generally sufficient to measure the transverse response of the beam in at least three spatial locations [17]. The most widely used transducers in vibration measurements are as follows: the accelerometer and the force transducer. Usually, force transducers are used to measure the force produced by excitation sources such as impulse hammers and electrodynamic shakers. Characteristics such as the accelerometer's weight, axial sensitivity and transverse sensitivity, frequency range, etc., should be considered during measurement planning. Other considerations include the selection of suitable transducer locations, and the method of attaching the transducers to the structure (cantilever beam). It is generally preferable to avoid attaching accelerometers and force transducers to the structure in the vicinity of nodes of eigenmodes that are important to identify by the experimental modal analysis. Methods such as distributed-parameter system modeling and finite element modeling of the structure may be utilized prior to measurement in order to predict the positions of relevant structural nodes. Now, let us assume that we have selected three adequate response and excitation positions for measurement and excitation in the transverse direction of the example cantilever beam, as illustrated in Fig. 6. In the setup of an electrodynamic shaker, it is usually important to suspend the shaker by flexible strings. This is done in order to isolate eventual excitation of the structure to be analyzed via the shaker suspension. The shaker should ideally only apply force strictly in the desired excitation direction to the structure via a force transducer, and, if possible, the shaker should not impose any mass loading on a structure. The spatial dynamic properties of a structure modeled as an N degree-of-freedom system may usually be described by symmetric stiffness [$\mathbf{K}$], mass [$\mathbf{M}$] and damping [$\mathbf{C}$] matrices [17, 22]. Thus, in the frequency domain, the relation between the input forces and the output accelerations of the system approximated by the N degrees-of-freedom may, principally, be described by a $N \times N$ symmetric accellerance matrix or frequency response matrix [$\mathbf{H}(f)$] [19]. Hence, it may be sufficient to measure one row or one column in [$\mathbf{H}(f)$] in order to reconstruct the complete accelerance matrix [17]. In order to estimate the required accelerance functions of one row or of one column in [$\mathbf{H}(f)$], a suitable set of acceleration responses and excitation forces have to be measured and recorded. There are two common ways to perform the measurements. In the first case, the excitation force is applied and measured in the transverse direction in one of the cantilever beam measurement positions simultaneous with its response at the three measurement locations using three vibration sensors, illustrated in Fig. 6. In the second case, only one vibration transducer is used to measure the cantilever beam response in one of the three measurement positions. The excitation force is applied and measured in the transverse direction in one of the three positions simultaneous with its response at the selected response measurement location. Subsequently, the excitation force is moved to the next measurement position and the force and response are again measured simultaneously. Finally, this is repeated, with the excitation force moved and applied to the remaining measurement position. Selecting a method for carrying out the measurements depends upon the number of available vibration transducers and the type of excitation signal that is required to extract a sufficient modal model [17, 19] for the system, etc. Basically, a modal model is an approach to describe the frequency response function matrix of a system in terms of partial fraction expansion where residues are dependent on mode shapes and poles are dependent on the damped natural frequencies of the system [17, 19].

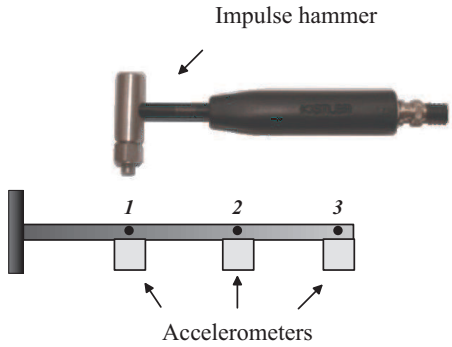

Figure 6: Experimental setup for experimental modal analysis of the cantilever beam example.

Frequency Response Function Measurement The excitation forces and structure's response signals from the transducers are recorded by means of a signal analyzer. Modern signal analyzers are usually based on a PC with (for example) experimental modal analysis software, connected to a data acquisition system with a suitable number of input and output channels. The sensor output signals are basically low-pass filtered, analog-to-digital converted by a data acquisition system. Generally, parallel with the measurements, the acquired data are transferred to the PC. Fast Fourier Transform (in combination with windowing and averaging) is utilized to estimate power spectral density for the force signals or excitation signals, and cross-power spectral density between the response signals and excitation signals. These quantities are used to produce an estimate of the accelerance function matrix or the frequency response function matrix. The coherence function and the random error are usually calculated to ensure the quality of the estimates produced [17, 23].

Modal Data Extraction At this phase of experimental modal analysis (EMA) the dynamic properties of the structure are estimated. This process is also often referred to as a *curve fitting* procedure. The curve fitting procedure can be carried out using various techniques both in the time and frequency domain [17, 20]. However, simple single mode or SDOF methods are sufficient to explain the concept of the modal data extraction. In the case of EMA of the cantilever beam example (with well separated modes), the natural frequencies and relative damping ratios may be estimated from the driving point frequency response function (the FRF estimate between the excitation signal and the response signal, measured along the same direction and at the same position on the structure). The three damped natural frequencies can be estimated simply by choosing the frequencies corresponding to the three maximum values of the magnitude function $|H(f)|$, illustrated for one peak in Fig. 8. The relative damping can be estimated using the "Half-power" bandwidth method (see Fig. 8). Subsequently, with the aid of this information and the damped eigenfrequencies, estimates of the undamped natural frequencies can be produced [19, 24].

The next step involves extracting the mode shapes from the measured data. An illustrative but rough approach is to construct a mode shape as follows: first, one of the damped eigenfrequencies, f_{di}, where $i \in \{1, 2, 3\}$, is selected. Subsequently, the peak values of the imaginary part of the accelerance functions $Im\{H_{s1}(f_{di})\}$, where

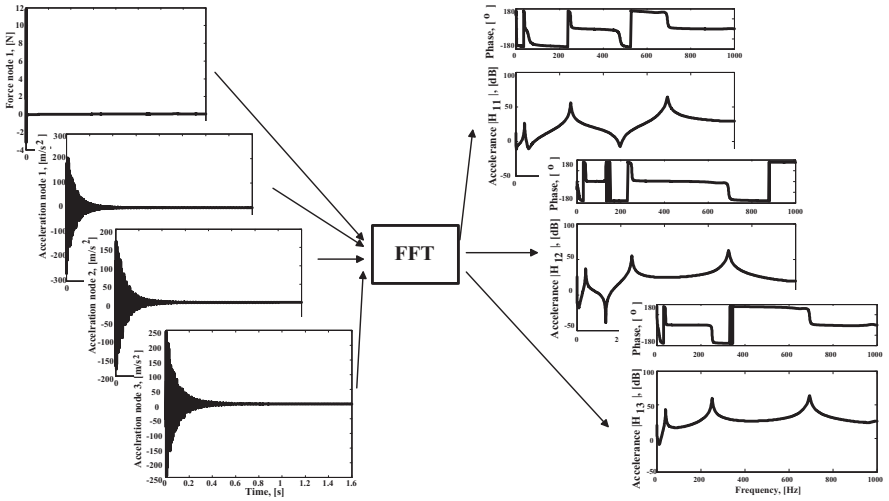

Figure 7: Measured force and responses for the cantilever beam example, and corresponding frequency response functions' estimates or magnitude and phase functions of accelerance functions.

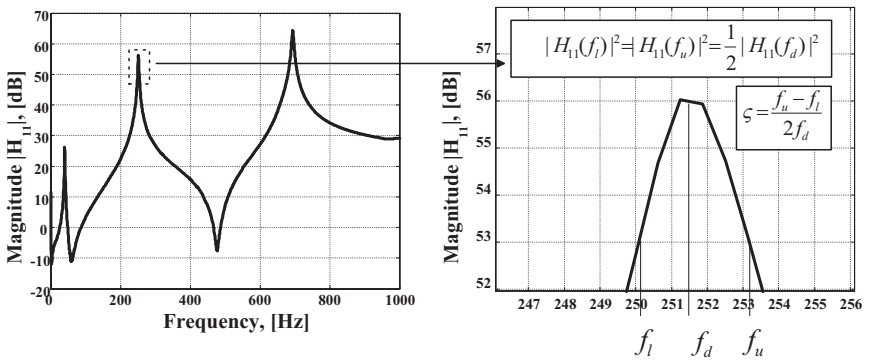

Figure 8: Magnitude function of the point accelerance function for the cantilever beam example; identification of a damped natural frequency and corresponding relative damping using the "Half-power" bandwidth method.

$s \in \{1, 2, 3\}$ (assuming that the cantilever beam is excited at position 1) corresponding to the selected eigenfrequency, are extracted. The mode shapes are finally constructed as $\{\ Im\{H_{11}(f_{di})\},\ Im\{H_{21}(f_{di})\},\ Im\{H_{31}(f_{di})\}\}^T$ where $i \in \{1, 2, 3\}$. The three extracted mode shapes are illustrated in Fig. 9. The validity of this statement follows from the modal model [19].

Distributed-Parameter System Model

In practice, all engineering structures can be considered as systems with distributed parameters. This implies that a structure consists of an infinite number of contin-

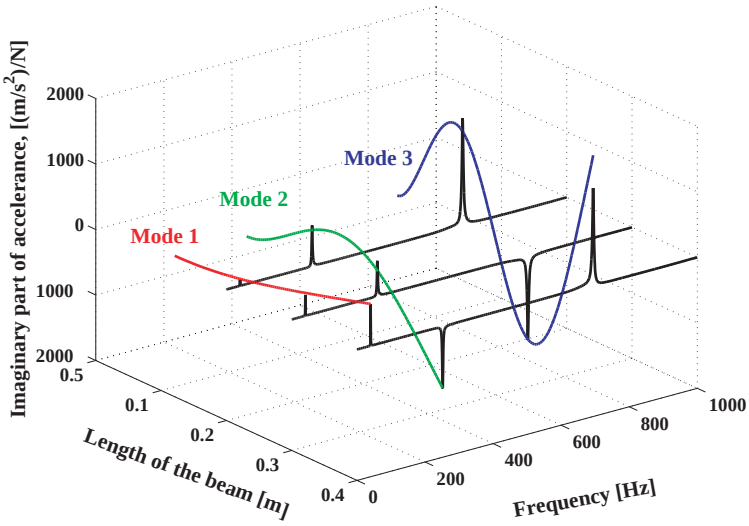

Figure 9: Illustration of the mode shape extraction.

uously distributed infinitesimal mass particles connected to each other with some elasticity and energy dissipation mechanism. Thus, structure's inertial, elastic and damping properties are distributed in space and often referred to as "distributions" [2].

The distributed-parameter system model is considered to be a model with an infinite number of degrees-of-freedom. This relates to another distinctive feature of these models - they are characterized by an infinite number of eigenmodes [19]. The displacement of the structure is described by a continuous function dependent on time and spatial variables. In the simplest case (if the transverse vibration of a "1-D" beam is considered, see Fig. 10) the transversal displacement is $w(z,t)$.

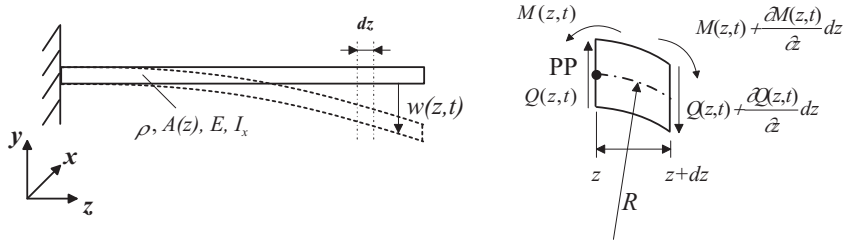

Figure 10: Distributed-parameter model of transverse vibration of a cantilever beam.

The equation of motion for a system with distributed parameters such as the transverse vibration of a simple beam may conveniently be derived based on Newton's second law, and is a partial differential equation [19]. For instance, the Euler-Bernoulli model of the transverse vibration of the beam is derived considering an infinitesimal element of the beam with the length dz, see Fig. 10.

Basically, two equilibrium equations are formed: all forces acting on the element in the vertical direction are summed, and the moments acting on the element about the "x"-axis through point PP are summed.

The summation of moments and forces are carried out based on the right-hand rule and the general positive rotation convention [16]. Shear deformation is neglected by this model, yielding a shear force $Q(z,t)$ that is proportional to the spatial change in the bending moment $Q(z,t) = -\frac{\partial M(z,t)}{\partial z}$. The influence of rotary inertia is also neglected [19]. The model assumes that the bending moment is inversely proportional to the radius of curvature of the bent element $M(z,t) = -\frac{EI_x}{R} = -\frac{EI_x \partial^2 w(z,t)}{\partial z^2}$ [16]. The equation of motion for the free transverse vibration of the distributed parameter cantilever beam is given by the following fourth order partial differential equation:

$$\rho A(z)\frac{\partial^2 w(z,t)}{\partial t^2} + EI_x \frac{\partial^4 w(z,t)}{\partial z^4} = 0. \tag{10}$$

In order to find a closed-form solution to this equation, four boundary conditions and two initial conditions are required. The combination of the partial differential equation (describing the dynamic motion of the structure) and the boundary conditions (which are imposed upon the structure) is often referred to as a *boundary-value problem* [2].

A closed-form solution to the boundary-value problem may only be found if the structure's material is homogeneous, elastic and isotropic [25]. The dynamic response can, in this case, be produced as a sum of the normal mode contributions [19].

$$w(z,t) = \sum_{i=1}^{\infty} T_i(t) Z_i(z), \tag{11}$$

where $T_i(t)$ is ith temporal solution and $Z_i(z)$ is ith normal mode. The closed-form solution contains an infinite number of mode shapes. However, in most cases it is sufficient to consider only a few of them, i.e., those contributing the most to the structure's dynamic response [25].

A closed-form solution is often impossible to obtain for a general type of structure, e.g., a structure combining various boundary conditions [25]. In the case of modeling nonlinear systems, discrete-parameter systems with approximate solutions are suggested.

Finite Element Model

The finite element method (FEM) was developed for the modeling and analysis of complicated structures when closed form solutions are difficult to obtain. This method is based on the approximation of a continuum structure by the assembly of a finite number of parts (elements), and is based on the variational and interpolation methods for modeling and solving boundary value problems [19, 22].

In the modeling of a structure with the finite element method, a spatial model, assembled with discrete *finite elements* connected via the endpoints called *nodes* (should not be mistaken for the nodes of the vibrating modes of a structure) that approximate the actual structure's spatial geometry, is produced. The force-displacement relationships are established for each finite element based on the principal of virtual work [2, 22]. A spatial solution is assumed for each finite element and approximated by a low-order polynomial known as a *shape function*. At this stage, local stiffness and mass matrices can be derived based on relations for the kinetic and strain energies, and for the shape functions. The finite elements are assembled into a finite element model of the structure. Global stiffness and mass matrices are constructed based on the local ones. The model of the structure's dynamic response, unlike in the case

of the distributed-parameter system, is governed by a system of ordinary differential equations. During the solution process, the equilibrium of forces at the joints and the compatibility of displacements between the elements are satisfied, so the assembled finite elements are made to behave as a complete "structure". The time response can be found using well-developed numerical integration techniques [1, 21].

The concept of the finite element method can be described using the example of the transverse vibration of the cantilever beam. The finite element model of the "clamped-free" beam consists of four nodes and three finite elements (see Fig. 11).

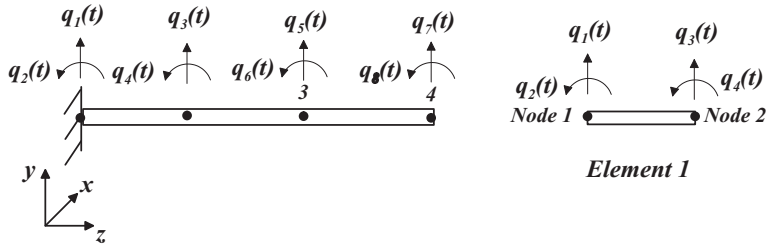

Figure 11: Finite element model of a cantilever beam.

In order to describe transverse vibrations of the beam, each node has one translational and one rotational degree-of-freedom. Thus, the simplest beam element has two nodes, with four degrees-of-freedom in total.

The displacement of any point within the finite element can be described by the function [2]:

$$w(z,t) = \sum_{i=1}^{4} q_i(t) n_i(z), \tag{12}$$

where $q_i(t)$ are *generalized coordinates*, or degrees-of-freedom and $n_i(z)$ are *shape functions* [2]. In the case of the Euler-Bernoulli beam element, the generalized coordinates are translational displacements $q_1(t)$ and $q_3(t)$, and rotational displacements $q_2(t)$ and $q_4(t)$ at the first and second node of the element respectively (see Fig. 11).

The shape functions are determined over a finite element. They have a maximum amplitude equal to unity, and are equal to zero outside the finite element [22]. However, the shape functions are the same for all elements of a certain type.

In this case, the shape functions can be derived from the fact that the transverse displacement must satisfy $\frac{\partial^2}{\partial z^2}\left[EI_x \frac{\partial^2 w(z,t)}{\partial z^2}\right] = 0$ and boundary conditions at the ends of the element with the length l.

The element stiffness $[\mathbf{K}]_e$ and mass matrices $[\mathbf{M}]_e$ can be derived based on the expressions for the strain energy $\mathcal{V}(t)$ and the kinetic energy $\mathcal{T}(t)$ of the Euler-Bernoulli beam element [19].

$$\mathcal{V}(t) = \frac{1}{2}\int_0^l EI_x \left[\frac{\partial^2 w(z,t)}{\partial z^2}\right]^2 dz, \tag{13}$$

$$\mathcal{T}(t) = \frac{1}{2}\int_0^l \rho A \left[\frac{\partial w(z,t)}{\partial t}\right]^2 dz. \tag{14}$$

The dimension of the element matrices $[\mathbf{K}]_e$ and $[\mathbf{M}]_e$ is 4×4, in correspondence with the amount of degrees-of-freedom assigned to an Euler-Bernoulli beam finite element. The system of differential equations describing the free vibration of the single element can be written as follows:

$$[\mathbf{M}]_e\{\ddot{\mathbf{w}}(t)\}_e + [\mathbf{K}]_e\{\mathbf{w}(t)\}_e = \{\mathbf{0}\}, \tag{15}$$

where $\{\mathbf{w}(t)\}_e = [q_1(t), q_2(t), q_3(t), q_4(t)]^T$ is the vector of the Euler-Bernoulli beam element displacements.

The global stiffness and mass matrices are assembled from individual element matrices by summarizing their elements at common degrees of freedom, see Fig. 12.

$$[\mathbf{K}] = \sum_{e=1}^{N_e} [\mathbf{K}]_e, \tag{16}$$

for common degrees of freedom.

$$[\mathbf{M}] = \sum_{e=1}^{N_e} [\mathbf{M}]_e, \tag{17}$$

for common degrees of freedom, where N_e is the number of finite elements in the model.

If the damping of a system can be assumed to be proportional, the global damping matrix $[\mathbf{C}]$ can be calculated as a linear combination of the global stiffness and the global mass matrices, i.e. $[\mathbf{C}] = \alpha[\mathbf{M}] + \beta[\mathbf{K}]$ (where α and β are constants) [19].

Boundary conditions, for instance for a fixed support, may be applied in the following manner: rows and columns corresponding to restricted degrees-of-freedom are removed from the global stiffness and mass matrices, see Fig. 12.

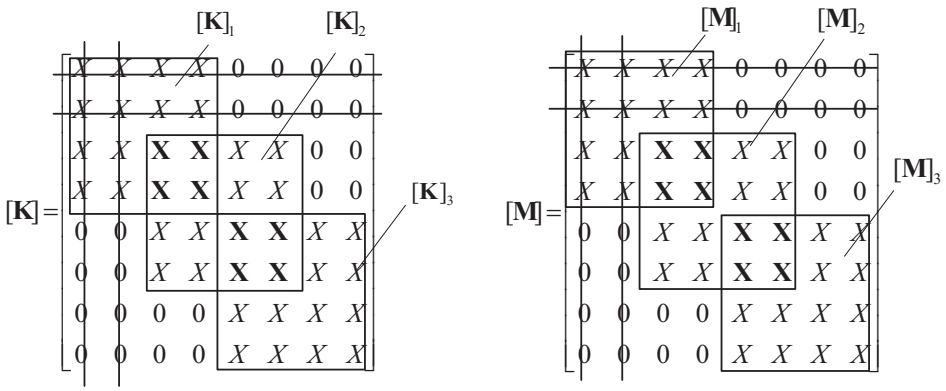

Figure 12: Illustration of the process of assembling global stiffness and mass matrices including application of the boundary conditions.

The equations of motion for the free vibration of an undamped mechanical system can now be described by a system of linear differential equations:

$$[\mathbf{M}]\{\ddot{\mathbf{w}}(t)\} + [\mathbf{K}]\{\mathbf{w}(t)\} = 0, \tag{18}$$

where $\{\mathbf{w}(t)\}$ is the vector containing unknown displacements of all degrees-of-freedom in the finite element model.

The natural frequencies and mode shapes can be calculated based on Eq. 18, assuming that the temporal solution is harmonic, yielding [22]:

$$(-(2\pi f)^2[\mathbf{M}] + [\mathbf{K}])\{\psi\} = \{\mathbf{0}\}, \tag{19}$$

where ψ is a *normal mode* of the system [22]. This *general linear eigenvalue* or *characteristic value* problem can be solved using standard modal analysis procedure [19]. In finite element analysis software methods such as Inverse Power Sweep or Lanczos are implemented for this purpose [1].

Nonlinear Interpolation of the Dynamic Properties for Active Boring Bars

One way to estimate an active boring bar's dynamic properties is to use finite element modeling. Utilization of this approach allows the creation of a broad but still finite set of models of an active boring bar with different actuator positions, see Fig. 13. By utilizing a suitable method for nonlinear interpolation between the dynamic properties of FE models of active boring bars with different actuator positions, the dynamic properties of active boring bars with actuator positions in between the FE models may be estimated.

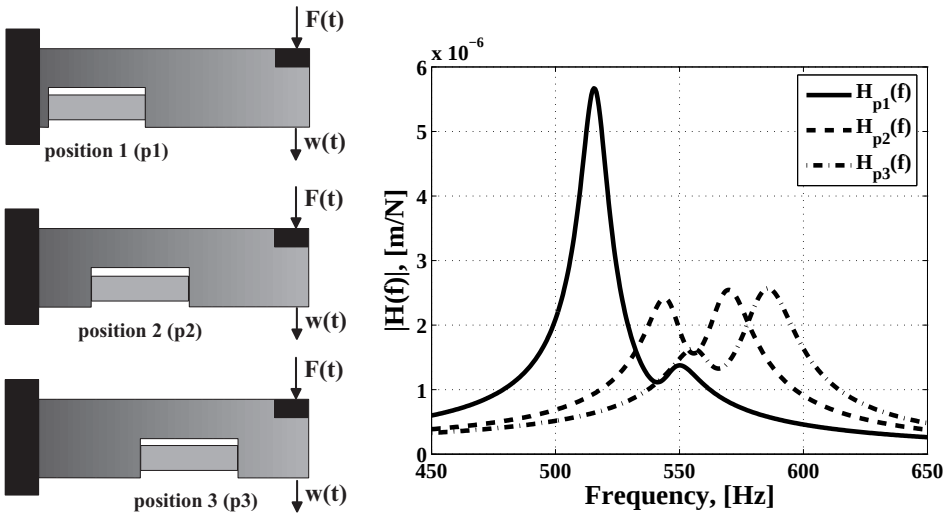

Figure 13: Magnitude of the point receptance frequency response function estimates produced based on the simulation of harmonic response of "3-D" FE models of active boring bars with three different longitudinal actuator positions.

Different methods may be utilized to conduct nonlinear interpolation between dynamic properties of a finite set of active boring bar FE models. These methods include polynomial interpolation, least mean squares approximations and artificial neural networks [26–28]. The global polynomial interpolation between known data points can be carried out using the Newton or Lagrange polynomial interpolation methods and the polynomial Least Mean Squares (LMS) approximation [26, 28]. The interpolation

polynomial obtained using these methods is unique. However, the success of these methods is conditioned by the selection of a favorable polynomial degree, ensuring a minimal interpolation error. Unfortunately, the suitable polynomial degree is rarely known in advance. Moreover, these methods are not applicable in the case of an excessive number of data points, which leads to large interpolation errors [28]. Some of these problems can be avoided by using local interpolation performed by means of e.g. splines (or, in general, low-order polynomials on the subsets of data points). This interpolation method is better suited to the problem of approximating a function with abrupt variations and usually results in lower interpolation errors.

Another way to approximate a nonlinear multivariable function such as $f(x_1, x_2, \ldots, x_n)$ is to use a multilayer perceptron neural network (MLP NN) [27,28]. A general MLP NN consists of a layer of input neurons, followed by a number of hidden layers of neurons and a layer of output neurons. A neuron here is referred to as a computation node that consists of a vector of inputs that are multiplied with synaptic weights, whereafter the result is subjected to a nonlinear activation function. The function of the neuron is to intervene between the network's input and output [27]. The accuracy of the approximation of a nonlinear function produced by a MLP NN is dependent on its architecture, which is not known in advance. However, for most applications, a 3-layered MLP NN containing two hidden layers is sufficient to exactly represent the continuous function of several variables [29] (see Fig. 14).

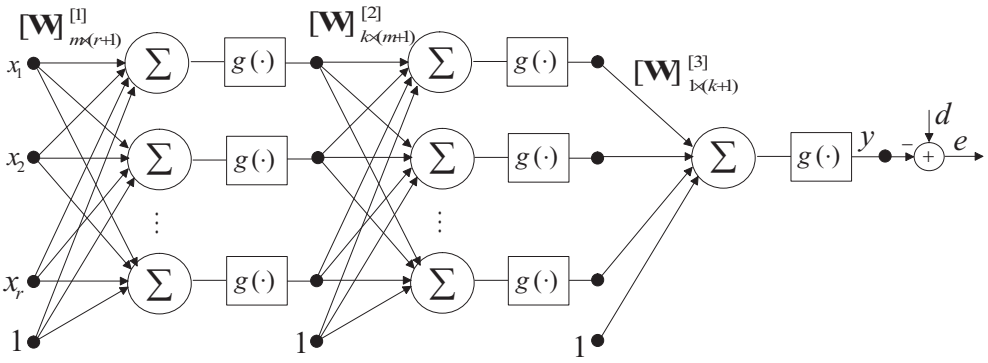

Figure 14: Architecture of a three-layer neural network.

The input to the first hidden layer is a vector consisting of r elements and containing measured data and a bias stimuli $[x_1, \ldots, x_r, 1]^T$. Weighting of the inputs at each layer of neurons is performed by means of matrices $[\mathbf{W}]^{[1]}$, $[\mathbf{W}]^{[2]}$ and $[\mathbf{W}]^{[3]}$ that contain the synaptic weights [27]. The synaptic weights can be considered as characteristics of the neural network. The network has m neurons in the first hidden layer and k neurons in the second hidden layer as well as one neuron in the output layer. The output from each neuron is the outcome of the activation function. The argument of the activation function is a weighted sum of the outputs from the previous layer. An activation function $g(\cdot)$ is usually a sigmoidal function which performs a nonlinear transformation between the input and the output. Each neuron in every layer is connected to each neuron in the next and in the previous layers correspondingly. However, the neurons in the same layer are not connected. The outcome of the output layer y is a prediction of the value of a nonlinear function. The error e

is calculated as a difference between the measured or known value of the function d and the prediction made by MLP NN y, i.e., $e = d - y$. The error is minimized in the least squares sense by means of training the MLP NN using, e.g., the Back-propagation algorithm [27, 30]. Training is performed on a set of training examples $(x_1(i), x_2(i), \ldots, x_r(i); d(i))$, where $i = 1, \ldots, I_{examples}$.

Investigations concerning the accuracy of using the MLP NN for a nonlinear function approximation reported in [28] indicate that this method requires a smaller computational load to perform interpolation compared to the polynomial methods that give the same level of interpolation errors. Moreover, the MLP NN has been successfully used to estimate the dynamic properties of mechanical systems [28, 31, 32].

PART I - On Accurate FE-modeling of a Boring Bar with "Free-Free" Boundary Conditions

The first part of this thesis focuses on the development of an accurate model of a standard boring bar used in industry. This is done as a first step in order to build an accurate model of an active boring bar. The finite element method, utilizing "3-D" finite elements, is suggested in order to obtain a precise description of the boring bar's geometry. The natural frequencies, mode shapes and rotational angles of the mode shapes of the boring bar were estimated based on the "3-D" FE model with "free-free" boundary conditions, see Fig. 15. Results from the FE modeling were compared and correlated with estimates produced by experimental modal analysis. The FE modeling results were also compared with results produced by the Euler-Bernoulli model of the boring bar with "free-free" boundary conditions. The influence of the mesh density of the "3-D" FE model on its spatial dynamic properties was investigated. The finite element's edge size was addressed with respect to the accuracy of the FE model. Finally, mass loading effects introduced by accelerometers attached to the boring bar were considered, with respect to the FE modeling. Incorporation of the mass loading effects into the FE model resulted in a significant reduction in the relative error of natural frequencies estimated with the help of the FE model.

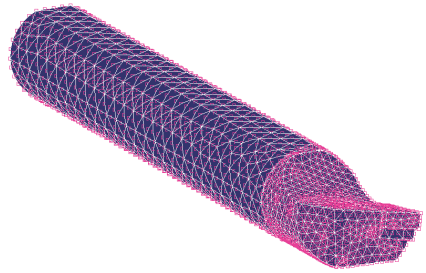

Figure 15: The finite element model of the boring bar with "free-free" boundary conditions.

PART II - Dynamic Modeling of a Boring Bar Using Theoretical and Experimental Engineering Methods Part 1: Distributed-Parameter System Modeling and Experimental Modal Analysis

Part II addresses the next step in building an accurate model of an active boring bar. Here, the standard boring bar clamped in the lathe was modeled using distributed-parameter system modeling. Initially, the Euler-Bernoulli and Timoshenko beam theories were used to describe the dynamics of the boring bar with "clamped-free" boundary conditions. In order to obtain a more adequate distributed-parameter system model, the flexibility of the section of the boring bar clamped inside the clamping house was described by means of "pinned-pinned-free" boundary conditions. Estimates of the natural frequencies and mode shapes obtained by means of various distributed-parameter system models were compared to the estimates produced by experimental modal analysis.

PART III - Dynamic Modeling of a Boring Bar Using Theoretical and Experimental Engineering Methods Part 2: Finite Element Modeling and Sensitivity Analysis

In part III, the finite element method is introduced for the modeling of a clamped boring bar. Initially, "1-D" finite element models corresponding to the distributed-parameter system models reported in part II are utilized to estimate the boring bar's natural frequencies and mode shapes. In order to further improve the spatial dynamic properties estimates, a "3-D" FE model of the boring bar with boundary conditions imposed by the rigid clamping house, and a "3-D" FE model of the system boring bar - deformable clamping house, were utilized (see Fig. 16). Estimates of the natural frequencies and mode shapes obtained by means of various finite element models were compared to the estimates produced by experimental modal analysis. Finally, the sensitivity of the spatial dynamic properties was investigated with respect to the variation in the structural parameters' values.

PART IV - Modeling of an Active Boring Bar

Part IV summarizes the development of a "3-D" FE model of the active boring bar. A mathematical model such as this is required in order to simplify the design procedure of an active boring bar, a process that involves a choice of the actuator's characteristics, the actuator size, the position of the actuator in the boring bar, etc. The "3-D" FE model contains the sub-models of the boring bar, the actuator and the clamping house, and incorporates the piezo-electric effect. The spatial dynamic properties are predicted using the "3-D" FE model and compared to estimates produced by means of experimental modal analysis of the actual active boring bar clamped in the lathe. The control path transfer functions (i.e., the frequency response functions between the actuator voltage and the accelerations at the error sensors positions) are calculated based on the "3-D" FE model by means of harmonic response and transient response

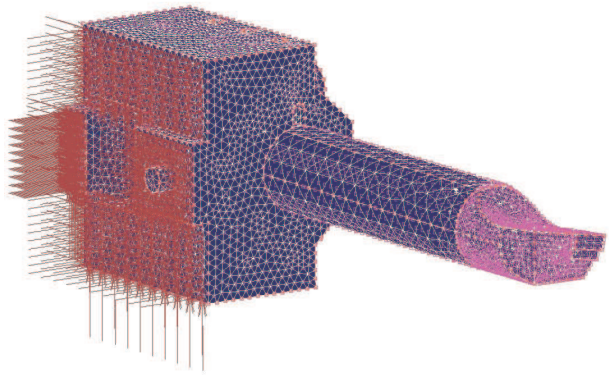

Figure 16: ”3-D” finite element model of the system boring bar - clamping house. In this case, the clamping house is deformable.

simulations. Again, the results are compared to those estimated experimentally. The influence of the Coulomb friction force on the active boring bar's dynamics was investigated by means of arctangent and bilinear models, initially, with respect to the example of the SDOF model and subsequently on the ”3-D” FE model of the active boring bar. Finally, receptance functions for the interfaces between the boring bar and the actuator were estimated using the ”3-D” FE model.

PART V - Initial Development of an Actuator Positioning Method for Active Boring Bars

The manufacturing process of an active boring bar is based on the structural modification of a standard boring bar. This implies that a part of the standard boring bar material is removed to produce an actuator groove. The position of the actuator groove is one of the key issues when designing an active boring bar, since it influences both the dynamic stiffness of the boring bar and its ability to produce secondary ”anti vibrations”. To improve the efficiency of the design procedure of active boring bars, a new strategy is suggested in part V. Finite element models of the system boring bar - actuator - clamping house with different actuator positions in combination with artificial neural networks are introduced and objective functions to suggest an actuator position at which to embed an actuator into an active boring bar are given. An active boring bar with an actuator position suggested by the method was manufactured. The spatial dynamic properties of the active boring bar prototype were estimated by means of experimental modal analysis and compared with the dynamic properties of the corresponding finite element model. The results indicate a fairly good correlation between the natural frequencies of the fundamental bending modes of the boring bar prototype and the corresponding ”3-D” finite element model. Moreover, results from the experimental evaluation of the active boring bar prototype and the finite element model show agreement concerning peak magnitudes, at the fundamental bending resonance frequencies of the bar, of control path frequency functions.

PART VI - Simulation of the Active Suppression of Boring Bar Vibrations by Means of a Boring Bar "1-D" Finite Element Model

Attenuation of boring bar vibration during the internal turning operation may be achieved by means of active vibration control. One way of implementing active vibration control in the internal turning operation is to use an active boring bar (e.g. the one addressed in part IV) together with a suitable controller. In this case, the primary boring bar vibrations originating from the material deformation process may be suppressed with secondary "anti vibrations" induced by the actuator. In order to simplify the design procedure of the active boring bar, both a mathematical model of a boring bar capable of incorporating the effect of the actuator and a model of the digital feedback controller to control the dynamic response of the active boring bar need to be considered. In part VI, a simple "1-D" finite element model of a clamped boring bar and a model of an adaptive digital controller realized by the feedback filtered-x lms algorithm are considered, see Fig. 17. The control algorithm has been incorporated into the ODE solver based on the Newmark integration scheme. The performance of the controller to suppress the boring bar's displacement induced by the broadband excitation force was simulated based on the boring bar's "1-D" FE model.

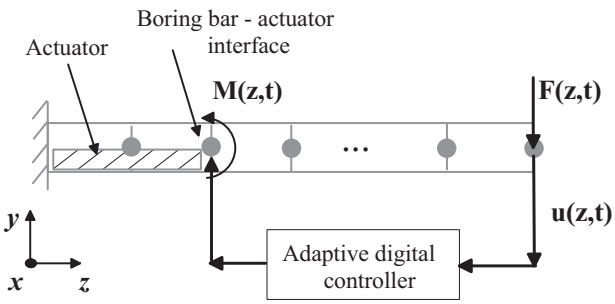

Figure 17: Schematic view of the "1-D" finite element model of a clamped active boring bar together with the adaptive digital controller.

References

[1] J.W. Tedesco, W.G. McDougal, and C.A. Ross. *Structural Dynamics: Theory and Applications*. Addison Wesley Longman, Inc., 1999.

[2] L. Mierovitch. *Fundamentals of Vibrations*. McGraw-Hill Companies, Inc., 2001.

[3] E. I. Rivin. Tooling structure: Interface between cutting edge and machine tool. *Annals of the CIRP*, 49(2):591–634, 2000.

[4] L. Håkansson, S. Johansson, and I. Claesson. *Chapter 78 - Machine Tool Noise, Vibration and Chatter Prediction and Control to be published in John Wiley & Sons Handbook of Noise and Vibration Control, Malcolm J. Crocker (ed.)*. John Wiley & Son, 2007.

[5] S.A. Tobias. *Machine-Tool Vibration*. Blackie & Son, 1965.

[6] H. E. Merritt. Theory of self-excited machine-tool chatter. *Journal of Engineering for Industry*, pages 447–454, 1965.

[7] C. M. Nicolescu. On-line identification and control of dynamic charactersitics of slender workpieces in turning. *Journal of Material Processing Technology*, 58:374–378, 1996.

[8] E. Al-Regib, J. Ni, and S.-H. Lee. Programming spindle speed variation for machine tool chatter suppression. *International Journal of Machine Tool & Manufacture*, 43(12):1229–1240, 2003.

[9] N. A. Ruud, R. Karlsen, K. Sørby, and C. Richt. Minimizing vibration tendencies in machining. *Technical Article at: http://www.coromant.sandvik.com*, 2005.

[10] S. G. Tewani, K. E. Rouch, and B. L. Walcott. A study of cutting process stability of a boring bar with active dynamic absorber. *International Journal of Machine Tools & Manufacture*, 35(1):91–108, 1995.

[11] I. Claesson and L. Håkansson. Adaptive active control of machine-tool vibration in a lathe. *IJAV - International Journal of Acoustics and Vibration*, 3(4):155–162, 1998.

[12] H. Åkesson, T. Smirnova, I. Claesson, and L. Håkansson. On the development of a simple and robust active control system for boring bar vibration in industry. *IJAV-International Journal of Acoustics and Vibration*, 12(4):139–152, 2007.

[13] L. Håkansson, S. Johansson, M. Dahl, P. Sjösten, and I. Claesson. *Chaper 12 - Noise cancelling headsets for speech communication in CRC Press Handbook on Noise Reduction in Speech Applications, Gillian M. Davis (ed.)*. CRC Press, first edition, 2002.

[14] S.J. Elliot. *Signal Processing for Active Control*. Academic Press, London, 2001.

[15] M.H. Hayes. *Statistical Digital Signal Processing and Modeling*. John Wiley and Sons, 1996.

[16] C.H. Hansen and S.D. Snyder. *Active Control of Noise and Vibration*. E& FN Spon, 1997.

[17] D.J. Ewins. *Modal Testing: Theory and Practice*. Research Studies Press, distributed by Wiley, 1984.

[18] D. Ewins. New strategies for model validation using modal test data. *Proceeding of the Fourteenth International Congress on Sound and Vibration*, July 2007.

[19] D.J. Inman. *Engineering Vibration*. Prentice-Hall, second edition, 2001.

[20] N.M.M. Maia and J.M.M. Silva. *Theoretical and Experimental Modal Analysis*. Research Studies Press Ltd., 1997.

[21] S.S. Rao. *Mechanical Vibrations*. Addison-Wesley Publishing Company, third edition, 1995.

[22] O. S. Zienkiewicz, R. L. Taylor, and J.Z. Zhu. *The Finite Element Method: Its Basis and Fundamentals*. Butterworth-Heinemann, 2005.

[23] J.S. Bendat and A.G. Piersol. *Engineering Application of Correlation and Spectral Analysis*. John Wiley & Sons, second edition, 1993.

[24] A. Brandt. *Introductory Noise & Vibration Analysis*. Saven EduTech AB, 2003.

[25] C.W. de Silva. *Vibration: Fundamentals and Practice*. CRC Press, 2000.

[26] M.J.D. Powell. *Approximation Theory and Methods*. Cambridge University Press, 1981.

[27] S. Haykin. *Neural Networks: A Comprehensive Foundation*. Prentice-Hall, Inc., second edition, 1999.

[28] J. M. D. Pereira, P. M. B. S. Gir ao, and O. Postolache. Fitting transducer characteristics to measured data. *IEEE Instrumentation & Measurements Magazine*, pages 26–39, 2001.

[29] R.D. Reed and R.J. Marks II. *Neural Smithing: Supervised Learning in Feedforward Artificial Neural Networks*. Prentice-Hall, Inc., second edition, 1999.

[30] D. E. Rumelhart, G. E. Hinton, and R. J. Williams. Learning representations by back propagating errors. *Nature*, 323(6088):533–536, 1986.

[31] Y. Lu and Z. Tu. A two-level network approach for dynamic fe model updating including damping. *Journal of Sound and Vibration*, 275:931–952, 2004.

[32] M.J. Atalla and D.J. Inman. On model updating using neural netwoks. *Journal of Mechanical Systems & Signal Processing*, 12(1):135–161, 1998.

Part I

On accurate FE-modeling of a Boring Bar with "Free-Free" Boundary Condition

This part is based on the publication:

T. Smirnova, H. Åkesson, L. Håkansson, I. Claesson, and T. Lagö, *Accurate FE-modeling of a Boring Bar Correlated with Experimental Modal Analysis*, In proceedings of the IMAC-XXV A Conference and Exposition on Structural Dynamics, February 19-22, 2007, Orlando, Florida USA.

On accurate FE-modeling of a Boring Bar with "Free-Free" Boundary Condition

T. Smirnova[1], H. Åkesson[1], L. Håkansson[1], I. Claesson[1], and T. Lagö[1,2]
[1]Blekinge Institute of Technology,
Department of Signal Processing,
372 25 Ronneby
Sweden

[2]Acticut International AB
Gjuterivägen 6, 311 32 Falkenberg, Sweden

Abstract

In metal cutting, the problem of boring bars vibration leads to significant degrading of productivity. A boring bar is very flexible and easily subject to vibrations, due to the large length to diameter ratio, required to perform internal turning. Boring bar vibrations appear at the bar's first eigenfrequncies, which correspond to the boring bar's first bending modes affected by boundary conditions applied by the clamping and workpiece in the lathe. Therefore, investigation of the spatial dynamic properties of boring bars is of great importance for the understanding of the mechanism and nature of boring bar vibrations. This paper addresses the problem of building an accurate "3-D" finite element model of a boring bar with "free-free" boundary conditions. Considerations related to appropriate meshing and its influence on the boring bar FE models spatial dynamic properties, as well as modeling the effect of mass loading are discussed. Results from simulations of the "3-D" finite element model of the boring bar (i.e., its first eigenmodes and eigenfrequencies) are correlated with results obtained both from experimental modal analysis and analytical calculations using an Euler-Bernoulli model.

1 Introduction

A boring bar is the tool holder used when performing metal cutting in internal turning operations. It is clamped inside the clamping house with screws at one end and has a cutting tool attached to the other end, and is used for machining deep precise geometries inside the workpiece material. High levels of boring bar vibration frequently occur under the load applied by the material deformation process. Boring bar vibrations are easily excited due to the bar's large length-to-diameter ratio (usually required to perform internal turning operations) and also because of flexibility in the clamping system, i.e., clamping house and clamping screws, etc. High levels of vibrations result in a poor surface finish, reduced tool life, severe acoustic noise in

the working environment, and occur at frequencies related to the boring bar's natural frequencies, which correspond to its low-order bending modes [5, 7].

Conventional techniques of vibrational suppression which could be applied in this application, i.e., incorporation of a passive vibrational absorber into the boring bar [1, 8] or use of an active boring bar [1, 6], require detailed knowledge of the spatial dynamic properties of the system boring bar - clamping house.

The natural frequencies and mode shapes of this system can be estimated using different approaches, such as experimental modal analysis, distributed-parameter system modeling (e.g., an Euler-Bernoulli model) and numerical modeling (for instance, using finite element analysis). Finite element analysis offers the possibility to develop an accurate model of the desired system in order to obtain its spatial dynamic properties, and to use this model later for the design of active tool holders.

The paper is focused on the development of a "3-D" finite element model of the boring bar with "free-free" boundary conditions as a first step towards the construction of a "3-D" finite element model of the system boring bar - clamping house. The accuracy of the model is verified based on results obtained using experimental modal analysis and a distributed-parameter system Euler-Bernoulli model. Modification of the finite element model (incorporating the effect of mass loading of the structure by 14 accelerometers) is performed in order to obtain a higher correlation to the results of experimental modal analysis.

2 Materials and Methods

This section describes the following: experimental setup used in experimental modal analysis of the boring bar with "free-free" boundary conditions, physical properties of the boring bar's material, and methods of identifying the boring bar's spatial dynamic properties.

2.1 Physical Properties of Boring Bar Material

The boring bar used in experiments and modeling is a standard boring bar S40T PDUNR15 F3 WIDAX, composed of 30CrNiMo8 material with the following physical properties: Young's elastic modulus $E = 205\ GPa$, density $\rho = 7850\ kg/m^3$, Poisson's coefficient $\nu = 0.3$.

2.2 Measurement Equipment and Experimental Setup

Experimental modal analysis was carried out on a boring bar suspended by wire bands attached to the ceiling of the laboratory; see experimental setup in Fig. 1. The following equipment was used to conduct the experimental modal analysis.

- 14 PCB 333A32 accelerometers;
- 1 Kistler 9722A500 Impulse Force Hammer;
- HP VXI E1432 front-end data acquisition unit;
- PC with IDEAS Master Series version 6.

The spatial motion of the boring bar was measured by 14 accelerometers. The accelerometers were glued to the boring bar with the distance of 0.045 m: 7 in the

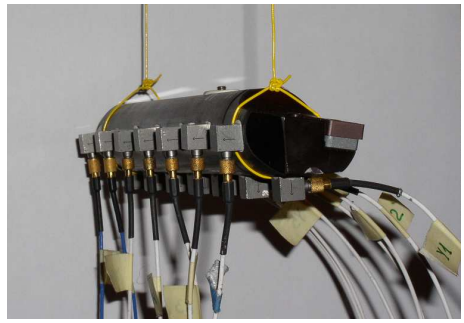

Figure 1: Setup for the experimental modal analysis.

cutting depth direction and 7 in the cutting speed direction. The boring bar was excited using an impulse hammer. The excitation force and acceleration signals were collected simultaneously.

2.3 Euler-Bernoulli Model

Since the boring bar is long and slender (i.e., its length-to-diameter ration is 7.5) and only the first bending modes are of interest, an Euler-Bernoulli model can be used to obtain a sufficiently accurate estimate of its low-order natural frequencies. However, if a shorter beam is under consideration, or if higher eigenfrequencies are of interest, the Timoshenko beam model (which describes bending deformation, shear deformation and rotary inertia) is preferable in order to obtain accurate estimates. According to Euler-Bernoulli beam theory, the free vibration of the boring bar in the cutting speed direction can be described by the following equation (bending motion in the cutting depth direction is described by the same equation, where I_x is replaced by I_y) [2]:

$$\rho A \frac{\partial^2 w(z,t)}{\partial t^2} + \frac{\partial^2}{\partial z^2}[EI_x \frac{\partial^2 w(z,t)}{\partial z^2}] = 0, \tag{1}$$

where $w(z,t)$ is the bending deformation; A is the area of the boring bar's cross section; I_x is the cross-sectional area moment of inertia about "x"-axis; I_y is the cross-sectional area moment of inertia about "y"-axis; ρ is the density of the material; E is the Young's modulus of elasticity.

The area and cross-sectional moments of inertia were calculated based on geometric dimensions of the boring bar's cross section (see Fig. 2). The following properties were used in Euler-Bernoulli model calculations:

Property	Cutting speed direction	Cutting depth direction	Units
l	0.3		m
A	1.1933×10^{-3}		m^2
I	1.1386×10^{-7}	1.1379×10^{-7}	m^4

Table 1: Properties used in Euler-Bernoulli model calculations.

The boring bar's natural frequencies and mode shapes are calculated from Eq. 1

using separation-of-variables procedure and boundary conditions in the form of Eqs. 2.

$$EI_x \frac{\partial^2 w(z,t)}{\partial z^2}|_{z=0} = 0, \quad \frac{\partial}{\partial z}\left[EI_x \frac{\partial^2 w(z,t)}{\partial z^2}\right]|_{z=0} = 0, \tag{2}$$
$$EI_x \frac{\partial^2 w(z,t)}{\partial z^2}|_{z=l} = 0, \quad \frac{\partial}{\partial z}\left[EI_x \frac{\partial^2 w(z,t)}{\partial z^2}\right]|_{z=l} = 0.$$

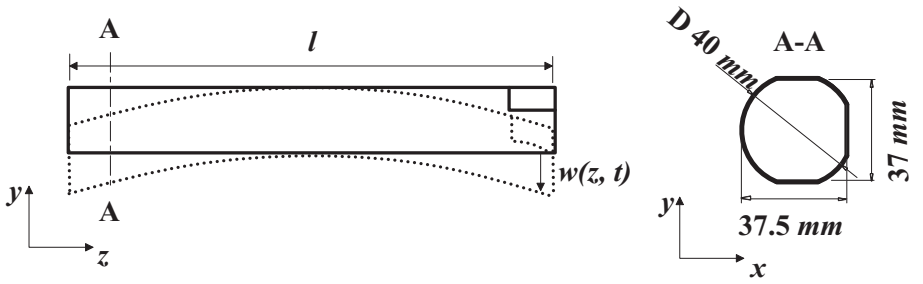

Figure 2: Euler-Bernoulli model of the boring bar with "free-free" boundary conditions.

where x is the cutting depth direction (CDD); y is the cutting speed direction (CSD); z is the feed direction; l is the length of the boring bar.

2.4 Experimental Modal Analysis

An alternative approach used to verify the finite element model of the boring bar is experimental modal analysis (EMA). It allows identification of the boring bar's natural frequencies, mode shapes and relative damping ratios based on the modal model (given by the accelerance matrix [2], Eq. 3):

$$[\mathbf{H}(f)] = -2\pi f^2 \sum_{n=1}^{N} \left[\frac{Q_n \{\psi\}_n \{\psi\}_n^T}{jf - (-f_n\zeta_n + jf_n\sqrt{1-\zeta_n^2})} + \right. \tag{3}$$
$$\left. + \frac{Q_n^* \{\psi^*\}_n \{\psi^*\}_n^T}{jf - (-f_n\zeta_n - jf_n\sqrt{1-\zeta_n^2})} \right],$$

where N is the total number of degrees-of-freedom; $\{\psi\}_n$ is a mode shape vector; ζ_n is a modal damping ratio; f_n is an undamped system's eigenfrequency; Q_n is a modal scaling factor.

An estimate of the accelerance matrix $[\mathbf{H}(f)]$ is obtained experimentally based on power spectral density and cross-power spectral density estimates obtained from excitation force signal applied to the boring bar by impulse hammer, and 14 accelerometer response signals recorded simultaneously. The spatial dynamic properties of the boring bar were identified using the time-domain polyreference least squares complex exponential method.

The orthogonality of the extracted mode shapes $\{\psi_{EMA}\}_k$ and $\{\psi_{EMA}\}_l$ was checked using Modal Assurance Criterion [3]:

$$MAC_{kl} = \frac{|\{\psi_{EMA}\}_k^T \{\psi_{EMA}\}_l|^2}{(\{\psi_{EMA}\}_k^T \{\psi_{EMA}\}_k)(\{\psi_{EMA}\}_l^T \{\psi_{EMA}\}_l)}. \quad (4)$$

The Modal Assurance Criterion can also be used to provide a measure of correlation between the experimentally-measured mode shape $\{\psi_{EMA}\}_k$ and the numerically-calculated mode shape $\{\psi_{FEM}\}_l$

$$MAC_{kl} = \frac{|\{\psi_{EMA}\}_k^T \{\psi_{FEM}\}_l|^2}{(\{\psi_{EMA}\}_k^T \{\psi_{EMA}\}_k)(\{\psi_{FEM}\}_l^T \{\psi_{FEM}\}_l)}. \quad (5)$$

2.5 Finite Element Analysis

The finite element method was used to develop a numerical model of the boring bar in order to predict the system's dynamic behavior. The boring bar's finite element model with "free-free" boundary conditions was constructed and verified for later use in the finite element model of the complete system of interest boring bar-actuator-clamping house. The "3-D" finite element model was developed in order to describe the actual geometry of the boring bar. The finite element method is advantageous in that it allows the approximation of a system with distributed parameters (i.e., with infinite number of degrees-of-freedom) with a discrete system of elements with large but finite number of degrees-of-freedom. Thus, mode shapes can be estimated with considerably higher resolution (which depends only on element size) than mode shapes extracted by experimental modal analysis, where the resolution is limited by the amount and physical dimensions of sensors used.

The first two natural frequencies and mode shapes of the boring bar were calculated based on the general matrix equation of free vibrations for an undamped system

$$[\mathbf{M}]\{\ddot{\mathbf{w}}(t)\} + [\mathbf{K}]\{\mathbf{w}(t)\} = \{\mathbf{0}\}, \quad (6)$$

where $[\mathbf{M}]$ is the global mass matrix of the finite element model of the system; $[\mathbf{K}]$ is the global stiffness matrix of the finite element model of the system; $\{\mathbf{w}(t)\}$ is the space- and time-dependent displacement vector.

The tetrahedron with 10 nodes and quadratic shape functions was used as a basic finite element to develop the model of the boring bar. To simplify the meshing process, the finite element model of the boring bar consisted of two sub-models: the sub-model of the boring bar with the constant cross-section - "body", and the sub-model of the "head". These sub-models were "glued" together; i.e., contacting nodes from the sub-models were tied to each other to avoid relative normal or tangential motion between the sub-models in these nodes. The finite element model of the boring bar is shown in Fig. 3 a).

It is well known that the procedure of experimental modal analysis can affect the dynamic properties of the boring bar. For instance, the 14 accelerometers attached to the boring bar will result in an unwanted effect known as "mass-loading" of the structure, in which the boring bar's natural frequencies are altered by the attached accelerometer masses. In order to correlate the results obtained from finite element analysis and experimental modal analysis, the finite element model was modified. 14 acclerometers were modeled as homogeneous cubes with a certain material density to equate the mass of the accelerometer to 0.005 kg. The modified finite element model of the boring bar is shown in Fig. 3 b).

Natural frequencies and mode shapes were extracted using Lanczos iterative method with the use of MSC.MARC software [4, 9].

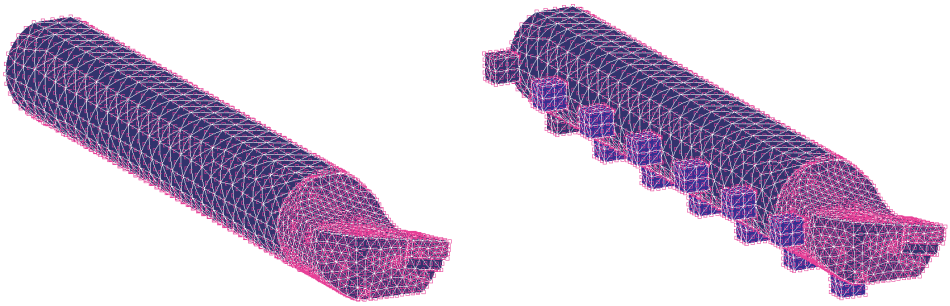

a) b)

Figure 3: The finite element model of the boring bar with "free-free" boundary conditions a) without, and b) with finite element models of the accelerometers.

3 Results

3.1 Mesh Development

This section presents results concerning the influence of different boring bar FE model mesh densities on estimated natural frequencies. The "3-D" finite element model of the boring bar consisted of the two sub-models the "body" and the "head".

These two sub-models were meshed separately with different element sizes varying from 0.01 m to 0.003 m. In total, four models of the boring bar were created. The estimated fundamental boring bar natural frequencies are presented in Table 2.

Sub-model "body", element edge length, $[m]$	Sub-model "head" element edge length, $[m]$	Total number of elements	Mode 1 Freq., $[Hz]$	Mode 2 Freq., $[Hz]$
0.01	0.005	7366	2006.68	2009.55
0.005	0.005	19248	2007.51	2010.43
0.005	0.003	27481	2007.06	2009.5
0.003	0.003	53009	2007.36	2009.83

Table 2: The estimates of the boring bar's fist two natural frequencies using four different FE model meshes.

3.2 Spatial Dynamic Properties Estimates

Table 3 presents the spatial dynamic properties (i.e., natural frequencies, mode shapes, angles of mode shape rotation relative the chosen coordinate system) of the boring bar with "free-free" boundary conditions estimated using experimental modal analysis, the distributed-parameter system Euler-Bernoulli model, the finite element model

of the boring bar, and the modified finite element model of the boring bar with incorporated effect of mass loading by 14 accelerometers.

Model	Mode 1			Mode 2		
	Freq., $[Hz]$	Angle between mode shape and CDD, [°]	Relative natural freq. error, [%]	Freq., $[Hz]$	Angle between mode shape and CDD, [°]	Relative natural freq. error, [%]
EMA	1969.60	-10	-	1970.43	80	-
Euler-Bernoulli	1974.36	0	0.24	1974.97	0	0.23
FE	2006.68	-23.9	2.05	2009.55	67.5	1.76
Modified FE	1976.19	-22	0.49	1979.5	67	0.24

Table 3: Calculated eigenfrequencies, estimated angles of mode shape rotation, relative error between natural frequencies estimated by experimental modal analysis and calculated based on basic and modified finite element model as well as Euler-Bernoulli model.

The first two mode shapes are shown in Fig. 4. Since finite element analysis allows the construction of a model of the system with a large but finite number of degrees of freedom, mode shapes were obtained with significantly higher resolution than those obtained by experimental modal analysis. However, in order to compare numerically calculated mode shapes with those obtained experimentally, deflection was considered only in the nodes of the finite element model corresponding to the positions of the accelerometers' attachment.

The MAC-matrix was used as a quality measure for mode shapes estimated by experimental modal analysis.

$$[MAC]_1 = \begin{bmatrix} MAC_{EMA_1,EMA_1} & MAC_{EMA_1,EMA_2} \\ MAC_{EMA_2,EMA_1} & MAC_{EMA_2,EMA_2} \end{bmatrix} = \tag{7}$$
$$= \begin{bmatrix} 1.000 & 0.001 \\ 0.001 & 1.000 \end{bmatrix}.$$

Corresponding cross-MAC matrices were calculated as a measure of correlation between the two first mode shapes calculated based on the basic finite element model (FEM_1, FEM_2), modified finite element model ($FEMM_1$, $FEMM_2$), Euler-Bernoulli model (EB_1, EB_2) and the two first mode shapes estimated from the experimental modal analysis (EMA_1, EMA_2).

$$[MAC]_2 = \begin{bmatrix} MAC_{EMA_1,FEM_1} & MAC_{EMA_1,FEM_2} \\ MAC_{EMA_2,FEM_1} & MAC_{EMA_2,FEM_2} \end{bmatrix} = \tag{8}$$
$$= \begin{bmatrix} 0.787 & 0.225 \\ 0.235 & 0.745 \end{bmatrix}.$$

$$[MAC]_3 = \begin{bmatrix} MAC_{EMA_1,FEMM_1} & MAC_{EMA_1,FEMM_2} \\ MAC_{EMA_2,FEMM_1} & MAC_{EMA_2,FEMM_2} \end{bmatrix} = \tag{9}$$
$$= \begin{bmatrix} 0.964 & 0.039 \\ 0.046 & 0.943 \end{bmatrix}.$$

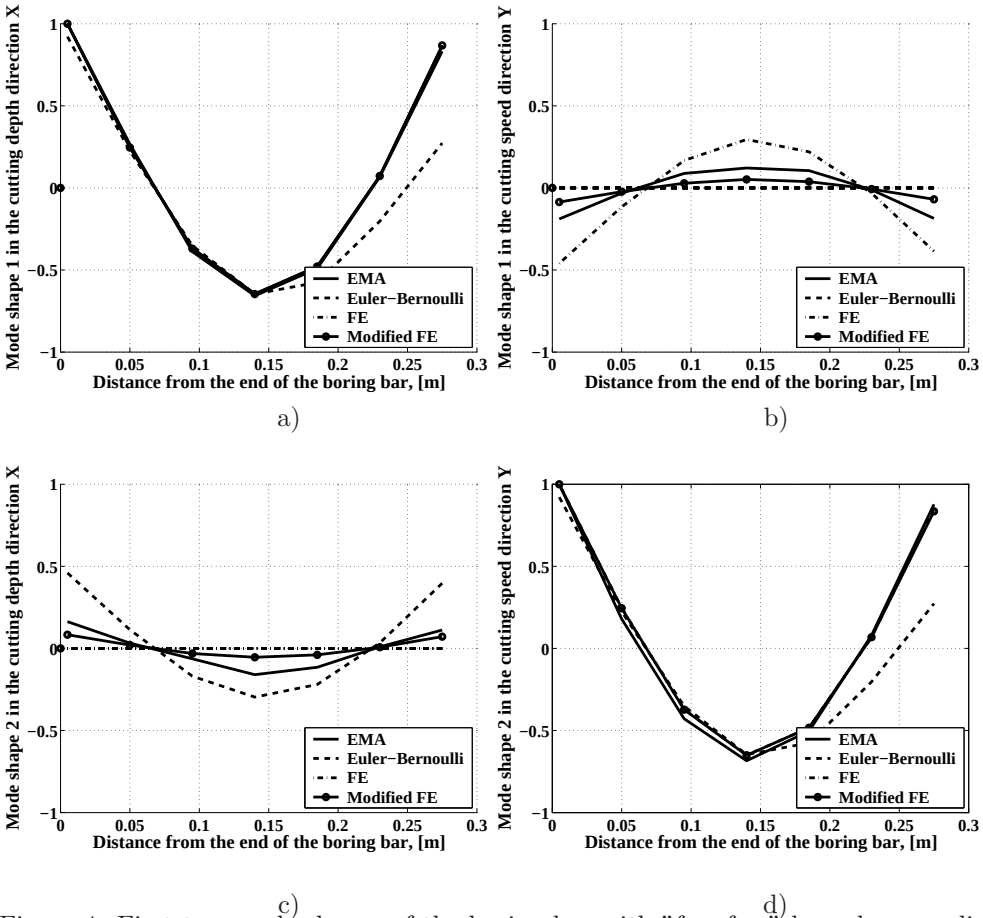

Figure 4: First two mode shapes of the boring bar with "free-free" boundary conditions a) component of mode shape 1 in the cutting depth direction, b) component of mode shape 1 in the cutting speed direction, c) component of mode shape 2 in the cutting depth direction, and d) component of mode shape 2 in the cutting speed direction estimated based on Euler-Bernoulli model, experimental modal analysis and finite element models.

$$[MAC]_4 = \begin{bmatrix} MAC_{EMA_1,EB_1} & MAC_{EMA_1,EB_2} \\ MAC_{EMA_2,EB_1} & MAC_{EMA_2,EB_2} \end{bmatrix} = \begin{bmatrix} 0.816 & 0.031 \\ 0.027 & 0.809 \end{bmatrix}. \quad (10)$$

4 Conclusions

Experimental modal analysis is used as a conventional tool to identify the spatial dynamic properties of the boring bar. However, the finite element model of the boring bar was developed in order to predict its natural frequencies and mode shapes for further use in the design of active tool holders.

Four different meshes were used to create the "3-D" finite element model of the boring bar (see Table 2). It may be observed that the estimates of the first two natural frequencies are not especially sensitive to the number of elements used in the model.

However, convergence is not uniform due to the use of the two sub-models that were meshed separately. Therefore, it is preferable to use a mesh containing the minimum number of elements. This mesh consists of the sub-models "body" and "head" meshed with edge length of tetrahedrons with 0.01 and 0.005 m, correspondingly.

Results obtained from the finite element model were verified based on experimental modal analysis, and compared with the results from a distributed-parameter system Euler-Bernoulli model.

The distributed-parameter system Euler-Bernoulli model allows the sufficiently accurate estimation of the first two natural frequencies of the boring bar (see Table 3). However, it may be observed that mode shapes estimated using the Euler-Bernoulli model differ from those obtained by experimental modal analysis (see Fig. 4, Eq.10). This discrepancy can be explained given the fact that the constant cross-sectional area of the boring bar is assumed in Euler-Bernoulli model calculations.

The experimental modal analysis slightly underestimates natural frequencies in comparison with values predicted by the "3-D" finite element model (see Table 3). This fact can be explained by the effect of mass loading of the structure with 14 accelerometers. The modified "3-D" finite element model of the boring bar allows reduction of the relative error of natural frequencies estimates from 2.05 and 1.76, to 0.49 and 0.24 % in the cutting depth and cutting speed directions, correspondingly. The discrepancy between results obtained from the modified finite element model and experimental modal analysis (see Fig. 4, Table 3) can be explained by following: imperfection of the geometrical model of the boring bar used in the finite element analysis, differences in material properties and uncertainty in measurements.

The angles of rotations of the experimentally estimated mode shapes with respect to the chosen coordinate system can be explained partly by the transverse sensitivity of the accelerometers, and partly by uncertainty in the measurements (suspension of the structure by cables); see Fig. 4. The rotation angles of the mode shapes of the finite element model differ from the rotation angles of the mode shapes obtained from the experimental modal analysis, thus resulting in significant off-diagonal element values of the cross-MAC matrix in Eq. 8. However, this may be explained by the fact that the mass distribution of the finite element model, related to the mesh used in the model, is not identical with the actual mass distribution of the modeled boring bar. It is possible to reduce errors in the rotation angles of the finite element model mode shapes by, for instance, improving the model using a mesh symmetric about "x-z" plane in the section of the boring bar with a constant cross-section, i.e. the "body". However, utilizing the symmetric mesh does not improve accuracy of the natural frequency estimates, and leads to a tremendous increase in model size. This is undesirable and problematic with respect to, for instance, calculating the boring bar's transient response.

From the results presented it may be concluded that it is possible to estimate the natural frequencies of the first two bending modes of the boring bar from the "3-D" finite element model with sufficient accuracy. It is also possible to predict the correct direction of the extracted mode shapes.

Acknowledgments

The present project is sponsored by the Foundation for Knowledge and Competence Development and Acticut International AB.

References

[1] C.H. Hansen and S.D. Snyder, *Active Control of Noise and Vibration*. E & FN Spon, London, 1997.

[2] D.J. Inman, *Engineering vibrations*. Prince-Hall, New Jersey, 2001.

[3] N.M.M. Maia and J.M.M. Silva, *Theoretical and Experimental Modal Analysis*. Research Studies Press Ltd., New York, 1997.

[4] O.C. Zeinkiewicz, R.L. Taylor, and J.Z. Zhu, *The Finite Element Method: Its Basis and Fundamentals*. SElsevier Butterworth-Heinemann, 2005.

[5] L. Andrèn, L. Håkansson, A. Brandt and I. Claesson, "Identification of Dynamic Properties of Boring Bar Vibrations in a Continuous Boring Operation", Journal of Mechanical Systems & Signal Processing, 18(4):869-901, 2004.

[6] I. Claesson and L. Håkansson, *Adaptive Active Control of Machine-Tool Vibrations in a Lathe*, International Journal of Acoustics and Vibration, 3(4):155-162, 1998.

[7] E. Marui, S. Ema and S. Kato, *"Chatter vibration of lathe tools. Part 1: General characteristics of chatter vibration"*, Journal of Engineering for Industry, Transactions of the ASME, 105:100-106, 1983.

[8] E.I. Rivin, *"Tooling Structure: Interface Between Cutting Edge and Machine Tool"*, Annals of the CIRP, 49(2):591-634, 2000.

[9] "MSC.MARC Volume A: Theory and User's Information", MSC. Software, 2005.

Part II

Dynamic Modeling of a Boring Bar Using Theoretical and Experimental Engineering Methods Part 1: Distributed-Parameter System Modeling and Experimental Modal Analysis

This part is published as:

T. Smirnova, H. Åkesson and L. Håkansson, Dynamic Modeling of a Boring Bar Using Theoretical and Experimental Engineering Methods Part 1: Distributed-Parameter System Modeling and Experimental Modal Analysis, *IJAV-International Journal of Acoustics and Vibration*, 14(3), (pp. 124-133), 2009.

Dynamic Modeling of a Boring Bar Using Theoretical and Experimental Engineering Methods Part 1: Distributed-Parameter System Modeling and Experimental Modal Analysis

T. Smirnova[1], H. Åkesson[1,2] and L. Håkansson[1]
[1]Blekinge Institute of Technology,
Department of Signal Processing,
PO Box 520, 372 25 Ronneby, Sweden

[2]Acticut International AB,
Gjuterivägen 7, 311 32 Falkenberg, Sweden

Abstract

Boring bar vibration is a common problem during internal turning operations and is a major problem for the manufacturing industry. High levels of boring bar vibration generally occur at frequencies related to the first two fundamental bending modes of a boring bar. This is the first of two companion papers that summarize the theoretical and experimental work carried out concerning modeling of dynamic properties of boring bars. This paper introduces the Timoshenko beam theory for the modeling of clamped boring bars. Also, the traditional Euler-Bernoulli beam theory is applied. These continuous system methods have been utilized to produce fixed-free beam models of the clamped boring bar. In order to improve accuracy of dynamic models of clamped boring bars, the modeling of the boring bar clamping is addressed by means of multi-span beam models with pinned boundary conditions. The derived boring bar models have also been compared with results obtained by means of experimental modal analysis, conducted on the actual boring bar clamped in a lathe. The multi-span beam boring bar models display higher correlation with experimental modal analysis results as compared to fixed-free beam models. For the fixed-free beams the Timoshenko model results in the highest correlation with the experimental results. On the other hand, the interval in frequency and the orientation of the two fundamental modes demonstrate differences, particularly between the continuous system models and the experimental results.

1 Introduction

The internal turning operation is known to be one of the most troublesome with regard to vibrations in metal cutting. During such an operation a boring bar tool

cuts deep, precise cavities into a workpiece material. However, due to geometric dimensions that a boring bar generally is required to have in order to perform the boring operation (i.e., large length to diameter ratio), the bar is easily subjected to vibrations. The boring bar vibrations are generally dominated by one of the two fundamental bending modes of the bar, and the vibration level is usually greatest in the cutting speed direction [1, 2]. Boring bar vibrations commonly lead to a poor workpiece surface finish, reduced tool life, and severe acoustic noise levels, and have a negative impact on factors such as productivity and production costs.

A number of experimental and analytical studies have been carried out to study boring bar dynamics. Most research has usually been carried out on modeling of cutting dynamics and frequently concentrates on the prediction of stability limits. Based on a two-degrees-of freedom analytical model of a boring bar with two input forces, one proportional to the variation of chip thickness and the other proportional to the penetration velocity, Parker [3] predicted stability limits of a slender boring bar in external longitudinal turning [3]. From boring bar point receptance estimates, the modal constants of the model were determined. However, there was a wide range of cutting speeds resulting in extensive vibration in the cutting speed direction, which was not predicted by the model. Zhang et al. also modeled a boring bar as a system with two degrees-of-freedom, but in the form of a linear state-variable system model [4]. As state variables, the displacements and velocities of the two first principal modes of the boring bar were used. The impulse response method was used to estimate natural frequencies and damping ratios for the two principal modes. Also, a dynamic cutting force model based on four cutting force components was included. Based on their analytical model, Zhang et al. predicted the limit width-of-cut for a boring bar in an external thread cutting process. They assert that a good agreement was found between the predicted and measured values of the limit width of cut. Pratt et al. developed among other things a model of cutting dynamics based on a two-degree-of-freedom system to predict the limit width of cut [5]. They state that the predicted limit width of cut is in reasonable agreement with that observed experimentally. Rao et al. approximated a boring bar as a continuous system cantilever beam with "fixed-free" boundary conditions [6]. The effects of shear deformations and rotatory inertia were neglected. The boring bar model in combination with an analytical, dynamic, boring force model was used to predict vibration amplitudes and chatter frequencies. They claim that their predictions compare favorably with experimental results. Mei modeled boring bar cutting dynamics based on a Euler-Bernoulli boring bar model with "fixed-free" boundary conditions [7]. The cutting dynamics model was used to evaluate a controller for broadband active control of the boring bar vibration that was designed in this work. Andrèn et al. used a time series approach to investigate experimental data of boring bar vibration and an Euler-Bernoulli model of the boring bar with "clamped-free" boundary conditions [1]. They state that the Euler-Bernoulli model estimates of the first two fundamental resonance frequencies show at what frequency range to expect severe boring bar vibration when machining. Andrèn et al. investigated the spatial dynamic properties of a boring bar using Euler-Bernoulli beam theory, experimental modal analysis, and operating deflection shape analysis [2]. They modeled a boring bar as a cantilever beam with "clamped-free" boundary conditions. They state that the Euler-Bernoulli model overestimates the fundamental natural frequencies and that its mode shapes display differences compared to the experimental mode shapes. Andrèn et al. partially explained the discrepancy between analytical and experimental results by compensating the Euler-Bernoulli model for the flexibility

in the actual clamping by increasing the length of the beam model of the boring bar.

As the above literature review indicates, it appears like the only continuous-system theory used to describe dynamic properties of boring bars is the Euler-Bernoulli theory. Also, there seems to be a lack of research concerning the modeling of the clamping in the dynamic models of clamped boring bars and its impact on the accuracy of continuous-system boring bar models. The importance of addressing the modeling of the clamping to further improve the accuracy of dynamic models of clamped boring bars has, however, been indicated in a previous work [2]. Frequently, boring bars can be considered long and slender, i.e., the length-to-diameter ratio of the boring bar exceeds ten [8]. The clamping of a boring bar, however, commonly reduces its free end so that it is below the limit of long and slender. The recommended clamping length of a boring bar is usually in excess of three to four times the diameter of the boring bar [9]. This imposes that a Timoshenko beam model with appropriate boundary conditions seems to be a suitable choice for modeling a clamped boring bar. Also, to further improve the accuracy of dynamic models of clamped boring bars the literature review shows the need to address the modeling of the boring bar clamping. Hence, this concerns a need for further extension of research on the modeling of the actual boundary conditions of a boring bar in order to achieve improved accuracy. This paper addresses continuous-system modeling of dynamic properties of a clamped boring bar and experimental modal analysis of the actual boring bar, and the focus is on the bars two fundamental bending modes. Euler-Bernoulli and Timoshenko beam models of a clamped boring bar using "fixed-free" boundary conditions have been derived. In order to incorporate clamping flexibility in the distributed-parameter models, two-span Euler-Bernoulli and Timoshenko boring bar models with "pinned-pinned-free" boundary conditions have been produced. An experimental modal analysis of a clamped boring bar is conducted while the boring bar is not in contact with the workpiece. Modal parameters provided by the experimental modal analysis and the developed distributed-parameter models of the clamped boring bar are compared and discussed.

2 Materials and Methods

This section describes the experimental setup used in the experimental modal analysis, physical properties of the boring bar material, and methods of modeling and identification of the boring bar modal parameters.

2.1 Measurement Equipment and Experimental Setup

The experimental modal analysis was carried out in a MAZAK 250 Quickturn lathe with 18.5 kW spindle power, a maximum machining diameter of 300 mm, and 1007 mm between the centers. A standard boring bar, WIDAX S40T PDUNR15 F3, was used. The boring bar was clamped with a standard clamping housing, a Mazak 8437-0 40 mm holder, attached to the turret in the lathe. The following equipment was used to carry out experimental modal analysis:

- 14 PCB 333A32 accelerometers;
- 2 Ling Dynamic Systems shakers v201;
- 2 Brüel & Kjær 8001 impedance heads;
- HP VXI E1432 front-end data acquisition unit;

- PC with IDEAS Master Series version 6.

Experimental modal analysis was performed on the boring bar clamped in the clamping house with four bolts in the direction corresponding to the cutting speed direction. The boring bar was simultaneously excited in the cutting speed and cutting depth directions by two shakers (see Fig. (1)) via two impedance heads situated at the distance $l_1 = 0.1$ m from the clamped end of the boring bar (see Fig. (2)). Spatial motion of the boring bar was measured by accelerometers glued in the following order: two accelerometers were placed in the cutting speed and cutting depth direction corresponding to $l_2 = 0.01$ m from the clamped end of the boring bar, the other two accelerometers were placed at a distance of $l_3 = 0.04$ m from the first two, and the rest of the accelerometers were equidistantly placed at $l_4 = 0.025$ m from each other (see Fig. (2)). In total, 14 accelerometers were used: seven in the cutting speed direction and seven in the cutting depth direction.

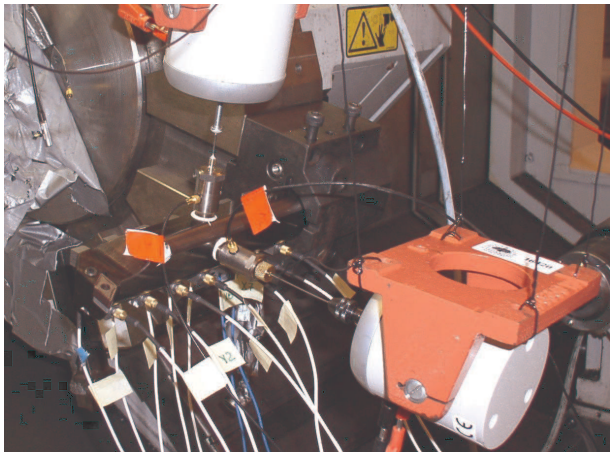

Figure 1: Setup for the experimental modal analysis.

The following notation for the coordinate system is utilized in this paper (including Fig. (2)): x - cutting depth direction (positive direction pointing outside the figure's plane towards the reader), y - cutting speed direction, and z - feed direction.

2.2 Physical Properties of the Boring Bar

The boring bar used in experiments and modeling is composed of 30CrNiMo8 material with the following physical properties: Young's elastic modulus $E = 205\ GPa$, density $\rho = 7850\ kg/m^3$, and Poisson's coefficient $\nu = 0.3$.

2.3 Distributed-Parameter Boring Bar Models

Distributed-parameter system Euler-Bernoulli and Timoshenko models may be utilized in order to provide estimates of the lower-order natural frequencies and mode shapes of a boring bar [2, 10]. In the Euler-Bernoulli model, the boring bar is considered to be a system with distributed mass and an infinite number of degrees of freedom. This classical beam model considers only transverse beam vibrations, ignoring the shear deformation and rotary inertia [8]. Thus, the Euler-Bernoulli model

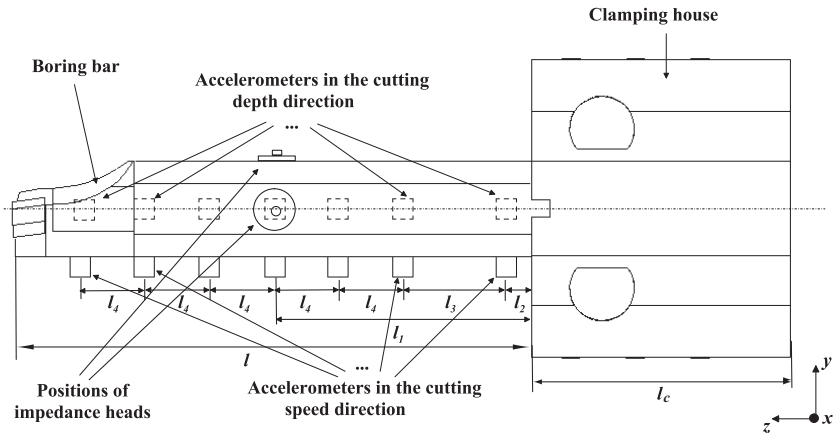

Figure 2: Drawing of the clamped boring bar with accelerometers and cement studs for attachment of impedance heads.

tends to slightly overestimate the eigenfrequencies; this problem increases for the eigenfrequencies of the higher order modes [2, 8]. The Euler-Bernoulli differential equation describing the transversal motion of the boring bar in the cutting speed direction or y-direction can be written as (transversal motion in the cutting depth direction is described by the same equation, where I_x is replaced by I_y) [8]:

$$\rho A \frac{\partial^2 w(z,t)}{\partial t^2} + \frac{\partial^2}{\partial z^2}\left[EI_x \frac{\partial^2 w(z,t)}{\partial z^2}\right] = f(z,t), \tag{1}$$

where ρ = density of boring bar material, A = boring bar's cross-section area, I_x and I_y = cross-sectional area moments of inertia about "x axis" and about "y axis", E = Young's elastic modulus, $w(z,t)$ = deflection in the y-direction, and $f(z,t)$ = external excitation force per unit of length. A model of the boring bar with "fixed-free" boundary conditions is shown in Fig. (3).

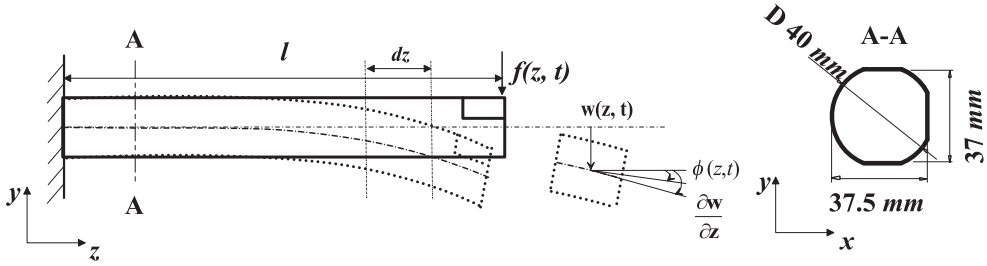

Figure 3: A "fixed-free" model of a boring bar displaying shear and bending deformation.

In the case of short beams or non-slender beams, i.e., beams with a length-to-diameter ratio less than ten, or when higher-order bending modes are considered for slender beams, the effects of shear deformation and rotary inertia (ignored by Euler-Bernoulli beam theory) are not negligible [8]. The Timoshenko beam model describes

these effects [11]. The Timoshenko differential equations describing the transversal motion in the cutting speed direction or y-direction of the boring bar are given by a system of coupled partial differential equations [11]:

$$EI\frac{\partial^2\phi(z,t)}{\partial z^2} + kAG(\frac{\partial w(z,t)}{\partial z} - \phi(z,t)) = \rho I\frac{\partial^2\phi(z,t)}{\partial t^2}, \tag{2}$$

$$kAG(\frac{\partial^2 w(z,t)}{\partial z^2} - \frac{\partial\phi(z,t)}{\partial z}) - \rho A\frac{\partial^2 w(z,t)}{\partial t^2} = f(z,t), \tag{3}$$

where $\phi(z,t)$ is the angle due to pure bending deformation of the beam, $\frac{dw(z,t)}{dz}$ is the total slope of the centerline of the beam and the difference $\frac{dw(z,t)}{dz} - \phi(z,t)$ provides the shear angle (see Fig. (3)), ν is Poisson's coefficient, k is the shear coefficient that describes the distribution of the shear stress in the cross-section depending on the cross-section shape, and $G = \frac{E}{2(1+\nu)}$ is the modulus of elasticity in shear [12]. Since the cross-section shape of the boring bar is almost circular, the value of k was selected for a circular cross-section shape, i.e., $k = \frac{6(1+\nu)}{7+6\nu}$.

Four distributed parameter system models of a clamped boring bar were considered: an Euler-Bernoulli beam model with "fixed-free" boundary conditions, a Timoshenko beam model with "fixed-free" boundary conditions, an Euler-Bernoulli beam model with "pinned-pinned-free" boundary conditions, and a Timoshenko beam model with "pinned-pinned-free" boundary conditions. A model of the boring bar with "fixed-free" boundary conditions is shown in Fig. (3), and a two-span model of the boring bar with "pinned-pinned-free" boundary conditions is shown in Fig. (4).

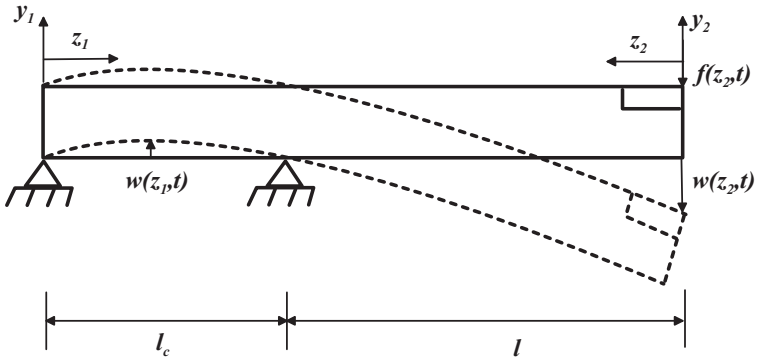

Figure 4: A "pinned-pinned-free" model of a boring bar, where l_c corresponds to the length of the part of the boring bar clamped inside the clamping house and l is the overhang of the boring bar.

The natural frequencies and mode shapes may be determined from the general spatial solution to the distributed parameter system by applying the particular boundary conditions suitable for the purpose of modeling [8]. The boundary conditions used in the two Euler-Bernoulli boring bar models may be found in Ref. [8, 13]. The boundary conditions used in the two Timoshenko beam models are given in Ref. [8, 14] for the "fixed-free" case and in Ref. [15] for the "pinned-pinned-free" case. The quantities related to material properties and/or geometry of the boring bar used in the

distributed parameter models of the boring bar are summarized in Table 1. The expressions for the eigenfunctions, and the frequency equation for the Euler-Bernoulli and Timoshenko models of the boring bar are given in Appendix A.

Quantity	Cutting speed direction	Cutting depth direction	Units
l	0.2		m
l_c	0.1		m
A	1.1933×10^{-3}		m^2
E	205		GPa
ν	0.3		-
ρ	7850		kg/m^3
I	1.1386×10^{-7}	1.1379×10^{-7}	m^4

Table 1: Quantities related to material properties and/or geometry of the boring bar.

2.4 Experimental Modal Analysis

In experimental modal analysis, the boring bar is considered as a multiple degree-of-freedom system [16]. In this approach, simultaneously measured data records of excitation forces and responses of a structure (e.g., a clamped boring bar) are utilized to produce a parametric estimate of the dynamic properties of the structure [16]. Experimental modal analysis enables the estimation of a system's modal parameters: natural frequencies, mode shapes, relative damping coefficients, and the modal scaling factors. Further, experimental modal analysis serves as a tool for verifying and updating distributed-parameter system and finite element models.

The concept of experimental modal analysis models the boring bar as a system with N degrees-of-freedom. In this case, the equation of motion in matrix form is given by [17]:

$$[\mathbf{M}]\{\ddot{\mathbf{w}}(t)\} + [\mathbf{C}]\{\dot{\mathbf{w}}(t)\} + [\mathbf{K}]\{\mathbf{w}(t)\} = \{\mathbf{f}(t)\}, \tag{4}$$

where N_{ema} - is the number of degrees of freedom corresponding to the number of points on the boring bar where its response is measured. Matrix $[\mathbf{M}]$ is the $N \times N$ mass matrix, $[\mathbf{C}]$ is the $N \times N$ damping matrix, and $[\mathbf{K}]$ is the $N \times N$ elastic stiffness matrix. The vector $\{\mathbf{f}(t)\}$ is the space- and time-dependent load vector. The vector $\{\mathbf{w}(t)\}$ is the space- and time-dependent displacement vector, and its i-th element generally contains the displacement measured in the point with coordinates (x_i, y_i, z_i) , $i = 1, \ldots N$, at time instant t. Thus, the displacement vector may be written as

$$\{\mathbf{w}(t)\} = \left\{ \begin{array}{c} w(x_1, y_1, z_1, t) \\ w(x_2, y_2, z_2, t) \\ \vdots \\ w(x_N, y_N, z_N, t) \end{array} \right\}. \tag{5}$$

The spatial dynamic properties of the boring bar were identified using the time-domain polyreference least squares complex exponential method [16]. This method was based on the impulse response function matrix $[h(t)]$ or the time-domain version of the modal model, given by Ref. [16].

$$[h(t)] = \sum_{n=1}^{N} \left(Q_n \{\psi\}_n \{\psi\}_n^T e^{j(2\pi f_n \sqrt{1-\zeta_n^2})t} + Q_n^* \{\psi^*\}_n \{\psi^*\}_n^T e^{-j(2\pi f_n \sqrt{1-\zeta_n^2})t} \right), \quad (6)$$

where $\{\psi\}_n$ is the $N \times 1$ mode shape vector for mode n, ζ_n is the modal damping ratio for mode n, f_n is the undamped system's eigenfrequency for mode n, and Q_n is the modal scaling factor for mode n.

The orthogonality of the extracted mode shapes $\{\psi\}_k$ and $\{\psi\}_l$ was examined using the Modal Assurance Criterion [10]:

$$MAC_{kl} = \frac{|\{\psi\}_k^T \{\psi\}_l|^2}{(\{\psi\}_k^T \{\psi\}_k)(\{\psi\}_l^T \{\psi\}_l)}. \quad (7)$$

The Modal Assurance Criterion can also be used to provide a measure of correlation between mode shapes that were calculated (for instance) based on a distributed-parameter Euler-Bernoulli beam model $\{\psi_{EB}\}_k$ and mode shapes that were estimated based on the experimental modal analysis $\{\psi_{EMA}\}_l$ according to

$$MAC_{EB_k, EMA_l} = \frac{|\{\psi_{EB}\}_k^T \{\psi_{EMA}\}_l|^2}{(\{\psi_{EB}\}_k^T \{\psi_{EB}\}_k)(\{\psi_{EMA}\}_l^T \{\psi_{EMA}\}_l)}. \quad (8)$$

Table 2 summarizes power spectral density estimation parameters and the excitation signal properties used whilst conducting the experimental modal analysis.

Parameter	Value
Signal type	Burst random (90/10)
Excitation frequency range	300-800 Hz
Sampling frequency, F_s	1280 Hz
Number of spectral lines, N	1601
Frequency resolution, Δf	0.3125 Hz
Number of averages	100
Window	Rectangular
Frequency range for curve fitting	400-600 Hz

Table 2: Experimental modal analysis parameters.

3 Results

This section presents the results of the experimental modal analysis and the modal analysis based on the distributed-parameter systems models (i.e., estimates of the first two natural frequencies and corresponding mode shapes). Results are presented in the following order: first, to facilitate the interpretation of the results, the produced models are reported, and their respective short notation is given. Second, estimates are given for the boring bar's natural frequency, for each of the different models used. Third, mode shape estimates are given for the free part of the boring bar, as well as for the complete boring bar. Fourth, results obtained by the different models are compared using the Modal Assurance Criterion.

Four different distributed-parameter system models of the clamped boring bar were produced: an Euler-Bernoulli boring bar model with "fixed-free" boundary conditions (EB1), an Euler-Bernoulli boring bar model with "pinned-pinned-free" boundary conditions (EB2), a Timoshenko boring bar model with "fixed-free" boundary conditions (T1), and a Timoshenko boring bar model with "pinned-pinned-free" boundary conditions (T2).

Experimental modal analysis (EMA) of the clamped boring bar was carried out while the boring bar was not in contact with the workpiece and the modal parameters of the two fundamental bending modes were estimated. In the experimental modal analysis, the boring bar was excited both in the cutting speed (CSD) and in the cutting depth directions (CDD) with electrodynamic shakers via impedance heads. The spectrum estimation parameters and the excitation signal properties used in the experimental modal analysis are given in Table 2.

In order to emphasize the quality of the modal parameters extracted in the experimental modal analysis of the clamped boring bar, both accelerance functions (synthesized based on the extracted modal parameters and the corresponding measured accelerance function estimates) were plotted in the same diagram. In Fig. (5 a) the synthesized accelerance and measured accelerance functions for the driving point in the cutting depth direction are shown, and in (Fig. 5 b) the synthesized accelerance and measured accelerance functions for the driving point in the cutting speed direction are shown. For the first eigenmode, corresponding to the lowest bending eigenfrequency, the relative damping ratio was estimated as $\zeta_1 = 0.978\%$. For the second eigenmode, corresponding to the highest eigenfrequency of the two fundamental bending modes, the relative damping ratio was estimated as $\zeta_2 = 0.770\%$.

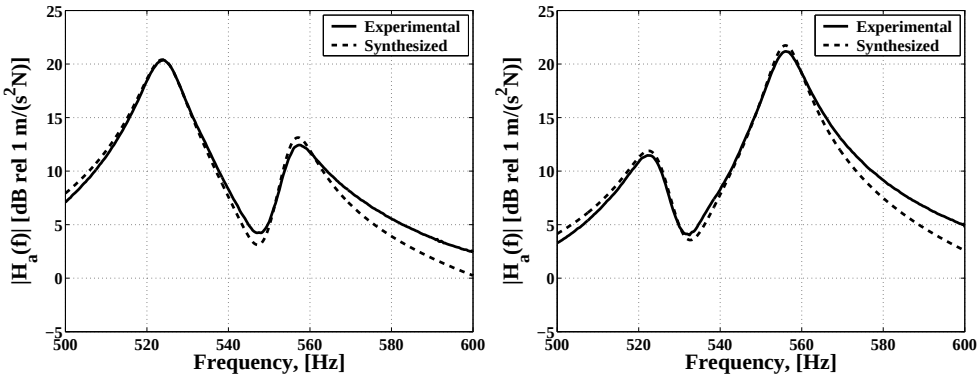

Figure 5: Experimental and synthesized magnitude functions of driving-point accelerance function a) in the cutting depth direction, and b) in the cutting speed direction zoomed into the first two resonance peaks.

The multiple coherence function estimates for the two excitation forces and respective driving point acceleration were greater than or equal to 0.997 at each fundamental eigenfrequency, see Fig. (6 a). Figure (6 b) displays the estimated normalized random errors for the multiple coherence function estimates [18].

The two fundamental boring bar eigenfrequencies were estimated in the experimental modal analysis and calculated for the continuous-system models (see Table

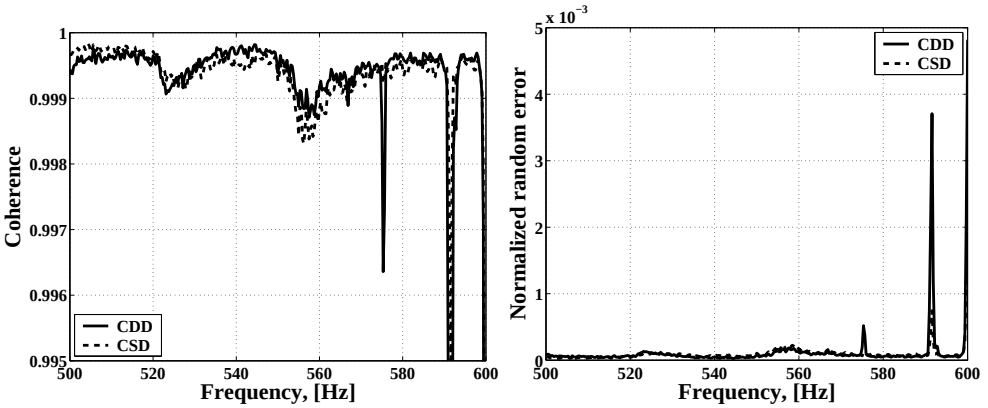

a) b)

Figure 6: a) Multiple coherence function estimates between the two excitation forces and respective driving-point acceleration, and b) normalized random error estimates for the corresponding multiple coherence function estimates zoomed into the frequency range corresponding to the first two resonance peaks.

3).

In the present discussion (concerning the two fundamental bending modes of the boring bar) the mode corresponding to the lowest fundamental eigenfrequency is referred to as mode 1. The mode corresponding to the highest fundamental eigenfrequency is referred to as mode 2. Correspondingly, the mode shapes are referred to as mode shape 1 and mode shape 2.

Model	Resonance freq., [Hz]	
	Mode 1	Mode 2
Experimental Modal Analysis, (EMA)	524.069	555.885
Distributed-parameter Euler-Bernoulli, "fixed-free" boundary conditions, (EB1)	698.120	698.335
Distributed-parameter Euler-Bernoulli, "pinned-pinned-free" boundary conditions, (EB2)	539.112	539.278
Distributed-parameter Timoshenko, "fixed-free" boundary conditions, (T1)	687.015	687.218
Distributed-parameter Timoshenko, "pinned-pinned-free" boundary conditions, (T2)	525.094	525.247

Table 3: Natural frequencies estimates.

The mode shapes calculated based on distributed-parameter system models and estimated based on the experimental modal analysis are presented in two groups. Observe, that for each of these models the corresponding resonance frequencies of the first two fundamental bending modes are presented in Table 3. The first group consists of the mode shapes for the distributed-parameter system models (EB1, T1, EB2, T2) with both "fixed-free" and "pinned-pinned-free" boundary conditions; the mode shapes produced with the experimental modal analysis are shown in Fig (7). Observe that the mode shapes presented in Fig. (7), corresponding to group 1, are sampled

spatially, corresponding to the positions of accelerometers at the actual boring bar.

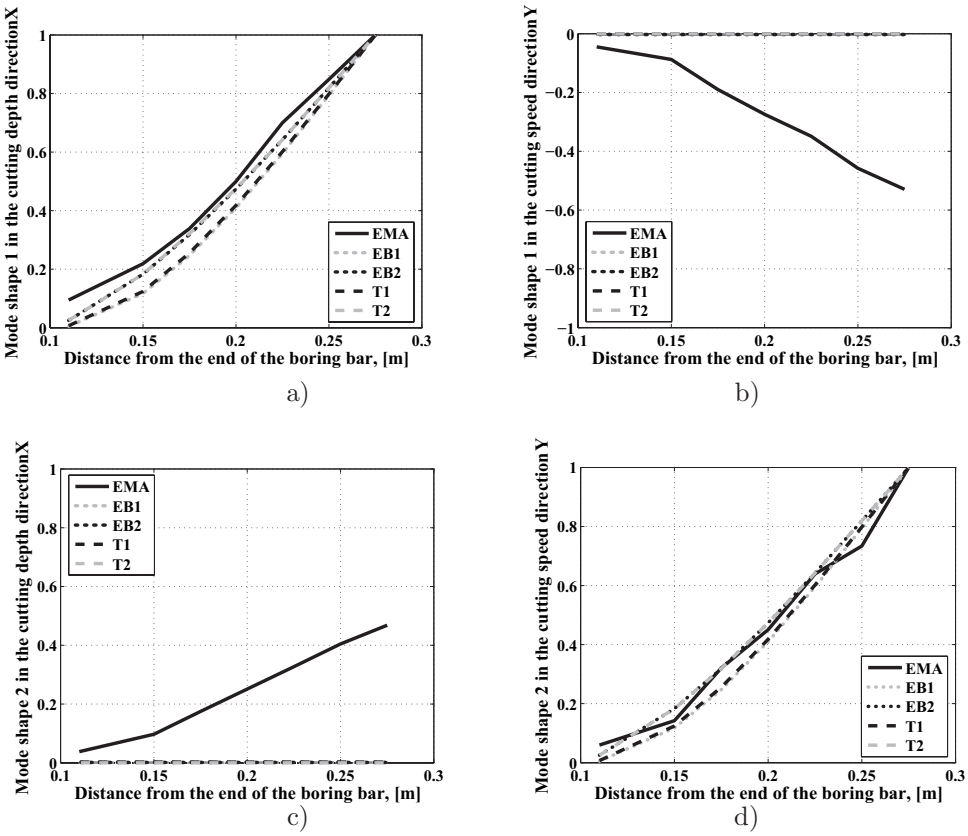

Figure 7: The first two fundamental mode shapes of the boring bar: a) component of mode shape 1 in the cutting depth direction, b) component of mode shape 1 in the cutting speed direction, c) component of mode shape 2 in the cutting depth direction, and d) component of mode shape 2 in the cutting speed direction. Produced based on experimental modal analysis (EMA) and continuous system models (EB1, EB2, T1, T2), correspondingly.

The second group (see Fig. (8)) consists of the mode shapes calculated based on the continuous-system models (EB2, T2), both with the "pinned-pinned-free" boundary conditions. The second group illustrates, for example, the flexibility of the boring bar part clamped inside the clamping house. In this group, spatial sampling related to the accelerometer positions was not imposed on the displayed mode shapes.

As a quality measure of the mode shapes extracted by the experimental modal analysis, the MAC-matrix was calculated based on Eq. (7) yielding

$$[MAC]_{EMA} = \begin{bmatrix} MAC_{EMA_1,EMA_1} & MAC_{EMA_1,EMA_2} \\ MAC_{EMA_2,EMA_1} & MAC_{EMA_2,EMA_2} \end{bmatrix} = \\ = \begin{bmatrix} 1.000 & 0.000 \\ 0.000 & 1.000 \end{bmatrix}, \tag{9}$$

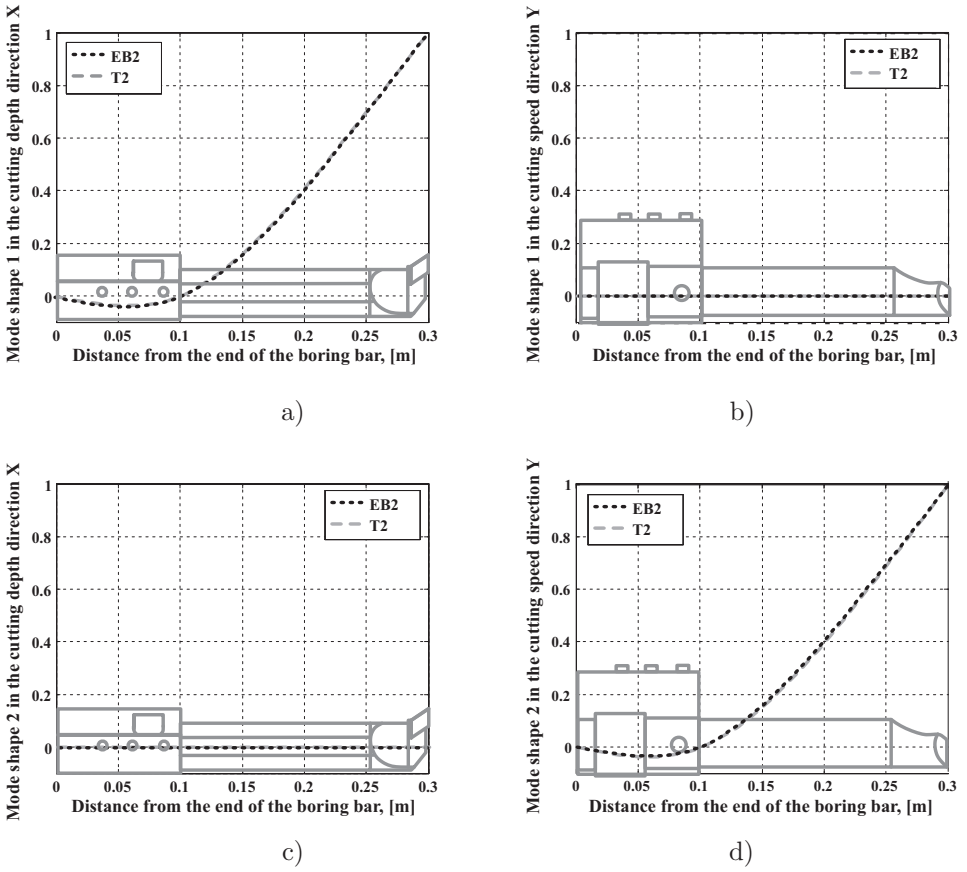

Figure 8: The first two fundamental mode shapes of the boring bar: a) component of mode shape 1 in the cutting depth direction, b) component of mode shape 1 in the cutting speed direction, c) component of mode shape 2 in the cutting depth direction, and d) component of mode shape 2 in the cutting speed direction. Produced based on continuous system models (EB2, T2) correspondingly.

where EMA_1 is the mode shape at 524.069 Hz, and EMA_2 is the mode shape at 555.885 Hz, estimated by the experimental modal analysis [10].

To provide a quantitative measure on the correlation between the mode shapes from the experimental modal analysis and the mode shapes for the distributed-parameter system, cross-MAC matrices were produced based on Eq. (7) [10]. First, cross-MAC matrices were calculated between mode shapes estimated by the distributed-parameter system and mode shapes from the experimental modal analysis. The cross-MAC matrix between modes shapes calculated by the Euler-Bernoulli model with "fixed-free" boundary conditions ($EB1$) and the mode shapes from the experimental modal analysis (EMA) is given by

$$[MAC]_{EB1,EMA} = \begin{bmatrix} MAC_{EB1_1,EMA_1}, & MAC_{EB1_2,EMA_1} \\ MAC_{EB1_1,EMA_2} & MAC_{EB1_2,EMA_2} \end{bmatrix} = \\ = \begin{bmatrix} 0.772 & 0.215 \\ 0.204 & 0.787 \end{bmatrix}. \quad (10)$$

The cross-MAC matrix between modes shapes calculated by the Timoshenko model with "fixed-free" boundary conditions ($T1$) and mode shapes from the experimental modal analysis (EMA) is given by

$$[MAC]_{T1,EMA} = \begin{bmatrix} MAC_{T1_1,EMA_1}, & MAC_{T1_2,EMA_1} \\ MAC_{T1_1,EMA_2} & MAC_{T1_2,EMA_2} \end{bmatrix} = \begin{bmatrix} 0.773 & 0.216 \\ 0.204 & 0.788 \end{bmatrix}. \quad (11)$$

The cross-MAC matrix between modes shapes calculated by the Euler-Bernoulli beam model with "pinned-pinned-free" boundary conditions ($EB2$) and mode shapes from the experimental modal analysis (EMA) is given by

$$[MAC]_{EB2,EMA} = \begin{bmatrix} MAC_{EB2_1,EMA_1}, & MAC_{EB2_2,EMA_1} \\ MAC_{EB2_1,EMA_2} & MAC_{EB2_2,EMA_2} \end{bmatrix} = \\ = \begin{bmatrix} 0.780 & 0.217 \\ 0.206 & 0.790 \end{bmatrix}. \quad (12)$$

The cross-MAC matrix between modes shapes calculated by the Timoshenko model with "pinned-pinned-free" boundary conditions ($T2$) and mode shapes from the experimental modal analysis (EMA) is given by

$$[MAC]_{T2,EMA} = \begin{bmatrix} MAC_{T2_1,EMA_1} & MAC_{T2_2,EMA_1} \\ MAC_{T2_1,EMA_2} & MAC_{T2_2,EMA_2} \end{bmatrix} = \begin{bmatrix} 0.780 & 0.217 \\ 0.206 & 0.790 \end{bmatrix}. \quad (13)$$

4 Discussion and Conclusions

From the results, it follows that the introduced "fixed-free" Timoshenko beam model of the clamped boring bar gives the estimates of its two fundamental natural frequencies with higher correlation to the corresponding experimental modal analysis (EMA) estimates as compared to a "fixed-free" Euler-Bernoulli model. Clamping flexibility in the Euler-Bernoulli and Timoshenko models, incorporated by means of two-span models with "pinned-pinned-free" boundary conditions, yielded higher correlation of both the mode shape and the eigenfrequency estimates of the two models with the corresponding EMA estimates as compared to the "fixed-free" Timoshenko model. However, the continuous-system models do not describe the frequency difference between the two fundamental natural frequencies and the mode shape rotation with respect to the coordinate system, which are observable in the estimates provided by the experimental modal analysis.

The "fixed-free" Timoshenko model of the boring bar (T1) includes effects of shear deformation and rotary inertia. Compared to the "fixed-free" Euler-Bernoulli model, the "fixed-free" Timoshenko model of the boring bar (T1) results in an improvement of estimates of the first two fundamental natural frequencies, which are lower by about

12 Hz. However, these fundamental natural frequency estimates are still significantly overestimated compared to the corresponding experimental modal analysis estimates (see Table 3). The next step in building a more accurate distributed-parameter system model of the boring bar involved improving the modeling of the actual boundary conditions of the boring bar. Thus, the length of the beam model was extended to the full length of the boring bar, and the beam was pinned at two positions along the part of the beam model corresponding to the clamped part of the actual boring bar. As a result of introducing clamping flexibility in the beam models, a new set of fundamental eigenfrequencies with significantly lower frequency values was obtained (see Table 3). Moreover, the Timoshenko beam model (T2) produced natural frequency estimates close to the estimates obtained experimentally: a fundamental resonance frequency of 525.2 Hz (cf. EMA, 555.7 Hz) in the cutting speed direction and 525.1 Hz (cf. EMA, 524.1 Hz) in the cutting depth direction.

The mode shapes for the distributed-parameter models with "fixed-free" boundary conditions (EB1, T1) display the largest difference from the experimental mode shape estimates (see Fig. (7)). The models with "pinned-pinned-free" boundary conditions (EB2, T2) result in mode shapes with a slightly higher correlation to the experimental mode shapes (see Fig. (7)). These observations are also quantified by the cross-MAC matrices in Eqs. (10), (11), (12) and (13). Furthermore, only the mode shape estimates from the EMA are rotated with respect to the coordinate system; i.e., the two mode shapes have non-zero components in both the cutting depth and in the cutting speed directions. Because of the "fixed-free" boundary conditions, the mode shape estimates produced using models EB1, T1 do not display any flexibility of the boring bar adjacent to the clamping house. Some flexibility in this area is, however, introduced by "pinned-pinned-free" boundary conditions, and this can be observed from the mode shapes estimates calculated based on models EB2, T2 (see Fig. (8)). These mode shapes also display some flexibility in the part of the boring bar clamped inside the clamping house.

However, none of the continuous-system models of the boring bar provide the frequency difference of approximately 30 Hz between the two fundamental natural frequencies, which is observable in the results from the experimental modal analysis. This can be explained by the fact that continuous models give a rough approximation of the actual geometry and clamping conditions of the boring bar. The actual boring bar has a non-circular cross-section and is clamped inside the cylindrical cavity of the clamping house by means of clamping screws on the tool side and on the opposite side of the boring bar. Furthermore, the mode shapes calculated based on the distributed-parameter system models (EB1, EB2, T1, T2) are (by their model definition) only in the cutting speed direction, or cutting depth direction. Thus, it seems like a more complete mathematical model of the clamped boring bar is required in order to provide estimates of its dynamic properties with higher accuracy (see Part 2 [19]).

Furthermore, mass loading of the structure introduced by the sensors attached to the boring bar is likely lower its natural frequencies [20]. Also, during a continuous cutting operation, the workpiece applies boundary conditions on the cutting tool. In the experimental modal analysis, the boring bar was not in contact with the workpiece and, thus, the boundary conditions of the tool side of the boring bar was "free". During machining, the boundary conditions applied by the workpiece will affect dynamic properties of the boring bar [1, 2]. This implies that modeling of dynamic properties of a boring bar during machining requires, for instance, that the model include both an adequate model of the boring bar clamping and the boundary conditions on the

cutting tool applied by the workpiece in the cutting zone.

Acknowledgments

The present project is sponsored by Acticut International AB.

Appendix

Frequency Equations and Mode Shapes

Euler-Bernoulli Model with "Fixed-Free" Boundary Conditions

The boring bar's eigenfrequencies and eigenmodes are calculated from Eq. (1) by setting $f(z,t) = 0$. The solution of Eq. (1) is found using the separation-of-variables procedure in the form of $w(z,t) = T(t)Z(z)$, where $T(t)$ is a temporal solution and $Z(t)$ is a spatial solution [8].

The frequency equation to determine the weighted wave number βl is obtained for the Euler-Bernoulli boring bar model with "fixed-free" boundary conditions is given by [8]

$$\cos(\beta l)\cosh(\beta l) = -1. \tag{A.1}$$

There are an infinite number of solutions for $\beta_n l$; $n = 1, 2\ldots$, to Eq. (A.1). Solutions to this equation were found by plotting the frequency equation versus β in combination with interval halving. The corresponding natural frequencies f_n can be calculated based on Eq. (A.2):

$$\beta^4 = \frac{(2\pi f)^2 \rho A}{EI}. \tag{A.2}$$

The mode shapes for each value of weighted wave number $\beta_n l$ may be calculated as:

$$Z_n(z) = C_n \left[\cosh(\beta_n z) - \cos(\beta_n z) - \frac{\cos(\beta_n l) + \cosh(\beta_n l)}{\sin(\beta_n l) + \sinh(\beta_n l)} \left(\sinh(\beta_n z) - \sin(\beta_n z)\right)\right], \tag{A.3}$$

where n is the mode shape number, $n = 1, 2\ldots$, and C_n is an independent constant.

Euler-Bernoulli Model with "Pinned-Pinned-Free" Boundary Conditions

The general spatial solution now consists of spatial solutions for two spans: $Z_1(z_1)$ and $Z_2(z_2)$, $0 \leqslant z_1 \leqslant l_c$ and $0 \leqslant z_2 \leqslant l$.

The frequency equation for the Euler-Bernoulli boring bar model with "pinned-pinned-free" boundary conditions was derived as follows:

$$\begin{aligned} &2\sin(\beta l_c)\sinh(\beta l_c) + 2\sin(\beta l_c)\sinh(\beta l_c)\cos(\beta l)\cosh(\beta l) - \\ &- \sin(\beta l_c)\cosh(\beta l_c)\sin(\beta l)\cosh(\beta l) + \sin(\beta l_c)\cosh(\beta l_c)\cos(\beta l)\sinh(\beta l) + \\ &+ \cos(\beta l_c)\sinh(\beta l_c)\sin(\beta l)\cosh(\beta l) - \cos(\beta l_c)\sinh(\beta l_c)\cos(\beta l)\sinh(\beta l) = 0. \end{aligned} \tag{A.4}$$

By solving the frequency equation, the weighted wave numbers for both spans $\beta_n l_c$ and $\beta_n l$, $n = 1, 2 \ldots$, can be obtained. The mode shapes were derived based on every weighted wave number, yielding

$$Z_{1n}(z_1) = C_n \tfrac{p_{1n}}{p_{2n}}, \quad 0 \leqslant z_1 \leqslant l_c, \tag{A.5}$$

where

$$p_{1n} = (2 + 2\cos(\beta_n l)\cosh(\beta_n l))\left(\sin(\beta_n l_c)\sinh(\beta_n z_1) - \sinh(\beta_n l_c)\sin(\beta_n z_1)\right). \tag{A.6}$$

$$p_{2n} = (\sin(\beta_n l) + \sinh(\beta_n l))(\cosh(\beta_n l_c)\sin(\beta_n l_c) - \cos(\beta_n l_c)\sinh(\beta_n l_c)), \tag{A.7}$$

$$\begin{aligned} Z_{2n}(z_2) \quad = \quad & C_n \left[\cos(\beta_n z_2) + \cosh(\beta_n z_2) - \right. \\ & \left. -(\sin(\beta_n z_2) + \sinh(\beta_n z_2))\tfrac{\cos(\beta_n l)+\cosh(\beta_n l)}{\sin(\beta_n l)+\sinh(\beta_n l)}\right], 0 \leqslant z_2 \leqslant l, \end{aligned} \tag{A.8}$$

where n is the mode shape number, $n = 1, 2 \ldots$, and C_n is an independent constant.

Timoshenko Model with "Fixed-Free" Boundary Conditions

In order to obtain the natural frequencies and mode shapes, the homogeneous problem is considered by setting $f(z,t) = 0$ and utilizing the method of separation of variables. By separating both $w(z,t)$ and $\phi(z,t)$ into two functions [such that $w(z,t) = Z(z)T(t)$ and $\phi(z,t) = \Phi(z)T(t)$], and assuming that $w(z,t)$ and $\phi(z,t)$ are synchronized in time, the equations of motion (Eqs. (2) and (3)) can be separated into three ordinary differential equations [11]. This yields one temporal equation, $T(t)$, and two spatial equations that may be decoupled: $Z(\xi)$ and $\Phi(\xi)$, where ξ is a non-dimensional variable, i.e., $\xi = \frac{z}{l}$.

The frequency equation for the boring bar Timoshenko model with "fixed-free" boundary conditions is given by [11]:

$$2 + \left[2 + b^2(r^2 - s^2)^2\right]\cos(bo)\cosh(bg) - \frac{b(r^2 + s^2)}{\sqrt{1 - r^2 b^2 s^2}}\sin(bo)\sinh(bg) = 0, \tag{A.9}$$

where b^2, r^2 and s^2 are calculated according to

$$b^2 = \tfrac{\rho A l^4 (2\pi f)^2}{EI}, \quad r^2 = \tfrac{I}{Al^2} \text{ and } \quad s^2 = \tfrac{EI}{kAGl^2}. \tag{A.10}$$

Estimates of the natural frequencies f_n of the boring bar may, for instance, be obtained by plotting the frequency equation versus frequency in combination with interval halving. When the natural frequencies are obtained, it is possible to calculate the parameters: b_n, g_n, and o_n based on Eqs. (A.10), (A.11), (A.12):

$$g = \frac{1}{\sqrt{2}}\sqrt{-(r^2 + s^2) + \sqrt{(r^2 - s^2)^2 + 4/b^2}}, \tag{A.11}$$

and

$$o = \frac{1}{\sqrt{2}}\sqrt{(r^2 + s^2) + \sqrt{(r^2 - s^2)^2 + 4/b^2}}. \tag{A.12}$$

Now, the mode shapes can be written as

$$Z_n = C_n \frac{g_n}{g_n^2 + s^2} \left[\frac{p_{3n}}{\vartheta_n \varsigma_n} \sin(b_n o_n \xi) - \cos(b_n o_n \xi) - p_{3n} \sinh(b_n g_n \xi) + \cosh(b_n g_n \xi) \right], \tag{A.13}$$

$$\Phi_n = C_n \left[\vartheta_n \varsigma_n \sin(b_n o_n \xi) + p_{3n} \cos(b_n o_n \xi) + \sinh(b_n g_n \xi) - p_{3n} \cosh(b_n g_n \xi) \right], \tag{A.14}$$

where $0 \leqslant \xi \leqslant 1$, $n = 1, 2 \ldots$ is a mode shape number, and C_n is an arbitrary constant.

$$\vartheta_n = \frac{g_n}{o_n}, \tag{A.15}$$

$$\varsigma_n = \frac{o_n^2 - s^2}{g_n^2 + s^2}, \tag{A.16}$$

$$p_{3n} = \frac{\vartheta_n(\varsigma_n \cos(b_n o_n) + \cosh(b_n g_n))}{\sin(b_n o_n) + \vartheta_n \sinh(b_n g_n)}. \tag{A.17}$$

Timoshenko Model with "Pinned-Pinned-Free" Boundary Conditions

In the case of the two-span beam, there are two sets of spatial solutions: $Z_1(\xi_1)$, $\Phi_1(\xi_1)$ and $Z_2(\xi_2)$, $\Phi_2(\xi_2)$ (one for each span), which satisfy the boundary conditions and are defined by the selected model and conditions of continuity in the intermediate support. Both solutions are functions of non-dimensional variables (one for each respective span, ξ_1 and ξ_2) and are normalized to the length of the whole beam: $l_b = l_c + l$.

The frequency equation for the boring bar Timoshenko model with "pinned-pinned-free" boundary conditions was derived as follows:

$$\begin{aligned}
&\frac{go(g^2+o^2)}{(g^2+s^2)^3(o^2-s^2)^3}(-2go(g^2+s^2)(o^2-s^2)\sin(bo\xi_1^m)\sinh(bg\xi_1^m)- \\
&-(g^2-o^2)(g^2+s^2)(o^2+s^2)\sin(bo\xi_1^m)\sinh(bg\xi_1^m)\sin(bo\xi_2^m)\sinh(bg\xi_2^m)- \\
&-go\left((o^2-s^2)^2+(g^2+s^2)^2\right)\sin(bo\xi_1^m)\sinh(bg\xi_1^m)\cos(bo\xi_2^m)\cosh(bg\xi_2^m)- \\
&-go(g^2+s^2)^2\sin(bg\xi_1^m)\cosh(bg\xi_1^m)\cos(bo\xi_2^m)\sinh(bg\xi_2^m)+ \\
&+g^2(g^2+s^2)(o^2-s^2)\cos(bo\xi_1^m)\sinh(bg\xi_1^m)\cos(bo\xi_2^m)\sinh(bg\xi_2^m)+ \\
&+o^2(g^2+s^2)(o^2-s^2)\sin(bo\xi_1^m)\cosh(bg\xi_1^m)\sin(bo\xi_2^m)\cosh(bg\xi_2^m)- \\
&-go(o^2-s^2)^2\cos(bo\xi_1^m)\sinh(bg\xi_1^m)\sin(bo\xi_2^m)\cosh(bg\xi_2^m))=0.
\end{aligned} \tag{A.18}$$

When the natural frequencies f_n are obtained from the frequency equation, the mode shapes can be expressed in terms of b_n, g_n, and o_n.

Thus, the mode shapes for span 1 can be expressed as follows:

$$Z_{1n}(\xi_1) = C_n \frac{l}{b_n} \frac{g_n p_{4n}}{(g_n^2 + s^2) p_{5n}} \left[\frac{\sinh(b_n g_n \xi_1) \sin(b_n o_n \xi_1^m) - \sin(b_n o_n \xi_1) \sinh(b_n g_n \xi_1^m)}{\sin(b_n o_n \xi_1^m)} \right], \tag{A.19}$$

$$\Phi_{1n}(\xi_1) = C_n \frac{p_{4n}}{p_{5n}} \left[\frac{\cosh(b_n g_n \xi_1) \sin(b_n o_n \xi_1^m) - \phi_n \zeta_n \cos(b_n o_n \xi_1) \sinh(b_n g_n \xi_1^m)}{\sin(b_n o_n \xi_1^m)} \right], \tag{A.20}$$

where $0 \leqslant \xi_1 \leqslant \xi_1^m$.

For span 2, the mode shape expressions are given by:

$$\begin{aligned} Z_{2n}(\xi_2) &= \frac{C_n l g_n}{b_n(g_n^2+s^2)} \left[\frac{1}{\vartheta_n} \sin(b_n o_n \xi_2) + \frac{p_{6n}}{(o_n^2-s^2)(g_n^2+s^2)} \cos(b_n o_n \xi_2) + \right. \\ &+ \left. \sinh(b_n g_n \xi_2) + p_{6n} \cosh(b_n g_n \xi_2) \right], \end{aligned} \tag{A.21}$$

$$\Phi_{2n}(\xi_2) = C_n \left[\vartheta_n p_{6n} \sin(b_n o_n \xi_2) - \varsigma_n \cos(b_n o_n \xi_2) - p_{6n} \sinh(b_n g_n \xi_2) - \cosh(b_n g_n \xi_2) \right], \tag{A.22}$$

where $0 \leqslant \xi_2 \leqslant \xi_2^m$, C_n is an arbitrary constant, and ϑ_n and ς_n are given by Eq. (A.15) and Eq. (A.16). Polynomials p_{4n}, p_{5n} and p_{6n} are defined as follows:

$$\begin{aligned} p_{4n} &= \sin(b_n o_n \xi_1^m)[-2\vartheta_n \varsigma_n + (1-\vartheta_n^2)\varsigma_n \sin(b_n o_n \xi_2^m) \sinh(b_n g_n \xi_2^m) - \\ &- \vartheta_n(1+\varsigma_n^2) \cos(b_n o_n \xi_2^m) \cosh(b_n g_n \xi_2^m)]; \end{aligned} \tag{A.23}$$

$$\begin{aligned} p_{5n} &= \vartheta_n^2 [\tfrac{\varsigma_n}{\vartheta_n} \cosh(b_n g_n \xi_1^m) \sin(b_n o_n \xi_1^m) \cosh(b_n g_n \xi_2^m) + \\ &+ \tfrac{1}{\vartheta_n} \cosh(b_n g_n \xi_1^m) \sin(b_n o_n \xi_1^m) - \varsigma_n^2 \sinh(b_n g_n \xi_1^m) \cos(b_n o_n \xi_1^m) - \\ &- \varsigma_n \sinh(b_n g_n \xi_1^m) \cos(b_n o_n \xi_1^m) \cos(b_n o_n \xi_2^m)], \end{aligned} \tag{A.24}$$

$$p_{6n} = \frac{-\varsigma_n(\frac{1}{\vartheta} \sin(b_n o_n \xi_2^m) + \sinh(b_n g_n \xi_2^m))}{\varsigma_n \cosh(b_n g_n \xi_2^m) + \cos(b_n o_n \xi_2^m)}. \tag{A.25}$$

References

[1] L. Andrèn, L.Håkansson, A. Brandt, and I. Claesson, Identification of Dynamic Properties of Boring Bar Vibrations in a Continuous Boring Operation, *Mechnical Systems & Signal Processing*, **18**(4), 869–901, (2004).

[2] L. Andrèn, L. Håkansson, A. Brandt, and I. Claesson, Identification of Motion of Cutting Tool in a Continuous Boring Operation - Correlation to Structural Properties, *Mechnical Systems & Signal Processing*, **18**(4), 903–927, (2004).

[3] E. Parker, Dynamic Stability of a Cantilever Boring Bar With Machined Flats Under Regenerative Cutting Conditions, *Journal of Mechanical Engineering Science*, **12**(2), 104–115, (1970).

[4] G. Zhang and S. Kapoor, Dynamic Modeling and Analysis of the Boring Machining System, *Journal of Engineering for Industry, Transactions of the ASME*, **109**, 219–226, (1987).

[5] J. R. Pratt and A. Nayfeh, Design and Modeling for Chatter Control, *Nonlinear Dynamics*, **19**(1), 49–69, (1999).

[6] P. N. Rao, U. R. K. Rao, and J. S. Rao, Towards Improved Design of Boring Bars Part 1: Dynamic Cutting Force Model with Continuous System Analysis for the Boring Bar Performnca, *Journal of Machine Tool Manufacture*, **28**(1), 33–44, (1988).

[7] C. Mei, Active regenerative chatter suppression during boring manufacturing process, *Robotics and Computer-Integrated Manufacturing*, **21**, 153–158, (2005).

[8] D. Inman, *Engineering Vibration*, Prentice-Hall, second edition, (2001).

[9] Sandvik, *Modern Metal Cutting - a practical handbook*, AB Sandvik Coromant, 1st edition, (1994).

[10] N. Maia and J. Silva, *Theoretical and Experimental Modal Analysis*, Research Studies Press Ltd., (1997).

[11] O. Lebedeva, *Formulas for Structural Dynamics: Tables, Graphs and Solutions*, McGraw-Hill Professional Book Group, (2000).

[12] R. Blevins, *Formulas for natural frequency and mode shape*, KRIEGER PUBLISHING COMPANY, (2001).

[13] J. Tedesco, W. McDougal, and C. Ross, *Structural dynamics: theory and applications*, Addison Wesley Longman, Inc., (1999).

[14] B. Geist and J. McLaughlin, Eigenvalue formulas for the uniform Timoshenko beam: the free-free problem, *Electronic Research Announcements of the American Mathematical Society*, **4**, 12–17, (1998).

[15] I. Elishakoff, J. Ari-Gur, and P. S. Das, Refined theories may be needed for vibration analysis of structures with overhang, *International Journal of Solids and Structures*, **36**, 3581–3589, (1999).

[16] D. Ewins, *Modal Testing: Theory, Practice and Application*, Research Studies Press LTD, second edition, (2000).

[17] P.-O. H. Sturesson, L. Håkansson, and I. Claesson, Identification of the Statistical Properties of the Cutting Tool Vibration in a Continuous Turning Operation - Correlation to Structural Properties, *Mechanical Systems and Signal Processing, Academic Press*, **11**(3), 459–489, (1997).

[18] J. Bendat and A. Piersol, *Engineering Application of Correlation and Spectral Analysis*, John Wiley & Sons, second edition, (1993).

[19] T. Smirnova, H. Åkesson, and L. Håkansson, Dynamic Modeling of a Boring Bar Using Theoretical and Experimental Engineering Methods part 2: Finite Element Modeling and Sensitivity Analysis, *submitted to the International Journal of Acoustics and Vibration (IJAV)*, (2009).

[20] H. Åkesson, T.Smirnova, L. Håkansson, and T. Lago, Analysis of Dynamic Properties of Boring Bars Concerning Different Clamping Conditions, *Research Report*, (2007).

Part III

Dynamic Modeling of a Boring Bar Using Theoretical and Experimental Engineering Methods Part 2: Finite Element Modeling and Sensitivity Analysis

This part is published as:

T. Smirnova, H. Åkesson and L. Håkansson, Dynamic Modeling of a Boring Bar Using Theoretical and Experimental Engineering Methods Part 2: Finite Element Modeling and Sensitivity Analysis, *IJAV-International Journal of Acoustics and Vibration*, 14(3), (pp. 134-142), 2009.

Dynamic Modeling of a Boring Bar Using Theoretical and Experimental Engineering Methods Part 2: Finite Element Modeling and Sensitivity Analysis

T. Smirnova[1], H. Åkesson[1,2] and L. Håkansson[1]
[1]Blekinge Institute of Technology,
Department of Signal Processing,
PO Box 520, 372 25 Ronneby, Sweden

[2]Acticut International AB,
Gjuterivägen 7, 311 32 Falkenberg, Sweden

Abstract

This is the second of two companion papers that summarize the theoretical and experimental work carried out concerning modeling of dynamic properties of boring bars. This paper introduces the finite element method for the modeling of clamped boring bars. The "3-D" FE models of the system boring bar - clamping house as well as the "1-D" FE models of the clamped boring bar were derived. In particular, the modeling of the boring bar clamping is addressed. Dynamic properties predicted based on the developed FE models of the clamped boring bar were compared with the ones estimated by means of experimental modal analysis conducted on the actual boring bar clamped in the lathe. The "3-D" FE models display substantially higher correlation with the experimental modal analysis results compared to the "1-D" FE models. A "3-D" FE model of the boring bar - clamping house manages to model the distance in frequency and the orientation of the two fundamental modes to a large extent. The importance of the modeling of the boring bar boundary conditions for the accuracy of dynamic models of boring bars is demonstrated. The sensitivity of the natural frequency estimates produced by means of the FE and the continuous system (presented in Part I) boring bar models with respect to variations in material density and Young's elastic modulus has been addressed.

1 Introduction

This paper is focused on modeling of dynamic properties of clamped boring bars by means of finite element method. A number of research works have been completed that includes the modeling of a boring bar as a system with a large but finite number of degrees-of- freedom, using finite element analysis. Wong et al. used Timoshenko beam finite elements to model a boring bar [1]. He designed an electromagnetic

dynamic absorber and simulated its performance, utilizing modal control and direct feedback control based on the finite element model of the boring bar. Wong claims that both controllers succeed in significant damping of boring bar vibrations at the lowest vibration mode. Nagano et al. used pitched-based carbon-fiber reinforced plastic (CFRP) material to develop a chatter-resistant boring bar with a large overhang [2]. He made an attempt to create a "3-D" finite element model in order to predict natural frequencies and improve dynamic characteristics of the boring bar by modeling embedded steel cores of various shapes. The cutting performance and stability of the designed boring bars regarding chatter were investigated experimentally. He claims that utilization of the CFRP material with the cross-shaped steel core allows for the successful, stable machining for boring bars with a length-to-diameter of more than seven. Nagano also mentioned the necessity concerning the development of improved models for the clamping of the boring bar. Baker et al. used FEM in the stability analysis of a turning operation [3]. He approximated the cutting force by using the orthogonal cutting model. Baker also based his method of stability prediction on the assumption of the linearity of the tooling structure's behavior. Two different types of FE models were considered: first, "1-D" FE models of a boring bar and a workpiece attached to a rigid base, and second, "3-D" FE models of a boring bar and a workpiece attached to a deformable "3-D" FE model of machine tool. The FE models were used to extract structural matrices, with the purpose of using them in stability analysis. The maximum stable width of cut was predicted for a set of geometric dimensions of the tool holder and the workpiece (for both types of models) as a function of spindle speed. However, no experimental results were presented.

In addition, a number of research works have been completed concerning external longitudinal turning in which the tool holder shank, etc. have been modeled using the finite element method. Sturesson et al. developed a "3-D" finite element model of a tool holder shank - clamping house for external longitudinal turning [4]. They used normal mode analysis to evaluate the natural frequencies, modal masses, and mode participation factors of the tool holder shank. The modal damping was estimated using the free vibration decay method. Spectral density estimates were also utilized to obtain natural frequencies. The results of the normal mode analysis and spectral densities' estimates were well-correlated. Later, in Ref. [5], Mahdavinejad also tried to predict maximum width of cut, ensuring stable cutting in external longitudinal turning with the use of a "3-D" FE model of a machine tool. Several "3-D" FE models containing different machine tool parts were developed. Natural frequencies and the mode shapes of the tailstock were estimated based on the "3-D" FE models and compared with results obtained from experimental modal analysis. The stability lobe diagrams were obtained for the chuck-center with and without tailstock cases. In both cases the stability lobe diagrams were calculated based on analytical considerations and experiments. Results from the modal analysis as well as the stability lobe diagrams produced with the use of FE models are claimed to be well correlated to corresponding experimental estimates.

As indicated by the above literature review and the literature review in the companion paper Part 1, it appears that little work has been done that focuses on the modeling of dynamic properties of clamped boring bars and its resulting accuracy [6]. This paper continues the discussion concerning modeling of dynamic properties of clamped boring bars as well as modeling of the clamping in the dynamic models started in Part 1 [6] by addressing the finite element method for this purpose. Two "1-D" finite elements models of the boring bar, one based on Euler-Bernoulli beam finite

elements and one based on Timoshenko beam finite elements, with "fixed-free" boundary conditions, have been derived [7, 8]. In order to incorporate clamping flexibility in the "1-D" finite elements models, two-span Euler-Bernoulli and Timoshenko beam finite element boring bar models with "pinned-pinned-free" boundary conditions have been produced. To provide more complete mathematical models of a clamped boring bar, two different "3-D" finite element boring bar models have been derived; the first utilizes a rigid clamping house model, and the second utilizes a deformable clamping house finite element model. The latter "3-D" finite element boring bar model illustrates, e.g., the importance of the flexibility assumption when modeling the clamping system. Both the modal parameters provided by the experimental modal analysis of the actual boring bar and by the developed distributed-parameter models of the clamped boring bar in companion paper Part 1 are compared with the corresponding modal parameters estimated by means of the derived finite element boring bar models [6]. A sensitivity analysis has been carried out on the distributed-parameter system, derived in companion paper Part 1, and on numerical finite element boring bar models with respect to variation in material properties.

2 Materials and Methods

This section describes a boring bar and a standard clamping house, frequently used in industry, for internal turning. It also present FE methods for modeling and identification of the boring bar modal parameters as well as a method for natural frequency sensitivity analysis of the models. In Fig. (1) the machining room in a Mazak SUPER QUICK TURN - 250M CNC lathe with boring bar and clamping house, etc., is shown.

2.1 Physical Properties of the Boring Bar and Clamping-House Material

The boring bar used is a standard boring bar WIDAX S40T PDUNR15 F3. It is composed of 30CrNiMo8 material with the following physical properties: Young's elastic modulus $E = 205\ GPa$, density $\rho = 7850\ kg/m^3$, and Poisson's coefficient $\nu = 0.3$. The boring bar was clamped with a standard clamping housing, a Mazak 8437-0 40 mm holder, attached to the turret in the lathe. For simplicity, the properties of the clamping house material were assumed to be identical to those of the boring bar. In Fig. (2) a sketch of the boring bar clamped in the clamping house is shown.

2.2 Finite Element Analysis

The finite element method was used to model the spatial dynamic properties of a clamped boring bar. Based on the derived finite element models, estimates of the spatial dynamic properties of the clamped boring bar were produced using the general matrix equation for dynamic equilibrium of an undamped system, i.e.:

$$[\mathbf{M}]\{\ddot{\mathbf{w}}(t)\} + [\mathbf{K}]\{\mathbf{w}(t)\} = \{\mathbf{0}\}, \tag{1}$$

where $[\mathbf{M}]$ is the global mass matrix of the system, $[\mathbf{K}]$ is the global stiffness matrix of the system, and $\{\mathbf{w}(t)\}$ is the space- and time-dependent displacement vector [9]. One advantage of the finite element method is that it enables the approximation of

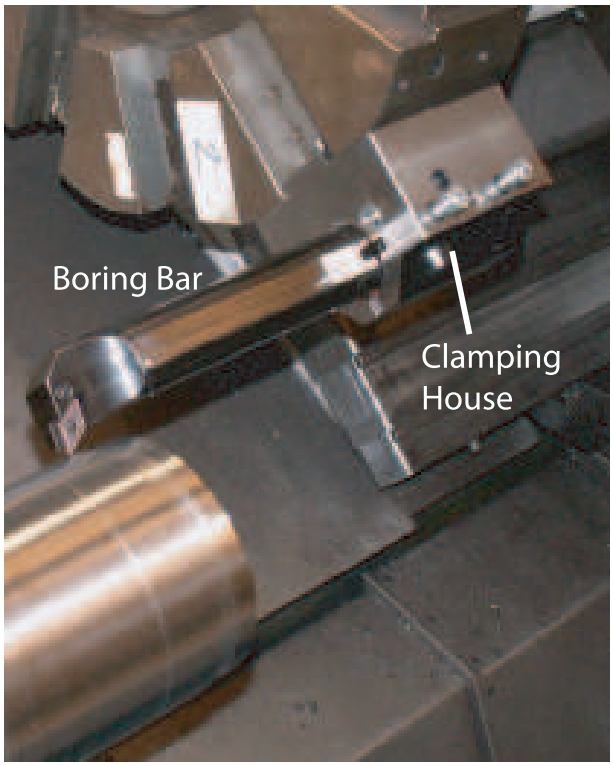

Figure 1: The machining room in a Mazak SUPER QUICK TURN - 250M CNC lathe.

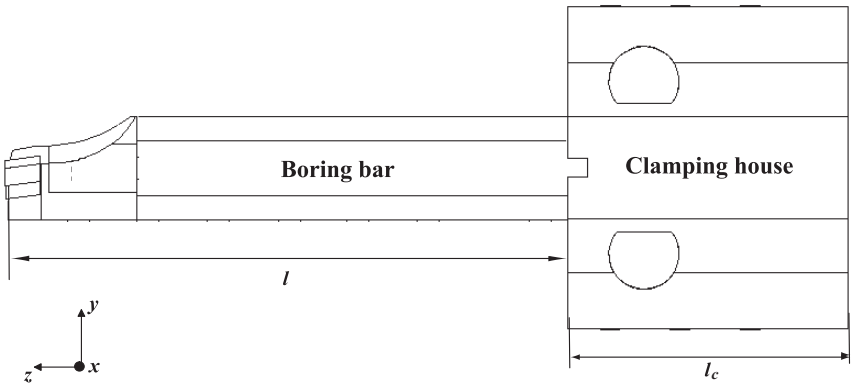

Figure 2: Sketch of the boring bar clamped in the clamping house, l=200 mm is the boring bar overhang and l_c=100 mm is the lengt of the clamping house.

the system with distributed parameters, i.e., with an infinite number of degrees-of-freedom, by means of discrete elements with a small number of degrees-of-freedom. This means that the system has a large but finite number of degrees-of-freedom [9]. Thus, the modal parameters and mode shapes in particular can be estimated with considerably higher resolution (dependent on the selected element size) than mode shapes extracted by experimental modal analysis, in which resolution is limited by the amount and the physical dimensions of the sensors utilized, etc.

2.2.1 *"1-D" Finite Element Models*

Two types of beam finite elements were used to produce "1-D" finite element models: the Euler-Bernoulli beam element and Timoshenko beam element. A simple two-noded Euler-Bernoulli beam element has four degrees-of-freedom: two translational to describe transverse displacement, and two rotational to describe angle of rotation due to the pure bending. The expressions for the shape functions, stiffness, and mass matrices of the Euler-Bernoulli beam element can be found in Refs. [7] and [8]. The simplest Timoshenko beam element may be modeled with five degrees of freedom: two translational to express displacement due to both bending and shear deformation, two rotational to describe angle of beam's end planes rotation due to both bending and shear deformation, and the third rotational degree of freedom to describe the angle of rotation due to the pure shear deformation. For convenience, the third rotational degree of freedom is normally condensed to an internal degree-of-freedom. Thus, the Timoshenko beam element has the same topology as the Euler-Bernoulli beam element, and it can be used without standard mesh modification. The condensation procedure, expressions for the shapes function, and stiffness matrix may be found in Ref. [8]. Another formulations of the Timoshenko beam element may found in, for example, Refs. [10–12].

In order to estimate spatial dynamic properties of the boring bar two kinds of boundary conditions were used for each "1-D" finite element model: "fixed-free" and "pinned-pinned-free". The following notation is used for the coordinate system: x - cutting depth direction, y - cutting speed direction, and z - feed direction. In Fig. (3) the "fixed-free" model of the boring bar is shown. Here, $w(z,t)$ is the bending deformation and $f(z,t)$ is the external excitation force. Figure (4) illustrates the

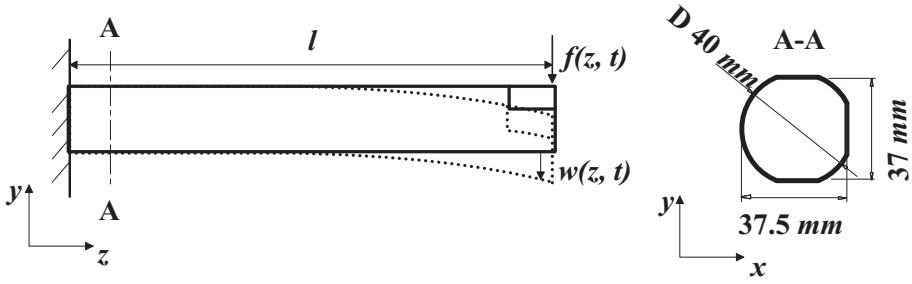

Figure 3: The model of the boring bar with "fixed-free" boundary conditions.

"pinned-pinned-free" two-span model of the boring bar, where $l_c = 0.1$ $[m]$ corresponds to the length of the part of the boring bar clamped inside the clamping house and $l = 0.2$ $[m]$ corresponds to the overhang of the boring bar.

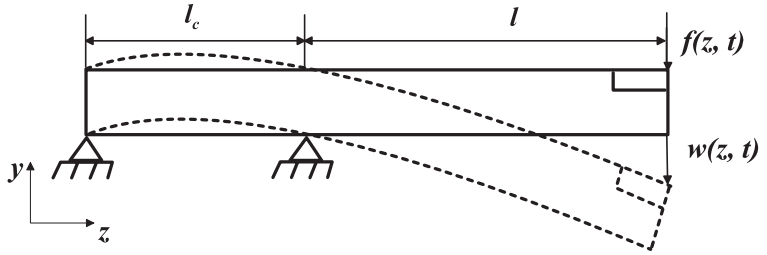

Figure 4: The two-span model of the boring bar with "pinned-pinned-free" boundary conditions.

The quantities related to material properties and/or geometry of the boring bar used in the "1-D" finite element models of the boring bar are the same as for corresponding distributed-parameter boring bar models described in Part 1 [6].

2.2.2 *"3-D" Finite Element Model of the Boring-Bar*

The "3-D" finite element model of the boring bar was built using the commercial finite element analysis software MSC.MARC [13]. A tetrahedron was selected as a basic finite element, as it enables an easy finite element mesh generation, which provides a close approximation of the boring bar's geometry. A tetrahedron with ten nodes and a quadratic shape function was used for the boring bar finite element model. The finite element model of the boring bar consists of three sub-models: the sub-model of the boring bar with the constant cross-section - "body"; the sub-model of the boring bar with the varying cross-section called "head"; and the sub-model of the "tool". All these sub-models were "glued" together, i.e., contacting nodes from the sub-models were locked to each other, ensuring that no relative normal or tangential motion occurred between the sub-models in these nodes.

Two types of boundary conditions were applied to the finite element model of the boring bar at its clamped end. First, the boring bar FE model was clamped in the "rigid" clamping house. This implies that the clamping house and clamping screws were modeled as one non-deformable body constituted of "3-D" surfaces in order to restrict the motion of the boring bar inside the clamping house (see Fig. (5 a)).

Second, a finite element model of the system "boring bar - clamping house" was developed. In this case the boring bar finite element model was inserted in a deformable clamping house model, which consisted of the FE-model of the clamping house combined with the clamping screws as one body. In this finite element model of the "boring bar - clamping house" system, contact between the two deformable bodies (the boring bar and the clamping house) is assumed to be frictionless. The finite element sub-model of the clamping house used tetrahedron elements with four nodes and linear shape functions. This choice was made in light of the following facts: first, the model of the clamping house is used only to approximate actual boundary conditions; second, the lowest natural frequency of the clamping house is significantly higher than the first natural frequencies of the boring bar that are of interest. The finite element edge lengths used in meshing different sub-models are given in Table 1. No displacements were allowed in the nodes of the clamping house surface that corresponded to the real clamping house attached to the turret. The finite element model of the system "boring bar - clamping house" is shown in Fig. (5 b).

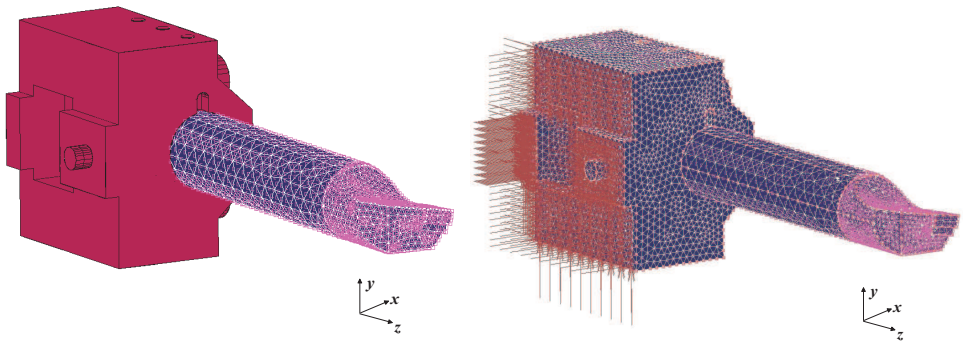

a) b)

Figure 5: "3-D" finite element models of the system "boring bar - clamping house", a) with rigid clamping house, and b) with deformable clamping house.

In order to obtain natural frequencies and mode shapes, Eq. (1) was solved using Lanczos iterative method with the use of MSC.MARC software [9, 13].

The element sizes used in different FE models are summarized in Table 1.

Model	Element Size, [m]	Element Edge Length, [m]
FEM Euler-Bernoulli, "fixed-free" boundary conditions, (FEM1)	0.01	-
FEM Euler-Bernoulli, "pinned-pinned-free" boundary conditions, (FEM2)	0.01	-
FEM Timoshenko, "fixed-free" boundary conditions, (FEM3)	0.01	-
FEM Timoshenko, "pinned-pinned-free" boundary conditions, (FEM4)	0.01	-
Boring bar body in "3-D" FEM (FEM5 and FEM6)	-	0.01
Boring bar head in "3-D" FEM (FEM5 and FEM6)	-	0.005
Boring bar tool in "3-D" FEM (FEM5 and FEM6)	-	0.005
Clamping housing in "3-D" FEM with deformable clamping house, (FEM6)	-	0.005

Table 1: Finite element size and finite element edge length.

The Modal Assurance Criterion can be used to provide a measure of correlation between mode shapes that were estimated based on the experimental modal analysis $\{\psi_{EMA}\}_k$, and numerically-calculated mode shapes based on a finite element model $\{\psi_{FEM}\}_l$; see Part 1 [6].

2.3 Natural Frequency Sensitivity Analysis

Analytical and numerical methods of structural dynamic modeling require a priori information regarding the material properties and dimensions of the structure un-

der analysis, i.e., in our case, the boring bar. The information concerning material properties and dimensions used in a dynamic model of a structure is generally based on estimates. For instance, tabulated values of material parameters in engineering literature and/or data provided by the manufacturer, as well as estimates of material parameters and geometrical dimensions based on measurements of a structure, may be utilized in a dynamic model. The sensitivity of natural frequencies calculated based on modal analysis of a dynamic model of a structure concerning, for instance, differences between the value of a material parameter used in the dynamic model and the actual value of this parameter, may be investigated according to Refs. [14] and [15]. An interval analysis technique may be utilized for this purpose [16].

If material parameters such as Young's elastic modulus E and material density ρ are considered, the interval structural parameters vector $\{\mathbf{p^I}\}$ may be written as (see Appendix A for the basic definitions of the interval analysis):

$$\{\mathbf{p^I}\} = \{\mathbf{p^c}\} + \{\Delta\mathbf{p^I}\} \ ; \tag{2}$$

$$\{\mathbf{p}^c\} = \left\{ \begin{array}{c} \rho^c \\ E^c \end{array} \right\}, \quad \{\Delta\mathbf{p}^I\} = \left\{ \begin{array}{c} \mathbf{\Delta}\rho^{\mathbf{I}} \\ \mathbf{\Delta E^I} \end{array} \right\} \ ; \tag{3}$$

where ρ_c and E_c are the assumed values for the density, respective the Young's elastic modulus of the boring bar material (these values are given in Table 1 in Part 1) [14]. In the interval analysis, real numbers may be presented as degenerate intervals (see Appendix A).

$$\rho_c = [\rho_c, \rho_c]; \tag{4}$$

$$E_c = [E_c, E_c]. \tag{5}$$

The components of vector $\{\Delta\mathbf{p}^I\}$ are intervals, and can be written as follows [14]:

$$\mathbf{\Delta}\rho^{\mathbf{I}} = \frac{\rho_{max} - \rho_{min}}{2}[-1, 1]; \tag{6}$$

$$\mathbf{\Delta E^I} = \frac{E_{max} - E_{min}}{2}[-1, 1]. \tag{7}$$

Based on the interval structural parameters vector $\{\mathbf{p^I}\}$, the interval stiffness $[\mathbf{K}(\{\mathbf{p^I}\})]$, and the interval mass matrices $[\mathbf{M}(\{\mathbf{p^I}\})]$ can be calculated. An interval eigenvalue problem may now be formulated as [15]

$$[\mathbf{K}(\{\mathbf{p^I}\})]\{\mathbf{u}\} = \lambda[\mathbf{M}(\{\mathbf{p^I}\})]\{\mathbf{u}\}. \tag{8}$$

For convenience, standard eigenvalue problem can be considered as follows:

$$[\mathbf{K}(\{\mathbf{p}\})]\{\mathbf{u}\} = \lambda[\mathbf{M}(\{\mathbf{p}\})]\{\mathbf{u}\}, \tag{9}$$

where the stiffness $[\mathbf{K}(\{\mathbf{p}\})]$ and mass $[\mathbf{M}(\{\mathbf{p}\})]$ matrices are uncertain, but bounded, and defined for each structural parameter vector $\{\mathbf{p}\} \in \{\mathbf{p^I}\}$.

If $[\mathbf{K}]$ and $[\mathbf{M}]$ are $N \times N$ matrices, a set of N eignvalues exists for each $\{\mathbf{p}\} \in \{\mathbf{p^I}\}$. In order to obtain the convex hull, or smallest interval$\{\lambda^{\mathbf{I}}\}_k = [\underline{\lambda}_k, \bar{\lambda}_k]$, including all eigenvalues for each λ_k, $k = 1, 2 \ldots, N$ that satisfy

$$[\mathbf{K}(\{\mathbf{p}\})]\{\mathbf{u}\}_k = \lambda_k[\mathbf{M}(\{\mathbf{p}\})]\{\mathbf{u}\}_k, \quad \forall\{\mathbf{p}\} \in \{\mathbf{p^I}\} \quad and \quad k \in \{1, 2, \ldots, N\} \ . \tag{10}$$

The interval for the *kth* eigenvalue due to the given interval of the structural parameters $\{\mathbf{p}^I\}$ can be found using a global optimization procedure, yielding [15]

$$\{\lambda^{\mathbf{I}}\}_k = \left[\min_{\{\mathbf{p}\}\in\{\mathbf{p^I}\}}(\lambda_k(\{\mathbf{p}\})), \max_{\{\mathbf{p}\}\in\{\mathbf{p^I}\}}(\lambda_k(\{\mathbf{p}\}))\right]. \tag{11}$$

A global optimization procedure may, however, become very time consuming, especially for a large numerical model. However, since structural dynamics problems generally exhibit a monotonic behavior, the vertex method may be used to search for the maximal value and the minimal value of an eigenvalue [17]. Thus, in order to predict an eigenvalue interval, the vertex method will only consider all combinations of the boundaries of the structural parameters' intervals. Hence, in this case, the set of all combinations of boundaries of the structural parameters intervals $\{\mathbf{p}^I\}_b$ contains four vectors:

$$\{\mathbf{p}^I\}_b = \left\{ \begin{bmatrix} \rho^c - \Delta\rho \\ E^c - \Delta E \end{bmatrix}, \begin{bmatrix} \rho^c + \Delta\rho \\ E^c - \Delta E \end{bmatrix}, \begin{bmatrix} \rho^c - \Delta\rho \\ E^c + \Delta E \end{bmatrix}, \begin{bmatrix} \rho^c + \Delta\rho \\ E^c + \Delta E \end{bmatrix} \right\}. \tag{12}$$

Thus, an interval for an eigenvalue λ_k can be found in accordance with [18]

$$\{\lambda^I\}_k = \left[\min_{\{\mathbf{p}\}\in\{\mathbf{p^I}\}_\mathbf{b}}(\lambda_k(\{\mathbf{p}\})), \max_{\{\mathbf{p}\}\in\{\mathbf{p^I}\}_\mathbf{b}}(\lambda_k(\{\mathbf{p}\}))\right]. \tag{13}$$

3 Results

This section presents the results of the modal analysis based on the developed finite element models of the clamped boring bar. Results concerning the estimates of the first two natural frequencies as well as corresponding mode shapes produced that are based on finite element models of the clamped boring bar are presented in the same order as in Part 1 [6]. The Modal Assurance Criterion was used again to compare mode shape estimates produced by different models. The mode shapes and corresponding eigenfrequencies provided by the experimental modal analysis in Part 1 are used as a reference [6]. Finally, results concerning the sensitivity of the calculated natural frequencies for the derived finite element models and the distributed-parameter system models derived in Part 1, to changes in the structural parameters used in these models, are presented [6].

Four different "1-D" finite element models of the clamped boring bar have been produced in correspondence with distributed-parameter system models considered in Part 1: an Euler-Bernoulli beam element model with "fixed-free" boundary conditions (FEM1), an Euler-Bernoulli beam element model with "pinned-pinned-free" boundary conditions (FEM2), a Timoshenko beam element model with "fixed-free" boundary conditions (FEM3), and a Timoshenko beam element model with "pinned-pinned-free" boundary conditions (FEM4) [6]. For the four "1-D" finite element models, the fundamental bending mode shapes and the corresponding natural frequencies were calculated using the standard modal analysis procedure based on the eigenvalue problem [7].

Two "3-D" finite element models of the clamped boring bar have also been developed: a "3-D" finite element model with "rigid" clamping house (FEM5) and a "3-D" finite element model with deformable clamping house (FEM6). The two fundamental boring bar eigenfrequencies were calculated for the FE-models of the clamped boring bar (see Table 2). These eigenfrequencies are compared to the ones estimated by means of the experimental modal analysis reported in Part 1 [6].

In the present discussion, concerning the two fundamental bending modes of the boring bar, the mode corresponding to the lowest fundamental eigenfrequency is referred to as mode 1. The mode corresponding to the highest fundamental eigenfrequency is referred to as mode 2. Correspondingly, the mode shapes are referred to as mode shape 1 and mode shape 2.

Model	Resonance freq., [Hz]	
	Mode 1	Mode 2
Experimental Modal Analysis, (EMA)	524.069	555.885
FEM Euler-Bernoulli, "fixed-free" boundary conditions, (FEM1)	698.120	698.335
FEM Euler-Bernoulli, "pinned-pinned-free" boundary conditions, (FEM2)	539.112	539.278
FEM Timoshenko, "fixed-free" boundary conditions, (FEM3)	687.026	687.231
FEM Timoshenko, "pinned-pinned-free" boundary conditions, (FEM4)	525.116	525.269
"3-D" FEM of the boring bar and rigid clamping house, (FEM5)	581.361	609.708
"3-D" FEM of the boring bar and deformable clamping house, (FEM6)	540.194	563.376

Table 2: Natural frequencies estimates.

The mode shapes calculated based on finite element models and estimated based on the experimental modal analysis (Part 1) are presented in two groups [6]. For each of these models the corresponding resonance frequencies of the first two fundamental bending modes are presented in Table 2. The first group consists of the mode shapes calculated based on the "1-D" finite element models (FEM1, FEM2, FEM3, FEM4) with both "fixed-free" and "pinned-pinned-free" boundary conditions, the mode shapes produced with the experimental modal analysis in Part 1, and the mode shapes estimated from "3-D" finite element models (FEM5, FEM6) [6]. The mode shapes are plotted with respect only to the free end of the boring bar. Mode shapes presented in group 1 (see Fig. (6)) were produced based on the finite element models of the clamped boring bar and compared to the mode shapes estimated experimentally. To enable comparison, the mode shapes presented in Fig. (6) are sampled spatially, corresponding to the positions of accelerometers at the actual boring bar.

The second group (see Fig. (7)) consists of the mode shapes calculated based on the "1-D" finite element models (FEM2, FEM4), both with the "pinned-pinned-free" boundary conditions, and the mode shapes estimated from "3-D" finite element models (FEM5, FEM6). The mode shapes in the second group are displayed with respect to the whole length of the boring bar to demonstrate the flexibility of the boring bar clamped inside the clamping house. Since the mode shapes shown in Fig. (7) are produced solely based on the finite element models, no spatial sampling was utilized.

To provide a quantitative measure of the correlation between the mode shapes

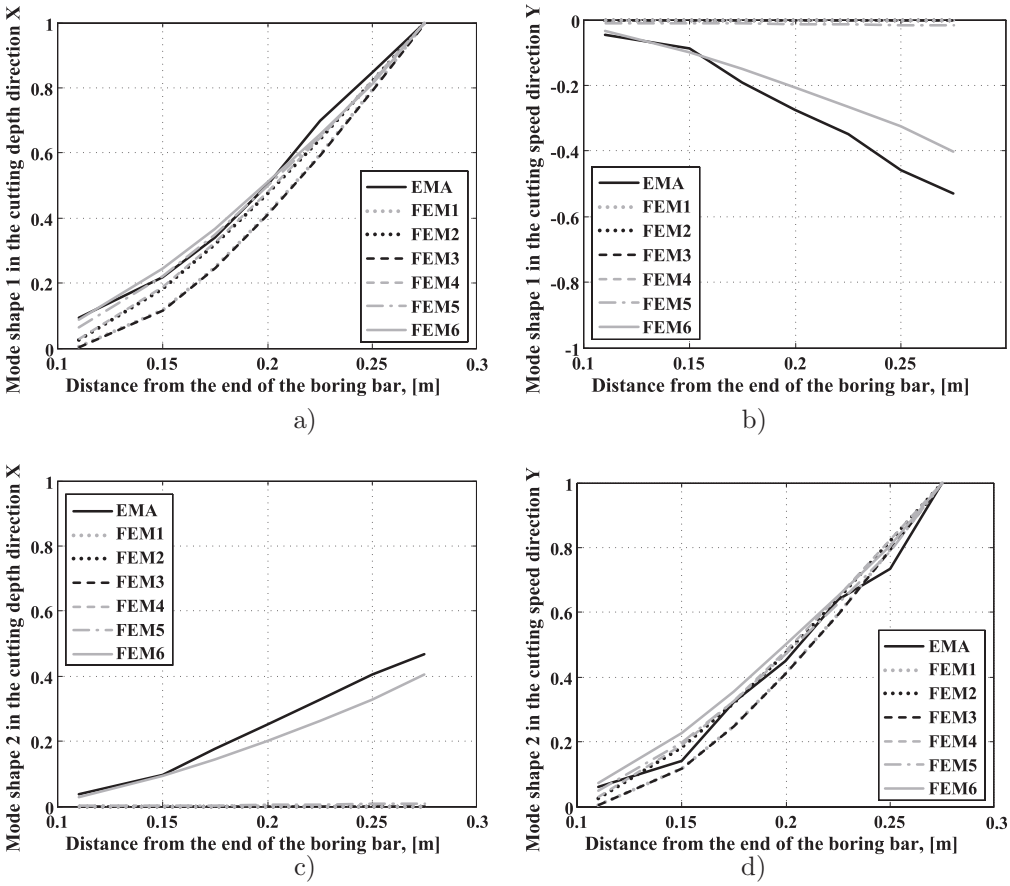

Figure 6: The first two fundamental mode shapes of the boring bar: a) component of mode shape 1 in the cutting depth direction, b) component of mode shape 1 in the cutting speed direction, c) component of mode shape 2 in the cutting depth direction, and d) component of mode shape 2 in the cutting speed direction. Produced based on experimental modal analysis (EMA), finite element models (FEM1, FEM2, FEM3, FEM4, FEM5, FEM6), correspondingly.

from the experimental modal analysis and the mode shapes for the finite element models, cross-MAC matrices have been produced [6].

The cross-MAC matrix between the modes shapes calculated using the "1-D" finite element model with Euler-Bernoulli beam elements and "fixed-free" boundary conditions ($FEM1$) and the mode shapes from the experimental modal analysis (EMA) is given by

$$[MAC]_{FEM1,EMA} = \begin{bmatrix} MAC_{FEM1_1,EMA_1} & MAC_{FEM1_2,EMA_1} \\ MAC_{FEM1_1,EMA_2} & MAC_{FEM1_2,EMA_2} \end{bmatrix} = \begin{bmatrix} 0.772 & 0.215 \\ 0.204 & 0.787 \end{bmatrix}. \quad (14)$$

The cross-MAC matrix between the modes shapes calculated using the "1-D" finite

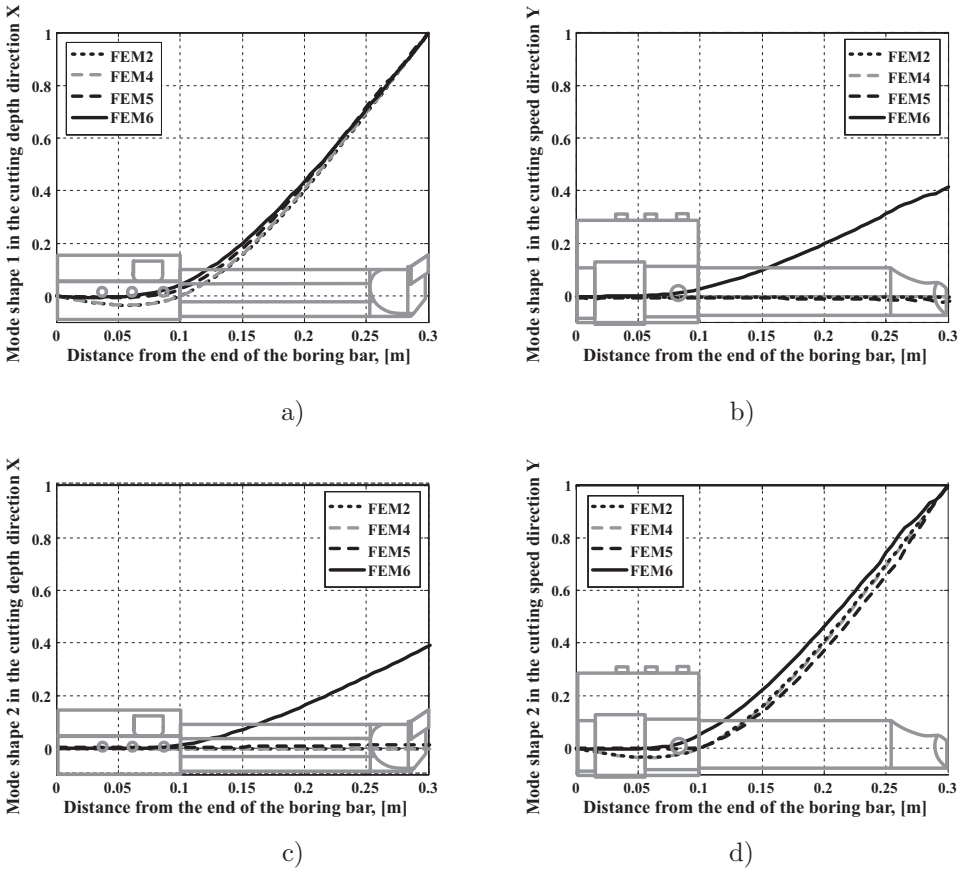

Figure 7: The first two fundamental mode shapes of the boring bar: a) component of mode shape 1 in the cutting depth direction, b) component of mode shape 1 in the cutting speed direction, c) component of mode shape 2 in the cutting depth direction, and d) component of mode shape 2 in the cutting speed direction. Produced based on finite element models (FEM2, FEM4, FEM5, FEM6) correspondingly.

element model with Timoshenko beam elements and "fixed-free" boundary conditions ($FEM3$) and the mode shapes from the experimental modal analysis (EMA) is given by

$$[MAC]_{FEM3,EMA} = \begin{bmatrix} MAC_{FEM3_1,EMA_1}, & MAC_{FEM3_2,EMA_1} \\ MAC_{FEM3_1,EMA_2} & MAC_{FEM3_2,EMA_2} \end{bmatrix} = \\ = \begin{bmatrix} 0.772 & 0.215 \\ 0.204 & 0.787 \end{bmatrix}. \quad (15)$$

The "1-D" finite element models (FEM2, FEM4) with "pinned-pinned-free" boundary conditions include flexibility along the segment of a boring bar model inside the "clamping house". For these boring bar models, the calculated mode shapes are shown in Fig. (6), as are the mode shapes estimated based on the "3-D" finite element models (FEM5, FEM6). Also, cross-MAC matrices have been calculated between the

mode shapes presented in this group.

The cross-MAC matrix between the modes shapes calculated using the "1-D" finite element model with Euler-Bernoulli beam elements and "pinned-pinned-free" boundary conditions ($FEM2$) and the mode shapes from the experimental modal analysis (EMA) is given by

$$[MAC]_{FEM2,EMA} = \begin{bmatrix} MAC_{FEM2_1,EMA_1,} & MAC_{FEM2_2,EMA_1} \\ MAC_{FEM2_1,EMA_2} & MAC_{FEM2_2,EMA_2} \end{bmatrix} = \\ = \begin{bmatrix} 0.780 & 0.217 \\ 0.206 & 0.790 \end{bmatrix}. \tag{16}$$

The cross-MAC matrix between the modes shapes calculated using the "1-D" finite element model with Timoshenko beam elements and "pinned-pinned-free" boundary conditions ($FEM4$) and the mode shapes from the experimental modal analysis (EMA) is given by

$$[MAC]_{FEM4,EMA} = \begin{bmatrix} MAC_{FEM4_1,EMA_1,} & MAC_{FEM4_2,EMA_1} \\ MAC_{FEM4_1,EMA_2} & MAC_{FEM4_2,EMA_2} \end{bmatrix} = \\ = \begin{bmatrix} 0.780 & 0.217 \\ 0.207 & 0.790 \end{bmatrix}. \tag{17}$$

Cross-MAC matrices were also calculated between mode shapes estimated using the "3-D" finite element models (FEM5, FEM6) and mode shapes obtained with the experimental modal analysis. The cross-MAC matrix between mode shapes calculated using the "3-D" finite element model with the rigid clamping house ($FEM5$) and mode shapes estimated with the experimental modal analysis (EMA) is given by

$$[MAC]_{FEM5,EMA} = \begin{bmatrix} MAC_{FEM5_1,EMA_1} & MAC_{FEM5_2,EMA_1} \\ MAC_{FEM5_1,EMA_2} & MAC_{FEM5_2,EMA_2} \end{bmatrix} = \\ = \begin{bmatrix} 0.788 & 0.211 \\ 0.201 & 0.797 \end{bmatrix}. \tag{18}$$

The cross-MAC matrix between the mode shapes calculated using the "3-D" finite element model with the deformable clamping house ($FEM6$) and mode shapes estimated with the experimental modal analysis (EMA) is given by

$$[MAC]_{FEM6,EMA} = \begin{bmatrix} MAC_{FEM6_1,EMA_1,} & MAC_{FEM6_2,EMA_1} \\ MAC_{FEM6_1,EMA_2} & MAC_{FEM6_2,EMA_2} \end{bmatrix} = \\ = \begin{bmatrix} 0.988 & 0.010 \\ 0.008 & 0.988 \end{bmatrix}. \tag{19}$$

As model complexity increases and as the system's geometry description evolves, a gradual increase is observable in the correlation between the experimentally obtained mode shapes and the FE-models mode shapes. This increase may also be observed by comparing the mode shapes calculated based on the distributed-parameter system (from Part 1) and FE models with mode shapes estimated experimentally (see Figs. (6), (7)). Thus, the degree of correlation between predicted and estimated mode shapes is increased from 77.12% for the Euler-Bernoulli "fixed-free" beam model (EB1) in Part 1, to 98.76% for the "3-D" FE-model with the deformable clamping house (FEM6) [6].

3.1 Natural Frequency Sensitivity Estimates

An investigation of the sensitivity of the calculated natural frequencies was carried out with respect to variations in material density and Young's elastic modulus used in the distributed-parameter system models and the finite element models of the boring bar. The sensitivity of the natural frequencies was examined by means of the vertex method with respect to variations of 2% in the assumed material density $\rho^c = 7850\ kg/m^3$, and Young's elastic modulus $E^c = 205$ GPa. Most steel sorts have a material density ranging from 7600 to 8000 kg/m^3. This range corresponds to a material density interval that allows for approximately 2% variation around the assumed material density $\rho = 7850\ kg/m^3$. A change of 40^o C in the temperature of a steel structure results in approximately a 2% change of the Young's elastic modulus [19]. The natural frequency intervals for each of the boring bar models, fundamental eigenfrequencies are calculated in accordance with Eq. (13) and are given in Table 3.

Model	Resonance frequency			
	Mode 1, $[Hz]$		Mode 2, $[Hz]$	
	$f_{1,min}$	$f_{1,max}$	$f_{2,min}$	$f_{2,max}$
EB1	684.295	712.225	684.505	712.444
EB2	528.435	550.004	528.598	550.173
T1	673.409	700.895	673.609	701.104
T2	514.695	535.703	514.845	535.859
FEM1	684.295	712.225	684.505	712.444
FEM2	528.435	550.004	528.598	550.173
FEM3	673.416	700.903	673.617	701.111
FEM4	514.715	535.723	514.865	535.880
FEM5	569.848	593.107	597.633	622.027
FEM6	529.496	551.109	552.219	574.759

Table 3: Natural frequency intervals for ± 2% variations in the material density and the Young's elastic modulus.

4 Discussion and Conclusions

The above results demonstrate that the "1-D" finite element models of the boring bar with clamping flexibility, the two-span models with "pinned-pinned-free" boundary conditions, yield both mode shape and eigenfrequency estimates that have higher correlation with the corresponding experimental modal analysis estimates (from Part 1) as compared to the "fixed-free" "1-D" FE models [6]. By introducing a "3-D" finite element model of the clamped boring bar, particularly one that includes a "3-D" finite element model of the clamping house, the correlation with the experimental results is increased substantially. This "3-D" finite element model of the clamped boring bar provides the greatest correlation with the mode shape and eigenfrequency estimates provided by the experimental modal analysis. Of significance, it is the only boring bar model that to a large extent describes the frequency difference between the two fundamental natural frequencies and the mode shape rotation, with respect to the coordinate system, that are observable in the estimates provided by the experimental modal analysis. Quantitative information on the sensitivity of natural frequencies

calculated with the applied distributed-parameter system (see Part 1) and numerical finite element boring bar models, with respect to variation in material properties, is given [6]. Small deviations in the selected values for the material density ρ^c and Young's elastic modulus E^c may be impeding factors for the final accuracy of a boring bar model.

Both the "fixed-free" "1-D" finite element models of the boring bar overestimated fundamental natural frequency estimates compared to the corresponding experimental modal analysis (EMA) estimates (see Table 2). To improve the "1-D" finite element models of the boring bar, the modeling of the actual boundary conditions of the boring bar was modified. As in the case of the distributed-parameter system models (see Part 1), the length of the beam element model was extended to the full length of the boring bar, and the beam was pinned at two positions along the part of the beam model corresponding to the clamped part of the actual boring bar [6]. The introduced clamping flexibility resulted in natural frequency estimates with significantly lower frequency values (see Table 2). Again, the Timoshenko beam element model (FEM 4) produced natural frequency estimates close to the estimates obtained experimentally: a fundamental resonance frequency of 525.2 Hz (cf. EMA, 555.7 Hz) in the cutting speed direction, and 525.1 Hz (cf. EMA, 524.1 Hz) in the cutting depth direction. The finite element models produced a good approximation of the corresponding distributed-parameter system models (see Part 1), even when a low number of elements were used (see Table 2) [6].

The "1-D" models of the boring bar are unable to provide the frequency difference of approximately 30 Hz between the two fundamental natural frequencies, which is observable in the results from the experimental modal analysis (see Table 2). In order to obtain a model of the clamped boring bar that provided a higher correlation with the results of the experimental modal analysis (EMA), a "3-D" finite element model was developed. First, the "3-D" finite element model of the boring bar was analyzed with the following boundary conditions: frictionless contact with a rigid clamping house (FEM5). This boring bar finite element model provided a separation of 28 Hz in the fundamental natural frequencies. However, it yielded significantly higher values for the fundamental resonance frequency compared with the EMA results (see Table 2). To improve the accuracy of the "3-D" finite element model of the boring bar, the rigid boundary conditions were replaced by means of a "3-D" finite element model of the clamping house. The combined "3-D" finite element model of the boring bar and "3-D" finite element model of the clamping house (FEM6) resulted in a separation of the fundamental natural frequencies by 23 Hz; the fundamental resonance frequency was 563.4 Hz (cf. EMA, 555.7 Hz) in the cutting speed direction and 540.2 Hz (cf. EMA, 524.1 Hz) in the cutting depth direction. From the mode shape estimates shown in Figs. (6) and (7) it can be observed that mode shapes calculated based on model FEM6 display the highest correlation with the mode shapes from the experimental modal analysis. The mode shapes for the "1-D" finite element models with "fixed-free" boundary conditions (FEM1, FEM3) display the largest difference from the experimental mode shape estimates. The models with "pinned-pinned-free" boundary conditions (FEM2, FEM4) result in mode shapes with slightly higher correlation to the experimental mode shapes. These observations are also quantified by the cross-MAC matrices in Eqs. (14), (15), (16), (17), (18), and (19). Only the mode shape estimates from the FEM6 model and the EMA are rotated with respect to the coordinate system; i.e., the two mode shapes have non-zero components in both the cutting depth and in the cutting speed directions. Moreover, the mode shapes from

the experimental modal analysis, the FEM5 model, and the FEM6 model indicate a pronounced deformation of the boring bar adjacent to the clamping house (see Figs. (6)). As in the case of corresponding distributed-parameter system models (EB1, T1, see Part 1), the mode shape estimates produced based on the "1-D" finite element models with "fixed-free" boundary conditions (FEM1, FEM3) do not display any flexibility of the boring bar in the point located close to the clamping house [6]. Some flexibility at this point is introduced by "pinned-pinned-free" boundary conditions and can be observed from the mode shapes estimates calculated based on models FEM2 and FEM4. There is a fairly good correlation between the mode shapes in the second group estimated by models FEM2, FEM4, FEM5 and FEM6 (see Fig. (7)). These mode shapes show some flexibility in the part of the boring bar clamped inside the clamping house.

However, also in the case of the boring bar model FEM6, whose mode shapes and natural frequencies display the greatest correlation with the results from the experimental modal analysis, there is still some discrepancy. This may, for instance, be explained by factors such as imperfections in the geometrical model of the boring bar, clamp screws, and clamping house; differences between actual material properties and those used in the models; and uncertainty in measurements. These factors will all affect the correlation between the finite element model and the EMA model. The influence of a variation of $\pm 2\%$ in both the material density ρ value and Young's elastic modulus E value have been considered with respect to natural frequencies estimates produced by the different models. The estimates given in Table 3 indicate that a $\pm 2\%$ change in the aforementioned material properties yields a variation of approximately 22-30 Hz in the fundamental natural frequencies.

Acknowledgments

The present project is sponsored by Acticut International AB.

Appendix

Basic Definitions of the Interval Analysis

A closed real interval $X = [a, b]$ is considered as a set of real numbers $X = \{x | a \leqslant x \leqslant b\}$. In the interval analysis, the interval X is usually referred to as an ***interval number*** [16, 20].

A real number x is presented in the interval analysis as an interval $x = [x, x]$, which is referred to as ***degenerate interval***.

An interval vector is a vector whose components are intervals. Suppose we have a vector of real numbers $\{\mathbf{x}\} = \{x_1, ..., x_i, ..., x_n\}$ and an interval vector $\{\mathbf{x^I}\} = \{X_1, ..., X_i, ..., X_n\}$, where $X_i = \{\underline{x}_i, \bar{x}_i\}$ and $\underline{x}_i$, $\bar{x}_i$ represents the lower- and upper-boundary values for the real number x_i.

Then $\{\mathbf{x}\} \in \{\mathbf{x^I}\}$ if and only if $x_i \in X_i$ or $\underline{x}_i \leqslant x_i \leqslant \bar{x}_i$ for $\forall i \in 1, ..., n$.

An interval matrix $[\mathbf{A^I}]$ is a matrix whose elements are intervals. Let $[\mathbf{A}]$ be a real matrix $[\mathbf{A}] = (a_{ij})$, where $i \in 1, ..., n$ and $j \in 1, ..., m$. Let $[\mathbf{A^I}]$ be an interval matrix $[\mathbf{A^I}] = (A_{ij})$, where $A_{ij} = [\underline{a}_{ij}, \bar{a}_{ij}]$ and $\underline{a}_{ij}$, $\bar{a}_{ij}$ are lower- and upper- boundary values for the real number a_{ij}.

Then $[\mathbf{A}] \in [\mathbf{A^I}]$ if and only if $\underline{a}_{ij} \leqslant a_{ij} \leqslant \bar{a}_{ij}$ for $\forall i \in 1, ..., n$ and $\forall j \in 1, ..., m$ [16, 20].

Basic Operations

Suppose a set of basic arithmetic operations is denoted by $\bullet = \{+, -, \times, \div\}$, then an arithmetic operation on the two interval numbers $X = [\underline{x}, \bar{x}]$ and $Y = [\underline{y}, \bar{y}]$ is defined as

$$Z = X \bullet Y = \{x \bullet y | x \in X, y \in Y\}. \tag{A.1}$$

Thus, the interval Z contains every possible number that can be formed as $x \bullet y$ for each $x \in X$ and $y \in Y$ [16, 20].

$$X + Y = [\underline{x} + \underline{y}, \bar{x} + \bar{y}]; \tag{A.2}$$

$$X - Y = [\underline{x} - \bar{y}, \bar{x} - \underline{y}]; \tag{A.3}$$

$$X \times Y = [\min\{\underline{xy}, \underline{x}\bar{y}, \bar{x}\underline{y}, \bar{x}\bar{y}\}, \max\{\underline{xy}, \underline{x}\bar{y}, \bar{x}\underline{y}, \bar{x}\bar{y}\}]. \tag{A.4}$$

The division is considered for intervals that do not contain zero, i.e., if $0 \notin Y$, then

$$\frac{1}{Y} = \left[\frac{1}{\bar{y}}, \frac{1}{\underline{y}}\right], \tag{A.5}$$

and

$$\frac{X}{Y} = X \times \left(\frac{1}{Y}\right). \tag{A.6}$$

References

[1] B. W. Wong, B. L. Walcott, and K. I. Rouch, Active Vibration Control via Electromagnetic Dynamic Absorbers, in *Proceedings of the 4th IEEE Conference on Control Applications*, 868–874, (1995).

[2] S. Nagano, T. Koizumi, T. Fujii, N. Tsujiuchi, H. Ueda, and K. Steel, Development of a composite boring bar, *Composite Structures*, **38**(1), 531–539, (1997).

[3] J. Baker and K. Rouch, Use of finite element structural models in analyzing machine tool chatter, *Finite Elements in Analysis and Design*, **18**, 1029–1046, (2002).

[4] P.-O. H. Sturesson, L. Håkansson, and I. Claesson, Identification of the Statistical Properties of the Cutting Tool Vibration in a Continuous Turning Operation - Correlation to Structural Properties, *Mechanical Systems and Signal Processing, Academic Press*, **11**(3), 459–489, (1997).

[5] R. Mahdavinejad, Finite element analysis of machine and workpiece instability in turning, *International Journal of Machine Tools & Manufacture*, **45**, 753–760, (2005).

[6] T. Smirnova, H. Åkesson, and L. Håkansson, Dynamic Modeling of a Boring Bar Using Theoretical and Experimental Engineering Methods part 1: Distributed-Parameter System Modeling and Experimental Modal Analysis, *submitted to the International Journal of Acoustics and Vibration (IJAV)*, (2009).

[7] D. Inman, *Engineering Vibration*, Prentice-Hall, second edition, (2001).

[8] R. Astley, *Finite Elements in Solids and Structures*, Chapman & Hall, (1992).

[9] O. S. Zienkiewicz, R. L. Taylor, and J. Zhu, *The Finite Element Method: Its Basis and Fundamentals*, Butterworth-Heinemann, (2005).

[10] J. B. Kosmatka, An improved finite element for stability and natural frequencies of axial-loaded Timoshenko beams, *Computers and Structures*, **57**(1), 141–149, (1995).

[11] T. Yokoyama, Vibration analysis of Timoshenko beam-columns or two-parameter elastic foundation, *Computers and Structures*, **61**(6), 995–1007, (1996).

[12] M. Petyt, *Introduction to finite element vibration analysis*, Cambridge University Press, (1980).

[13] *MSC.MARC Volume A: Theory and User's Information*, MSC.Software, (2005).

[14] S. H. Chen, H. D. Lian, and X. W. Yang, Interval eigenvalue analysis for structures with interval parameters, *Finite Elements in Analysis and Design*, **39**, 419–431, (2003).

[15] Z. Qiu and X. Wang, Solution theorems for the standard eigenvalue problem of structures with uncertain-but-bounded parameters, *Journal of Sound and Vibration*, **282**, 381–399, (2004).

[16] E.Hansen and G.W.Walster, *Global optimization using interval analysis*, Marcel Dekker, Inc. (2004).

[17] Z. Qiu and X. Wang, Several solution methods for generalized complex eigenvalue problem with bounded uncertainties, *International Journal of Solids and Structures*, **42**, 2883–2900, (2005).

[18] W. Dong and H. Shah, Vertex method for computing functions of fuzzy variables, *Fuzzy Sets and Systems*, **4**, 65–78, (1987).

[19] O. Erlandsson, S. Lagerkrans, R. Naslund, and E. Vuorinen, *Maskin handboken*, Studentlitteratur, (2000).

[20] G. Alefeld and G. Mayer, Interval analysis: theory and applications, *Journal of Computational and Applied Mathematics*, **121**, 421–464, (2000).

Part IV

Modeling of an Active Boring Bar

Part IV is based on the publications:

T. Smirnova, H. Åkesson and L. Håkansson *Modeling of an Active Boring Bar*, Research Report No 2007:14, Blekinge Institute of Technology, ISSN: 1103-1581 December 2007.

T. Smirnova, H. Åkesson, L. Håkansson, Ingvar Claesson, and Thomas Lagö, *Initial Experiments with a Finite Element Model of an Active Boring Bar*, published in proceedings of The Fourteenth International Congress on Sound and Vibration, ICSV14, Cairns, Australia, 9 - 12 July, 2007.

Modeling of an Active Boring Bar

T. Smirnova, H. Åkesson, and L. Håkansson
Department of Signal Processing
Blekinge Institute of Technology
372 25 Ronneby
Sweden

Abstract

Vibration problems occurring during internal turning operations in the manufacturing industry urge for adequate passive and/or active control techniques in order to increase the productivity of machine tools. Usually, passive solutions are based on either boring bars made partly in high Young's modulus non-ductile materials such as sintered tungsten carbide or boring bars with tuned vibration absorbers adjusted to increase the dynamic stiffness in the frequency range of a certain resonance frequency of the boring bar. By utilizing an active boring bar with an embedded piezoceramic actuator and a suitable controller, the primary boring bar vibrations originating from the material deformation process may be suppressed with actuator-induced secondary "anti vibrations". In order to design an active boring bar, several issues have to be addressed, i.e., selecting the characteristics of the actuator, the actuator size, the position of the actuator in the boring bar, etc. This usually implies the manufacturing and testing of several prototypes of an active boring bar, and this is a time-consuming and costly procedure. Therefore, mathematical models of active boring bars incorporating the piezo-electric effect that enable the accurate prediction of their dynamic properties and responses are of great importance. This report addresses the development of a "3-D" finite element model of the system boring bar-actuator-clamping house. The spatial dynamic properties of the active boring bar, i.e., its natural frequencies and mode shapes, as well as the transfer function between actuator voltage and boring bar acceleration are calculated based on the "3-D" FE model and compared to the corresponding experimentally obtained estimates. Two types of approximations of the Coulomb friction force, the arctangent and the bilinear models, are evaluated concerning modeling contact between the surface of the boring bar and the clamping house.

1 Introduction

The internal turning operation is generally considered as one of the most vibration-prone metal working processes. In such operations, a boring bar is used to machine deep, precise geometries to required tolerances inside a pre-drilled hole in a workpiece. A boring bar can usually be characterized as a slender beam and is generally the weakest link in a machine tool system. During turning, the material deformation process induces a broad-band excitation of the machine tool, and, as a result, relative

dynamic motion between the boring bar and the workpiece frequently occurs, commonly referred to as chatter. High levels of boring bar vibration result in poor surface finish, excessive tool wear, tool breakage and severe levels of acoustic noise. Thus, boring bar vibration has a negative impact on productivity, working environment, etc. Usually, the high vibration level is excited at the natural frequencies related to low-order bending modes of the boring bar and are dominated by the bending mode in the cutting speed direction, since it is in this direction that the cutting force has the largest component [1–3]. In industry, there are considerable demands concerning methods improving the stability of internal turning operations. The motive is mainly to increase the productivity, but the working environment is also a growing issue.

From at least the beginning of the twentieth century, research in metal cutting has been devoted to expanding the existing knowledge of cutting dynamics, etc., by means of mathematical modeling and experimental studies [3–9]. Most research carried out on the dynamic modeling of cutting dynamics has concerned the prediction of stability limits, i.e., predicting cutting data for stable cutting [3, 8].

The strategies for controlling boring bar vibrations can be classified into two directions. The first direction refers to control of cutting data in order to maintain stable cutting, i.e., to avoid cutting data resulting in chatter or to continuously vary cutting data in a structured manner to avoid chatter [9–11]. The second direction concerns modifications of the dynamic stiffness of one or several parts of the chain insert - tool holder - clamping - machine tool, with the purpose of increasing the system's resistance to machine tool chatter [9, 12–16]. Generally, the boring bar vibration control methods modifying the dynamic stiffness are divided into two groups: passive and active control. In passive boring bar vibration control, the dynamic stiffness may be increased by changing the static stiffness of the bar, e.g., for instance by using a boring bar produced completely or partly (composite boring bar) of materials with higher modulus of elasticity such as sintered tungsten carbide [9, 12]. Another passive control strategy is to use passive Tuned Vibration Absorbers (TVA) to resist machine tool chatter [9,12]. A TVA consists of a tube which contains a reactive mass inside a layer of damper oil and is usually built into the boring bar close to the tool tip [12,13]. TVA boring bars offer solutions with a fixed enhancement of the dynamic stiffness, frequently tuned for a narrow frequency range comprising the fundamental bending modes eigenfrequencies [9]. On the other hand, active feedback control of turning operations produces a selective increase of the dynamic stiffness at the actual frequency of the dominating bending mode [14–16].

An active control approach was reported by Tewani et al. [14] concerning active dynamic absorbers in boring bars controlled by a digital state feedback controller. It was claimed to provide a substantial improvement in the stability of the cutting process. Browning et al. [15] reported an active clamp for boring bars controlled by a feedback version of the filtered-x LMS algorithm. They assert that the method enables one to extend the operable length of boring bars. Claesson and Håkansson [16] controlled tool vibration by using the feedback filtered-x LMS algorithm to control tool shank vibration in the cutting speed direction, without applying the traditional regenerative chatter theory.

Two important constraints concerning the active control of tool vibration involve the difficult environment in a lathe and industry demands. It is necessary to protect the actuator and sensors from the metal chips and cutting fluid. Also, the active control system should be applicable to a general lathe. Pettersson et al. [17] reported an adaptive active feedback control system based on a tool holder shank with embedded

actuators and vibration sensors. This control strategy was later applied to boring bars by Pettersson et al. [18]. Åkesson et al. [19] reported the successful application of the active adaptive control of boring bar vibration in industry using an active boring bar with embedded actuators and vibration sensors.

The active control of boring bar vibration is based on an active boring bar equipped with embedded actuators and vibration sensors in conjunction with a feedback controller. The active boring bar typically has an accelerometer attached close to the tool-end, which measures boring bar vibration in the cutting speed direction. The controller uses the accelerometer signal to produce secondary or "anti vibrations" via an actuator embedded inside a groove milled in the longitudinal direction below the center line of the boring bar. Due to the piezoelectrical properties of the actuator material, the dynamic control signal will steer the length expansion of the actuator. The actuator will in turn apply a bending moment to the boring bar to counteract the primary vibration excited by the material deformation process [20].

In order to design an active boring bar with embedded actuator, several issues have to be addressed, i.e., selecting the characteristics of the actuator, the actuator size, the position of the actuator in the boring bar, etc. Obtaining adequate performance from an active boring bar usually implies the manufacturing and testing of several prototypes of the active boring bar, this is a complex, time consuming and costly procedure. Thus, it is likely that the efficiency of design procedure can be increased by means of dynamic modeling of active boring bar, for instance, by utilizing "3-D" finite element modeling. It is plausible that such a model can be used, e.g., for predicting of the dynamic properties of an active boring bar, describing the interaction of the boring bar and actuator, and accounting for nonlinearities introduced into its response by the contact between the boring bar, clamping house and clamping screws.

A number of research works have been carried out concerning the modeling of a boring bar as a system with a large but finite number of degrees-of-freedom, using finite element analysis. Wong [21] used Timoshenko beam finite elements to model a boring bar. He designed an electromagnetic dynamic absorber and simulated its performance, utilizing modal control and direct feedback control based on the finite element model of the boring bar. Wong claims that both controllers succeed in significant damping of boring bar vibrations at the lowest vibration mode. Nagano [22] used pitched-based carbon fiber reinforced plastic (CFRP) material to develop a chatter resistant boring bar with a large overhang. He made an attempt to create a "3-D" finite element model in order to predict natural frequencies and improve dynamic characteristics of the boring bar by modeling embedded steel cores of various shapes. The cutting performance and stability of the designed boring bars regarding chatter were investigated experimentally. He claims that utilization of the CFRP material together with the cross-shaped steel core allows for the successful stable machining for boring bars with length-to-diameter of more then seven. Nagano also mentioned the necessity concerning the development of improved models for the clamping of the boring bar. Later, Sturesson et al. [23] developed a "3-D" finite element model of a tool holder shank. They used normal mode analysis to evaluate the natural frequencies, modal masses and mode participation factors of the tool holder shank. The modal damping was estimated using the free vibration decay method. The spectral densities' estimates were also utilized to obtain natural frequencies. The results of the normal mode analysis and spectral densities' estimates were well-correlated. Baker et al. [24] used FEM in the stability analysis of a turning operation. He approximated the cutting force by using the orthogonal cutting force model. Baker also based his

method of stability prediction on the assumption of the linearity of the tooling structure's behavior. Two different types of FE models were considered: firstly, "1-D" FE models of the tool holder and the workpiece attached to the rigid base; secondly, "3-D" FE models of the tool holder and the workpiece attached to the deformable "3-D" FE model of machine tool. The FE models were used to extract structural matrices, with the purpose of using them in stability analysis. The maximum stable width of cut was predicted for a set of geometric dimensions of the tool holder and the workpiece (for both types of models) as a function of spindle speed. However, no experimental results were presented. Later, in [25], Mahdavinejad also tried to predict maximum width of cut, ensuring stable cutting with the use of a "3-D" FE model of a machine tool. Several "3-D" FE models containing different machine tool parts were developed. Natural frequencies and the mode shapes of the tailstock were estimated based on the "3-D" FE models and compared with results obtained from experimental modal analysis. The stability lobe diagrams were obtained for the chuck-center with and without tailstock cases. In both cases the stability lobe diagrams were calculated based on analytical considerations and experiments. Results from the modal analysis as well as the stability lobe diagrams produced with the use of FE models are claimed to be well-correlated to corresponding experimental estimates.

Thus, it appears as though no work has been carried out on the finite element modeling of active boring bars with embedded piezoelectric stack actuators.

This report addresses the process of developing a "3-D" finite element model of the system boring bar - actuator - clamping house. Estimates of the first two natural frequencies and the corresponding mode shapes have been produced based on both an initial linear "3-D" finite element model and an experimental modal analysis of the active boring bar, and also compared. A more advanced nonlinear "3-D" finite element model of the active boring bar, enabling variable contact between clamping house and boring bar, has also been considered. As a further extension of this "3-D" finite element model, a model that incorporates nonlinear friction force acting between the contacting surfaces of the boring bar and clamping house has been evaluated. Two different models of the Coulomb friction force, the bilinear and the arctangent, have been considered. The nonlinear active boring bar FE models were evaluated in comparison with the experimental modal analysis results. Estimates of control path frequency response functions between the voltage applied to the actuator and the acceleration in the position of the error accelerometer in the cutting speed direction and in the cutting depth direction, have been produced. These frequency response functions were estimated both for data obtained from the numerical simulations using the "3-D" finite element models and for experimental data from the lathe. Also, a simple distributed-parameter Euler-Bernoulli model of the active boring bar has been introduced.

2 Materials and Methods

2.1 Experimental Setup

2.1.1 System Overview

The experimental modal analysis and control path estimates were conducted in a Mazak SUPER QUICK TURN - 250M CNC and a Mazak QUICK TURN NEXUS 300-II CNC turning centers. The Mazak SUPER QUICK TURN - 250M CNC machine tool has a spindle power of 18.5 kW and a maximal machining diameter of 300

mm, a maximal spindle speed of 4000 (r.p.m.), with 1007 mm between the centers and a turret capacity of 12 tools (see Fig. 1). The Mazak QUICK TURN NEXUS 300-II CNC machine tool has a spindle power of 26.1 kW and a maximal machining diameter of 420 mm, a maximal spindle speed of 4000 (r.p.m.), with 1250 mm between the centers and a turret capacity of 12 tools (see Fig. 2).

Figure 1: Mazak 250 SUPER QUICK TURN - 250M CNC turning center.

Active Boring Bar The active boring bar was based on a standard boring bar, S40T PDUNR15 F3 WIDAX (see Fig. 3). The WIDAX boring bar is made of the material 30CrNiMo8; in the modeling, it is assumed that Young's elastic modulus $E = 205\ GPa$, density $\rho = 7850\ kg/m^3$ and Poisson's coefficient $\nu = 0.3$.

It has an actuator embedded into a milled space below the center line of the boring bar and an accelerometer attached close to the insert (see Fig. 4).

The coordinate system is defined as follows: x is the cutting depth direction, y is the negative cutting speed direction and z is the feed direction.

Clamping House As a clamping house, a standard 8437-0 40 mm Mazak holder was used (see Fig. 5). The clamping house is attached to the turret by four screws. The boring bar can be clamped in the clamping house using either four or six screws. In the experiments and simulations presented in the current report, only four screws were used to clamp the boring bar.

Piezoelectric Actuator The piezoelectric stack actuator used in the experiments is made of the piezoelectric material Lead Zirconate Titanate (PZT-5H) and is shown in Fig. 6. The actuator material properties (in the finite element modeling) were chosen as they are similar to the properties of PZT-5H material, with modifications made for the strain coefficients d_{33} and d_{31} in order to match the specification for

Figure 2: Mazak 300 QUICK TURN NEXUS 300-II CNC turning center.

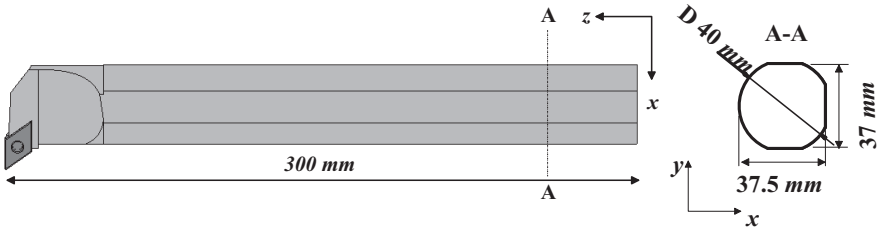

Figure 3: Top-view and cross-section of a standard boring bar, S40T PDUNR15 F3 WIDAX.

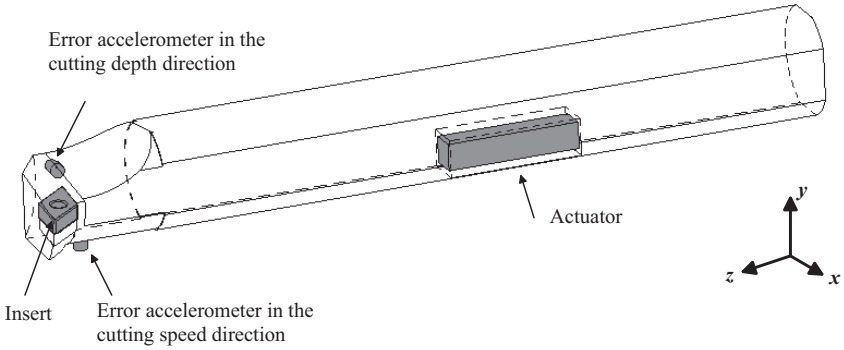

Figure 4: Schematic view of an active boring bar.

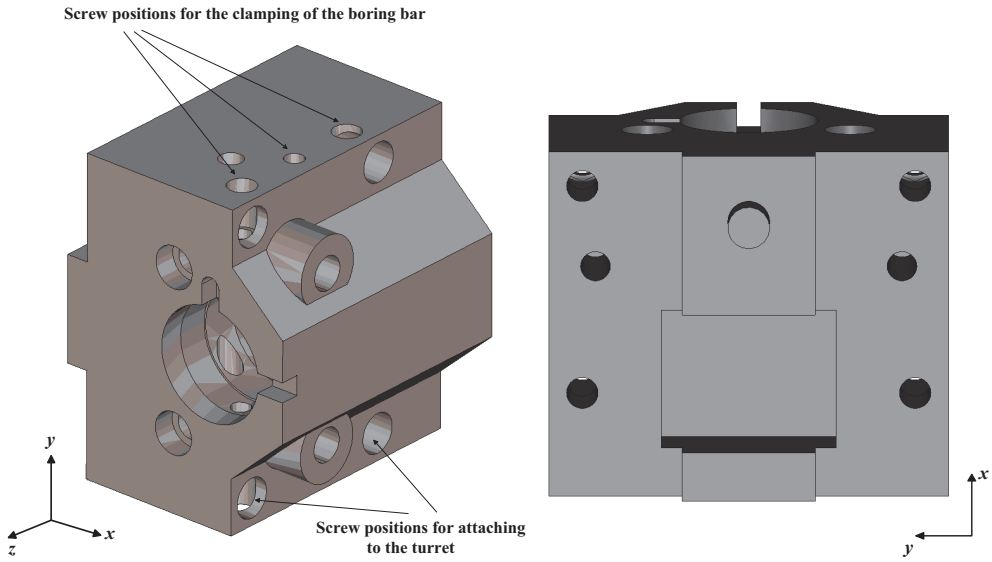

a) b)

Figure 5: Standard 8437-0 40 mm Mazak holder: a) general view; b) view of the side for the turret contact.

the maximum stroke of the actuator [26, 27]. The actuator specifications are given in Table 1, [26, 27].

Property name	Value
Actuator material	PZT-5H
Free expansion ΔL_a, $[m]$	38×10^{-6}
Strain coefficient d_{33}, $[m/V]$	640×10^{-12}
Max operating voltage (P-P) V_{max}, $[V]$	150
Density ρ, $[kg/m^3]$	7500
Actuator stiffness k_a, $[N/m]$	125×10^6

Table 1: Actuator specifications.

Furthermore, the piezoelectric material properties such as the elastic coefficient matrix $[\mathbf{c^E}]$, the piezoelectric matrix $[\mathbf{e}]$ and the dielectric matrix $[\varepsilon]$ for this material are given in Eq. 1, Eq. 2 and Eq. 3 respectively [26, 27].

$$[\mathbf{c^E}] = \begin{bmatrix} 12.72 & 8.02 & 8.47 & 0 & 0 & 0 \\ 8.02 & 12.72 & 8.47 & 0 & 0 & 0 \\ 8.47 & 8.47 & 11.74 & 0 & 0 & 0 \\ 0 & 0 & 0 & 2.30 & 0 & 0 \\ 0 & 0 & 0 & 0 & 2.30 & 0 \\ 0 & 0 & 0 & 0 & 0 & 2.35 \end{bmatrix} \times 10^{10}, \ [Pa] \tag{1}$$

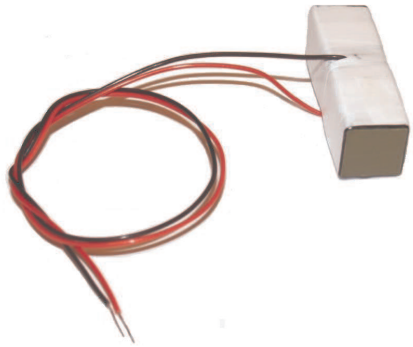

Figure 6: Piezoelectric stack actuator.

$$[\mathrm{e}] = \begin{bmatrix} 0 & 0 & -6.62 \\ 0 & 0 & -6.62 \\ 0 & 0 & 23.24 \\ 0 & 17.03 & 0 \\ 17.03 & 0 & 0 \\ 0 & 0 & 0 \end{bmatrix}, \ [C/m^2] \tag{2}$$

$$[\varepsilon] = \begin{bmatrix} 27.71 & 0 & 0 \\ 0 & 27.71 & 0 \\ 0 & 0 & 30.10 \end{bmatrix} \times 10^{-9}, \ [F/m] \tag{3}$$

2.1.2 Measurement Equipment and Setup

The following equipment was used to carry out experimental modal analysis:

- 12 PCB 333A32 accelerometers;
- 1 Ling Dynamic Systems shaker v201;
- 1 Gearing & Watson Electronics shaker v4;
- 2 Brüel & Kjær 8001 impedance heads;
- HP VXI E1432 front-end data acquisition unit;
- PC with IDEAS Master Series version 6.

The boring bar was simultaneously excited in the cutting speed direction and cutting depth direction by two shakers via impedance heads attached at the distance $l_1 = 100\ mm$ from the clamped end of the active boring bar (see Figure 7). The spatial motion of the boring bar was measured by 12 accelerometers and 2 impedance heads glued with the distance of $l_2 = 25\ mm$ from each other starting at 25 mm from the free end of the boring bar: 6 accelerometers and one impedance head in the cutting speed direction and 6 accelerometers and the other impedance head in the cutting depth direction.

The following equipment was used to carry out control path identification:

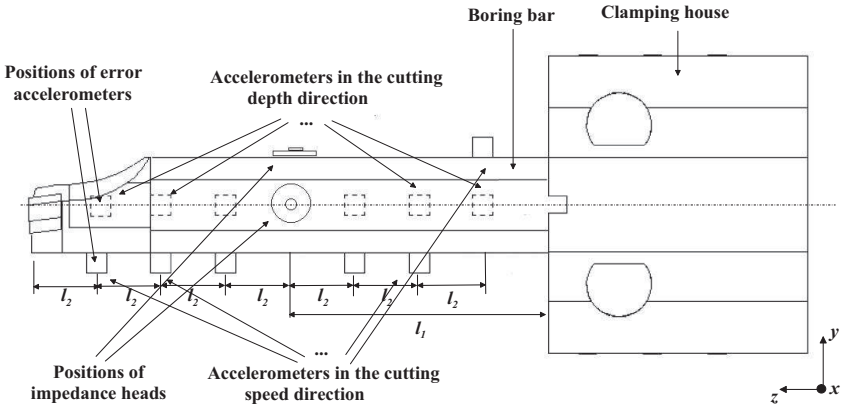

Figure 7: Drawing of the clamped active boring bar with accelerometers and cement studs for the attachment of impedance heads.

- 2 PCB 333A32 accelerometers;
- 1 KEMO Dual Variable Filter VBF 10M;
- A custom designed amplifier for capacitive loads;
- HP VXI E1432 front-end data acquisition unit;
- PC with IDEAS Master Series version 6.

During the control path identification, the active boring bar, clamped in the lathe, was excited by means of voltage applied over the actuator. The response of the boring bar was measured by two accelerometers located at the error sensor positions, which were at a distance of 25 *mm* from the free end of the boring bar in the cutting speed and cutting depth direction respectively.

Also system identification was carried out for the transfer paths between the voltage applied to the actuator and the strain measured at the points P1, P2, P3 and P4 close to the "boring bar - actuator" interfaces (see Fig. 8). Four KYOWA strain gages were used for this purpose.

2.1.3 System Identification

System identification in general concerns the production of a mathematical model of the dynamic properties of an unknown system, based on experimentally obtained data. In the case of mechanical systems, system identification usually implies estimating the frequency response functions between an input excitation force signal and an output signal which can be displacement, velocity or acceleration. Since it is most convenient to measure the acceleration of a mechanical system, accelerance frequency response functions are frequently considered.

Spectral properties The frequency response function can be estimated as a ratio of the cross-power spectral density between the excitation and the response signals

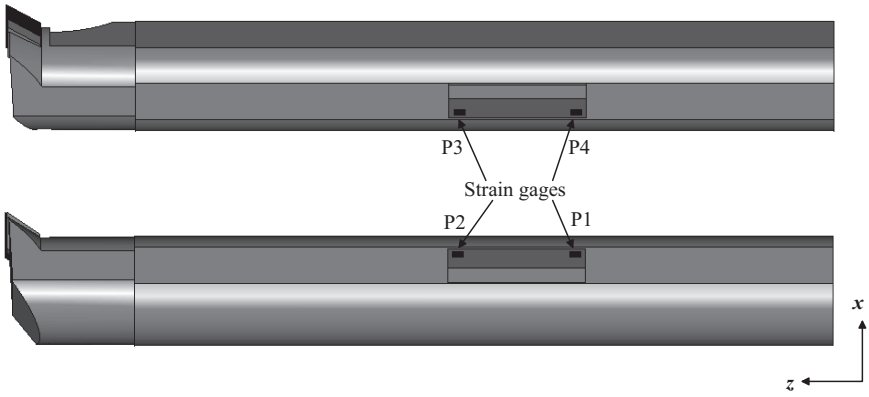

Figure 8: Drawing of the active boring bar with strain gages positions.

and the power spectral density of the excitation signal. Most of the non-parametric methods for spectrum estimation are based on the averaging of periodograms [28]. The most general is Welch's method, which allows one to average modified periodograms, which are produced based on the windowed sequences of a signal that may be overlapping to a certain extent.

The double-sided power spectral density of a discrete time signal $x(n)$ can be estimated using Welch's method as follows [28]:

$$\begin{aligned} \hat{P}_{xx}^{PSD}(f_k) &= \frac{1}{MF_s \sum_{n=0}^{N-1} w^2(n)} \sum_{m=0}^{M-1} \left| \sum_{n=0}^{N-1} x_m(n) w(n) e^{-j2\pi nk/N} \right|^2, \qquad (4) \\ f_k &= \frac{k}{N} F_s, \end{aligned}$$

where N is the block length or periodogram length, $k = 0, \ldots, N-1$, $x_m(n) = x(n+mD)$, $m = 0, 1, ..., M-1$ is the data segment of the signal $x(n)$ with the length L, M is the number of periodograms, D is the overlapping increment, i.e., for 50% overlap D=N/2, F_s is the sampling frequency and $w(n)$ is the window function. In the case of power spectral density estimation, the Hanning window is commonly used [28].

In practice, the excitation and response signals can be corrupted with noise. Depending on whether the noise is affecting the measured excitation signal or response signal, frequency response function estimators appropriate for the respective case may be utilized. The H_1 estimator is usually implemented in FFT-analyzers [29] and may be used when noise is only assumed to corrupt the response signal.

$$\hat{H}_1(f_k) = \frac{\hat{P}_{yx}^{PSD}(f_k)}{\hat{P}_{xx}^{PSD}(f_k)}. \qquad (5)$$

The $\hat{H}_2$ estimator is used when noise is assumed to only affect the measured excitation signal.

$$\hat{H}_2(f_k) = \frac{\hat{P}_{yy}^{PSD}(f_k)}{\hat{P}_{yx}^{PSD}(f_k)}. \tag{6}$$

The quality of the frequency response function estimate can be evaluated via the coherence function estimate $\hat{\gamma}_{yx}^2$, which is the ratio of two estimators [30].

$$\hat{\gamma}_{yx}^2(f_k) = \frac{\hat{H}_1(f_k)}{\hat{H}_2(f_k)} = \frac{|\hat{P}_{yx}^{PSD}(f_k)|^2}{\hat{P}_{xx}^{PSD}(f_k)\hat{P}_{yy}^{PSD}(f_k)}. \tag{7}$$

The normalized random error of the frequency response function's magnitude function estimate can be estimated according to [30]:

$$\varepsilon_r[|\hat{H}_{xy}(f_k)|] \approx \frac{(1-\hat{\gamma}_{xy}^2(f_k))^{1/2}}{\sqrt{2\hat{\gamma}_{xy}^2(f_k)M_e}}, \tag{8}$$

where M_e is the equivalent number of averages. The equivalent number of averages is given by [31]:

$$M_e = \frac{M}{1+2\sum_{m=1}^{M-1}\frac{M-m}{M}\varrho(m)}, \tag{9}$$

where $\varrho(m)$ is given by [31]:

$$\varrho(m) = \frac{\left[\sum_{n=0}^{N-1} w(n)w(n+mD)\right]^2}{\left[\sum_{n=0}^{N-1} w^2(n)\right]^2}. \tag{10}$$

In the case when power and cross-power spectral densities estimates are produced without the overlapping of data blocks, $M_e = L/N$. This typically corresponds to the case when burst random noise is used as an excitation signal.

The normalized random error for the coherence function can be estimated by [30]:

$$\varepsilon_r[\hat{\gamma}_{xy}^2(f)] \approx \frac{\sqrt{2}(1-\hat{\gamma}_{xy}^2(f))}{\sqrt{\hat{\gamma}_{xy}^2(f)M_e}}. \tag{11}$$

The normalized random error of the multiple coherence function is given by [30]:

$$\varepsilon_r[\hat{\gamma}_{y:x}^2(f)] \approx \frac{\sqrt{2}[1-\hat{\gamma}_{y:x}^2(f)]}{\sqrt{\hat{\gamma}_{y:x}^2(f)(M_e+1-s)}}. \tag{12}$$

where s is the number of excitation signals.

The power spectral density estimation parameters used in the production of the experimental control path frequency response function estimates are summarized in Table 2.

The power spectral density estimation parameters used in the production of the numerical control path frequency response function estimates are summarized in Table 3.

Parameter	Value
Signal type	True random
Excitation frequency range	0-1000 Hz
Sampling frequency, F_s	2560
Number of spectral lines, N	3201
Frequency resolution, Δf	0.3125 Hz
Number of averages	200
Window	Hanning
Overlap	50 %

Table 2: Parameters for the experimental spectral density estimation.

Parameter	Value
Signal type	True random
Excitation frequency range	0-1000 Hz
Sampling frequency, F_s	1536 Hz
Number of spectral lines, N	1536
Frequency resolution, Δf	1 Hz
Number of averages	5
Window	Hanning
Overlap	50 %

Table 3: Parameters for the spectral density estimation concerning the finite element models.

2.2 Experimental Modal Analysis

In the concept of experimental modal analysis, the boring bar is considered as a multiple degree-of-freedom system. Excitation forces and responses are measured spatially at discrete positions on the boring bar and collected simultaneously for subsequent parameter estimation or curve fitting. Experimental modal analysis allows for the identification of a system's modal parameters: natural frequencies, mode shapes and relative damping ratios. Experimental modal analysis serves as a tool for, e.g., the verification and updating of finite element models [29]. The theory and methods of experimental modal analysis are essentially built on four assumptions: the system is linear, the system is time-invariant, the system is observable and the system obeys Maxwell's reciprocity theorem [32].

2.2.1 Parameter Estimation

In the concept of the experimental modal analysis the boring bar is modeled as a system with N_{ema} degrees-of-freedom. The boring bar vibration can be described by the equation of motion in matrix form.

$$[\mathbf{M}]\{\ddot{\mathbf{w}}(t)\} + [\mathbf{C}]\{\dot{\mathbf{w}}(t)\} + [\mathbf{K}]\{\mathbf{w}(t)\} = \{\mathbf{f}(t)\}, \tag{13}$$

where N_{ema} is the number-of-degrees of freedom, the matrix $[\mathbf{M}]$ is the $N_{ema} \times N_{ema}$ mass matrix, $[\mathbf{C}]$ is the $N_{ema} \times N_{ema}$ damping matrix and $[\mathbf{K}]$ is the $N_{ema} \times N_{ema}$

elastic stiffness matrix. Vector $\{\mathbf{f}(t)\}$ is the space- and time-dependent load vector. Vector $\{\mathbf{w}(t)\}$ is the space- and time-dependent displacement vector. Its i-th element contains displacement measured in the point with coordinates (x_i, y_i, z_i) and $i = 1, ..., N_{ema}$ at time instant t. The displacement vector may be written as:

$$\{\mathbf{w}(t)\} = \left\{ \begin{array}{c} w(x_1, y_1, z_1, t) \\ w(x_2, y_2, z_2, t) \\ \vdots \\ w(x_{N_{ema}}, y_{N_{ema}}, z_{N_{ema}}, t) \end{array} \right\}. \tag{14}$$

The spatial dynamic properties of the boring bar were identified using the time-domain polyreference least squares complex exponential method [29]. This method is based on the discrete-time version of the impulse response function matrix:

$$[\mathbf{h}(n)] = \sum_{r=1}^{N_{ema}} \left([\mathbf{A}]_r e^{\lambda_r T_s n} + [\mathbf{A}^*]_r e^{-\lambda_r T_s n} \right) = \sum_{r=1}^{2N_{ema}} [\mathbf{A}]_r e^{\lambda_r T_s n}, \tag{15}$$

where $[\mathbf{A}]_r = Q_r \{\psi\}_r \{\psi\}_r^T$ and $\lambda_r = 2\pi(-f_r\zeta_r + j f_r \sqrt{1-\zeta_r^2})$; $\{\psi\}_r$ is the $N_{ema} \times 1$ mode shape vector, ζ_r is the modal damping ratio; f_r is the undamped system's eigenfrequency; Q_r is the modal scaling factor and T_s is the sampling time interval. An estimate of the impulse response function matrix $[\hat{\mathbf{h}}(n)]$ is produced based on the Inverse Fourier Transform of an estimate of the receptance matrix $[\hat{\mathbf{H}}_\mathbf{r}(f_k)]$. The estimate of the receptance matrix $[\hat{\mathbf{H}}_\mathbf{r}(f_k)]$ is assembled based on power spectral density estimates of the measured excitation forces and the cross-power spectral density estimates between the measured output responses and excitation forces.

Based on the simultaneously estimated impulse responses, between each of the input forces locations and all of the output response locations, the polyreference least squares complex exponential method utilizes Prony's method and the least squares method in the production of global estimates of eigenfrequencies f_r, damping ratios ζ_r and mode shapes $\{\psi\}_r$ [29, 32].

The orthogonality of extracted mode shapes $\{\psi_{EMA}\}_i$ and $\{\psi_{EMA}\}_j$, $i, j \in \{1, 2, \ldots, N_{ema}\}$, may be evaluated using the Modal Assurance Criterion [32]:

$$MAC_{ij} = \frac{|\{\psi_{EMA}\}_i^T \{\psi_{EMA}\}_j|^2}{(\{\psi_{EMA}\}_i^T \{\psi_{EMA}\}_i)(\{\psi_{EMA}\}_j^T \{\psi_{EMA}\}_j)}. \tag{16}$$

The Modal Assurance Criterion may also be used to provide a measure on the correlation between the experimentally-measured mode shapes $\{\psi_{EMA}\}_i$ and the numerically-calculated mode shapes $\{\psi_{FEM}\}_j$ of, e.g., a finite element model.

$$MAC_{ij} = \frac{|\{\psi_{EMA}\}_i^T \{\psi_{FEM}\}_j|^2}{(\{\psi_{EMA}\}_i^T \{\psi_{EMA}\}_i)(\{\psi_{FEM}\}_j^T \{\psi_{FEM}\}_j)}. \tag{17}$$

The parameters used in the modal analysis of the clamped active boring bar can be found in Table 4.

Parameter	Value
Signal type	Burst random (90/10)
Excitation frequency range	300-800 Hz
Sampling frequency, F_s	1280
Number of spectral lines, N	1601
Frequency resolution, Δf	0.3125 Hz
Number of averages	200
Window	Rectangular
Frequency range for curve fitting	400-600 Hz

Table 4: Experimental modal analysis parameters.

2.3 "3-D" Finite Element Model

A finite element model of the system boring bar - actuator - clamping house was built using the commercial finite element software MSC.MARC [33]. The initial "3-D" finite element model of the clamped boring bar includes separate models of a boring bar, a clamping house and a model of a piezoelectric actuator interacting by means of frictionless contact.

The spatial dynamic properties of the boring bar - actuator - clamping house system were calculated based on the general equation for the dynamic equilibrium of an undamped system, i.e.,

$$[\mathbf{M}]\{\ddot{\mathbf{w}}(t)\} + [\mathbf{K}]\{\mathbf{w}(t)\} = \{\mathbf{0}\}, \tag{18}$$

where $[\mathbf{M}]$ is the global $N_{fem} \times N_{fem}$ mass matrix of the system; $[\mathbf{K}]$ is the global $N_{fem} \times N_{fem}$ stiffness matrix of the system; $\mathbf{w}(t)$ is the space- and time-dependent $N_{fem} \times 1$ displacement vector and N_{fem} is the number of degrees-of-freedom of the finite element model. The modal analysis was conducted by using the Lanczos iterative method in the MSC.MARC software [33, 34]. The dynamic behavior of the system was also examined by means of transient and harmonic response simulations.

2.3.1 Model of the System Boring Bar - Clamping House

The model of the system boring bar - clamping house consists of two sub-models: a sub-model of the boring bar and a sub-model of the clamping house. The sub-models are connected in terms of variable contact [33]. As a basic finite element, a tetrahedron was chosen.

The sub-model of the boring bar consists of three parts: the "body" which models the part of the boring bar with a constant cross-section, the "head" which models the part of the boring bar with a varying cross-section, and the "tool", which models the attached insert. In order to simplify the meshing process and keep down the number of degrees-of-freedom in the system while still maintaining accuracy within the model, the three boring bar parts were meshed separately with different element edge lengths (see Table 5). These three parts were connected using "glue" contact, which implies that the contacting nodes of both parts are tied to each other in such a way that there is no relative normal or tangential motion between the two parts in these nodes. The finite element model of the boring bar is shown in Fig. 9 a).

Sub-model	Element Edge Length, $[m]$	Polynomial order
Boring bar, "body"	0.01	2
Boring bar, "head"	0.005	2
Boring bar, "tool"	0.005	2
Clamping house	0.005-0.01	1
Actuator	0.01	1

Table 5: Finite element size and order of the approximation polynomial used in the shape functions.

For the sake of simplicity, the clamping house and the four clamping screws were modeled as one body. The sub-model of the clamping house was built using four-noded tetrahedrons with linear shape functions. The element edge length varies from 0.005 m to 0.01 m, depending on the location of the finite element in the model, i.e., surfaces of the clamping house that are in contact with the boring bar have a mesh with higher density than the rest of the clamping house surfaces. For the clamping house surfaces in contact with the turret, the following boundary conditions were used: nodal displacements on the surfaces of the clamping house, which correspond to surfaces of the real clamping house attached to the turret (see Fig. 5 b)) in $x-$, $y-$ and $z-$ directions are set to zero. The finite element model of the clamping house is shown in Fig. 9 b).

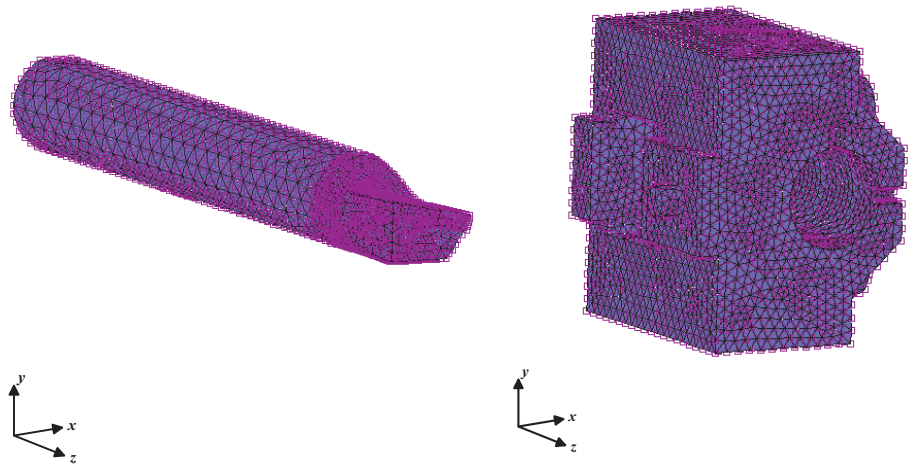

a) b)

Figure 9: The "3-D" finite element model of a) a boring bar and b) a clamping house.

2.3.2 Model of the Actuator

A "3-D" finite model of a piezoelectric actuator was developed. Thin layers of an electrically active ceramic material connected in parallel were modeled as a stack of eight-noded bricks with piezoelectrical properties, i.e., in addition to three translational degrees-of-freedom, each node has a fourth degree-of-freedom - electric potential. The number of bricks or piezoelectric layers η_a can be calculated based on the formula for the free expansion of an unloaded stack actuator [35].

$$\Delta L_a = \eta_a d_{33} V_{max}(t) \tag{19}$$

where d_{33} is the actuator's strain coefficient, $V_{max}(t)$ is the max operating voltage and ΔL_a is the free expansion of the actuator. These values are given in Table 1. This yields $\eta_a = 400$ bricks or piezoelectric layers in the actuator stack.

The large number of layers affects the computational complexity of the finite element model. For this reason, it is desirable to have a model with a minimal number of degrees-of-freedom ensuring sufficient accuracy. The number of the peizoelectric layers was reduced with a factor of 10 and the strain constant d_{33}, which yields the specified free expansion ΔL_a, was increased with a factor of 10. Since the reduced number of layers is still large, i.e., 40 layers, only a principal sketch of the "3-D" finite element model of the actuator is shown in Fig. 10.

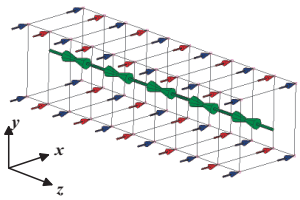

Figure 10: Sketch of a "3-D" finite element model of an actuator.

The electrostatic boundary conditions are shown in Fig. 10. The blue arrows show the nodes with applied negative or zero potential, and the red arrows correspond to the nodes with applied positive potential. Furthermore, the large green arrows show the material orientations within the finite elements. The material orientation in this case determines the direction of current flow inside the finite element.

2.3.3 Contact Modeling in the Finite Element Analysis

The adequate modeling of the boring bar dynamic motion requires incorporation of the contact conditions between the boring bar, clamping house and clamping screws into the "3-D" finite element model.

By a numerical contact problem, a complex process of the interaction of two or more numerical regions' boundaries may be defined in the computational domain based on constraints and boundary conditions specified by the physical nature of the contact between the bodies, e.g., friction or heat transfer [36].

Three objectives of the contact between the boring bar, clamping house and clamping screws may be stated:

- Detection of the contact between pre-defined contacting bodies;

- Application of constraints to avoid penetration;
- Application of boundary conditions to simulate frictional behavior.

The two basic types of contact bodies are implemented in MSC.MARC, [33]: deformable and rigid. Thus, there are two types of contact: a contact between deformable and deformable bodies and a contact between deformable and rigid bodies.

A "3-D" deformable body is described by the "3-D" finite elements, and the nodes on its external surfaces are defined as potential contact nodes. Their "3-D" faces form the outer surfaces and are considered as potential contact segments.

Rigid bodies are usually composed of the analytically defined "3-D" Non Uniform Rational Basis (NURBS) surfaces, which are treated as potential contact segments. Rigid bodies do not deform.

Conventionally, the contact between two "3-D" bodies is implemented in the following way: one body is determined to be the "master", and the other is determined to be the "slave" body [37].

The "master" body is always deformable. The contacting element of the "master" body is a node. The "slave" body can be deformable or rigid. The contacting element of the "slave" body is a segment which can be assembled by a patch of the "3-D" finite element faces in the case of a deformable body or segments in the case of a rigid body.

Deformable-rigid contact In this case, contact between the deformable "master" body and the rigid "slave" body is considered.

Contact tolerance In order to simplify the numerical implementation of the contact, contact tolerance was introduced to determine the distance below which bodies are considered to be in contact. For instance, node A in Fig. 11 is not inside the contact tolerance interval, thus the "master" and the "slave" bodies are not in contact. The contact tolerance in the MSC.MARC software is defined as 5 % of the smallest element edge length in the finite element model [33].

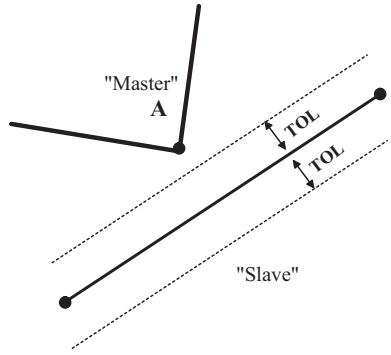

Figure 11: Contact tolerance.

Contact detection If node A is within the contact tolerance interval, then the "master" and the "slave" bodies are considered to be in contact (see Fig. 12). In the

MSC.MARC software, the contact problem is resolved by using the direct constraint method [33]. This implies that when contact is detected, the motion of the contacting bodies is constraint by means of boundary conditions, i.e., displacements and nodal forces are recalculated.

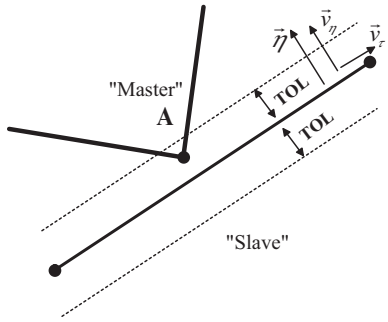

Figure 12: Contact detection.

When variable contact occurs, the constraints are imposed on degrees-of-freedom of node A. The displacement of node A is transformed into the local coordinate system of the rigid body, which has as its basis the normal $\{\eta\}$ and tangential $\{\tau\}$ vectors. The relative displacement of node A is updated as follows:

$$\Delta\{\mathbf{w}\}_\eta = \{\mathbf{v}\}^T\{\eta\}, \tag{20}$$

where $\{\mathbf{v}\}$ is the velocity vector of the rigid body. Thus in this case, the "master" and "slave" bodies move together with the same speed in the normal direction, however the "master" body can slide on the surface of the "slave" body in the tangential direction.

In the case of the glue contact, additional constraint is imposed, such that no relative tangential motion occurs between the "master" and the "slave" body:

$$\Delta\{\mathbf{w}\}_\tau = \{\mathbf{v}\}^T\{\tau\}. \tag{21}$$

Detection of penetration and separation When the contacting node A moves beyond the contact tolerance interval, it is considered to be penetrating the "slave" body, see Fig. 13. In this case, the iterative penetration checking procedure is invoked [33].

Application of Boundary Conditions - Direct Constraint Method In order to conduct contact analysis, different techniques can be utilized, e.g., the Lagrange multiplier procedure, the penalty method, hybrid and mixed methods, and the direct constraint method [33]. The direct constraint method provides an accurate solution for contact analysis [33]. The principle of the direct constraint method is enclosed in the application of constraints due to contact by means of boundary conditions, i.e., normal displacements and nodal forces.

The problem can be formulated as follows:

$$\begin{bmatrix} [\mathbf{K_{aa}}] & [\mathbf{K_{ab}}] \\ [\mathbf{K_{ba}}] & [\mathbf{K_{bb}}] \end{bmatrix} \begin{Bmatrix} \{\mathbf{w_a}\} \\ \{\mathbf{w_b}\} \end{Bmatrix} = \begin{Bmatrix} \{\mathbf{f_a}\} \\ \{\mathbf{f_b}\} \end{Bmatrix} + \begin{Bmatrix} \{\mathbf{0}\} \\ \{\mathbf{f_c}\} \end{Bmatrix}, \tag{22}$$

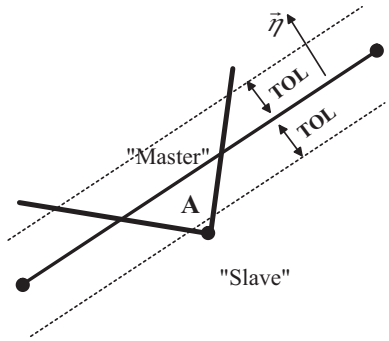

Figure 13: Penetration detection.

where subscript b is used for the transformed degrees-of-freedom associated with the nodes in contact, and subscript a is used for the other not transformed degrees-of-freedom; $[\mathbf{K_{aa}}]$ is a sub-matrix of the global stiffness matrix which corresponds to the degrees-of-freedom of nodes which are not in contact; $[\mathbf{K_{bb}}]$ is a sub-matrix of the global stiffness matrix which corresponds to the degrees-of-freedom associated with nodes in contact; $[\mathbf{K_{ab}}]$ and $[\mathbf{K_{ba}}]$ are sub-matrices of the global stiffness matrix which corresponds to the degrees-of-freedom of nodes in contact respective non-contacting nodes; $\{\mathbf{w_a}\}$ is the space- and time-dependent vector of unknown displacements associated with non-contacting nodes; $\{\mathbf{w_b}\}$ is the space- and time-dependent vector of constrained displacements; $\{\mathbf{f_a}\}$ and $\{\mathbf{f_b}\}$ are space- and time-dependent vectors of external forces acting on the constrained and unconstrained degrees-of-freedom respectively and $\{\mathbf{f_c}\}$ is the space- and time-dependent vector of unknown contact forces. The unknown displacements and contact forces can be found by means of Gaussian elimination as follows [37]:

$$[\mathbf{K}^*]\{\mathbf{w_b}\} - \{\mathbf{f_c}\} = \{\mathbf{f}^*\}, \tag{23}$$

where $[\mathbf{K}^*]$ and $\{\mathbf{f}^*\}$ can be expressed as [37]:

$$[\mathbf{K}^*] = [\mathbf{K_{bb}}] - [\mathbf{K_{ba}}][\mathbf{K_{aa}}]^{-\mathbf{1}}[\mathbf{K_{ba}}]^{\mathbf{T}}, \tag{24}$$

$$\{\mathbf{f}^*\} = \{\mathbf{f_b}\} - [\mathbf{K_{ba}}][\mathbf{K_{aa}}]^{-\mathbf{1}}\{\mathbf{f_a}\}, \tag{25}$$

where $[\mathbf{K}^*]$ is the $(N_{dof} \cdot n_c) \times (N_{dof} \cdot n_c)$ stiffness matrix, N_{dof} is the number of degrees-of-freedom at the node of the finite element (in the case of a 10-noded tetrahedron, $N_{dof} = 3$), n_c is the number of contacting nodes. The vectors $\{\mathbf{f}^*\}$, $\{\mathbf{f_c}\}$, $\{\mathbf{w_b}\}$ have a length of $N_{dof} \cdot n_c$. Thus, the system of linear equations Eq. 23 has $2 \cdot N_{dof} \cdot n_c$ unknown and only $N_{dof} \cdot n_c$ equations. In order to obtain a unique solution of the system to linear equation Eq. 23, one has to complete this system by using additional conditions, e.g., conditions of compatibility and equilibrium [37].

Compatibility condition The compatibility condition implies, that when contact is detected within the contact tolerance, two bodies start to move together, i.e., Eq. 20 is used in the case of variable contact, and Eq. 20 and Eq. 21 are utilized in the case of glue contact.

Equilibrium condition The contact forces between the contacting node of the "master" body $\{\mathbf{f_m}\}$ and the contacting segment of the "slave" body $\{\mathbf{f_{sl}}\}$ should be equal and opposite, yielding:

$$\{\mathbf{f_m}\} + \{\mathbf{f_s}\} = 0. \tag{26}$$

For the glue contact, additional condition is applied:

$$\{\mathbf{f_m}\}^{\mathbf{T}}\{\tau\} = \{\mathbf{f_{sl}}\}^{\mathbf{T}}\{\tau\} = 0. \tag{27}$$

Deformable-deformable contact In the case of contact between two deformable bodies, the multi-point constraint is imposed on the contacting node. This means that for each contacting node, the retained nodes are found from the set of boundary nodes, e.g., for the 10-noded tetrahedrons, the number of retained nodes is seven - six from the patch plus the contacting node itself. Retained nodes are used to form a geometrical surface. After a normal vector $\{\eta\}$ to this surface is found, the analysis proceeds as in the case of the deformable-rigid contact. In the case of a deformable-deformable contact, there is no "master"-"slave" relationships; each contacting body is checked against every other body.

2.3.4 Coulomb Friction Modeling

Generally, the dynamic response of the boring bar during a continuous turning operation has nonlinear properties [38, 39]. Possible sources of nonlinearities are, for instance, the intermittent contact between the workpiece and the cutting tool, as well as a nonlinear contact between the boring bar, clamping screws and the inner surface of the clamping house cavity [38,39]. Only the second source of nonlinearities is considered in the present study. However, the incorporation of a cutting process model is of great importance for further research. When the boring bar is excited by the force originated from the material deformation process, relative motion between the contacting surfaces of the boring bar, clamping screws and clamping house occurs. Thus, it is likely that some of the energy introduced into the system by the cutting process dissipates via friction forces at contacting surfaces between the boring bar and clamping house [40]. Generally, no lubricating film is used between the boring bar and clamping house surfaces. Such contact may be considered as a dry frictional contact. Therefore, the Coulomb model of the friction force may be used (see Fig. 14). The model implies that for relative motion between contact surfaces, the static friction force f_{st}, which is greater than kinetic friction force f_k (due to the difference between the static and kinetic friction coefficients $\mu_k < \mu_{st}$), should be overcome. Thus, the stick-slip friction force can be expressed as follows [33]:

$$f = \begin{cases} |f_{st}| = \mu_{st} f_n, & \{\mathbf{v}\} = 0 \\ f_k = -\mu_k f_n sign(\{\mathbf{v}\}), & otherwise \end{cases} \tag{28}$$

where f_n - is a normal force acting on surface or body and $\{\mathbf{v}\}$ is the relative sliding velocity vector.

As the result of the dry friction force presence in the system, the relative motion of contacting surfaces or bodies can be considered as a stick-slip oscillation. Thus, it may affect the dynamic properties of the system boring bar - clamping house. The friction coefficients μ_k and μ_s are usually determined experimentally. As a kinetic

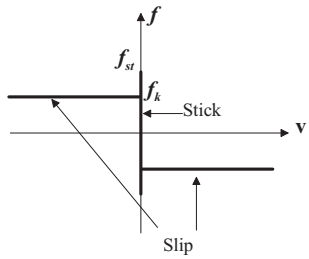

Figure 14: Coulomb model of dry friction force.

friction coefficient, for instance, $\mu_k = 0.4$ which corresponds to the typical friction coefficient of unlubricated materials such as chromium hard steel at low speeds in normal atmospheres against a mild steel counterface [40], may be used.

Two different Coulomb friction force model approximations were incorporated into the "3-D" finite element model of the system boring bar - actuator - clamping house: the arctangent model and the bilinear model.

Arctangent model This model approximates a discontinuous Coulomb friction force function by a continuously differentiable function of the relative sliding velocity (see Fig. 16) [33].

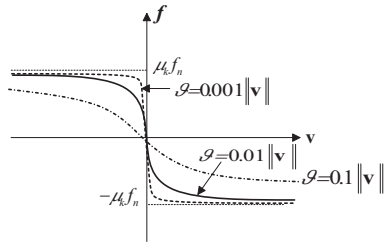

Figure 15: Arctangent approximation for the Coulomb friction model.

Thus, the friction force is described by [33]:

$$f = -\mu_k f_n \frac{2}{\pi} \tan^{-1}\left(\frac{\|\{\mathbf{v}\}\|}{\vartheta}\right) sign(\{\mathbf{v}\}) \tag{29}$$

where ϑ - is a value of relative velocity below which sticking occurs. It is expressed as a percentage of the maximum relative sliding velocity v_{max} and usually is taken from the interval $\vartheta \in [0.01v_{max}, \quad 0.1v_{max}]$. Small values of ϑ yield a narrow stick velocity interval, i.e., a closer approximation of the Coulomb friction model. This also implies that sticking will occur only at very low velocities, and the slipping mode will be dominant. On the other hand, large values of ϑ may result in insufficient influence of the friction in the boring bar model. One way to obtain the initial value of ϑ might be to estimate it based on transient analysis without incorporated friction force.

Bilinear model This model is based on relative displacement instead of relative velocity. It describes a sticking behavior in terms of elastic relative displacements and

a slipping mode in terms of plastic relative displacements [33].

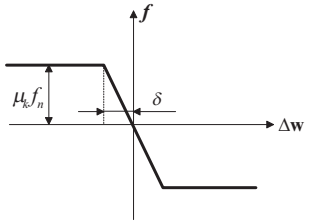

Figure 16: Bilinear approximation for the Coulomb friction model.

The friction force can be expressed as [33]:

$$f = \begin{cases} -\frac{\mu_k f_n}{\delta}\Delta\{\mathbf{w}\}, & |\Delta\{\mathbf{w}\}| < \delta \\ -\mu_k f_n sign(\Delta\{\mathbf{w}\}), & otherwise \end{cases} \tag{30}$$

where δ is the slip threshold or relative sliding displacement below which the sticking is simulated. The default value of δ is calculated in MSC.MARC as $0.0025 \times \bar{l}_e$, where $\bar{l}_e$ is the average edge length of the finite elements defining the contacting bodies [33]. According to the theory of tribology, the dimension of a single contacting spot on an engineering surface is in the order of 10^{-5} m, which can be assumed as a typical amplitude for the stick-slip oscillation [40].

Transient response Transient response simulation was conducted with the help of MSC.MARC software using the direct integration Single-Step Houbolt method [33]. This algorithm is recommended for nonlinear contact analysis due to its unconditional stability and second-order accuracy. A detailed description of this method can be found in [41]. The Single-Step Houbolt method uses a constant time step, which is convenient for the calculation of the response signal synchronized with the excitation signal.

The approximation of the system's equation of motion Eq. 13 by single-step algorithms in general form can be expressed as [41]:

$$\begin{aligned} \alpha_{m1}[\mathbf{M}]\{\mathbf{a}\}_{n+1} + \alpha_{c1}[\mathbf{C}]\{\mathbf{v}\}_{n+1} + \alpha_{k1}[\mathbf{K}]\{\mathbf{d}\}_{n+1} + \alpha_m[\mathbf{M}]\{\mathbf{a}\}_n + \\ +\alpha_c[\mathbf{C}]\{\mathbf{v}\}_n + \alpha_k[\mathbf{K}]\mathbf{d}_n = \alpha_{f1}\{\mathbf{f}\}_{n+1} + \alpha_f\{\mathbf{f}\}_n, \end{aligned} \tag{31}$$

$$\{\mathbf{d}\}_{n+1} = \{\mathbf{d}\}_n + \Delta t\{\mathbf{v}\}_n + \beta\Delta t^2\{\mathbf{a}\}_n + \beta_1\Delta t^2\{\mathbf{a}\}_{n+1}, \tag{32}$$

$$\{\mathbf{v}\}_{n+1} = \{\mathbf{v}\}_n + \gamma\Delta t\{\mathbf{a}\}_n + \gamma_1\Delta t\{\mathbf{a}\}_{n+1}, \tag{33}$$

where $\{\mathbf{a}\}_n$, $\{\mathbf{v}\}_n$ and $\{\mathbf{d}\}_n$ are the approximations of $\{\ddot{\mathbf{w}}(t_n)\}$, $\{\dot{\mathbf{w}}(t_n)\}$, $\{\mathbf{w}(t_n)\}$ respectively, Δt is a step size and α_{m1}, α_{c1}, α_{k1}, α_m, α_c, α_{k1}, α_{f1}, α_f, β_1, β, γ_1, γ are the algorithmic parameters. The algorithmic parameters may be tuned by means of conditions of asymptotic annihilation and second-order accuracy, as well as by certain overshoot behavior imposed on the response calculated by the algorithm [41].

According to [41], the algorithm begins with calculation of

$$\{\mathbf{a}\}_0 = [\mathbf{M}]^{-1}\left(\{\mathbf{f}\}_0 - [\mathbf{C}]\{\mathbf{v}\}_0 - [\mathbf{K}]\{\mathbf{d}\}_0\right). \tag{34}$$

Harmonic response The harmonic response of the "3-D" finite element model of the system boring bar - actuator - clamping house was calculated with the use of MSC.MARC software. In general, the solution process is based on the Fourier Transform of the equation motion of the damped system Eq. 13.

$$((j2\pi f)^2[\mathbf{M}] + (j2\pi f)[\mathbf{C}] + [\mathbf{K}])\{\mathbf{W}(f)\} = \{\mathbf{F}(f)\}. \tag{35}$$

The excitation force $\{\mathbf{F}\} = \{\mathbf{f}\}e^{j2\pi f}$ in this case is assumed to have a constant magnitude at all frequencies. Then, the displacement vector $\{\mathbf{W}\}$ is found by solving Eq. 35 for each frequency from the specified frequency range. Thus, the receptance frequency response function is found as a ratio of displacement $\{\mathbf{W}(f)\}$ and force $\{\mathbf{F}(f)\}$ vectors.

$$\{\mathbf{W}(f)\} = ((j2\pi f)^2[\mathbf{M}] + (j2\pi f)[\mathbf{C}] + [\mathbf{K}])^{-1}\{\mathbf{F}(f)\}, \tag{36}$$

$$[H_r(f)] = \frac{\{\mathbf{W}(f)\}}{\{\mathbf{F}(f)\}} = ((j2\pi f)^2[\mathbf{M}] + (j2\pi f)[\mathbf{C}] + [\mathbf{K}])^{-1}. \tag{37}$$

The damping in this case is assumed to be proportional, i.e., $[\mathbf{C}] = \alpha[\mathbf{M}] + \beta[\mathbf{K}]$, where the coefficients α and β are chosen such that relative damping ratios at the, for instance, two lowest eigenfrequencies correspond to the relative damping values estimated by experimental modal analysis. This condition can be expressed as follows [42]:

$$\zeta_r = \frac{\alpha}{4\pi f_r} + \beta\pi f_r, \tag{38}$$

where f_r, $r = 1, 2, ..., N_{ema}$ is the rth natural frequency.

One disadvantage of this approach is that the variable contact between the clamping house and the boring bar is disregarded.

2.3.5 SDOF Nonlinear Model

In order to investigate effects of the arctangent and bilinear approximations of the Coulomb friction force on the dynamics of a clamped boring bar, the simplest case when the boring bar is described by a SDOF model was considered.

The response of the boring bar during an internal turning operation in the lathe is usually dominated by the fundamental bending mode in the cutting speed direction [3, 4]. Therefore, a simple SDOF model with mass m, stiffness k and damping c corresponding to the modal mass, stiffness and damping of the respective fundamental bending mode is considered.

A simple SDOF system with nonlinear friction force included, described by the arctangent model, may be described by the following equation of motion [33]:

$$m\ddot{w}(t) + c\dot{w}(t) + kw(t) + \mu_k mg\frac{2}{\pi}\tan^{-1}\left(\frac{\dot{w}(t)}{\vartheta}\right) = f(t), \tag{39}$$

where $f(t)$ is the excitation force.

On the other hand, if the nonlinear friction force is approximated by the bilinear model, the equation of motion of the SDOF system is as follows:

$$m\ddot{w}(t) + c\dot{w}(t) + kw(t) + \mu_k mgw(t) = f(t), \quad if \quad w(t) > \delta \tag{40}$$

$$m\ddot{w}(t) + c\dot{w}(t) + kw(t) + \frac{\mu_k mg}{\delta}w(t) = f(t), \quad otherwise \tag{41}$$

The response of the SDOF system under random excitation force was calculated in Matlab with the help of the Runge-Kutta method, the ode45 solver [43]. The response of the SDOF system was calculated for the range of parameters ϑ and δ, as well as for a set of excitation force levels. The frequency response functions between the excitation force and the acceleration of the SDOF system were estimated in order to facilitate the interpretation of results obtained based on the "3-D" FE model.

3 Results

The results are presented in the following order: firstly, the estimates of the two fundamental natural frequencies and the corresponding mode shapes based on experimental modal analysis and the linear "3-D" FE-model are given. Secondly, the results of the system identification in terms of the frequency response functions of the so called control paths between the actuator voltage and the acceleration measured by error accelerometers (accelerometers attached close to the tool tip) both in the cutting speed and cutting depth directions are presented. Here, experimental modal analysis of the active boring bar, simulation of the harmonic response of the active boring bar finite element model with linear clamping conditions, and simulation of the transient response of the active boring bar finite element model enabling variable contact between the boring bar and the clamping house were utilized. Thirdly, frequency response function estimates for the dynamic response of the control paths of the "3-D" FE-model enabling variable contact between the boring bar and the clamping house with nonlinear Coulomb friction force between the contacting surfaces of the boring bar, clamping screws and clamping house are given. Here, results of two different Coulomb friction force models' influences on the dynamic response of a SDOF system in terms of frequency response function estimates are reported first. This is done in order to facilitate the interpretation of the frequency response function estimates of the dynamic response of the control paths of the active boring bar "3-D" FE-model with the Coulomb friction force and enabling clamping house variable contact. The control path frequency response functions are calculated for a range of values of the governing parameter in both the arctangent and bilinear models. Fourthly, receptance function estimates between the force produced by the actuator and the displacement of the "boring bar - actuator" interfaces obtained based on the simulated transient response of the active boring bar finite element model enabling variable contact between the boring bar and clamping house are given. Finally, frequency response function estimates between the actuator voltage and the strain at four different positions in the axial direction close to the "boring bar - actuator" interfaces for both FE model with variable contact and the actual boring bar are discussed.

3.1 Modal Analysis Results

3.1.1 Natural Frequencies

The two fundamental natural frequencies for the active boring bar estimated by experimental modal analysis and calculated based on the linear "3-D" finite element model are given in Table 6.

Model	Mode 1		Mode 2	
	Frequency, $[Hz]$	Damping ratio, [%]	Frequency, $[Hz]$	Damping ratio, [%]
Experimental Modal Analysis, (EMA)	501.638	1.044	520.852	1.244
"3-D" FEM of the active boring bar, (FEM)	496.232	-	529.046	-

Table 6: Two fundamental natural frequencies and corresponding damping ratios estimates.

3.1.2 Mode Shapes

The mode shapes estimated using experimental modal analysis and calculated based on the "3-D" finite element model of the system boring bar - actuator - clamping house are plotted in Fig. 17.

As a quality measure of the mode shapes extracted by experimental modal analysis, the MAC-matrix was calculated based on Eq. 16 [32], yielding:

$$[MAC]_1 = \begin{bmatrix} MAC_{EMA_1,EMA_1} & MAC_{EMA_1,EMA_2} \\ MAC_{EMA_2,EMA_1} & MAC_{EMA_2,EMA_2} \end{bmatrix} = \tag{42}$$
$$= \begin{bmatrix} 1.000 & 0.000 \\ 0.000 & 1.000 \end{bmatrix},$$

where EMA_1 is the mode shape at 501.638 Hz, and EMA_2 is the mode shape at 520.852 Hz.

To provide a quantitative measure on the correlation between the mode shapes from the experimental modal analysis and the mode shapes predicted by the finite element models, a cross-MAC matrix has been produced based on Eq. 17 [32]. The cross-MAC matrix between the mode shapes calculated using the "3-D" finite element model FEM_1 at 496.232 Hz and FEM_2 at 529.046 Hz and mode shapes estimated using experimental modal analysis EMA_1 at 501.638 Hz and EMA_2 at 520.852 Hz is given by:

$$[MAC]_2 = \begin{bmatrix} MAC_{FEM_1,EMA_1} & MAC_{FEM_2,EMA_1} \\ MAC_{FEM_1,EMA_2} & MAC_{FEM_2,EMA_2} \end{bmatrix} = \tag{43}$$
$$= \begin{bmatrix} 0.981 & 0.015 \\ 0.019 & 0.983 \end{bmatrix}.$$

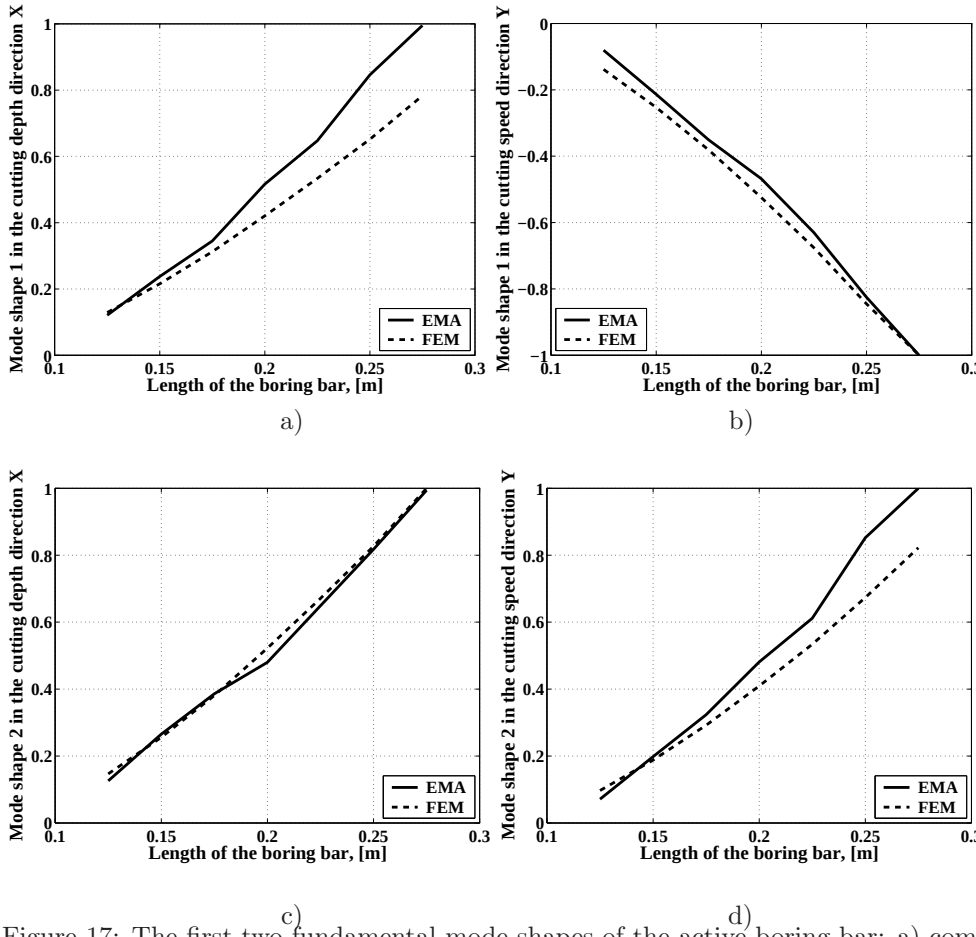

Figure 17: The first two fundamental mode shapes of the active boring bar: a) component of mode shape 1 in the cutting depth direction, b) component of mode shape 1 in the cutting speed direction, c) component of mode shape 2 in the cutting depth direction, and d) component of mode shape 2 in the cutting speed direction (estimated with experimental modal analysis (EMA) and finite element model (FEM)).

3.2 System Identification

This section addresses system identification of two active boring bar transfer paths or control paths. The two transfer paths are as follows: one between the actuator voltage and the output signal from the accelerometer measuring the boring bar vibration in the cutting speed direction close to the insert, and the other one between the actuator voltage and the output signal from the accelerometer measuring the boring bar vibration in the cutting depth direction close to the insert, see Fig. 7. These control paths are estimated for both the actual active boring bar and for the FE models of the active boring bar.

3.2.1 Experimentally Estimated Control Path Frequency Response Functions

Two control path frequency response functions for the active boring bar were estimated: one between the actuator input voltage and the error accelerometer in the cutting speed direction and one between the actuator input voltage and the error accelerometer in the cutting depth direction. The spectrum estimation parameters and the excitation signal properties are given in Table 2. The magnitude function for the two estimated frequency response functions for the active boring bar are presented in Fig. 18.

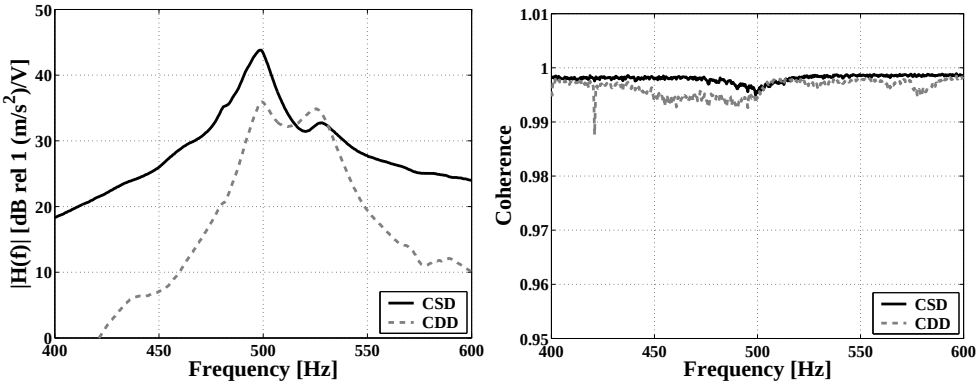

a) b)

Figure 18: a) Magnitude of control path frequency response function estimates, between the actuator voltage and the error accelerometer in the cutting speed (CSD) direction and between the actuator voltage and the error accelerometer in the cutting depth (CDD) directions for the actual active boring bar, and b) corresponding coherence functions estimates.

3.2.2 Harmonic Response Based on FEM

The harmonic response was simulated using the linear "3-D" finite element model of the active boring bar. The results of the harmonic analysis are presented as the magnitude of two control path frequency response functions between the actuator voltage and the acceleration (error acceleration) at the two positions corresponding to the error accelerometer positions at the actual boring bar (see Fig. 19). The peak value of the amplitude of the harmonic excitation was equal to 100 V.

3.2.3 Transient Response Based on FEM

The transient response of the "3-D" finite element model, enabling variable contact between the boring bar and the clamping house, was simulated with the use of the MSC.MARC software by means of the Single-Step Houbolt transient operator [33]. A uniformly distributed random excitation signal with a flat spectrum with an RMS value of 54.628 V was applied to the finite element model of the actuator. The results of the transient response simulation are presented as magnitude functions of frequency response function estimates between the actuator voltage and the acceleration at the

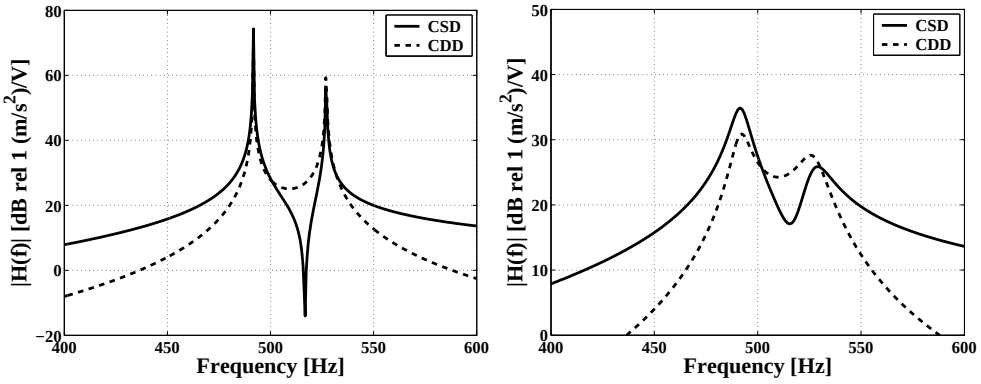

Figure 19: Magnitude of control path frequency response function estimates, between the actuator voltage and the error acceleration in the cutting speed direction (CSD) and between the actuator voltage and the error acceleration in the cutting depth direction (CDD), based on the harmonic analysis of the "3-D" finite element model of the active boring bar: a) without damping, and b) with damping in the model.

points corresponding to the error sensor positions at the actual active boring bar in the cutting speed and cutting depth direction correspondingly (see Fig. 20).

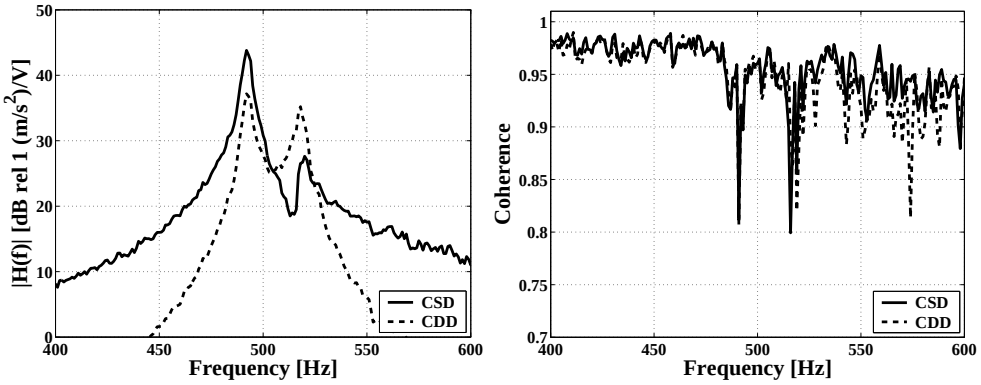

Figure 20: a) Magnitude of control path frequency response function estimates between the actuator voltage and the acceleration at the error sensor positions in the cutting speed (CSD), and in the cutting depth (CDD) directions, and b) corresponding coherence functions. Transient analysis of the "3-D" finite element model of the active boring bar enabling variable contact between the boring bar and the clamping house.

An estimated random error for the control path frequency response function estimates produced based on the "3-D" finite element model is shown in Fig. 21. The random error for the control path frequency response function estimate between the

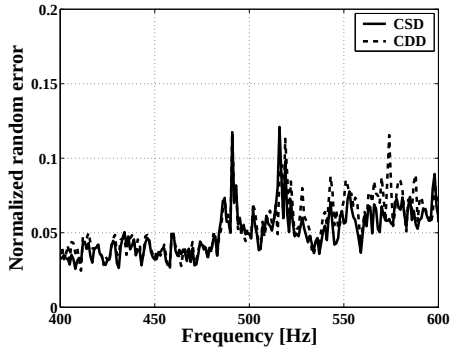

Figure 21: Normalized random error for control path frequency response functions estimated based on the "3-D" finite element model enabling variable contact between the boring bar and the clamping house.

actuator voltage and the error accelerometer in cutting speed direction at the resonance frequencies is 0.072 and 0.063. The random error for the control path frequency response function estimate between the actuator voltage and the error accelerometer in cutting depth direction at the resonance frequencies is 0.070 and 0.061 respectively.

The magnitude functions of control path frequency response functions estimated experimentally and based on the simulation of the harmonic response of the linear "3-D" FE model and the transient response of the "3-D" FE model enabling variable contact between the boring bar and the clamping house are plotted together in the same diagram in Fig. 22.

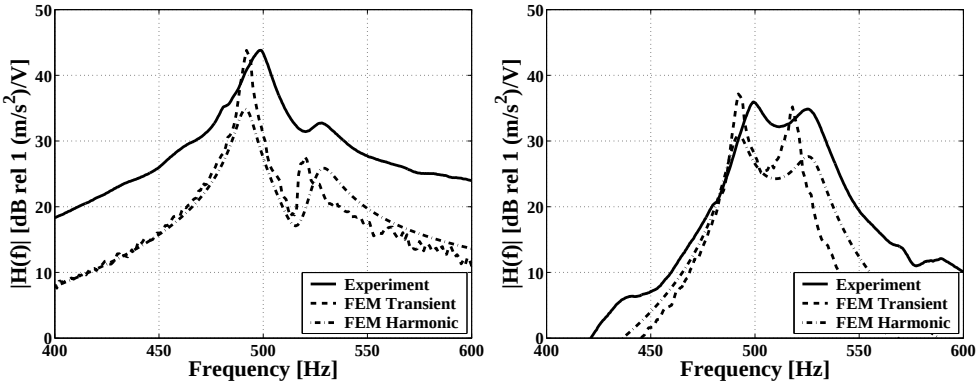

Figure 22: Magnitude of control path frequency response function estimates between the actuator voltage and the acceleration at the error sensor positions a) in the cutting speed (CSD), and b) in the cutting depth (CDD) directions obtained experimentally on the actual active boring bar and based on the simulation of the transient response and the harmonic response of the "3-D" finite element model of the active boring bar.

3.3 Dynamic Modeling of the Boring Bar with the Coulomb Friction Force Included

In order to improve the control path frequency response functions estimated based on the "3-D" finite element model enabling variable contact between the boring bar and the clamping house, the Coulomb friction force was included in the model. Two approximations of the Coulomb friction force were utilized: the arctangent and the bilinear. Dynamic motion of the boring bar excited by the actuator expansion results in the complex phenomenon of a variable contact between the boring bar and the clamping house. In order to investigate the influence of the Coulomb friction force on the dynamic behavior of the boring bar, accelerance functions were first calculated based on the simplest SDOF model of the boring bar for a range of values of the governing parameters and several excitation force levels. Then, the control path frequency response functions were calculated based on the "3-D" finite element model enabling variable contact between the boring bar and the clamping house for both the arctangent and the bilinear approximations of the Coulomb friction force. In this case, simulations of the transient response of the boring bar were carried out for the limited range of values of the governing parameters (for both the arctangent and the bilinear model) and a single excitation force level due to the long computational time required for each simulation.

3.3.1 Transient Response Based on the SDOF Model

In order to simulate the nonlinear SDOF system described by Eq. 39 or Eq. 40 and Eq. 41, the mass m, stiffness k and damping c have to be selected. For the sake of relevance, these quantities are estimated based on the point accelerance function estimate for the cutting speed direction produced in the experimental modal analysis of the active boring bar (see Fig. 23).

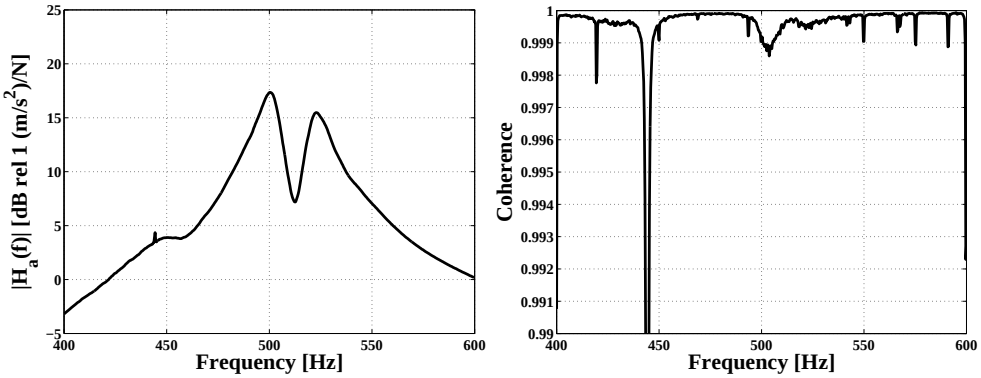

a) b)

Figure 23: Magnitude of point accelerance estimate for the boring bar in the cutting speed direction (CSD), and b) corresponding coherence function (produced in experimental modal analysis).

The modal parameters m, k and c can now be estimated based on the following expressions:

$$k = \frac{2\pi^2 f_n^2}{\zeta_n |H_a(f_n)|}, \tag{44}$$

$$m = \frac{k}{(2\pi f_n)^2}, \tag{45}$$

$$c = 2\zeta_n \sqrt{mk}. \tag{46}$$

where f_n is the undamped fundamental natural frequency in the cutting speed direction, ζ_n is the corresponding damping ratio, $|H_a(f_n)|$ is the value of the magnitude function of the point accelerance function estimate in the cutting speed direction at the fundamental natural frequency in the cutting speed direction.

The estimated values of the modal mass, stiffness and damping are as follows: $m = 6.489\ kg$, $k = 64.467 \times 10^6\ N/m$ and $c = 427.071\ Ns/m$. These mass, stiffness and damping values were used in the simulations of the response of the SDOF model with the arctangent and bilinear approximations of the nonlinear friction force for uniformly distributed broadband random force with RMS levels of 57.827 N, 289.088 N, 576.647 N, 2888.338 N and 5762.465 N.

The response of the SDOF model with the arctangent approximation of the Coulomb friction force was calculated for the following parameters of the relative sliding velocity:

$$\vartheta = [\ 0.005\dot{w}_{max} \quad 0.01\dot{w}_{max} \quad 0.05\dot{w}_{max} \quad 0.1\dot{w}_{max}\ ] \tag{47}$$

where $\dot{w}_{max}$ is the maximum velocity estimated based on the linear model. The relative damping ratios estimated for each value of parameter ϑ at each excitation force level are summarized in Table 7.

Excitation force RMS level, $[N]$	Damping ratio, [%]			
	$0.005\dot{w}_{max}$	$0.01\dot{w}_{max}$	$0.05\dot{w}_{max}$	$0.1\dot{w}_{max}$
57.827	72.447	68.034	29.007	17.136
289.088	4.572	4.572	4.175	3.746
576.647	3.047	3.047	2.847	2.624
2888.338	1.994	1.994	1.944	1.944
5762.465	1.844	1.844	1.894	1.894

Table 7: Estimates of the relative damping for the frequency response functions based on the SDOF nonlinear model with the arctangent approximation of the Coulomb friction force.

The magnitude function for the accelerance function estimates between the uniformly distributed random force with an RMS level of 576.647 N and the acceleration of the SDOF model calculated for the range of values of the parameter ϑ together with corresponding coherence functions are shown in Fig. 24.

The response of the SDOF model with the bilinear approximation of the Coulomb friction force was calculated for the following values of the slip threshold δ: $10^{-6}\ m$, $5 \cdot 10^{-6}\ m$, $10^{-5}\ m$, $5 \cdot 10^{-5}\ m$ and $10^{-4}\ m$. Natural frequency estimates for each of the combinations of δ and the excitation force levels are given in Table 8.

The magnitude function for the accelerance function estimates between the uniformly distributed random force with an RMS level of 576.647 N and the acceleration

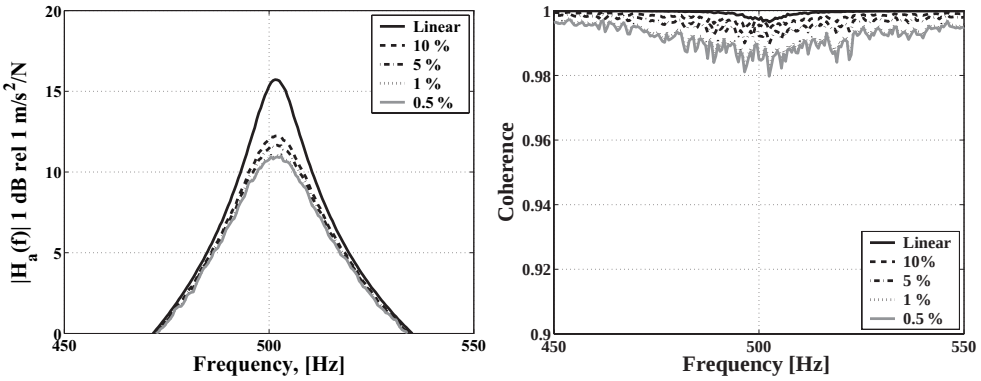

a) b)

Figure 24: a) Magnitude of accelerance functions calculated based on the response of the SDOF model with the arctangent approximation of nonlinear force for the different values of the relative velocity ϑ and b) corresponding coherence functions (excitation force RMS level 576.647 N).

Excitation force RMS level, $[N]$	Natural frequency, [Hz]				
	$\delta = 10^{-4}$, $[m]$	$\delta = 5 \cdot 10^{-5}$, $[m]$	$\delta = 10^{-5}$, $[m]$	$\delta = 5 \cdot 10^{-6}$, $[m]$	$\delta = 10^{-6}$, $[m]$
57.827	502.5	504	511.5	520	549
289.088	502.5	504	508	511.5	537.5
576.647	502.5	504	507	510	535
2888.338	502.5	502.5	505.5	509.5	532.5
5762.645	502.5	502.5	505	509.5	532.5

Table 8: Estimates of the natural frequency for the frequency response functions based on the SDOF nonlinear model with the bilinear approximation of the Coulomb friction force.

of the SDOF model calculated for the range of values of the parameter δ together with corresponding coherence functions are shown in Fig. 25.

3.3.2 Dynamics of the "3-D" Finite Element Model Enabling Variable Contact between the Boring Bar and the Clamping House and also with Coulomb Friction Force

The initial value of the relative sliding velocity ϑ was estimated based on the transient analysis of the finite element model enabling variable contact between the boring bar and the clamping house while allowing for no friction. The maximum velocity in the feed direction of the nodes of the boring bar finite element model corresponding to the screws clamping position on the boring bar was $\dot{w}_{max} = 0.007784\ m/s$. The arctangent friction model was tested for four different percentage values of the maximum sliding velocity: 10%, 5%, 1% and 0.5 %. The control path frequency response functions between the actuator voltage and the accelerations at the point of the active boring bar error sensor positions were estimated based on the transient analysis of the "3-D" finite element model with the arctangent friction model enabling variable contact

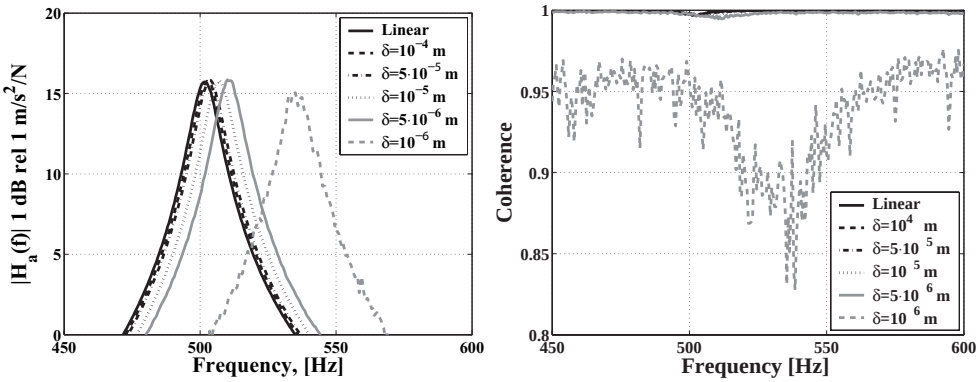

a) b)

Figure 25: a) Magnitude of accelerances calculated based on the response of the SDOF model with bilinear approximation of nonlinear force for the different values of the slip threshold δ and b) corresponding coherence function (excitation force RMS level 576.647 N).

between the clamping house and the boring bar for the four different relative sliding velocities. Magnitude functions for these control path frequency response functions are plotted together with the corresponding control path frequency response function for the finite element model enabling variable contact between the boring bar and the clamping house while allowing for no friction, in Figs. 26 a) and c). The corresponding coherence functions are shown in Figs. 26 b) and d).

The transient analysis was also carried out on the "3-D" finite element model with the bilinear model of the friction force enabling variable contact between the boring bar and the clamping house. To estimate the slip threshold, the average element length was calculated as $\bar{l}_e = 6.973 \cdot 10^{-3}\ m$, yielding the slip threshold $\delta = 1.743 \cdot 10^{-5}\ m$. The bilinear model of the friction force was tested for four different values of the slip threshold: $1.743 \cdot 10^{-5}\ m$, $5 \cdot 10^{-5}\ m$, $10^{-5}\ m$ and $5 \cdot 10^{-6}\ m$. The control path frequency response functions between the actuator voltage and the accelerations at the points of the active boring bar error sensor positions were estimated based on the transient analysis of the "3-D" finite element model (with the bilinear friction model and enabling variable contact between the boring bar and the clamping house) for the four different slip thresholds. Magnitude functions for these control path frequency response functions are plotted together with corresponding control path frequency response function for the finite element model, enabling variable contact between the boring bar and the clamping house while allowing for no friction in Figs. 27 a) and c). The corresponding coherence functions are shown in Figs. 27 b) and d).

3.4 Actuator Receptance

The "boring bar - actuator" interface receptance functions were estimated based on the transient response of the boring bar under applied random excitation voltage using the "3-D" finite element model of the boring bar enabling variable contact between the boring bar and the clamping house. The estimates of the receptance functions are produced using the calculated displacements and contact forces in the feed direction

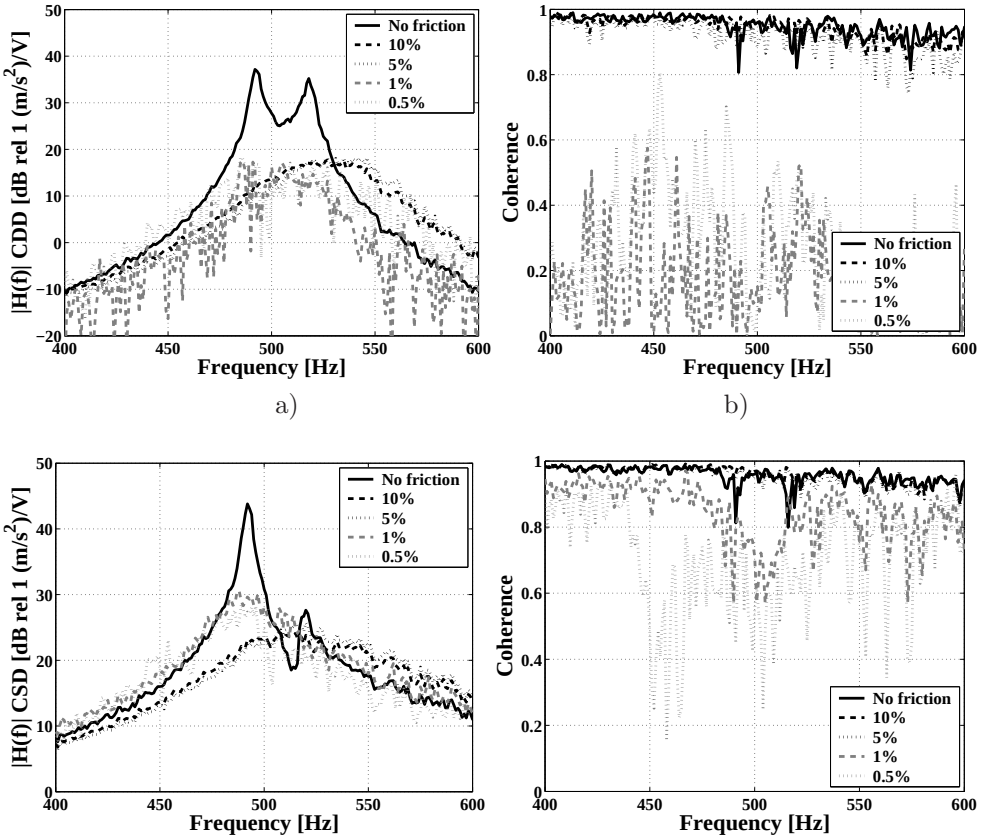

Figure 26: Magnitude of control path frequency response function estimates between the actuator voltage and acceleration in the error sensor positions a) in the cutting depth direction (CDD) and c) in the cutting speed direction (CSD). Coherence function estimates between the actuator voltage and the acceleration in the error sensor positions b) in the cutting depth direction (CDD) and d) in the cutting speed direction (CSD). Based on the transient analysis of the "3-D" finite element model of the active boring bar enabling variable contact between the boring bar and the clamping house and with the arctangent model of the friction force.

collected for the nodes of the boring bar finite element model corresponding to the actuator-boring bar interfaces (see Fig. 28). The random error for the receptance functions estimated based on the "3-D" finite element model is shown in Fig. 29. The random error for the receptance function at the second "boring bar-actuator" interface (the interface that is closest to the free end of the bar) at the resonance frequencies is 0.138 and 0.089 respectively. The random error of the receptance function at the first "boring bar-actuator" interface (the interface that is closest to the clamped end of the bar) at the resonance frequencies is 0.047 and 0.081 respectively.

It is difficult if not impossible to measure the acceleration and the actuator force (in the feed direction) of the active boring bar in the interface between the actuator and the boring bar. For these reasons, the "boring bar - actuator" interfaces accelerance functions have not been estimated for the actual boring bar. The strain at

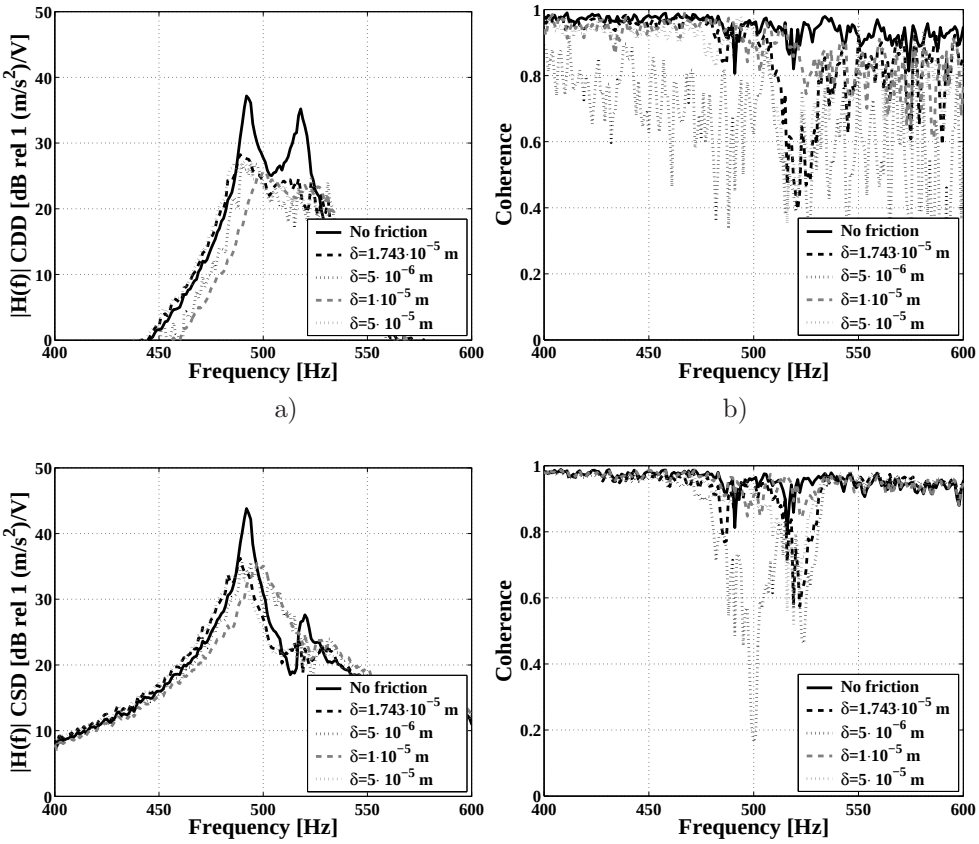

Figure 27: Magnitude of control path frequency response function estimates between the actuator voltage and the acceleration in the error sensor positions a) in the cutting depth direction (CDD) and c) in the cutting speed direction (CSD). Coherence function estimates between the actuator voltage and the acceleration in the error sensor positions b) in the cutting depth direction (CDD) and d) in the cutting speed direction (CSD). Based on the transient analysis of the "3-D" finite element model of the active boring bar enabling variable contact between the boring bar and the clamping house and with the bilinear model of the friction force.

positions close to the actuator interfaces of the actual active boring bar may, however, be measured. Thus, frequency response function estimates between the actuator voltage and the strain at four different positions (see Fig. 8) of the active boring bar have been produced based on both the linear "3-D" FE model and the model that enables variable contact between the clamping house and the boring bar. The magnitude functions for these frequency response functions are shown in Fig. 30. Also, frequency response function estimates between the actuator voltage and the strain at four different positions (see Fig. 8) have been estimated for the actual active boring bar, and they are illustrated in Fig. 31. Furthermore, in Fig. 32 the magnitude of the frequency response function estimates between the actuator voltage and the boring bar strain for both the "3-D" FE models and the actual boring bar are plotted together.

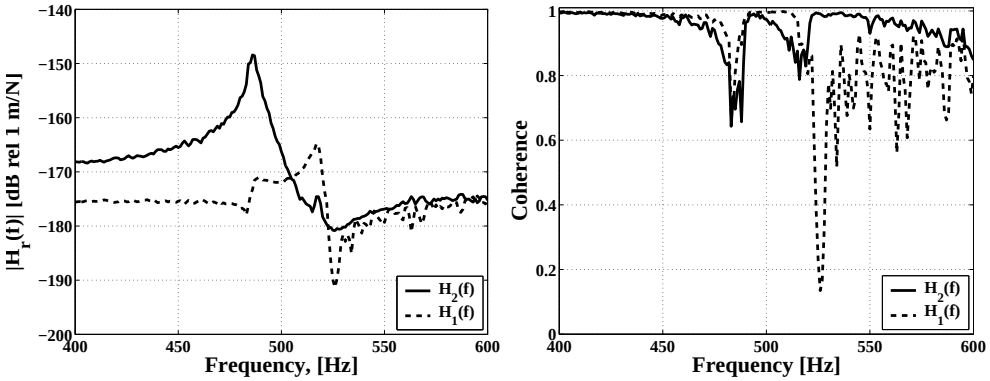

a) b)

Figure 28: a) Magnitude function of receptance function estimates for the "boring bar - actuator" interfaces based on the "3-D" finite element model of the active boring bar enabling variable contact between the boring bar and the clamping house and b) corresponding coherence functions.

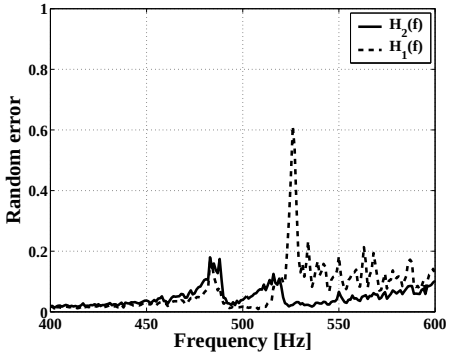

Figure 29: Random error for the receptances estimated based on the "3-D" finite element model of the the active boring bar enabling variable contact between the boring bar and the clamping house.

4 Summary and Conclusions

The "3-D" finite element model of the system boring bar - actuator - clamping house resulted in fairly accurate estimates of the boring bar's fundamental bending mode eigenfrequencies, 496.2 Hz and 529 Hz (see Table 6). Also, it provided estimates of the fundamental mode shapes that are well-correlated with the corresponding mode shapes extracted in the experimental modal analysis of the active boring bar (see Fig. 17 and the cross-MAC matrix in Eq. 43). The discrepancies between the natural frequency and mode shape estimates from the "3-D" finite element model and the

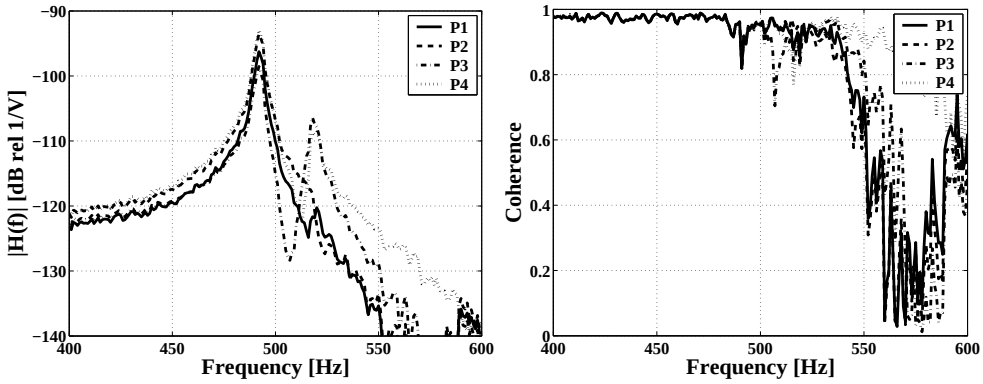

Figure 30: Magnitude of the frequency response function estimates between the actuator voltage and the boring bar strain, calculated based on the "3-D" FE model enabling variable contact between the boring bar and the clamping house, and b) the corresponding coherence function estimates.

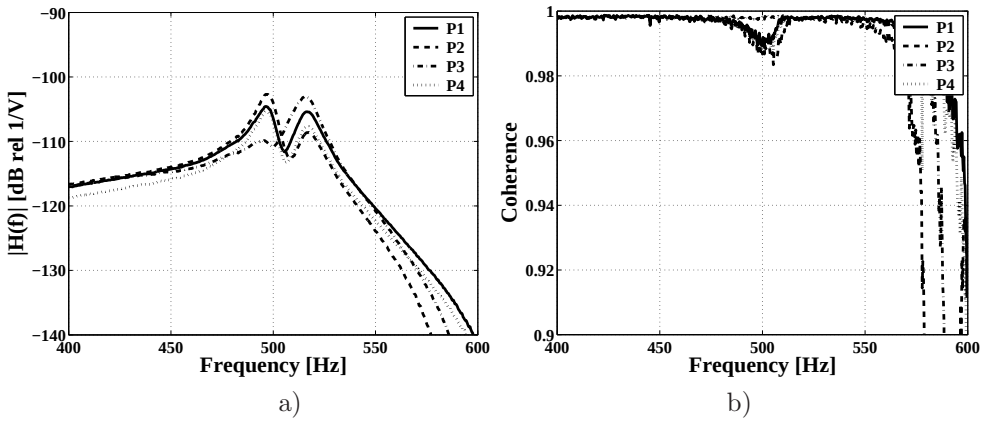

Figure 31: Magnitude of the frequency response estimates between the actuator voltage and the strain measured on the actual active boring bar, and b) the corresponding coherence function estimates.

experimental modal analysis may, for instance, be explained by differences between the actual active boring bar and the finite element model in dimensions and materials properties. Also, the fact that the attachment of the clamping house to the turret is modeled as infinitely rigid in the finite element model will introduce differences in the dynamic properties of the finite element model and the active boring bar.

Of significance is the ability to produce "3-D" finite element models of active boring bars which predict the control paths accurately. The following control paths have been considered: between the actuator input voltage and the output signal from the accelerometer measuring the boring bar vibration in the cutting speed direction close to the insert, and between the actuator input voltage and the output signal from

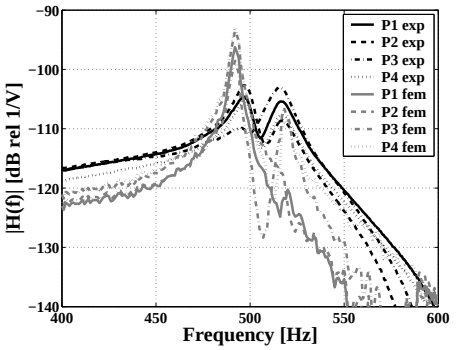

Figure 32: Magnitude of the frequency response estimates between the actuator voltage and the strain measured on the actual active boring bar and calculated based on the "3-D" FE model enabling variable contact between the boring bar and the clamping house.

the accelerometer measuring the boring bar vibration in the cutting depth direction close to the insert.

The ability to produce FE models of active boring bars enabling accurate modeling of the control paths is important for the development of efficient and accurate design procedure for active boring bars. The control path frequency response functions for the actual active boring bar were estimated (see Fig. 18 a)). The harmonic analysis of the linear "3-D" finite element model of the active boring bar results in control path frequency response function estimates with magnitude levels significantly higher as compared to the control path frequency response function estimates of the actual active boring bar. This can be observed by comparing the control path frequency response function estimates in Fig. 19 a) and Fig. 18 a). It is possible to reduce the magnitude of fundamental resonance frequency peaks in the control path frequency response function estimates produced based on the linear "3-D" finite element model by incorporating proportional damping (see Fig. 19 b)).

The harmonic response simulation of the finite element model is carried out in MSC.MARC is only enabled for linear systems and uses only the boundary conditions as defined in the initial phase of the calculations. On the other hand, the transient response analysis allows for simulation of the active boring bar's response based on the "3-D" finite element model with variable contact between the clamping house and the boring bar. Time variable boring bar boundary conditions imposed by the clamping house in the finite element model are enabled. The control path frequency response function estimates for the "3-D" finite element model of the active boring bar enabling variable contact between the clamping house and the boring bar display good correlation with the estimates produced by the linear FE models as well as the estimates produced experimentally, see Fig. 18 a), Fig. 19 b), Fig. 20 a) and 22. It may also be observed that the "3-D" finite element model of the active boring bar allowing variable contact between the clamping house provides an approximation that is stiffer than the actual boring bar. This may be explained by the fact that boundary conditions used for the attachment of the clamping house are modeled as infinitely rigid in the FE model. However, in the lathe the attachment of the clamping house to the turret as well as the attachment of the turret to the slide, etc., cannot be

considered completely rigid and, thus, flexibility is introduced.

The possibility to further improve the accuracy of the "3-D" finite element model enabling variable contact between the clamping house and the boring bar by incorporating damping into it has also been addressed. The Coulomb friction force between the surfaces of the clamping house and the boring bar was introduced. To facilitate interpretation of the transient response analysis results for the "3-D" finite element model with the Coulomb friction force, simulations of a simple nonlinear SDOF system were initially carried out for two different Coulomb friction force models; the arctangent model and the bilinear model. For a SDOF system with the Coulomb friction force approximated with the arctangent model, it can be observed from damping ratios estimated from simulations' results (see Table 7) that with an increasing excitation force RMS level, from 57.827 N till 5762.465 N the influence of the nonlinear friction force on the system's damping decreases. This is due to the fact that high excitation force levels induce vibration with the high velocities and the slip friction force magnitude is then negligible compared to the forces of the linear part of the system. At the constant excitation force level, different values of the relative sliding velocity ($\vartheta = 0.005\dot{w}_{max}$, $0.01\dot{w}_{max}$, $0.05\dot{w}_{max}$ and $0.1\dot{w}_{max}$) will introduce different levels of damping in the SDOF system (see Table 7 and Fig. 24 a). With a decreasing value of the relative sliding velocity, greater damping observed in the frequency response function estimates for the SDOF system (see Fig. 24 a)). Thus, the closer the arctangent friction model approximates the Coulomb friction force, the influence of the nonlinear friction force on the response of the system also increases which also is indicated by the coherence function estimates for the SDOF system in Fig. 24 b).

For a SDOF system with the Coulomb friction force approximated with the bilinear model, it can be observed from the natural frequencies estimated from simulations' results (see Table 8) that the influence of the nonlinear friction force on the systems stiffness will decrease with an increasing excitation force level. Thus, with an increasing force level the vibration displacement will increase and, as a consequence, the slip friction force magnitude will become more and more negligible compared to the forces of the linear part of the system. At the constant excitation force level, different values of the slip threshold δ from 10^{-4} m to 10^{-6} m will result in an increasing resonance frequency of the structure of approximately 9.5 %, i.e., from 501.5 Hz to 549 Hz (see Table 8 and Fig. 25 a)). With a decreasing value of the slip threshold, greater stiffness is observed in the frequency response function estimates for the SDOF system (see Fig. 25 a)). Thus, with a decreasing slip threshold the influence of the nonlinear friction force on the response of the system also increases which also is indicated by the coherence function estimates for the SDOF system in Fig. 25 b).

The dynamic behavior of the "3-D" finite element model of the system boring bar - actuator - clamping house including the Coulomb friction force and enabling variable contact is expected to be significantly more complicated to explain compared to the SDOF system. As time evolves, contact may occur or it may cease between nodes on the "3-D" surfaces of the clamping house and on the boring bar. Thus, the system has time-varying dynamic properties. Moreover, the "3-D" finite element model constantly changes its state, meaning that at a certain time instant contact is detected for some nodes, and friction force influence these nodes, while the other nodes, which were previously in contact, are separated and the friction ceases, etc. The introduction of the Coulomb friction force approximated with the arctangent model in the "3-D" finite element model of the active boring bar enabling variable contact between the clamping house and the boring bar resulted in significantly degraded

control path frequency response function estimates for the set of used relative sliding velocities compared to the case with no friction force in the FE model (see Figs. 26 a) and 26 c)). However, replacing the arctangent model with the bilinear model in the "3-D" finite element model of the active boring bar enabling variable contact resulted in improved control path frequency response function estimates compared to the case with the arctangent friction model (c.f. Figs. 26 and 27). These control path frequency response function estimates display a lower correlation with frequency response function estimates for the actual active boring bar compared to the the "3-D" finite element model of the active boring bar enabling variable contact (compare Figs. 18 a), 26 a) 26 c), 27 a) and 27 c)). In the bilinear approximation, the friction force is proportional to the relative displacement between contacting bodies within the slip threshold δ. Vibrations result in relative displacements between the contacting nodes of the boring bar and clamping house. If the relative displacements are within the slip threshold δ, the friction force introduces an increase in the stiffness between contacting nodes as compared to no contact. The selection of slip threshold δ seems to influence the fundamental resonance frequencies of the system boring bar - actuator - clamping house (see Fig. 27 a) and Fig. 27 b)).

The "boring bar - actuator" interface receptance functions were estimated based on the transient response of the boring bar under applied random excitation voltage using the "3-D" finite element model of the boring bar enabling variable contact between the clamping house and the boring bar. The estimates of the receptance functions are produced using the calculated displacements and contact forces in the feed direction collected for the nodes of the actuator finite element model corresponding to the actuator-boring bar engagement (see Fig. 28). It is difficult if not impossible to measure the acceleration and force (in the feed direction) of the active boring bar in the interface between the actuator and boring bar. For this reason, the "boring bar - actuator" interfaces accelerance functions have not been estimated for the actual boring bar. The strain at positions close to the actuator interfaces of the actual active boring bar may, however, be measured. Thus, frequency response function estimates between the actuator voltage and the strain at four different positions (see Fig. 8) of the active boring bar may be produced based on both the "3-D" FE model enabling variable contact between the clamping house and the boring bar (see Fig. 30 a)) and the actual active boring bar (see Fig. 31 a)). By comparing the frequency functions for the actual boring bar and the FE model, it follows that the FE model lacks damping and is slightly stiffer. Also, by examining Fig. 32 it follows that the orientation of the bending "modes" in the cutting depth/cutting speed plane is likely to differ between the actual active boring bar and the FE model enabling variable contact. One issue that seems to be of importance to address in future work, is to further improve the "3-D" FE model of the active boring bar by, e.g., the modeling of the boundary conditions imposed by the turret on the clamping house.

Acknowledgments

The present project is sponsored by Acticut International AB.

References

[1] E. Marui, S. Ema, and S. Kato. Chatter vibration of lathe tools, part 1: General characteristics of chatter vibration. *Journal of Engineering for Industry*, 105:100–106, May 1983.

[2] M. N. Hamdan and A. E. Bayoumi. An approach to study the effect of tool geometry on the primary chatter vibration in orthogonal cutting. *Journal of Sound and Vibration*, 128(3):451–469, 1989.

[3] G. M. Zhang. Dynamic modeling and analysis of the boring machine system. *Journal of Engineering for Industry*, 109:219–226, 1987.

[4] S.A. Tobias. *Machine-Tool Vibration*. Blackie & Son, 1965.

[5] H. E. Merritt. Theory of self-excited machine-tool chatter. *Journal of Engineering for Industry*, pages 447–454, 1965.

[6] E. W. Parker. Dynamic stability of a cantilever boring bar with machine flats under regenerative cutting conditions. *Journal Mechnical Engineering Science*, 12(2):104–115, 1970.

[7] P. N. Rao, U. R. K. Rao, and J. S. Rao. Towards improved design of boring bars, part 1: Dynamic cutting force model with continuous system analysis for the boring bar performnca. *Journal of Machine Tool Manufacture*, 28(1):33–44, 1988.

[8] F. Kuster. Cutting dynamics and stability of boring bars. *Annals of the CIRP*, 39(1):361–366, 1990.

[9] E. I. Rivin. Tooling structure: Interface between cutting edge and machine tool. *Annals of the CIRP*, 49(2):591–634, 2000.

[10] C. M. Nicolescu. On-line identification and control of dynamic charactersitics of slender workpieces in turning. *Journal of Material Processing Technology*, 58:374–378, 1996.

[11] E. Al-Regib, J. Ni, and S.-H. Lee. Programming spindle speed varioation for machine tool chatter suppression. *International Journal of Machine Tool & Manufacture*, 43(12):1229–1240, 2003.

[12] N. A. Ruud, R. Karlsen, K. Sørby, and C. Richt. Minimizing vibration tendencies in machining. *Technical Article at: http://www.coromant.sandvik.com*, 2005.

[13] *http://www.teeness.no*, 2005.

[14] S. G. Tewani, K. E. Rouch, and B. L. Walcott. A study of cutting process stability of a boring bar with active dynamic absorber. *International Journal of Machine Tools & Manufacture*, 35(1):91–108, 1995.

[15] D.R. Browning, I. Golioto, and N.B. Thompson. Active chatter control system for long-overhang boring bars. *Proceedings of SPIE*, 3044:270–280, 1997.

[16] I. Claesson and L. Håkansson. Adaptive active control of machine-tool vibration in a lathe. *IJAV-International Journal of Acoustics and Vibration*, 3(4):155–162, 1998.

[17] L. Pettersson, L. Håkansson, I. Claesson, and S.Olsson. Control of machine-tool vibration in a cnc lathe based on an active tool holder shank with embedded piezo ceramic actuators. *In Proceedings of the Eight International Congress on Sound and Vibration*, 2001.

[18] L. Pettersson, L. Håkansson, I. Claesson, and S.Olsson. Active control of boring bar vibration in cutting operations. *In Proceedings of the Ninth International Congress on Sound and Vibration, ICSV9*, 2002.

[19] H. Åkesson, T.Smirnova, I. Claesson, and L. Håkansson. On the development of a simple and robust active control system for boring bar vibration in industry. *IJAV-International Journal of Acoustics and Vibration*, 12(4):139–152, 2007.

[20] I. Claesson and L. Håkansson. Adaptive active control of machine-tool vibration in a lathe. *IJAV-International Journal of Acoustics and Vibration*, 3(4):155–162, 1998.

[21] B. W. Wong, B. L. Walcott, and K. I. Rouch. Active vibration control via electromagnetic dynamic absorbers. *IEEE*, pages 868–874, 1995.

[22] S. Nagano, T. Koizumi, N. Tsujiuchi T. Fujii, H. Ueda, and K. Steel. Development of a composite boring bar. *Composite Structures*, 38(1-4):531–539, 1997.

[23] P.-O. H. Sturesson, L. Håkansson, and I. Claesson. Identification of the statistical properties of the cutting tool vibration in a continuous turning operation - correlation to structural properties. *Journal of Mechanical Systems and Signal Processing, Academic Press*, 11(3):459–489, 1997.

[24] J.R. Baker and K.E. Rouch. Use of finite element structural models in analyzing machine tool chatter. *Finite Elements in Analysis and Design*, 38(11):1029–1046, 2002.

[25] R. Mahdavinejad. Finite element analysis of machine and workpiece instability in turning. *International journal of Macine Tools & Structure: Design, Research and Implementation*, 45(7-8):753–760, 2005.

[26] *http://www.efunda.com/Materials/piezo/material_data/matdata_output.cfm ?Material_ID=PZT_5H.*

[27] *Low voltage co-fired multilayer stacks, rings and chips for actuation.* Piezomechnik, GmbH, 2006.

[28] M.H. Hayes. *Statistical Digital Signal Processing and Modeling.* John Wiley & Sons, Inc., 1996.

[29] D.J. Ewins. *Modal Testing: Theory and Practice.* Research Studies Press, distributed by Wiley, 1984.

[30] J.S. Bendat and A.G. Piersol. *Engineering Application of Correlation and Spectral Analysis.* John Wiley & Sons, second edition, 1993.

[31] P.D. Welch. The use of fast fourier transform for the estimation of power spectra: A method based on time averaging over short modified periodograms. *IEEE Transaction on Audio and Electroacoustics*, pages 70–73, June 1967.

[32] N.M.M. Maia and J.M.M. Silva. *Theoretical and Experimental Modal Analysis*. Research Studies Press Ltd., 1997.

[33] *MSC.MARC Volume A: Theory and User's Information*. MSC.Software, 2005.

[34] O. S. Zienkiewicz, R. L. Taylor, and J.Z. Zhu. *The Finite Element Method: Its Basis and Fundamentals*. Butterworth-Heinemann, 2005.

[35] C.H. Hansen and S.C. Snyder. *Active Control of Noise and Vibration*. E&FN SPON, 1997.

[36] I. Doghri, A. Muller, and R.L. Taylor. A general three-dimensional contact procedure for implicit finite element codes. *Engineering Computations*, 15(2):233–259, 1998.

[37] K.Y. Wang, Y.L. Kang Q.H. Qin, J.S. Wang, and C.Y. Qu. A direct constraint-trefftz fem for analysing elastic contact problems. *International Journal for Numerical Methods in Engineering*, 63:1694–1718, April 2005.

[38] L. Andrèn, L.Håkansson, A. Brandt, and I. Claesson. Identification of dynamic properties of boring bar vibrations in a continuous boring operation. *Journal of Mechnical Systems & Signal Processing*, 18(4):869–901, 2004.

[39] L. Andrèn, L.Håkansson, A. Brandt, and I. Claesson. Identification of motion of cutting tool in a continuous boring operation - correlation to structural properties. *Journal of Mechnical Systems & Signal Processing*, 18(4):903–927, 2004.

[40] J. Williams. *Engineering Tribology*. Cambridge University Press, 2005.

[41] J. Chung and G. M. Hulbert. A family of single-step houbolt time integration algorithms for structural dynamics. *Computer Methods in Applied Mechanics and Engineering*, 118(1-2):1–11, 1994.

[42] D.J. Inman. *Engineering Vibration*. Prentice-Hall, second edition, 2001.

[43] *Using MATLAB*. The MathWorks, Inc., 2002.

Part V

Initial Development of an Actuator Positioning Method for Active Boring Bars

This part is published as:

T. Smirnova, H. Åkesson, L. Håkansson, I. Claesson and T. Lagö, *Initial Development of an Actuator Positioning Method for Active Boring Bars*, submitted for publication in *Journal of Mechanical Systems & Signal Processing*, September, 2010.

Initial Development of an Actuator Positioning Method for Active Boring Bars

T. Smirnova[1], H. Åkesson[1,2], L. Håkansson[1], Ingvar Claesson[1] and Thomas Lagö[2]
[1]Blekinge Institute of Technology,
Department of Electrical Engineering,
372 25 Ronneby, Sweden

[2]Acticut International AB
Gjuterivägen 6, 311 32 Falkenberg, Sweden

Abstract

Active control is a technique that may be used to solve vibration problems frequently occurring during internal turning operations in the manufacturing industry. By utilizing an active boring bar with an embedded piezoelectric actuator and a suitable controller, the primary boring bar vibrations originating from the material deformation process may be attenuated with the actuator-induced secondary "anti vibrations". One of the key issues, when designing an active boring bar, is the choice of the position of the piezoelectric actuator that influences both the dynamic stiffness of the boring bar and its ability to produce secondary "anti vibrations". In order to find an actuator position in a boring bar that enables adequate active boring bar performance, several prototypes of an active boring bar are generally required. This implies the manufacturing and testing of prototypes etc., which is time-consuming and costly. To improve the efficiency of the design procedure of active boring bars, a new strategy is suggested. Finite element models of the system boring bar - actuator - clamping house with different actuator positions in combination with artificial neural networks are introduced. Objective functions for selecting actuator position at which to embed an actuator into boring bar are given. An active boring bar with an actuator position suggested by the method was manufactured. Spatial dynamic properties of the active boring bar prototype were estimated by means of experimental modal analysis and compared with the corresponding finite element model's dynamic properties. The results indicate fairly good correlation between the natural frequencies of the fundamental bending modes of the boring bar prototype and the corresponding "3-D" finite element model. Moreover, results from the experimental evaluation of the active boring bar prototype and its finite element model display agreement concerning the boring bar performance in terms of control path frequency response functions.

1 Introduction

Boring bar vibration during internal turning operations in machine tools is a pronounced problem in the manufacturing industry. Boring bar vibration may easily be induced by the material deformation process, and is caused by the bar's normally slender geometry. Investigations in this area have shown that high vibration levels are excited at the natural frequencies related to the low-order bending modes of the boring bar and are usually dominated by the bending mode in the cutting speed direction [1–3]. High levels of boring bar vibration result in poor surface finish, excessive tool wear, tool breakage and severe levels of acoustic noise. Thus, boring bar vibration has a negative impact on productivity and the working environment, etc.

Active control has previously been successfully applied to reduce vibration during internal turning. Tewani utilized an active control approach based on active dynamic absorbers inside boring bars, controlled by a digital state feedback controller, to achieve an improvement in the stability of the cutting process [4]. Later, Browning et al. [5] described the use of an active clamp for boring bars, controlled by a feedback version of the filtered-x LMS algorithm. The use of this clamp extended the actual, operable length of boring bars. Claesson and Håkansson [6] controlled tool vibration by using the feedback filtered-x LMS algorithm to control tool shank vibration in the cutting speed direction. This was done without applying traditional regenerative chatter theory. Pettersson et al. [7] reported an adaptive active feedback control system based on a tool holder shank with embedded actuators and vibration sensors. This control strategy was later applied to boring bars by Pettersson et al. [8]. Finally, Åkesson et al. [9] described a simple and robust active control system for boring bar vibration in industry. This system made use of embedded actuators and vibration sensors.

Active feedback control of tool vibration in turning operations is generally based on a selective increase of the dynamic stiffness at the actual frequency of the dominating bending mode [4,9,10]. For instance, an active boring bar may have an accelerometer attached close to the tool-end. This accelerometer then measures the boring bar vibration in the cutting speed direction. The accelerometer signal may be fed to a controller to produce secondary or "anti vibrations" via an actuator embedded inside a groove milled in the longitudinal direction below the center line of a boring bar (see Fig. 1).

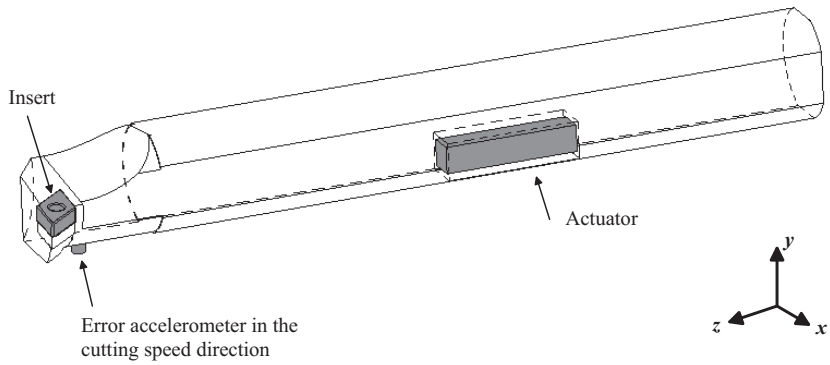

Figure 1: Schematic view of an active boring bar.

Because of the piezoelectric properties of the actuator material, a dynamic electrical control signal will steer a dynamic length expansion of the actuator. The actuator will in turn apply a dynamic bending moment to the boring bar. If the controller produces an adequate control signal to the actuator, it will counteract the primary vibration excited by the material deformation process [10]. One of the key issues when designing an active boring bar with an embedded actuator or actuators is the selection of the position of the actuator inside the boring bar. To select a suitable actuator position for an active boring bar, it is generally necessary to manufacture and test several prototypes of the active boring bar. This is a complex, time consuming and costly procedure. However, the efficiency of the design procedure may be improved by e.g. utilizing "3-D" finite element modeling to predict the dynamic response of active boring bars with different actuator positions. An initial "3-D" FE model of the system boring bar - actuator - clamping house, enabling variable contact between the surfaces of the boring bar, the clamping house and the clamping screws, has previously been addressed [11].

Mehrabian et al. [12] introduced a technique for optimal positioning of piezo patch actuators on a smart fin for active control. They used a finite element model of an active fin with a number of actuators and vibration sensors attached. Based on the FE model, control path frequency response functions for the different actuator positions were produced. The peak magnitudes for the first three fin modes in the control path frequency response functions were extracted and assembled to form a "3-D" surface for each of the modes. To increase the resolution in the peak magnitude "3-D" surfaces, multilayer perceptron neural networks (MLP NNs) were used to interpolate peak magnitudes between the actual coordinates for the actuators. To suggest the optimal actuator pair position, depending on the desired control authority over each mode, the invasive weed optimization (IWO) algorithm was used.

This paper addresses the initial development of an efficient actuator positioning method that may provide initial suggestions for suitable actuator positions in active boring bars with the purpose of reducing the number of required boring bar prototypes. Basically, the concept of the method is to replace a number of the active boring bar prototypes by utilizing FE modeling of the system boring bar - actuator - clamping house in combination with neural networks and an objective function indicating suitable actuator positions in a boring bar. For this purpose, thirty six "3-D" FE models of the system boring bar - actuator - clamping house with different actuator positions have been developed. The modeling focuses on the dynamic properties of the active boring bar's first two fundamental bending modes. To enable higher spatial resolution in the estimate of the actuator position, trained multilayer perceptron neural networks (MLP NNs) have been introduced. Objective functions for the selection of actuator positions are also suggested in the paper.

An active boring bar prototype with an actuator embedded at a position suggested by the actuator positioning method has been manufactured. Its spatial dynamic properties are correlated to the estimates produced by the finite element model of the corresponding active boring bar. Moreover, the finite element model provided a fairly accurate estimate of the active boring bar performance, in terms of the maximal magnitude of the control path frequency response functions at the frequencies of the fundamental boring bar bending modes.

2 Materials and Methods

2.1 Measurement Equipment and Experimental Setup

The experimental modal analysis and control path estimates were conducted in a Mazak QUICK TURN NEXUS 300-II CNC turning center. The machine tool has a spindle power of 26.1 kW and a maximal machining diameter of 420 mm, a maximal spindle speed of 4000 (r.p.m.), with 1250 mm between the centers, and a turret capacity of 12 tools (see Fig. 2).

Figure 2: Mazak 300 QUICK TURN NEXUS 300-II CNC turning center.

The following equipment was used to carry out experimental modal analysis:

- 12 PCB 333A32 accelerometers;
- 2 Gearing & Watson Electronics shakers v4;
- 2 Brüel & Kjær 8001 impedance heads;
- HP VXI E1432 front-end data acquisition unit;
- PC with IDEAS Master Series version 6.

The boring bar was excited simultaneously both in the cutting speed direction and in the cutting depth direction by two shakers via impedance heads attached at a distance of $l_1 = 0.1\ m$ from the clamped end of the active boring bar (see Fig. 3). The spatial motion of the boring bar was measured by 12 accelerometers and 2 impedance heads glued at a distance of $l_2 = 0.025\ m$ from each other, starting at $0.025\ m$ from the free end of the boring bar. Out of these, 6 accelerometers and one impedance head were used to measure the vibrations in the cutting speed direction $(-y)$, while the other 6 accelerometers and another impedance head were employed to measure the vibrations in the cutting depth direction (x). The two accelerometers

closest to the tool tip of the boring bar, one measuring vibration in the cutting speed direction and one measuring vibration in the cutting depth direction, are referred to as error accelerometers or error sensors.

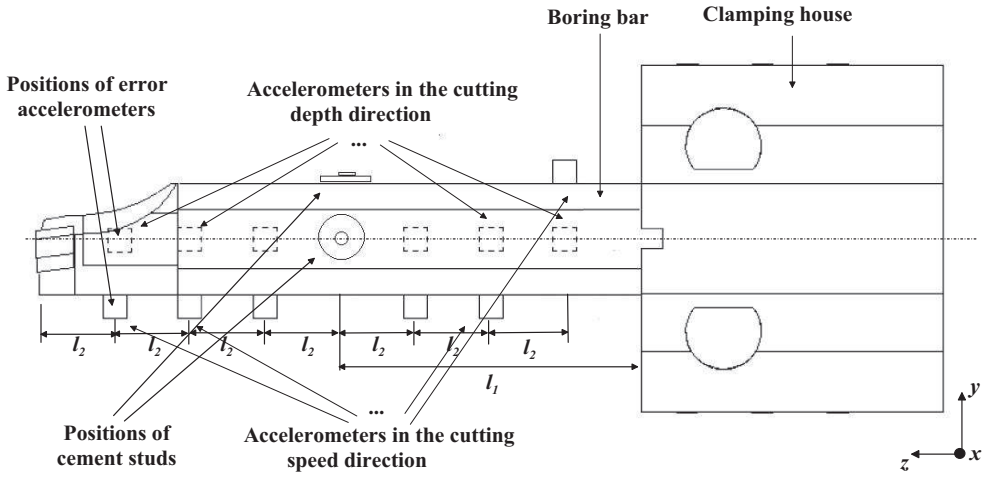

Figure 3: Drawing of the clamped active boring bar with accelerometers and cement studs for the attachment of impedance heads.

The coordinate system is defined as follows: x is the cutting depth direction, y is the negative cutting speed direction and z is the feed direction.

2.2 Active Boring Bar

The active boring bar prototype used in modeling and experiments was based on a standard boring bar S40T PDUNR15 F3 WIDAX. It is made of the material 30CrNiMo8 where Young's elastic modulus $E = 205\ GPa$, the density $\rho = 7850\ kg/m^3$ and Poisson's coefficient $\nu = 0.3$. The active boring bar was clamped in a standard 8437-0 40 mm Mazak holder clamping house. The clamping house is attached to the turret by four screws.

The active boring bar contains an actuator embedded into a milled space below the center line. The piezoelectric stack actuator used in the experiments is made of the piezoelectric material Lead Zirconate Titanate (PZT-5H). The actuator specifications are given in Table 1, [13, 14].

2.3 Experimental Modal Analysis

Experimental modal analysis enables the estimation of an active boring bar's modal parameters consisting of natural frequencies, mode shapes, relative damping coefficients and modal scaling factors.

In experimental modal analysis, the active boring bar is considered as a multiple degree-of-freedom system [15]. In this approach, the excitation forces and the responses of the structure to these forces were measured simultaneously. The data from

Property name	Value
Actuator material	PZT-5H
Free expansion ΔL_a, $[m]$	38×10^{-6}
Strain coefficient d_{33}, $[m/V]$	640×10^{-12}
Max operating voltage (P-P) V_{max}, $[V]$	150
Density ρ, $[kg/m^3]$	7500
Actuator stiffness k_a, $[N/m]$	125×10^6

Table 1: The actuator specifications.

these measurements are utilized to produce a parametric estimate of the dynamic properties of the structure [15].

The equation of the motion of a N_{ema} degrees-of-freedom system in matrix form is given by [16]:

$$[\mathbf{M}]\{\ddot{\mathbf{w}}(t)\} + [\mathbf{C}]\{\dot{\mathbf{w}}(t)\} + [\mathbf{K}]\{\mathbf{w}(t)\} = \{\mathbf{f}(t)\}, \tag{1}$$

where N_{ema} is the number of degrees of freedom corresponding to the number of points on the boring bar where its response is measured. Matrix $[\mathbf{M}]$ is the $N_{ema} \times N_{ema}$ mass matrix; $[\mathbf{C}]$ is the $N_{ema} \times N_{ema}$ damping matrix; and $[\mathbf{K}]$ is the $N_{ema} \times N_{ema}$ elastic stiffness matrix. The vector $\{\mathbf{f}(t)\}$ is the space- and time-dependent load vector. The vector $\{\mathbf{w}(t)\}$ is the space- and time-dependent displacement vector, and its i-th element generally contains the displacement measured in the point with the coordinates (x_i, y_i, z_i) , $i = 1, ..., N_{ema}$, at the time instant t. Thus, the displacement vector may be written as:

$$\{\mathbf{w}(t)\} = \left\{ \begin{array}{c} w(x_1, y_1, z_1, t) \\ w(x_2, y_2, z_2, t) \\ \vdots \\ w(x_{N_{ema}}, y_{N_{ema}}, z_{N_{ema}}, t) \end{array} \right\}. \tag{2}$$

The spatial dynamic properties of the boring bar were identified using the time-domain polyreference least squares complex exponential method [15]. This method is based on the impulse response function matrix $[\mathbf{h}(t)]$, which is a time domain version of the modal model, given by [15].

$$[\mathbf{h}(t)] = \sum_{n=1}^{N_{ema}} \left(Q_n \{\psi\}_n \{\psi\}_n^T e^{j(2\pi f_n \sqrt{1-\zeta_n^2})t} + Q_n^* \{\psi^*\}_n \{\psi^*\}_n^T e^{-j(2\pi f_n \sqrt{1-\zeta_n^2})t} \right), \tag{3}$$

where $\{\psi\}_n$ is the $N_{ema} \times 1$ mode shape vector for mode n; ζ_n is the modal damping ratio for mode n; f_n is the undamped system's eigenfrequency for mode n; Q_n is the modal scaling factor for mode n; and N_{ema} is the number of measured spatial positions.

The orthogonality of the extracted mode shapes $\{\psi\}_k$ and $\{\psi\}_l$ was examined using the Modal Assurance Criterion [17]:

$$MAC_{kl} = \frac{|\{\psi\}_k^T \{\psi\}_l|^2}{(\{\psi\}_k^T \{\psi\}_k)(\{\psi\}_l^T \{\psi\}_l)}. \tag{4}$$

The Modal Assurance Criterion can also be used to provide a measure of the correlation between the mode shapes estimated based, for instance, on a finite element model $\{\psi_{FEM}\}_k$, and the mode shapes that were estimated based on the experimental modal analysis $\{\psi_{EMA}\}_l$ according to:

$$MAC_{FEM_k,EMA_l} = \frac{|\{\psi_{FEM}\}_k^T\{\psi_{EMA}\}_l|^2}{(\{\psi_{FEM}\}_k^T\{\psi_{FEM}\}_k)(\{\psi_{EMA}\}_l^T\{\psi_{EMA}\}_l)}. \quad (5)$$

The parameters for the power spectral density estimation used when conducting the experimental modal analysis are summarized in Table 2.

Parameter	Value
Signal type	Burst random (90/10)
Excitation frequency range	0-1000 Hz
Sampling frequency, F_s	2560 Hz
Number of spectral lines, N	3201
Frequency resolution, Δf	0.3125 Hz
Number of averages	200
Window	Rectangular
Frequency range for curve fitting	400-600 Hz

Table 2: The modal analysis parameters.

2.4 System Identification

Non-parametric spectrum estimation may be utilized to produce non-parametric linear least-squares estimates of dynamic systems [18]. The frequency response function for a single-input single-out system may be estimated according to [18]:

$$\hat{H}(f_k) = \frac{\hat{P}_{yx}^{PSD}(f_k)}{\hat{P}_{xx}^{PSD}(f_k)}, \quad (6)$$

where $\hat{P}_{yx}^{PSD}(f_k)$ is the cross-power spectral density estimate between the input signal to the system and the output signal from the system; $\hat{P}_{xx}^{PSD}(f_k)$ is the power spectral density estimate of the input signal to the system; $f_k = \frac{Fs}{N}k$ $(k = 0, \ldots, N-1)$ is the discrete frequency and N is the block length. Estimates of the cross- and power spectral densities may be produced by using e.g., Welch's method [19].

The quality of the frequency response function estimate can be evaluated via the coherence function estimate $\hat{\gamma}_{yx}^2$ [18]:

$$\hat{\gamma}_{yx}^2(f_k) = \frac{|\hat{P}_{yx}^{PSD}(f_k)|^2}{\hat{P}_{xx}^{PSD}(f_k)\hat{P}_{yy}^{PSD}(f_k)}. \quad (7)$$

The parameters for the power spectral density estimation are given in Table 3.

Parameter	Value
Signal type	Continuous normally distributed random noise
Excitation frequency range	0-1000 Hz
Sampling frequency, F_s	2560 Hz
Number of spectral lines, N	3201
Frequency resolution, Δf	0.3125 Hz
Number of averages	200
Window	Hanning
Overlap	50 %

Table 3: The spectral density estimation parameters.

2.5 The "3-D" FE Model of an Active Boring Bar

Finite element modeling was used to predict the dynamic properties of active boring bars with different actuator positions. "3-D" finite element models of the system boring bar - actuator - clamping house were built using commercial finite element software MSC.MARC [20]. The initial "3-D" finite element model of the clamped boring bar included separate models of a boring bar and a clamping house interacting by means of frictionless contact, and a model of a piezoelectric actuator. The response at any node of the "3-D" mesh grid can be calculated based on this model.

The model of the system boring bar - clamping house consists of two sub-models: a sub-model of the boring bar and a sub-model of the clamping house. The sub-models are connected through what is termed "touching contact". As a basic finite element, a tetrahedron was chosen as the most convenient element to describe the geometric shape of the boring bar and the clamping house. The finite element model of the system boring bar - clamping house is shown in Fig. 4 a).

A "3-D" finite model of a piezoelectric actuator was developed. Thin layers of electrically active ceramic material connected in parallel were modeled as a stack of 8-noded bricks with piezoelectrical properties, i. e. besides three translational degrees of freedom, each node has a fourth degree of freedom: electric potential. The scheme of a "3-D" finite element model of the actuator is shown in Fig. 4 b). In FE modeling, the actuator material properties were chosen similar to the properties of the PZT-5H material, with modifications made for the strain coefficients d_{33} and d_{31} in order to match the specification for the maximum stroke of the actuator [13, 14]. Maximum stroke (free expansion of the actuator) is defined as $\Delta L = d_{33} n V(t)$, where n is the number of piezoelectric layers. To meet this specification, the length of a single layer should be 10^{-4} m. The thinness of this layer presents difficulties for FE modeling since the contact tolerance is too small. Thus, this contact tolerance is likely to result in poor estimates of the fundamental bending modes. This is why the number of layers was decreased 10 times to obtain the length of a single layer equal to 10^{-3} m while the corresponding strain constants were increased 10 times to meet the specification of the free expansion of the actuator.

The following mechanical boundary conditions were used: the nodal displacements on the surfaces of the clamping house, which correspond to the surfaces of the real clamping house attached to the turret, were set to zero in the $x-$, $y-$ and $z-$ directions.

The electrostatic boundary conditions were applied to the actuator (see Fig. 4 b)):

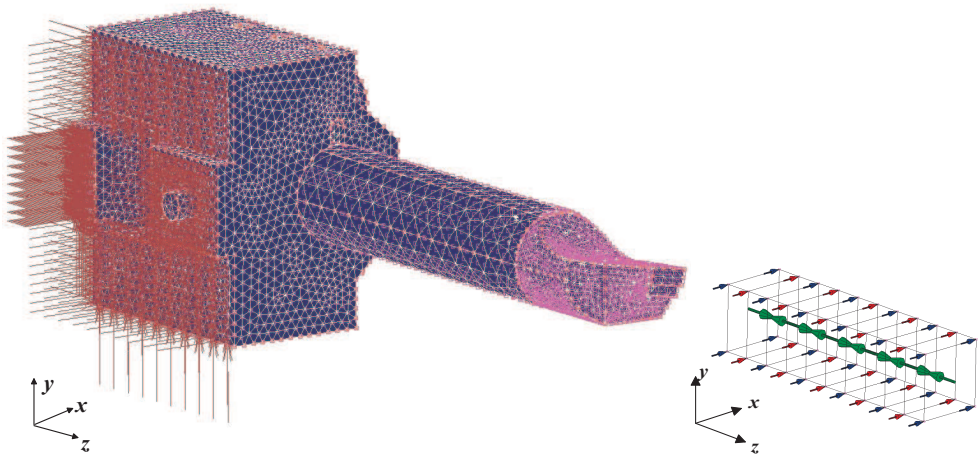

a) b)

Figure 4: a) The "3-D" finite element model of the system boring bar - clamping house and b) the sketch of a "3-D" finite element model of an actuator.

blue arrows show the nodes with applied negative or zero potential and red arrows correspond to the nodes with applied positive potential. Furthermore, the large green arrows show the material orientations within the finite elements.

Adequate modeling of the dynamic motion of the boring bar requires that the contact conditions between the boring bar, the clamping house and the clamping bolts are incorporated into the "3-D" finite element model.

A "3-D" deformable body is described by the "3-D" finite elements, and the nodes on its external surfaces are defined as potential contact nodes. The faces of the elements form the outer surfaces and are considered as potential contact segments. Contact tolerance was used to determine the distance below which bodies were considered to be in contact [20].

In harmonic response simulation, as well as in modal analysis, the contact detection occurs at the initial iteration and will define the contact used in this particular calculation. Therefore, the value of the contact tolerance is likely to influence the size of the modeled contact area between the boring bar and the clamping house. It is plausible that the larger contact tolerance will yield a larger contact area (compared to the default tolerance). This will naturally influence the estimates of the natural frequencies of the system. Therefore, it is of importance to investigate the influence of the value of the contact tolerance on the natural frequency estimates. The contact tolerance influence on the fundamental eigenfrequencies of the produced FE models was investigated for contact tolerances from the default value of $4.119 \times 10^{-5}\ m$ to $1 \times 10^{-4}\ m$.

2.6 Actuator Positions

Thirty six "3-D" FE models of the system boring bar - actuator - clamping house enabling variable contact between the boring bar, the clamping house and the clamping screws were developed with the actuator groove in different positions. The position of the actuator groove was varied in the longitudinal direction. The initial position of the actuator groove in the first model was denoted by p_1. In the second model, the actuator groove position was denoted by p_2 and located 0.055 m nearer to the insert in comparison to the first model. Finally, in the third model the actuator groove position was denoted p_3 and located 0.055 m nearer to the insert in comparison to the second model (see Fig. 5). Twelve different offset angles α between the negative cutting depth direction and the actuator radius which intersects the actuator center (see Fig. 5) was considered for each of these longitudinal positions.

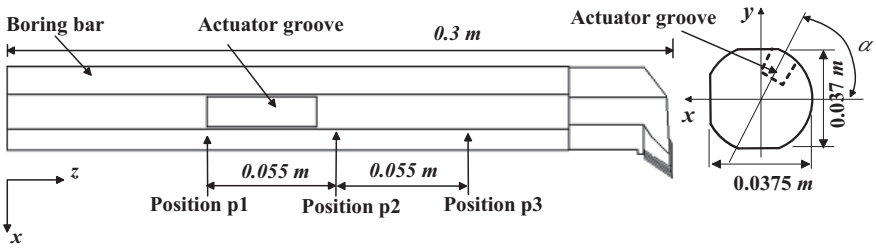

Figure 5: Schematic view of an active boring bar with the three positions of the actuator groove in the longitudinal direction of the bar. The figure also shows the boring bar cross section with the definition of the offset angle α of the actuator groove.

Another four FE models of the active boring bar were developed with the purpose of validating the prediction performance of the neural networks. Two models were developed with the longitudinal position p_4, located 0.0275 m nearer to the insert than the position p_1, and another two models with the position p_5, located 0.055 m nearer to the insert than the position p_4 (see Fig. 6). For each longitudinal position, two offset angles were considered: $\alpha = 45°$ and $\alpha = 225°$.

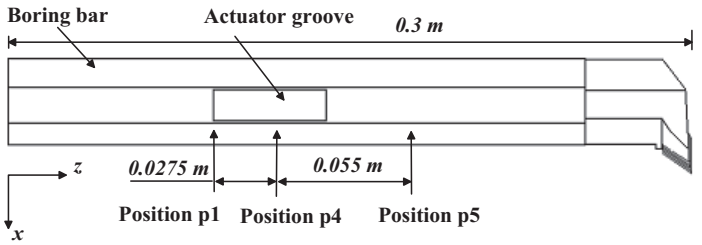

Figure 6: Schematic view of an active boring bar with the three positions of the actuator groove in the longitudinal direction of the bar.

2.7 Harmonic Analysis

The dynamic response of the finite element model of the active boring bar can be calculated e.g. by means of harmonic analysis. The solution process is based on the Fourier Transform of the equation of motion of the damped system, Eq. 8.

$$[\mathbf{M}]\{\ddot{\mathbf{w}}(t)\} + [\mathbf{C}]\{\dot{\mathbf{w}}(t)\} + [\mathbf{K}]\{\mathbf{w}(t)\} = \{\mathbf{f}(t)\}, \tag{8}$$

where $[\mathbf{M}]$ is the global $N_{fem} \times N_{fem}$ mass matrix of the system; $[\mathbf{K}]$ is the global $N_{fem} \times N_{fem}$ stiffness matrix of the system; $[\mathbf{C}]$ is the global $N_{fem} \times N_{fem}$ proportional damping matrix of the system; $\{\mathbf{w}(t)\}$ is the space- and time-dependent $N_{fem} \times 1$ displacement vector; $\{\mathbf{f}(t)\}$ is the space- and time-dependent $N_{fem} \times 1$ force vector and N_{fem} is the number of degrees-of-freedom of the finite element model.

The proportional damping matrix was calculated as follows:

$$[\mathbf{C}] = \beta_1[\mathbf{M}] + \beta_2[\mathbf{K}], \tag{9}$$

where the coefficients $\beta_1 = -134.147$ and $\beta_2 = 2.01279 \times 10^{-5}$ were calculated based on the relative damping coefficients estimated by experimental modal analysis of an active boring bar [11].

The Fourier Transform of Eq. 8 yields [21]:

$$((j2\pi f)^2[\mathbf{M}] + (j2\pi f)[\mathbf{C}] + [\mathbf{K}])\{\mathbf{W}(f)\} = \{\mathbf{F}(f)\}. \tag{10}$$

In this case, the excitation force vector $\{\mathbf{F}(f)\}$ is assumed to have a constant magnitude at all frequencies. Then, the displacement vector $\{\mathbf{W}(f)\}$ can be found by solving Eq. 10 for each frequency from a specified frequency range. Thus, the receptance frequency response function matrix $[\mathbf{H}_r(f)]$ is found as a ratio of the displacement $\{\mathbf{W}(f)\}$ and force $\{\mathbf{F}(f)\}$ vectors:

$$[\mathbf{H}_r(f)] = \frac{\{\mathbf{W}(f)\}}{\{\mathbf{F}(f)\}} = ((j2\pi f)^2[\mathbf{M}] + (j2\pi f)[\mathbf{C}] + [\mathbf{K}])^{-1}. \tag{11}$$

In the harmonic response simulations of the "3-D" finite element models, two cases of active boring bar excitation were considered. Firstly, an actuator excitation vector with a constant magnitude of 100 V at each discrete frequency in the analysis frequency range (see Table 4) was applied to the finite element model of the actuator. Secondly, an excitation force vector with a constant magnitude of 100 N at each discrete frequency in the analysis frequency range (see Table 4) was applied to the nodes of the "3-D" FE model. These nodes correspond to the error sensor position in the cutting speed direction and in the cutting depth directions (see Fig. 3).

The parameters for the frequency response function estimation used when utilizing harmonic analysis together with finite element modeling are given in Table 4.

Parameter	Value
Excitation frequency range	300-900 Hz
Number of spectral lines, N	1201
Frequency resolution, Δf	0.5 Hz

Table 4: The harmonic analysis parameters.

2.8 Positioning of the Actuator

The active boring bar is essentially a modified standard boring bar into which an actuator groove has been machined and into this groove a piezoceramic stack actuator has been placed. When designing an active boring bar, it is necessary to keep the geometrical shape identical to that of the standard boring bar it is based on, with exception for an electrical contact at the clamping end of the bar. Hence, if vibration problems occur with a standard boring bar, it may be replaced with an identical active boring bar without any significant modification of the lathe, etc. To manage the harsh environment in a lathe, e.g., metal chips, cutting fluids, etc., the actuator is embedded into the active boring bar.

A modification of a standard boring bar into an active boring bar results in an alteration of the boring bar's static stiffness and spatial dynamic properties. The resulting static stiffness and spatial dynamic properties, as well as the performance of the active boring bar, depend on factors such as the position and size of the actuator groove and the actuator material. Generally, vibration during internal turning is related to one of the two fundamental bending modes of the boring bar [22, 23]. The present work considers only actuator placements where the stack actuator's length direction is parallel with the longitudinal direction of the boring bar. Furthermore, the purpose of an active boring bar imposes limitations on the size and position of the actuator within the geometrical boundaries of the boring bar. To provide moment excitation of a fundamental boring bar bending mode, there must be a distance between the actuator centerline and the bar's natural axis. In addition to this, the two ends of an embedded stack actuator apply counteracting moment loads on the boring bar. Thus, to avoid counterproductive moment excitation of the fundamental boring bar bending modes, the actuator section might be positioned to include the area along the bar where these modes display the greatest bending deformation.

During machining, a cutting force $f(t)$ is generated between the tool and the workpiece as a result of the relative motion between the tool and the workpiece, both in the cutting speed direction and in the feed direction [22]. Generally, the cutting force $f(t)$ may be decomposed into three orthogonal force components: the primary cutting force acting in the cutting speed direction $f_v(t)$, the feed force acting in the feed direction $f_f(t)$, and the thrust force or radial force acting in the cutting depth direction $f_p(t)$ (see Fig. 7). During the internal turning operation, the primary cutting force and the thrust force will directly provide excitation of the two fundamental bending modes of the boring bar, while the feed force may provide moment excitation of these modes.

Let us assume that the cutting force $f(t)$ may be approximated as a point force, the point receptance functions in the cutting speed direction and in the cutting depth direction at the point where the primary cutting force is applied may be written:

$$H_{vv}(f) = \frac{W_v(f)}{F_v(f)} \tag{12}$$

and

$$H_{pp}(f) = \frac{W_p(f)}{F_p(f)}. \tag{13}$$

Here, f is the frequency in Hz; $F_v(f)$ is the Fourier transform of the primary cutting force; $W_v(f)$ is the frequency domain response of the active boring bar in the cutting speed direction in the point where the primary cutting force is applied; $F_p(f)$ is the Fourier transform of the thrust cutting force and $W_p(f)$ is the frequency domain

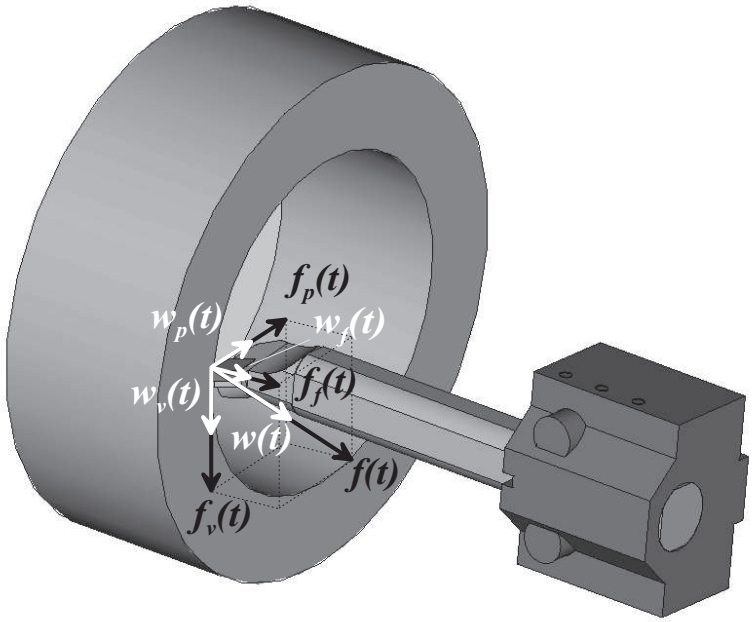

Figure 7: A clamped active boring bar.

response of a boring bar in the cutting depth direction in the point where the thrust force is applied.

Now, let us assume that the control path frequency functions for an active boring bar with an embedded piezostack actuator for the cutting speed direction and for the cutting depth direction are given by:

$$C_{va}(f) = \frac{W_v^a(f)}{U_a(f)} \tag{14}$$

and

$$C_{pa}(f) = \frac{W_p^a(f)}{U_a(f)}. \tag{15}$$

Here, $U_a(f)$ is the Fourier transform of the actuator input voltage signal; $W_v^a(f)$ is the actuator induced frequency domain response of the active boring bar in the cutting speed direction in the point where the primary cutting force is applied and $W_p^a(f)$ is the actuator induced frequency domain response of the active boring bar in the cutting depth direction in the point where the thrust force is applied.

To cancel the motion of the boring bar at the eigenfrequencies of the boring bar's fundamental bending modes excited by the primary cutting force, with the eigenfrequencies f_1 and f_2 in the cutting speed direction, it is required that:

$$C_{va}(f_i)U_a(f_i) + H_{vv}(f_i)F_v(f_i) = 0,\ i \in \{1, 2\}. \tag{16}$$

Let $(z, \alpha),\ z \in [z_l, z_u]$ and $\alpha \in [\alpha_l, \alpha_u]$ be the feasible actuator positions for a certain actuator size. Here, z is the actuator coordinate in the z-direction and it

refers to the actuator end closest to the clamping end of the boring bar, while α is the actuator offset angle (see Fig. 5). Now, for each feasible actuator position (z, α), assume the corresponding feasible control path frequency function $C_{va}(f, z, \alpha)$. Let $f_1 \leqslant f_2$, where f_1 is the eigenfrequency of the boring bar's fundamental bending mode with the lowest frequency value. Here, both f_1 and f_2 are likely to depend on the actuator position (z, α), i.e. $f_1(z, \alpha)$ and $f_2(z, \alpha)$. **Observe, in the text below, f_1 and f_2 will be used instead of $f_1(z, \alpha)$ and $f_2(z, \alpha)$ as notations for the the actuator position dependent eigenfrequencies of active boring bar's fundamental bending modes.**

For instance, for a certain actuator size, what actuator position or positions (z, α) enable the cancelation of the boring bar response in the cutting speed direction for the greatest primary cutting force at the lowest bending eigenfrequency $f_1(z, \alpha)$? Or in other words, what actuator position or positions (z, α) result in the greatest boring bar resistance for the cutting force excitation in the cutting speed direction at the eigenfrequency $f_1(z, \alpha)$? Assume that the actuator induced boring bar response perfectly cancels the response of an active boring bar excited by the primary cutting force in the cutting speed direction at the eigenfrequency $f_1(z, \alpha)$. In this case, the actuator position or set of actuator positions$\{(z_o, \alpha_o)\}$ that maximize the function

$$S_1(z, \alpha) = \left| \frac{C_{va}(f_1, z, \alpha)}{H_{vv}(f_1, z, \alpha)} \right|, \; z \in [z_l, z_u], \alpha \in [\alpha_l, \alpha_u], \tag{17}$$

provide the greatest boring bar stiffness for the cutting force excitation in the cutting speed direction at the eigenfrequency f_1.

If we consider cancelation of the motion of the boring bar excited by the primary cutting force at the eigenfrequencies of the boring bar's fundamental bending modes f_1 and f_2, in the cutting speed direction, we have a situation where:

$$\begin{bmatrix} C_{va}(f_1, z, \alpha) & 0 \\ 0 & C_{va}(f_2, z, \alpha) \end{bmatrix} \begin{Bmatrix} U_a(f_1) \\ U_a(f_2) \end{Bmatrix} + \\ \begin{bmatrix} H_{vv}(f_1, z, \alpha) & 0 \\ 0 & H_{vv}(f_2, z, \alpha) \end{bmatrix} \begin{Bmatrix} F_v(f_1) \\ F_v(f_2) \end{Bmatrix} = 0. \tag{18}$$

By introducing matrix notation, this may be written more concisely as:

$$[\mathbf{C}_{va}(z, \alpha)]\{\mathbf{U}_a\} + [\mathbf{H}_{vv}(z, \alpha)]\{\mathbf{F}_v\} = 0. \tag{19}$$

Assuming that the matrix of point receptances in the cutting speed direction $[\mathbf{H}_{vv}(z, \alpha)]$ is non-singular, the primary force component vector $\{\mathbf{F}_v\}$ may be expressed as:

$$-[\mathbf{H}_{vv}(z, \alpha)]^{-1}[\mathbf{C}_{va}(z, \alpha)]\{\mathbf{U}_a\} = \{\mathbf{F}_v\}. \tag{20}$$

The squared $\mathcal{L}_2$ norm of the vector $\{\mathbf{F}_v\}$ may be written as:

$$\|\{\mathbf{F}_v\}\|_2^2 = \{\mathbf{U}_a\}^H[\mathbf{C}_{va}(z, \alpha)]^H([\mathbf{H}_{vv}(z, \alpha)]^{-1})^H[\mathbf{H}_{vv}(z, \alpha)]^{-1}[\mathbf{C}_{va}(z, \alpha)]\{\mathbf{U}_a\} = \\ = \left| \frac{C_{va}(f_1, z, \alpha)}{H_{vv}(f_1, z, \alpha)} \right|^2 |U_a(f_1)|^2 + \left| \frac{C_{va}(f_2, z, \alpha)}{H_{vv}(f_2, z, \alpha)} \right|^2 |U_a(f_2)|^2. \tag{21}$$

An objective function for selecting the actuator position may now be produced as:

$$S_2(z, \alpha) = \left| \frac{C_{va}(f_1, z, \alpha)}{H_{vv}(f_1, z, \alpha)} \right|^2 \beta_1 + \left| \frac{C_{va}(f_2, z, \alpha)}{H_{vv}(f_2, z, \alpha)} \right|^2 \beta_2, \; z \in [z_l, z_u], \alpha \in [\alpha_l, \alpha_u], \tag{22}$$

where β_1 and β_2 are real and positive weighting factors such that $\beta_1, \beta_2 \in [0,1]$. Depending on the stiffness requirements for the respective fundamental mode in the cutting process, the values of the weighting factors may be selected. An actuator position (z_o, α_o) that maximize this function may be selected as favorable. The weighting factors may be selected depending on the stiffness requirements for the respective fundamental mode during machining.

Now, if it is desired to cancel the motion of the boring bar excited by the primary cutting force and the thrust force simultaneously at the eigenfrequencies of the boring bar's fundamental bending modes, with the eigenfrequencies f_1 and f_2, in the cutting speed direction, in other words

$$\begin{bmatrix} C_{va}(f_1,z,\alpha) & 0 \\ 0 & C_{va}(f_2,z,\alpha) \end{bmatrix} \begin{Bmatrix} U_a(f_1) \\ U_a(f_2) \end{Bmatrix} + \tag{23}$$

$$\begin{bmatrix} H_{vv}(f_1,z,\alpha) & 0 & H_{vp}(f_1,z,\alpha) & 0 \\ 0 & H_{vv}(f_2,z,\alpha) & 0 & H_{vp}(f_2,z,\alpha) \end{bmatrix} \begin{Bmatrix} F_v(f_1) \\ F_v(f_2) \\ F_p(f_1) \\ F_p(f_2) \end{Bmatrix} = 0,$$

where $H_{vp}(f_1)$ and $H_{vp}(f_2)$ are the transfer receptances between the cutting depth and the cutting speed directions. Equation 23 may, in terms of matrix notation, be written as

$$[\mathbf{C}_{va}(z,\alpha)]\{\mathbf{U}_a\} + [\mathbf{H}_{v,p}(z,\alpha)]\{\mathbf{F}_{v,p}\} = 0. \tag{24}$$

Assuming that the matrix of control paths $[\mathbf{C}_{va}(z,\alpha)]$ is non-singular, the vector with actuator input signal components $\{\mathbf{U}_a\}$ is related to the force component vector $\{\mathbf{F}_{v,p}\}$ as:

$$\{\mathbf{U}_a\} = -[\mathbf{C}_{va}(z,\alpha)]^{-1}[\mathbf{H}_{v,p}(z,\alpha)]\{\mathbf{F}_{v,p}\}. \tag{25}$$

The squared $\mathcal{L}_2$ norm of the vector with actuator input signal components $\{\mathbf{U}_a\}$ can be written as:

$$\|\{\mathbf{U}_a\}\|_2^2 = \{\mathbf{F}_{v,p}\}^H[\mathbf{H}_{v,p}(z,\alpha)]^H([\mathbf{C}_{va}(z,\alpha)]^{-1})^H[\mathbf{C}_{va}(z,\alpha)]^{-1}[\mathbf{H}_{v,p}(z,\alpha)]\{\mathbf{F}_{v,p}\}. \tag{26}$$

An upper bound for $\|\{\mathbf{U}_a\}\|_2^2$ is given by [24, 25]:

$$\|\{\mathbf{U}_a\}\|_2^2 \leqslant \sigma_1^2(z,\alpha)\|\{\mathbf{F}_{v,p}\}\|_2^2, \tag{27}$$

where $\sigma_1(z,\alpha)$ is the greatest singular value of the matrix $[\mathbf{C}_{va}(z,\alpha)]^{-1}[\mathbf{H}_{v,p}(z,\alpha)]$. A guiding objective function for selecting actuator position may now be written as:

$$S_3(z,\alpha) = \sigma_1^2(z,\alpha). \tag{28}$$

An actuator position (z_o, α_o) that minimize this function may be selected.

In reality, however, continuous system models are generally not used to provide accurate models of a clamped active boring bar [11, 26]. Suppose that Q "3-D" FE models of the system boring bar - actuator - clamping house with different actuator positions (z_q, α_q), $q \in \{1, 2, \ldots, Q\}$ have been developed. For each of the Q "3-D" FE models, estimates of the point receptance functions $\hat{H}_{vv}(f, z_q, \alpha_q)$, $\hat{H}_{pp}(f, z_q, \alpha_q)$ and transfer receptance functions $\hat{H}_{pv}(f, z_q, \alpha_q)$, $\hat{H}_{pv}(f, z_q, \alpha_q)$ as well as the control path frequency functions $\hat{C}_{va}(f, z_q, \alpha_q)$, $\hat{C}_{pa}(f, z_q, \alpha_q)$, may be produced based on dynamic response simulations. To select a suitable actuator position (z_o, α_o), one of

the objective functions in Eqs. 17 and 22 may be utilized. By e.g. replacing the point receptance functions and control path frequency functions with the corresponding estimates of them for each of the Q "3-D" FE models of the system boring bar - actuator - clamping house in the selected objective function, Q objective function expressions are produced. For instance, if the objective function S_2 in Eq. 22 is selected, we get:

$$S_2(q) = \left| \frac{\hat{C}_{va}(f_{1q}, z_q, \alpha_q)}{\hat{H}_{vv}(f_{1q}, z_q, \alpha_q)} \right|^2 \beta_1 + \left| \frac{\hat{C}_{va}(f_{2q}, z_q, \alpha_q)}{\hat{H}_{vv}(f_{2q}, z_q, \alpha_q)} \right|^2 \beta_2, \; q \in \{1, 2, \ldots, Q\}. \tag{29}$$

Here, f_{1q} and f_{2q} are used instead of $f_1(z_q, \alpha_q)$ and $f_2(z_q, \alpha_q)$ as notations for the estimates of the actuator position dependent eigenfrequencies of active boring bar's fundamental bending modes produced based on Q FE models. Furthermore, for the objective function S_3 in Eq. 28 we obtain:

$$S_3(q) = \hat{\sigma}_1^2(z_q, \alpha_q), \; q \in \{1, 2, \ldots, Q\}, \tag{30}$$

where $\hat{\sigma}_1(z_q, \alpha_q)$ is the greatest singular value of the matrix $[\hat{\mathbf{C}}_{va}(z_q, \alpha_q)]^{-1}[\hat{\mathbf{H}}_{v,p}(z_q, \alpha_q)]$.

2.9 Neural Networks for Surface Fitting

The dynamic properties of an active boring bar with an arbitrary actuator position may be estimated based on its finite element model. Thus, a set of FE models of an active boring bar for different actuator positions may be produced. By utilizing a suitable method for nonlinear interpolation between the dynamic properties (such as the peak magnitude of the control path frequency functions, the receptance functions, etc., at a certain eigenfrequency), calculated based on the set of FE models of active boring bars with different actuator positions, the dynamic properties of active boring bars with actuator positions in between the FE models from this set may be estimated. A multilayer perceptron neural network (MLP NN) may be utilized for the interpolation task.

A neural network can be viewed as a nonlinear mapping of the input into the output and should be designed to perform a good generalization, i.e. nonlinear interpolation between the data available to train the network [27]. There are two essential factors that influence good generalization of the neural network: the size and choice of the training data and the architecture of the neural network. The architecture of a MLP NN may be described by the number of inputs, the number of outputs, the number of hidden neurons and the number of hidden layers. As an example, a three-layer MLP NN, also referred to as a two-hidden-layer network, is shown in Fig. 8.

Here, the input to the first layer is a vector containing the measured data and a bias stimuli $[x_1, \ldots, x_n, 1]^T$; n is the number of inputs to the neural network; m is the number of computational units in the first hidden layer; k is the number of computational units in the second hidden layer; p is the number of outputs of the neural network; $[\mathbf{W}]^{[1]}$, $[\mathbf{W}]^{[2]}$ and $[\mathbf{W}]^{[3]}$ are matrices containing the synaptic weights [27]; $g(\cdot)$ is an activation function, (usually a sigmoidal function which performs a nonlinear transformation between the input to the activation function and its output); y_1, ..., y_p is the outcome of the output layer that represents a prediction produced by the MPL NN; and e_1, ..., e_p are the errors calculated as a difference between the

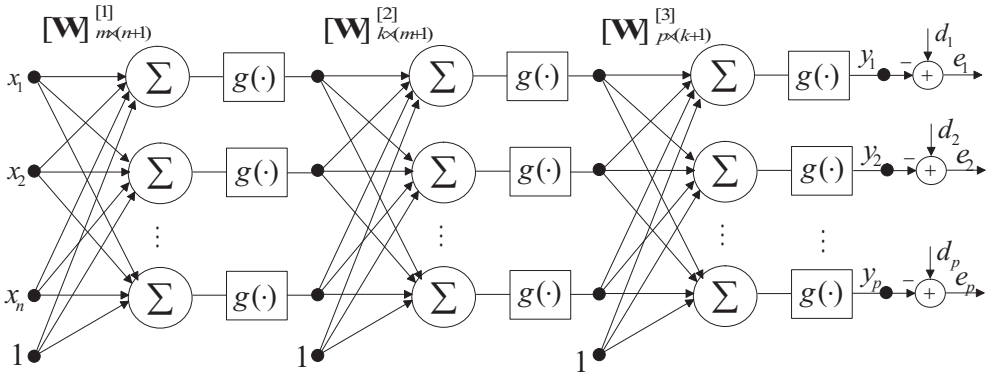

Figure 8: Architecture of a three-layer neural network.

measured or known values of the function d_1, ..., d_p and the predictions made by the MLP NN, i.e., $e_i = d_i - y_i$, where $i = 1, \ldots, p$. Training is performed based on a set of training examples $(x_1^l, x_2^l, \ldots, x_n^l; d_1^l, d_2^l, ..., d_p^l)$, where $l = 1, \ldots, L_{examples}$.

The task of the neural network is to interpolate, at a certain eigenfrequency, between the peak magnitudes of the frequency functions for FE models of an active boring bar with different actuator positions. Thus, the inputs to the network consist of the longitudinal position of the actuator z_q, the actuator offset angle α_q and the bias factor. A single peak value of a frequency function at a certain eigenfrequency, produced based on the FE model with the position $q = (z_q, \alpha_q)$, is used at the output of the neural network as the measured value d. Thirty six "3-D" finite element models of the system boring bar - actuator - clamping house have been developed and each of these provides a training example so that the number of training examples $L = 36$. This means that the number of inputs to the network is $I = 2$, while the number of outputs is $P = 1$. To define the network's architecture, it is therefore necessary to determine the number of hidden neurons and the number of hidden layers. The total number of weights W for the network can be calculated as: $W = (I+1)\times J+(J+1)\times P$, where I is the number of inputs, J is the number of hidden neurons, and P is the number of outputs. On the other hand, the number of weights can be calculated based on the number of training examples L and the accuracy parameter ε as $L = W/\varepsilon$ [27]. The value of an accuracy parameter equal to 0.1 corresponds to a 90% accuracy in prediction made by the MLP NN. For instance, a prediction with an accuracy parameter in the interval $0.1 \leqslant \varepsilon \leqslant 1$ can be made by the MLP NN if the number of training examples is within the interval $W \leqslant L \leqslant 10W$. Hence, the number of hidden neurons may be selected within the interval $0 \leqslant J \leqslant 8$. Two hidden layers are usually sufficient to approximate any desired, bounded continuous function [28]. Networks with six or eight hidden neurons and two hidden layers were designed and applied in the interpolation. These networks were trained using the Levenberg-Marquardt training algorithm. The activation functions at the two hidden layers were hyperbolic tangent functions and a linear function at the output layer. In Table 5 the parameters for the selected MLP NNs are given.

As a stopping parameter in the training procedure, the maximum number of epochs was used (where an epoch is a cycle of training the network with a given training set). The training data was normalized to assume a maximum magnitude

of 1. As a measure of the training performance of the MLP NN, the mean squared error (MSE) between the training data and the prediction made by the MLP NN is reported in Table 5. The neural networks interpolated peak magnitudes of the control path frequency functions and the point receptance functions for $\Theta = 3600$ actuator positions (3564 new actuator positions) $(z_\theta, \alpha_\theta)$, $\theta \in \{1, 2, \ldots, \Theta\}$ where the original 36 actuator positions (z_q, α_q), $q \in \{1, 2, \ldots, Q\}$ are a subset of these.

The neural networks specifications are given in the Table 5 (*To simplify the notations* $f_{1\theta} = f_1(z_\theta, \alpha_\theta)$ *and* $f_{2\theta} = f_2(z_\theta, \alpha_\theta)$).

Type of predicted output	Network's architecture	Number of epochs	Performance measure MSE
$\lvert\hat{C}_{va}(f_{1\theta}, z_\theta, \alpha_\theta)\rvert$	2-5-3-1	3000	9.98676×10^{-6}
$\lvert\hat{C}_{va}(f_{2\theta}, z_\theta, \alpha_\theta)\rvert$	2-5-3-1	3000	2.98813×10^{-4}
$\lvert\hat{C}_{pa}(f_{1\theta}, z_\theta, \alpha_\theta)\rvert$	2-5-3-1	3000	1.41963×10^{-4}
$\lvert\hat{C}_{pa}(f_{2\theta}, z_\theta, \alpha_\theta)\rvert$	2-5-3-1	3000	1.62106×10^{-5}
$\lvert\hat{H}_{vv}(f_{1\theta}, z_\theta, \alpha_\theta)\rvert$	2-5-3-1	3000	2.46820×10^{-3}
$\lvert\hat{H}_{vv}(f_{2\theta}, z_\theta, \alpha_\theta)\rvert$	2-5-3-1	3000	6.65616×10^{-6}
$\lvert\hat{H}_{pp}(f_{1\theta}, z_\theta, \alpha_\theta)\rvert$	2-4-2-1	3000	1.47418×10^{-3}
$\lvert\hat{H}_{pp}(f_{2\theta}, z_\theta, \alpha_\theta)\rvert$	2-5-3-1	3000	3.35156×10^{-4}

Table 5: The neural networks specifications.

Cross-validation is often used to estimate the generalization ability of the neural network [27, 28]. One approach to cross-validation is the "hold out" method. The validation of the trained networks was based on the "hold out" method. However, only the training set and the test set were used, and the training set was not divided into subsets. The performance of the networks was validated based on the test set that consisted of four actuator positions (10% of the training set).

3 Results

The results are presented in the following order: first, the influence of the contact tolerance used in the FE modeling of the active boring bars on the natural frequency estimates is reported. Second, the control path frequency response functions and the point receptance functions for the thirty six "3-D" FE models of the active boring bars with different actuator positions are presented. Third, the peak control path frequency function magnitude and the peak point receptance function magnitude at the fundamental eigenfrequencies of the boring bar estimated by means of the MLP NN are discussed. Fourth, suggestions of suitable actuator positions for an active boring bar are given based on the objective functions S_2 and S_3 using magnitude values for the control path frequency functions, point and transfer receptance functions based on the "3-D" finite element models. Suggestions concerning suitable actuator positions were also given using the objective function S_2 for MLP NN interpolated magnitude values of the control path frequency functions and the point receptance functions. Finally, the dynamic properties of an active boring bar prototype, with an actuator at a position suggested by the actuator positioning method, are compared to the corresponding estimates produced with the help of the "3-D" FE model.

3.1 Influence of the Contact Tolerance on the Natural Frequency Estimates

In order to investigate the sensitivity of the natural frequency estimates to the variation in contact tolerance, the first three natural frequencies were calculated for the thirty six "3-D" FE models using the different contact tolerance values: 1×10^{-5} m, 2×10^{-5} m, 3×10^{-5} m, ..., 1×10^{-4} m, as well as the default contact tolerance 4.112×10^{-5} m. The results of the calculations using the default contact tolerance 4.112×10^{-5} m, as well as 6×10^{-5} m and 1×10^{-4} m, are shown in Fig. 9.

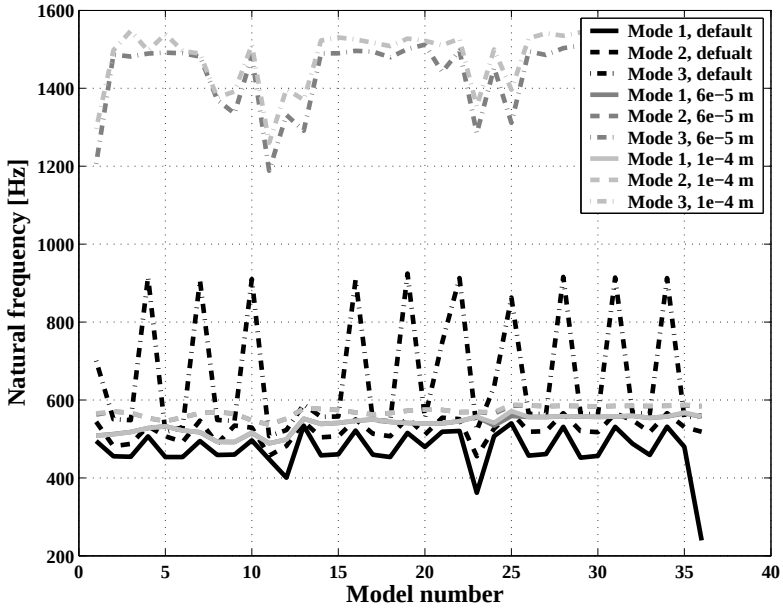

Figure 9: The estimates of the first three natural frequencies calculated for the thirty six "3-D" FE models using the default contact tolerance, a contact tolerance of 6×10^{-5} m and a contact tolerance of 1×10^{-4} m, respectively.

From Fig. 9, it can be observed that the first three natural frequencies for a number of models with the default contact tolerance are in the frequency range of 400 Hz and 600 Hz. However, the third natural frequency should correspond to a torsional mode, located substantially higher up in the frequency range. A contact tolerance of 6×10^{-5} m was selected for the simulations.

3.2 Prediction of Suitable Actuator Positions in an Active Boring Bar

3.2.1 Control Path Frequency Functions and Point Receptance Functions

In order to use the objective functions in Eqs. 17, 22 and 28 to provide suggestions for suitable actuator positions, the control path frequency functions and the point respective transfer receptance functions have been estimated for the thirty six "3-D" finite element models. The control path frequency functions between the actuator voltage and the displacement in the cutting speed direction at the nodes of the FE

models that correspond to the error sensor position for the measurement in the cutting speed direction and the displacement in the cutting depth direction at the nodes of the FE models that correspond to the error sensor position for the measurement in the cutting depth direction were estimated.

The magnitude and phase functions of the control path frequency functions for the active boring bar models with the actuator offset angle $\alpha = 0°$ and the longitudinal actuator positions p_1, p_2 and p_3 are shown in Figs. 10 a) and b). The magnitude and phase functions of the control path frequency functions for the active boring bar models with the actuator offset angle $\alpha = 240°$ and the longitudinal actuator positions p_1, p_2 and p_3 are shown in Figs. 10 c) and d).

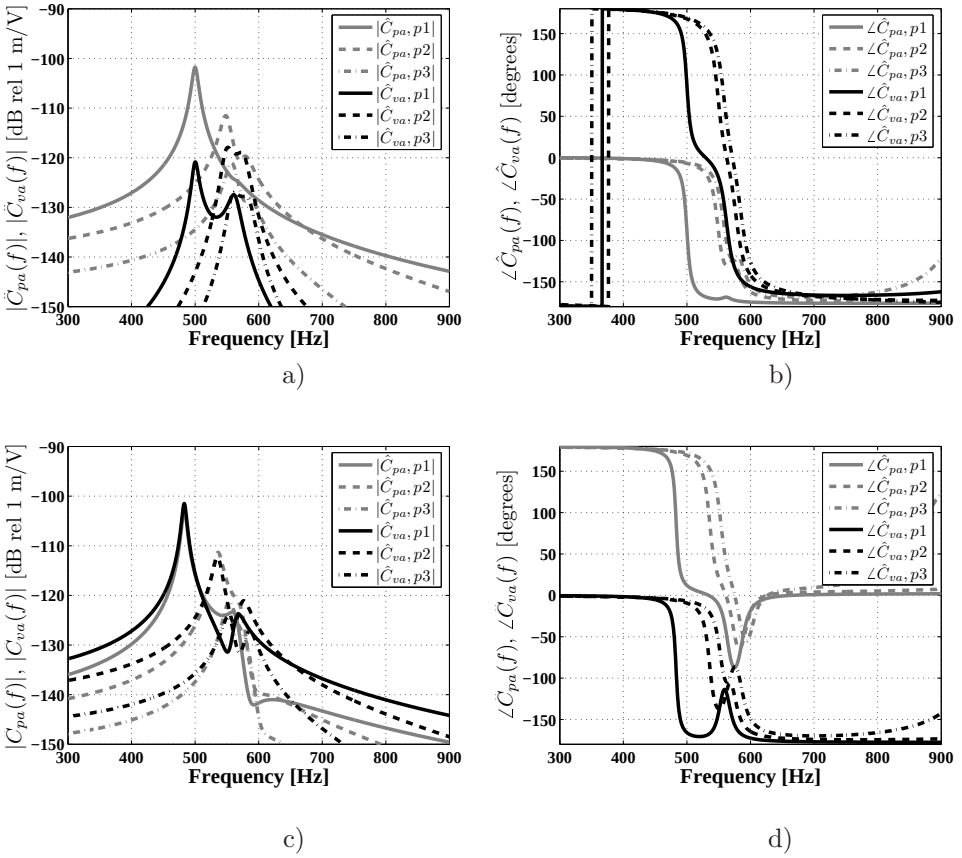

Figure 10: The control path frequency function estimates for the active boring bar "3-D" FE models, between the actuator voltage and the displacement in the cutting speed direction and the displacement in the cutting depth direction at the active boring bar error sensor positions. a) shows the magnitude functions and b) shows the phase functions for the actuator offset angle $\alpha = 0°$ and the longitudinal actuator positions p_1, p_2 and p_3. c) shows the magnitude functions and d) shows the phase functions for the actuator offset angle $\alpha = 240°$ and the longitudinal actuator positions p_1, p_2 and p_3.

The point receptance function estimates for the "3-D" FE models of the active

boring bars in the cutting speed direction, at the error sensor position for measurement in the cutting speed direction, and in the cutting depth direction at the error sensor position for measurement in the cutting depth direction, were produced. Also, the transfer receptance function estimates for the FE models between the cutting speed direction and the cutting depth direction at the error sensor positions were produced. The magnitude and phase functions of the point receptance functions for the active boring bar models with the actuator offset angles $\alpha = 0°$ and $\alpha = 240°$ and the longitudinal actuator positions p_1, p_2 and p_3, are shown in Figs. 11.

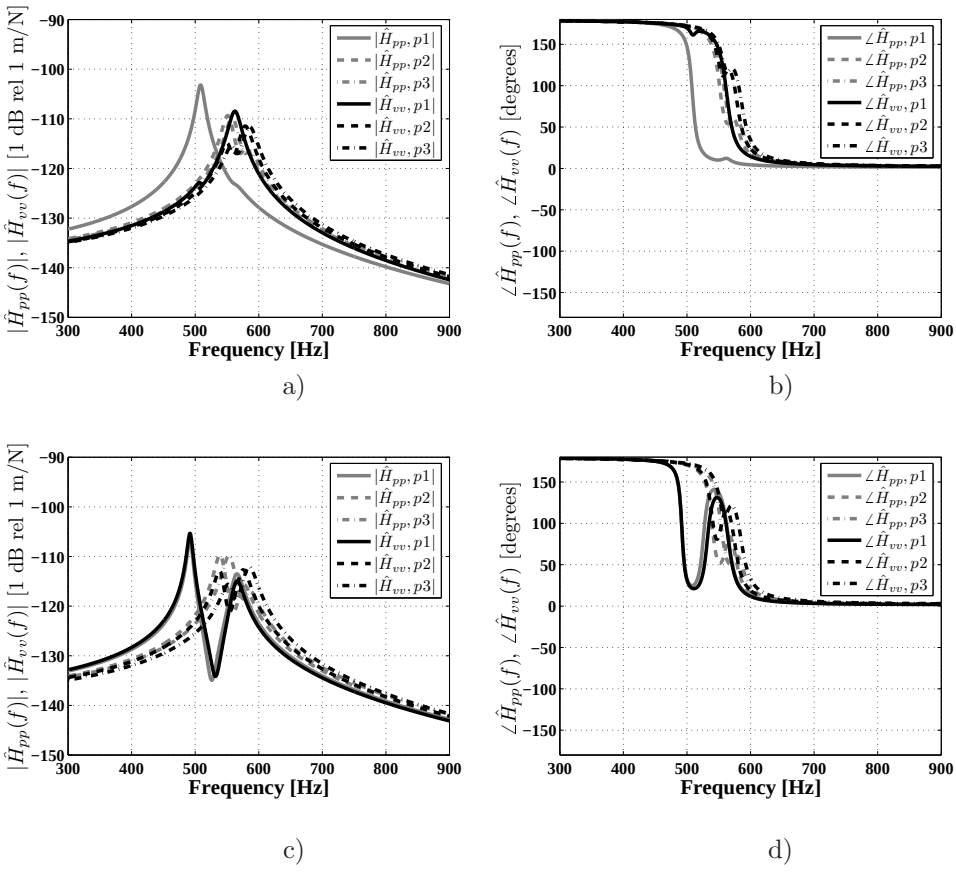

Figure 11: The point receptance function estimates for the nodes of the "3-D" FE models of the active boring bars corresponding to the error sensor position in the cutting speed direction and in the cutting depth direction. a) shows the magnitude functions and b) shows the phase functions for the actuator offset angle $\alpha = 0°$ and the longitudinal actuator positions p_1, p_2 and p_3. c) shows the magnitude functions and d) shows the phase functions for the actuator offset angle $\alpha = 240°$ and the longitudinal actuator positions p_1, p_2 and p_3.

In Fig. 9, Figs. 10 and Figs. 11, it can be observed that different actuator positions in the active boring bar FE models result in different eigenfrequencies of the fundamental boring bar's bending modes. It also follows that the magnitude levels of both the control path frequency functions and the point receptance functions in

the areas of the fundamental boring bar's eigenfrequencies vary for different actuator positions in the active boring bar FE models.

For the objective functions described by Eqs. 17 and 22, the only relevant values are those that pertain to the control path frequency functions and the point receptance functions for the frequency of the first bending mode f_{1q} and/or for the frequency of the second bending mode f_{2q}, for respective"3-D" FE model of the active boring bars. *It should be observed that in order to simplify the notations,* $f_{1q} = f_1(z_q, \alpha_q)$ *and* $f_{2q} = f_2(z_q, \alpha_q)$ *are introduced.*

Figure 12 a) shows a "3-D" surface plot of the control path frequency function magnitude estimates between the actuator voltage and the displacement at the node of the FE models corresponding to the the error sensor position in the cutting speed direction for the respective "3-D" FE model at the frequencies of the first bending mode f_{1q}. Figure 12 b) shows the corresponding "3-D" surface plot of the control path frequency function magnitude estimates in the cutting speed direction for the respective "3-D" FE model at the frequencies of the second bending f_{2q} mode. Moreover, the variations in the control path frequency function magnitude at the frequencies of the first bending mode f_{1q} and at the frequencies of the second bending mode f_{2q} can be observed in Fig. 12.

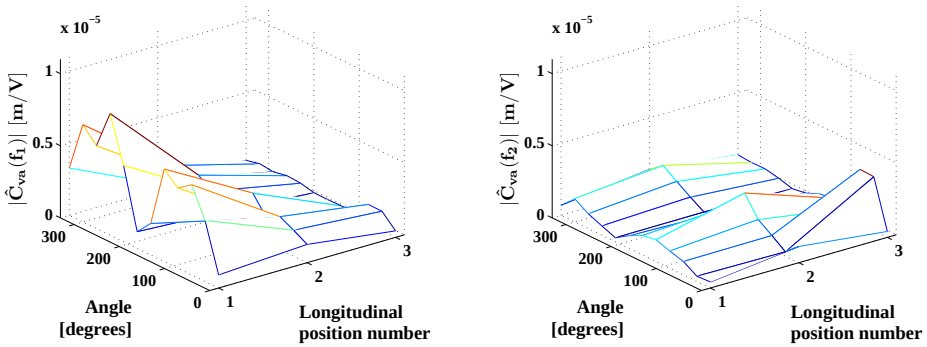

Figure 12: "3-D" surface plots of the control path frequency function magnitude estimates between the actuator voltage and the displacement signals collected at the nodes of the "3-D" FE models of the active boring bars corresponding to the error sensor position a) in the cutting speed direction at the frequencies of the first bending mode f_{1q} and b) in the cutting speed direction at the frequencies of the second bending mode f_{2q}. The longitudinal actuator positions shown are p_1, p_2 and p_3, and the actuator offset angles are $\alpha : 0°, 30°, 60°, \ldots, 330°$.

Figure 13 a) shows a "3-D" surface plot of the point receptance magnitude function estimates for the "3-D" FE models of the active boring bars in the cutting speed direction at the error sensor position for the measurement in the cutting speed direction at the frequencies of the first bending mode f_{1q}. Figure 13 b) illustrates the corresponding "3-D" surface plot of the point receptance magnitude function estimates for the frequencies of the second bending mode f_{2q}.

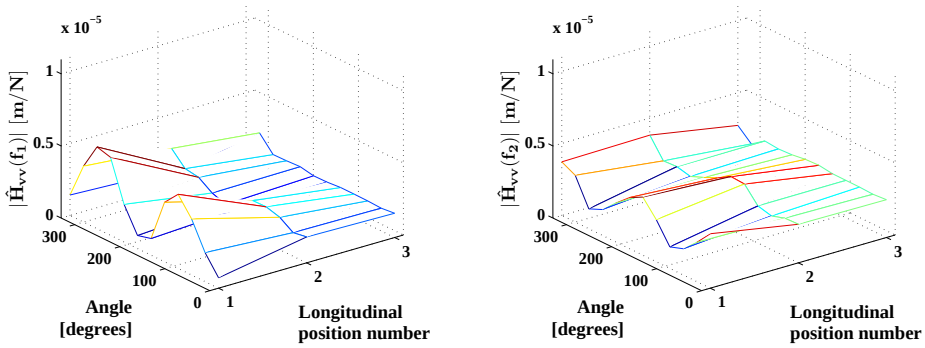

Figure 13: "3-D" surface plots the point receptance magnitude function estimates between the excitation force and the displacement signals collected at the nodes of the "3-D" FE models of the active boring bars corresponding to the error sensor position in the cutting speed direction at the frequencies of the first bending mode f_1q and b) in the cutting speed direction at the frequencies of the second bending mode f_2q. The longitudinal actuator positions shown are p_1, p_2 and p_3, and the offset angles are $\alpha : 0°, 30°, 60°, \ldots, 330°$.

3.2.2 Interpolation of the Control Path Frequency Functions and the Point Receptance Functions Magnitudes Using Neural Networks

To increase the spatial resolution in the prediction of the actuator position in a boring bar, produced using the suggested objective functions, nonlinear interpolations between the peak magnitudes of the control path frequency functions and the point receptance functions for the respective "3-D" FE models of the active boring bars were carried out using multilayer perceptron neural networks (MLP NN:s). Basically, for the cutting speed direction, one interpolation was carried out between the control path frequency function magnitudes of the "3-D" FE models at their respective frequency of the first bending mode f_{1q}. Another interpolation was carried out between the control path frequency function magnitudes of the "3-D" FE models at their respective frequency of the second bending mode f_{2q}. Similar interpolations of the control path frequency function magnitudes were carried out for the cutting depth direction. Furthermore, for the cutting speed direction, one interpolation was carried out between the point receptance magnitude functions of the "3-D" FE models at their respective frequency of the first bending mode f_{1q}. Another interpolation was carried out between the point receptance frequency function magnitudes of the "3-D" FE models at their respective frequency of the second bending mode f_{2q}. This procedure was repeated for the point receptance frequency function magnitudes in the cutting depth direction.

Eight neural networks were built. Four networks were constructed to interpolate between the peak magnitudes of the control path frequency functions both in the cutting speed direction and in the cutting depth direction. Another four networks were designed to interpolate between the peak magnitudes of the point receptance magnitude functions both in the cutting speed direction and in the cutting depth di-

rection. *It should be observed that in order to simplify the notations,* $f_{1\theta} = f_1(z_\theta, \alpha_\theta)$ *and* $f_{2\theta} = f_2(z_\theta, \alpha_\theta)$ *have been introduced.* Figure 14 a) shows a "3-D" surface plot of the normalized control path frequency function magnitude for the cutting speed direction produced by means of a neural network at the frequencies of the first bending mode $f_{1\theta}$. Figure 14 b) illustrates the corresponding "3-D" surface plot of the normalized control path frequency function magnitude for the cutting speed direction at the frequencies of the second bending mode $f_{2\theta}$.

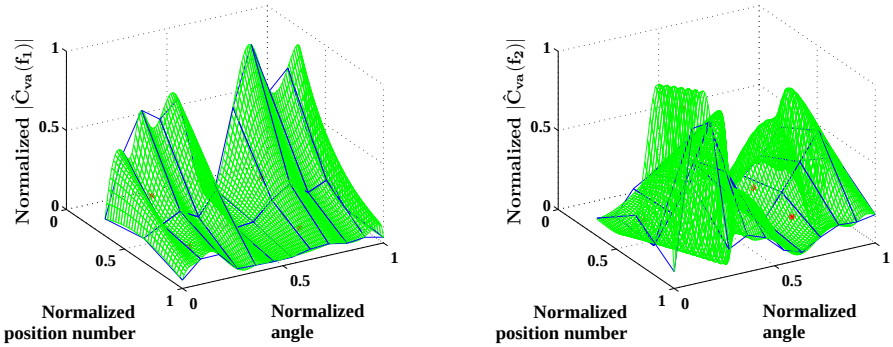

a) b)

Figure 14: "3-D" surface plots of the normalized control path frequency function magnitude a) in the cutting speed direction at the frequencies of the first bending mode $f_{1\theta}$ and b) in the cutting speed direction at the frequency of the second bending mode $f_{2\theta}$. Blue lines are used for the values calculated based on the thirty six "3-D" FE models, and green lines are used for the values predicted by the trained neural networks. Red stars represent the values from the test set of the "3-D" FE models.

Figure 15 a) shows a "3-D" surface plot of the normalized point receptance magnitude function estimates for the cutting speed direction predicted by means of the neural network at the frequencies of the first bending mode $f_{1\theta}$. Figure 15 b) illustrates the corresponding "3-D" surface plot of the normalized point receptance magnitude function estimates for the cutting speed direction at the frequencies of the second bending mode $f_{2\theta}$.

3.2.3 Actuator Positions

Suitable actuator positions for an active boring bar were investigated based on the thirty six "3-D" FE models using the objective function S_2 in Eq. 29. To provide suggestions on actuator positions, this objective function was utilized both for the cutting speed direction and for the cutting depth direction. In Fig. 16 a) the square root of the objective function $S_2(z_q, \alpha_q)$ for the cutting speed direction is shown and in Fig. 16 b) the square root of the objective function $S_2(z_q, \alpha_q)$ for the cutting depth direction is shown. The values of the weighting factors used were $\beta_1 = 1$ and $\beta_2 = 1$.

Figure 16 a) shows that several actuator positions can be suggested when the focus is on the active control of boring bar vibration in the cutting speed direction, for instance $(p_1, \alpha = 30°), (p_1, \alpha = 150°)$ and $(p_1, \alpha = 210°)$. When the focus is on the active control of tool vibration in the cutting depth direction, Fig. 16 b) suggests the actuator positions $(p_1, \alpha = 60°), (p_1, \alpha = 240°)$ and $(p_3, \alpha = 30°)$.

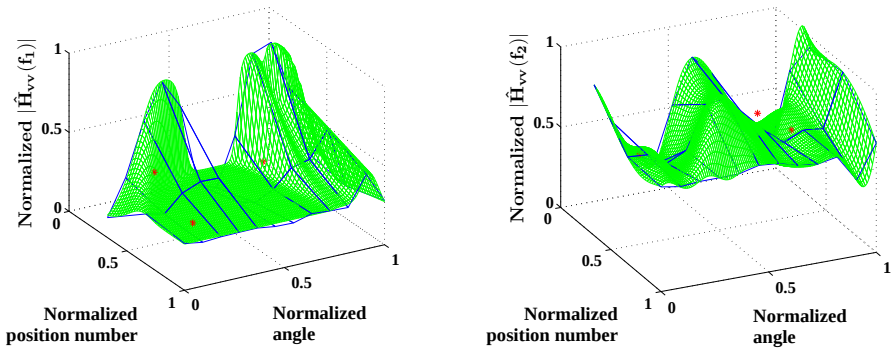

Figure 15: "3-D" surface plots of the normalized point receptance magnitude function a) in the cutting speed direction at the frequencies of the first bending mode $f_{1\theta}$ and b) in the cutting speed direction at the frequencies of the second bending mode $f_{2\theta}$. Blue lines are used for the values calculated based on the thirty six "3-D" FE models, and green lines are used for the values predicted by the trained neural networks. Red stars represent the values from the test set of the "3-D" FE models.

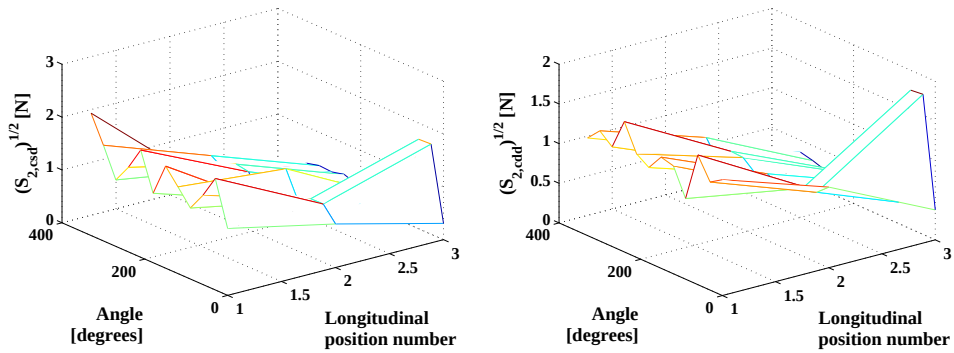

Figure 16: The "3-D" surface plot of the square root of the objective function $S_2(z_q, \alpha_q)$, based on the thirty six "3-D" FE models, a) for the cutting speed direction and b) for the cutting depth direction. Weighting factors $\beta_1 = 1$ and $\beta_2 = 1$.

Now, the MLP NN interpolated are utilized for the objective function S_2 in Eq. 29. Figure 17 a) shows the square root of the objective function $S_2(z_\theta, \alpha_\theta)$ for the cutting speed direction and Fig. 17 b) shows the square root of the objective function $S_2(z_\theta, \alpha_\theta)$ for the cutting depth direction. The values of the weighting factors that were used were $\beta_1 = 1$ and $\beta_2 = 1$.

The actuator position $(p_1, \alpha = 210°)$ might be suggested for the active control of boring bar vibration in the cutting speed direction, as can be observed in Fig. 17 a). However, for the active control of boring bar vibration in the cutting depth direction, the actuator positions $(p_1, \alpha = 240°)$ and $(p_3, \alpha = 30°)$ might be selected, as indicated

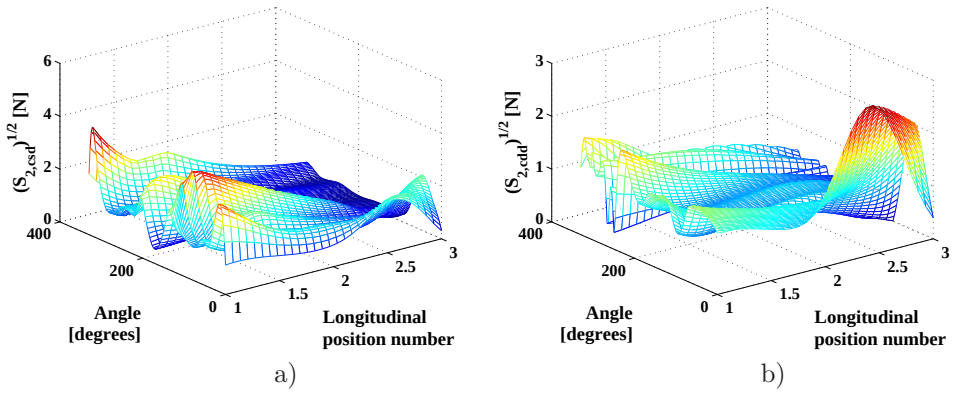

Figure 17: The "3-D" surface plot of the square root of the objective function $S_2(z_\theta, \alpha_\theta)$, based on the the MLP NN interpolated magnitude values for the control path frequency functions and the point receptance functions a) for the cutting speed direction and b) for the cutting depth direction. Weighting factors $\beta_1 = 1$ and $\beta_2 = 1$.

by Fig. 17 b).

Using the objective function S_3 in Eq. 30, actuator positions for an active boring bar were initially investigated based on the magnitude values for the control path frequency functions and the point and transfer receptance functions for the thirty six "3-D" FE models. This objective function was utilized both for the cutting speed direction and for the cutting depth direction. Figure 18 a) shows the square root of the objective function $S_3(z_q, \alpha_q)$ for the cutting speed direction and Fig. 18 b) shows the square root of the objective function $S_3(z_q, \alpha_q)$ for the cutting depth direction.

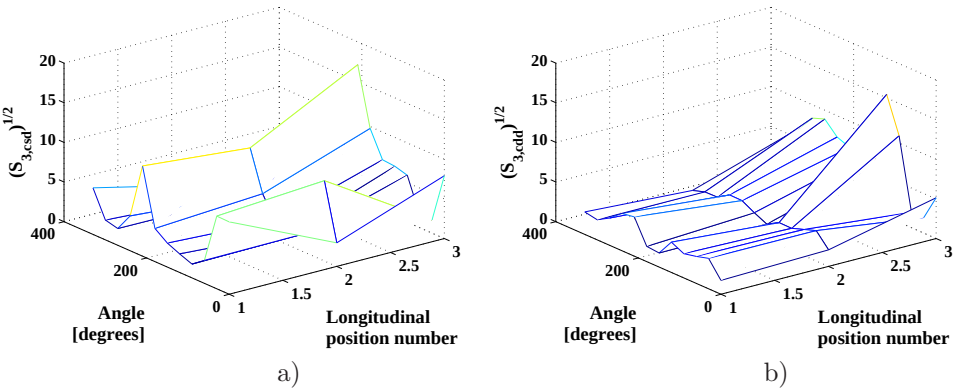

Figure 18: The "3-D" surface plot of the square root objective function $S_3(z_q, \alpha_q)$, based on the thirty six "3-D" FE models, a) for the cutting speed direction and b) for the cutting depth direction.

The the results from the objective function S_3 indicate that at the actuator posi-

tions $(p_2, \alpha = 120°)$, $(p_1, \alpha = 270°)$ and $(p_3, \alpha = 30°)$ the objective function S_3 has local minima for the active control of boring bar vibration in the cutting speed direction, as can be observed in Fig. 18 a). However, for the active control of boring bar vibration in the cutting depth direction, the objective function S_3 has local minima at the actuator positions $(p_1, \alpha = 0°)$ and $(p_1, \alpha = 150°)$, as indicated by Fig. 18 b).

One active boring bar prototype was manufactured with the actuator position $(p_1, \alpha = 240°)$.

3.3 Comparison of the Dynamic Properties of the Active Boring Bar Prototype with the Corresponding FE Model

In order to correlate the spatial dynamic properties of the actual active boring bar with the ones predicted by the "3-D" finite element model, experimental modal analysis was conducted. Experimental modal analysis (EMA) of the clamped active boring bar prototype was carried out while the boring bar was unconnected to the workpiece. This resulted in the estimation of modal parameters of the two fundamental bending modes. In order to emphasize the quality of the modal parameters extracted in the experimental modal analysis of the clamped boring bar, both accelerance functions (synthesized based on the extracted modal parameters and the corresponding measured accelerance function estimates) are plotted in the same diagram. Figure 19 a) shows the synthesized accelerance and the measured accelerance functions for the driving point in the cutting depth direction. Figure 19 b) shows the synthesized accelerance and the measured accelerance functions for the driving point in the cutting speed direction. For the first eigenmode, corresponding to the lowest eigenfrequency, the relative damping ratio was estimated as $\zeta_1 = 1.842\%$. For the second eigenmode, the relative damping ratio was estimated as $\zeta_2 = 1.629\%$.

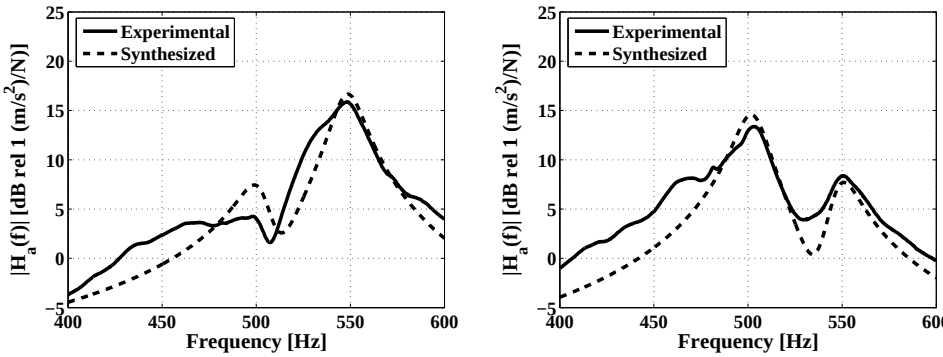

Figure 19: The experimental and synthesized magnitude functions of the point accelerance function a) in the cutting depth direction, and b) in the cutting speed direction zoomed in to the first two resonance peaks.

The multiple coherence function estimates for the two excitation forces and the respective point acceleration were greater than or equal to 0.998 at each fundamental eigenfrequency (see Fig. 20 a)). Figure 20 b) displays the estimated normalized random errors for the multiple coherence function estimates [18].

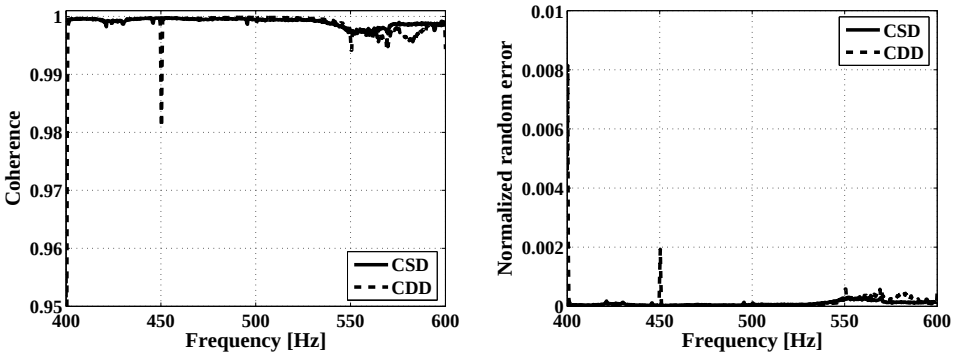

a) b)

Figure 20: a) Multiple coherence function estimates between the two excitation forces and the respective point acceleration, and b) normalized random error estimates for the corresponding multiple coherence function estimates zoomed into the frequency range corresponding to the first two resonance peaks.

The two fundamental active boring bar eigenfrequencies estimated in the experimental modal analysis and calculated based on the active boring bar's "3-D" finite element model are summarized in Table 6.

Model	Resonance freq., [Hz]	
	Mode 1	Mode 2
Experimental Modal Analysis, (EMA)	502.420	548.427
The "3-D" Finite Element Model of the Active Boring Bar Prototype, (FEM)	492.039	564.925

Table 6: Natural frequency estimates.

The mode shape estimates for the first two fundamental bending modes produced by means of experimental modal analysis of the active boring bar prototype, and by modal analysis calculations of the corresponding "3-D" finite element model, are plotted in Fig. 21.

As a quality measure of the mode shapes extracted by the experimental modal analysis, the MAC-matrix was calculated based on Eq. (4) [17]. This gives the following:

$$[MAC]_{EMA} = \begin{bmatrix} MAC_{EMA_1,EMA_1} & MAC_{EMA_1,EMA_2} \\ MAC_{EMA_2,EMA_1} & MAC_{EMA_2,EMA_2} \end{bmatrix} = \begin{bmatrix} 1.000 & 0.005 \\ 0.005 & 1.000 \end{bmatrix}, \quad (31)$$

where EMA_1 is the mode shape at 502.420 Hz and EMA_2 is the mode shape at 548.427 Hz, estimated by experimental modal analysis.

To provide a quantitative measure of the correlation between the mode shapes from the experimental modal analysis and the mode shapes predicted by the finite element

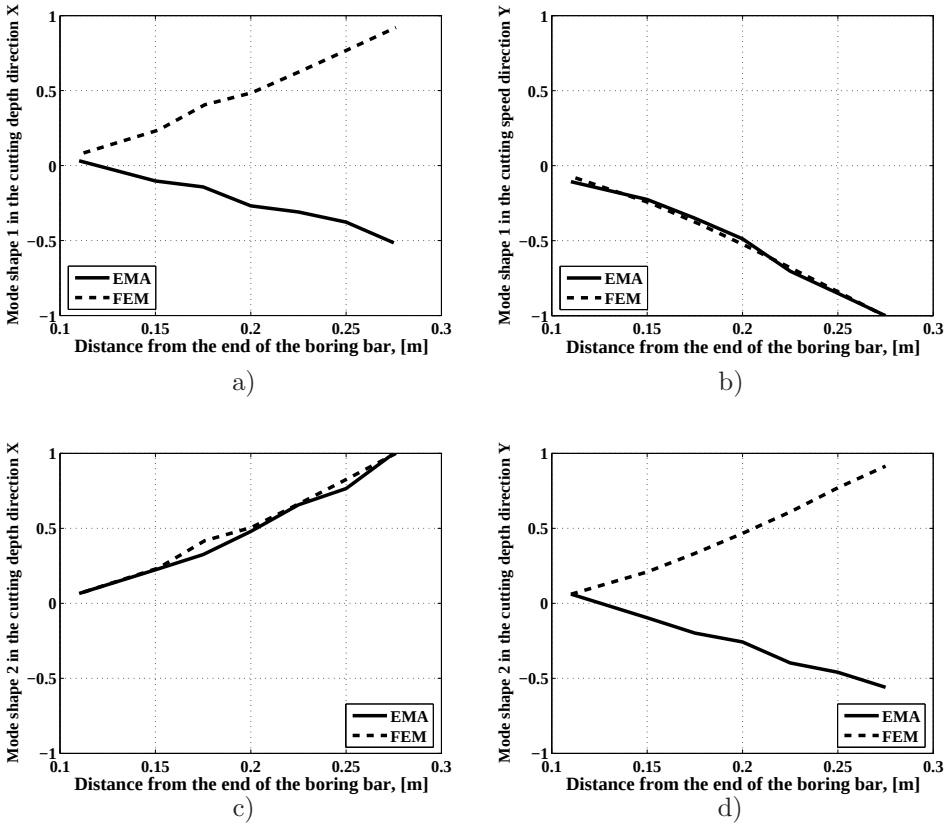

Figure 21: The first two fundamental mode shapes of the active boring bar. a) shows the component of mode shape 1 in the cutting depth direction; b) shows the component of mode shape 1 in the cutting speed direction; c) shows the component of mode shape 2 in the cutting depth direction and d) shows the component of mode shape 2 in the cutting speed direction. This was produced based on experimental modal analysis (EMA) and the "3-D" finite element model of the active boring bar prototype (FEM) correspondingly.

models, a cross-MAC matrix has been produced based on Eq. 5 [17]. The cross-MAC matrix between the mode shapes calculated using the "3-D" finite element model FEM_1 at 492.039 Hz and FEM_2 at 564.925 Hz, and the mode shapes estimated using experimental modal analysis EMA_1 at 502.420 Hz and EMA_2 at 548.427 Hz, is given by:

$$[MAC]_{FEM,EMA} = \begin{bmatrix} MAC_{FEM_1,EMA_1} & MAC_{FEM_2,EMA_1} \\ MAC_{FEM_1,EMA_2} & MAC_{FEM_2,EMA_2} \end{bmatrix} = \tag{32}$$
$$= \begin{bmatrix} 0.139 & 0.854 \\ 0.902 & 0.092 \end{bmatrix}.$$

Two control path frequency functions for the active boring bar prototype were estimated experimentally and calculated based on the "3-D" finite element model of

the active boring bar prototype: one between the voltage over the actuator and the acceleration at the error sensor position in the cutting speed direction and another between the voltage over the actuator and the acceleration at the error sensor position in the cutting depth direction. The spectrum estimation parameters and the excitation signal properties used in the experiments are given in Table 3. The magnitude function for the two estimated control path frequency response functions for the active boring bar prototype are presented in Fig. 22.

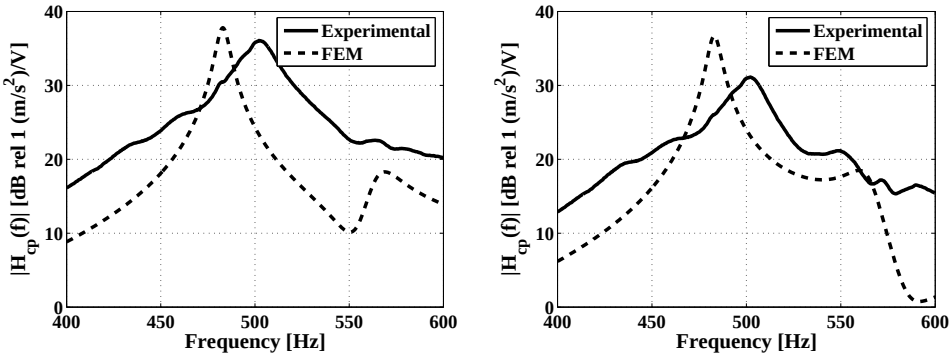

Figure 22: Control path frequency function magnitude estimates, estimated experimentally (solid line) and calculated based on the "3-D" finite element model (dashed line), a) between the voltage over the actuator and the acceleration at the error sensor position in the cutting speed (CSD) direction, and b) between the actuator voltage and the error acceleration in the cutting depth (CDD) direction.

4 Summary and Conclusions

The development of a new actuator positioning strategy with the purpose of improving the efficiency of the design procedure of active boring bars has been addressed in this paper. The concept of the methodology was to replace a number of the active boring bar prototypes by utilizing FE modeling of the system boring bar - actuator - clamping house in combination with neural networks and a suitable objective function that defines an appropriate actuator position in a boring bar. For this purpose, thirty six "3-D" FE models of the system boring bar - actuator - clamping house with different actuator positions were developed. The focus was on the dynamic properties of the active bar's two fundamental bending modes. To enable higher spatial resolution in the estimate of the actuator position, trained multilayer perceptron neural networks (MLP NNs) were introduced. Objective functions for the selection of suitable actuator positions were presented. A prototype of an active boring bar with an actuator embedded at a position suggested by the actuator positioning method was manufactured. Its spatial dynamic properties displayed correlation with the corresponding active boring bar finite element model. The maximal magnitude of the control path frequency response function at the frequency of the fundamental boring bar bending mode were fairly well-correlated for the active boring bar prototype and the finite element model.

A general observation can be made concerning the control path frequency functions estimates for the active boring bar FE model with different actuator positions: the magnitude of the resonance peaks that are present in the control path frequency function estimates decreases with increasing distance between the actuator position and the clamped end of the boring bar (see Fig. 10). This indicates that the actuator embedded into the boring bar at positions p_1 is likely to produces greater displacement amplitudes at the tool tip in comparison to a situation where the actuator is embedded into the boring bar at positions p_3. By examining the point receptance function estimates between the excitation force and the displacement at the nodes of the FE models corresponding to the error sensor positions, shown in Fig. 11, it follows that the values of the estimated natural frequencies of the first two bending modes increase with increasing distance between the actuator position and the clamped end of the boring bar. Also, the magnitude of the resonance peaks in the point receptance function estimates for the error sensor positions decreases with increasing distance between the actuator position and the clamped end of the boring bar.

The objective function in Eq. 29 was applied to select the actuator position in an active boring bar based on the control path frequency functions and the point receptance functions estimated for the thirty six active boring bar FE models. The suggested position of the actuator for vibration control in the cutting depth direction was the longitudinal actuator position p_1 and the actuator offset angle $\alpha = 240$ degrees. For vibration control in the cutting speed direction, the longitudinal actuator position p_1 and the actuator offset angle $\alpha = 210$ degrees was given (see Fig. 16). Nonlinear interpolations between the peak magnitudes of the control path frequency functions and the point receptance functions for the respective "3-D" FE models of the active boring bars were carried out using multilayer perceptron neural networks (MLP NNs). This was done in order to increase the spatial resolution in the prediction of the actuator position in a boring bar, using the suggested objective functions. The MLP NN interpolated magnitude values for the control path frequency functions and for the point receptance functions were used. The suggested positions of the actuator for vibration control in the cutting depth direction were the longitudinal actuator position p_1 and the actuator offset angle $\alpha = 240$ degrees, and the longitudinal actuator position p_3 and the actuator offset angle $\alpha = 30$ degrees (see Fig. 17 b)). For vibration control in the cutting speed direction, the longitudinal actuator position p_1 and the actuator offset angle $\alpha = 210$ degrees were given (see Fig. 17 a)). Based on the suggested actuator positions, one active boring bar prototype was manufactured with the longitudinal actuator position p_1 and the actuator offset angle $\alpha = 240$ degrees. The objective function in Eq. 30 have also been used based on the control path frequency functions, and the point and transfer receptance functions estimated for the thirty six active boring bar FE models. The suggested position of the actuator for vibration control in the cutting depth direction was the longitudinal actuator position p_1 and the actuator offset angle $\alpha = 0$ degrees. For vibration control in the cutting speed direction, the longitudinal actuator position p_1 and the actuator offset angle $\alpha = 270$ degrees were given (see Fig. 16).

Assume that for a given actuator input signal containing energy at the respective fundamental bending resonance frequencies, the active boring bar tool tip will respond in the cutting speed direction at these frequencies. A point force acting in parallel with the primary force, at the point where the primary cutting force is applied to the boring bar, exciting an identical boring bar tool tip response when the actuator is passive, might be described as an actuator equivalent tool tip force. Thus, a greater

actuator equivalent tool tip force in the cutting speed direction would make the tool tip response in the cutting speed direction controllable for a greater primary cutting force. Hence, this will yield an increase in the stiffness of the boring bar with respect to the primary cutting force excitation. The objective function S_2 provides a weighted sum of the squared magnitudes of the frequency function between actuator input voltage and the resulting actuator equivalent tool tip force, in the cutting speed direction or in the cutting depth direction, for the two frequencies of the fundamental boring bar bending modes f_1 and f_2. On the other hand, S_3 may be related to the maximal actuator input signal power required to attenuate the boring bar vibration in the cutting speed direction or the cutting depth direction at the frequencies of the fundamental boring bar bending modes and for the respective actuator position in an active boring bar for a force component vector magnitude of one. The actuator position or positions that results in the lowest value of S_3 yield the active boring bar, in the set of evaluated boring bars, that requires the lowest value on the maximal actuator input signal "power" for a force component vector magnitude of one. This position or positions might be suggested to attenuate the boring bar vibration in the cutting speed direction or in the cutting depth direction, at the frequencies of the fundamental boring bar bending modes. Basically, both S_2 and S_3 provide rough guidelines for selecting an actuator position in a boring bar. For instance, if S_2 is used for guidelines concerning an actuator position for vibration control in the cutting speed direction, only primary cutting force excitation is assumed. If S_2 is considered for vibration control in the cutting depth direction, only thrust force excitation is assumed.

The spatial dynamic properties of the active boring bar prototype were estimated by means of experimental modal analysis and compared to the corresponding dynamic properties of the finite element model of the active boring bar prototype. It can be observed that the resonance frequencies corresponding to the first two bending modes estimated by the "3-D" finite element model differ from the estimates produced by experimental modal analysis by approximately 10-15 Hz (see Table 6). It can also be observed that the mode shapes of the finite element model are poorly correlated with the ones estimated experimentally for the active boring bar prototype, see the MAC matrix in Eq. 32. This may indicate that there are still some uncertainties in the modeling of boundary conditions such as the contact between the boring bar and the clamping house and the contact between the boring bar and the actuator. However, the components of the mode shapes estimated experimentally and predicted numerically have approximately the same magnitude, i.e. the first mode shape has the largest component in the cutting speed direction and the second mode shape has the largest component in the cutting depth direction, respectively.

The control path frequency response functions estimates were also obtained experimentally and compared with the ones predicted by the finite element model (see Fig. 22). It can be observed that the peak magnitude at the frequency of the first fundamental bending mode of the control path frequency response function, between the voltage over the actuator and the acceleration at the error sensor position in the cutting speed direction, estimated based on the "3-D" finite element model, is in good agreement with the experimental estimate. Also, the peak magnitude at the frequency of the second fundamental bending mode of the control path frequency response function, between the voltage over the actuator and the acceleration at the error sensor position in the cutting depth direction, estimated based on the "3-D" finite element model, is in good agreement with the experimental estimate.

5 Future Work

Future research may concern the evaluation of the actuator positioning method based on active boring bars designed with the aid of the proposed method, both during internal turning and during no turning in a lathe. In the modeling of active boring bars, the modeling of the actual clamping/boundary conditions imposed by the clamping housing, and the boundaries between the actuator and the boring bar need to be addressed further. Also, the development of the actuator positioning method for vibration control of the cutting depth and the cutting depth directions simultaneously should be considered.

Acknowledgments

The present project is sponsored by Acticut International AB in Sweden. This company holds multiple approved patents and make use of active control technology for metal cutting.

References

[1] E. Marui, S. Ema, and S. Kato. Chatter vibration of lathe tools. part 1: General characteristics of chatter vibration. *Journal of Engineering for Industry*, 105:100–106, May 1983.

[2] G. M. Zhang. Dynamic modeling and analysis of the boring machine system. *Journal of Engineering for Industry*, 109:219–226, 1987.

[3] L. Andrén, L. Håkansson, A. Brandt, and I. Claesson. Identification of dynamic properties of boring bar vibrations in a continuous boring operation. *Journal of Mechanical Systems & Signal Processing*, 18(4):869–901, 2004.

[4] S. G. Tewani, K. E. Rouch, and B. L. Walcott. A study of cutting process stability of a boring bar with active dynamic absorber. *International Journal of Machine Tools & Manufacture*, 35(1):91–108, 1995.

[5] D.R. Browning, I. Golioto, and N.B. Thompson. Active chatter control system for long-overhang boring bars. *Proceedings of SPIE*, 3044:270–280, 1997.

[6] I. Claesson and L. Håkansson. Adaptive active control of machine-tool vibration in a lathe. *IJAV-International Journal of Acoustics and Vibration*, 3(4):155–162, 1998.

[7] L. Pettersson, L. Håkansson, I. Claesson, and S.Olsson. Control of machine-tool vibration in a cnc lathe based on an active tool holder shank with embedded piezo ceramic actuators. *In Proceedings of the Eight International Congress on Sound and Vibration*, 2001.

[8] L. Pettersson, L. Håkansson, I. Claesson, and S.Olsson. Active control of boring bar vibration in cutting operations. *In Proceedings of the Ninth International Congress on Sound and Vibration, ICSV9*, 2002.

[9] H. Åkesson, T.Smirnova, I. Claesson, and L. Håkansson. On the development of a simple and robust active control system for boring bar vibration in industry. *IJAV-International Journal of Acoustics and Vibration*, 12(4):139–152, 2007.

[10] I. Claesson and L. Håkansson. Adaptive active control of machine-tool vibration in a lathe. *IJAV-International Journal of Acoustics and Vibration*, 3(4):155–162, 1998.

[11] T. Smirnova, H. Åkesson, and L. Håkansson. Modeling of an Active Boring Bar. Research Report 2007:14, Blekinge Intitute of Technology.

[12] A.R. Mehrabiam and A. Yousefi-Koma. Optimal positioning of piezoelectric actuators on a smart fin using bio-inspired algorithms. *Aerospace Science and Technology*, (11):174–182, 2007.

[13] *http://www.efunda.com/Materials/piezo/material_data/matdata_output.cfm ?Material_ID=PZT_5H.*

[14] *Low voltage co-fired multilayer stacks, rings and chips for actuation.* Piezomechnik, GmbH, 2006.

[15] D.J. Ewins. *Modal Testing: Theory and Practice.* Research Studies Press, distributed by Wiley, 1984.

[16] P.-O. H. Sturesson, L. Håkansson, and I. Claesson. Identification of the statistical properties of the cutting tool vibration in a continuous turning operation - correlation to structural properties. *Journal of Mechanical Systems and Signal Processing, Academic Press*, 11(3):459–489, 1997.

[17] N.M.M. Maia and J.M.M. Silva. *Theoretical and Experimental Modal Analysis.* Research Studies Press Ltd., 1997.

[18] J.S. Bendat and A.G. Piersol. *Engineering Application of Correlation and Spectral Analysis.* John Wiley & Sons, second edition, 1993.

[19] M.H. Hayes. *Statistical Digital Signal Processing and Modeling.* John Wiley Sons, Inc., 1996.

[20] *MSC.MARC Volume A: Theory and User's Information.* MSC.Software, 2005.

[21] R. L. Taylor O. S. Zienkiewicz and J.Z. Zhu. *The Finite Element Method: Its Basis and Fundamentals.* Butterworth-Heinemann, 2005.

[22] L. Andrèn, L.Håkansson, A. Brandt, and I. Claesson. Identification of dynamic properties of boring bar vibrations in a continuous boring operation. *Journal of Mechnical Systems & Signal Processing*, 18(4):869–901, 2004.

[23] L. Andrèn, L.Håkansson, A. Brandt, and I. Claesson. Identification of motion of cutting tool in a continuous boring operation - correlation to structural properties. *Journal of Mechnical Systems & Signal Processing*, 18(4):903–927, 2004.

[24] P. Lancaster and M. Tismenetsky. *The Theory of Matrices, with applications.* ACADEMIC PRESS INC, second edition, 1985.

[25] A. Jennings and J.J. McKeown. *Matrix Computation.* John Wiley & Sons, second edition, 1992.

[26] D.J. Inman. *Engineering Vibration*. Prentice-Hall, second edition, 2001.

[27] S. Haykin. *Neural Networks: A Comprehensive Foundation*. Prentice-Hall, Inc., second edition, 1999.

[28] R.D. Reed and R.J. Marks II. *Neural Smithing: Supervised Learning in Feedforward Artificial Neural Networks*. Prentice-Hall, Inc., second edition, 1999.

Part VI

Simulation of Active Suppression of Boring Bar Vibrations by Means of a Boring Bar "1-D" Finite Element Model

This part is based on the publication:

T. Smirnova, H. Åkesson, L. Håkansson, I. Claesson and T. Lagö, *Simulation of Active Suppression of Boring Bar Vibrations by Means of Boring Bar's "1-D" Finite Element Model*, In proceedings of ACTIVE 2009 the 2009 International Symposium on Active Control of Sound and Vibration, August 20-22, 2009, Ottawa, Canada.

Simulation of Active Suppression of Boring Bar Vibrations by Means of a Boring Bar "1-D" Finite Element Model

T. Smirnova, H. Åkesson, L. Håkansson, I. Claesson and T. Lagö*
Department of Signal Processing,
Blekinge Institute of Technology
372 25 Ronneby
Sweden

*Acticut International AB
Gjuterivagen 6
311 32 Falkenberg, Sweden

Abstract

In metal cutting, active control is one method that may be used to attenuate the vibration of a boring bar during an internal turning operation. It is based on the utilization of an active boring bar with an embedded piezoceramic actuator and a suitable controller. In this case, the primary boring bar vibrations originating from the material deformation process may be suppressed with the help of secondary "anti vibration" induced by the actuator. The design of an active boring bar is usually a tedious and costly procedure, which involves decision making concerning the selection of the actuator characteristics, the actuator's position inside the boring bar and the production and testing of several active boring bar prototypes. Therefore, accurate mathematical modeling of the active control system, including an active boring and a controller, etc. is of importance. In this paper, a simple "1-D" finite element model of a boring bar is utilized to simulate the dynamic response while an adaptive digital controller realized by the feedback filtered-x LMS algorithm is used as a controller. Control system simulations are presented for the case of broadband excitation.

1 Introduction

The internal turning operation is known to be one of the most vibration prone operations in metal cutting. During the internal turning operation, a long and slender tool holder - a boring bar - is usually used to machine deep and precise cavities inside a workpiece material. Due to its geometric properties, the boring bar is easily subjected to vibrations induced by the material deformation process. The broadband excitation applied by the material deformation process during internal turning usually results in narrow-band boring bar vibrations [1]. High levels of boring bar vibration often occur

at frequencies related to the low-order fundamental bending modes of the boring bar. In particular, these appear at the bending mode in the cutting speed direction since the cutting force usually has the largest component in this direction [2–4]. Boring bar vibration may result in a degraded quality of the machined surface, insert breakage and severe acoustic noise in the working environment.

One approach to suppress boring bar vibrations is to use an active control technique. This technique is based on the selective increase of the dynamic stiffness of the boring bar at the actual frequency of the dominating bending mode [5,6]. Active control for internal turning may be implemented by using an active boring bar in combination with a digital feedback controller. An active boring bar is based on a standard boring bar. It has an error accelerometer attached close to the insert to measure the boring bar vibration in the cutting speed direction, see Fig. 1. The feedback controller uses the error accelerometer signal to produce a dynamic control signal. The voltage signal produced by the controller is applied to the piezoelectric actuator embedded into the milled groove below the central line of the boring bar. The controlled actuator forces apply moment loads on the boring bar that induce secondary or "anti vibration" that suppresses the primary vibration of the boring bar close to the insert [5].

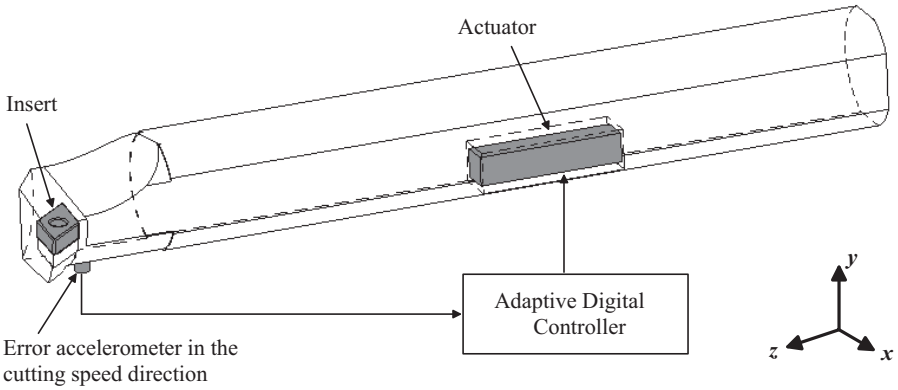

Figure 1: Schematic view of an active boring bar together with the adaptive digital controller.

The design of an active boring bar is usually a time consuming and costly procedure which involves making decisions concerning the most favorable actuator position. Therefore, mathematical models of a boring bar which could incorporate the effect of the actuator together with a model of the digital feedback controller to predict the dynamic response of the active boring bar are of importance. In this paper, a simple "1-D" beam finite element (FE) model of the clamped active boring bar is considered. The model is used to predict the dynamic response of the active boring bar. The bending moment is applied at the boring bar-actuator interfaces. Adaptive digital controller realized by the feedback filtered-x lms algorithm is used as a digital controller. The control algorithm has been incorporated into the ODE solver based, on the Newmark integration scheme. Furthermore, the results of the forward path estimation between the bending moment applied to the node corresponding to the boring bar-actuator interface and the simulated displacement at the node cor-

responding to the free end of the boring bar, are reported. In addition to this, the paper presents the results from the simulation of the suppression of the displacement at the node located at the free end of the boring bar under the broadband excitation force applied to the same node.

2 Materials and Methods

2.1 Physical Properties of the Boring Bar Material

The boring bar used in the model is a standard boring bar S40T PDUNR15 F3 WIDAX. It is made of the material 30CrNiMo8: Young's elastic modulus E=205 GPa, the density ρ=7850 kg/m^3 and Poisson's coefficient ν=0.3. The geometrical properties of the boring bar's cross section are as follows: the cross sectional area $A = 1.1933 \times 10^{-3}\ m^2$, the cross sectional moment of inertia $I_x = 1.1386 \times 10^{-7}\ m^4$.

2.2 A "1-D" Finite Element Model of the Active Boring Bar

The actual active boring bar clamped in the clamping house attached to the lathe was modeled by means of a "1-D" finite element model. The "1-D" finite element model of the active boring bar was developed based on Euler-Bernoulli beam elements. The geometry and the material properties were identical for all beam elements. A simple Euler-Bernoulli beam element has two nodes and four degrees-of-freedom: two translational to describe transverse displacement and two rotational to describe the angle of rotation due to pure bending. The expressions for the shape functions, stiffness and mass matrices of the Euler-Bernoulli beam element are widely accessible [7].

For simplicity, the active boring bar was assumed to be rigidly clamped inside the clamping house. This clamping was modeled by means of the fixed boundary conditions applied to the clamped end of the active boring bar. The actuator load was modeled by means of a bending moment applied to the node of the finite element model corresponding to the position of the actuator-boring bar interface in the actual active boring bar (see Fig. 2). It should be observed that, because of the assumption of fixed boundary conditions at the clamped end of the active boring bar, no moment is applied to the actuator-boring bar interface adjacent to the clamping.

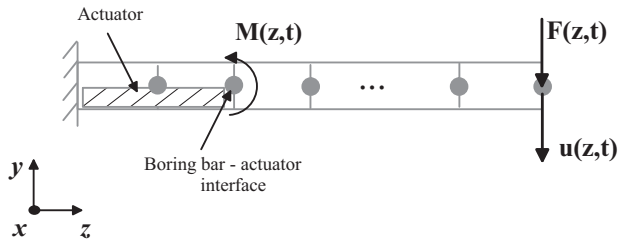

Figure 2: Schematic view of the "1-D" finite element model of a clamped active boring bar.

The coordinate system is defined as follows: x is the cutting depth direction, y is the negative cutting speed direction and z is the feed direction. Here, $F(z,t)$ is a

broadband excitation applied to the node corresponding to the free end of the boring bar, $u(z,t)$ is the displacement at the same node and $M(z,t)$ is the bending moment applied to the node of the finite element model corresponding to the position of the actuator-boring bar interface.

The dynamic response of the "1-D" finite element model of the active boring bar was simulated by means of the Newmark method of the direct integration [8]. Thus, the unconditionally stable Newmark integration scheme with the parameters $\alpha = \frac{1}{4}$ and $\delta = \frac{1}{2}$ was utilized as an ODE solver [8].

2.3 Feedback Filtered-x LMS Algorithm

In order to suppress the response of the active boring bar, induced by a primary broadband excitation force and simulated based on its "1-D" finite element model, a feedback filtered-x LMS algorithm is used. The primary excitation force signal is impossible to measure separately during the internal turning operation to produce a feedforward reference signal. Therefore, a feedback control algorithm is the most appropriate type of control algorithm in this practical application [5]. The block diagram of the feedback filtered-x LMS algorithm is shown in Fig. 3 and can be described by Eqs. (1-4).

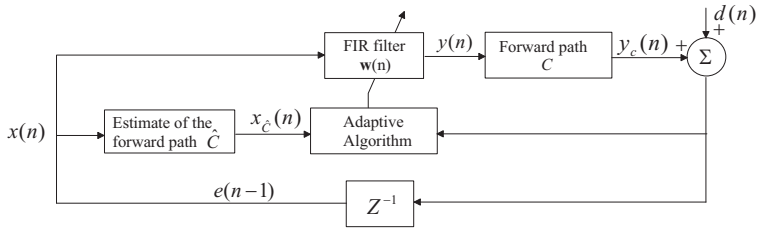

Figure 3: Block diagram of an active feedback control system based on the feedback filtered-x LMS algorithm.

$$y(n) = \mathbf{w}^T(n)\mathbf{x}(n), \tag{1}$$

$$e(n) = d(n) + y_c(n), \tag{2}$$

$$\mathbf{w}(n+1) = \mathbf{w}(n) - \mu \mathbf{x}_{\hat{\mathbf{C}}}(n)e(n), \tag{3}$$

$$\mathbf{x}_{\hat{\mathbf{C}}}(n) = \left[\sum_{i=0}^{I-1} \hat{c}_i x(n-i), \ldots, \sum_{i=0}^{I-1} \hat{c}_i x(n-i-M+1)\right]^T. \tag{4}$$

Here, $\mathbf{w}(n)$ is the adaptive finite impulse response (FIR) filter coefficient vector with the length M; $\mathbf{x}(n) = [x(n), x(n-1), \ldots, x(n-M+1)]^T$; $\mathbf{x}_{\hat{\mathbf{C}}}$ is the filtered reference signal vector that is usually produced by filtering the reference signal with the I -coefficients in the FIR filter estimate of the forward path; $\hat{c}_i$ is the ith coefficient in the FIR filter vector estimate of the forward path, $i \in 0, 1, \ldots, I-1$; $y(n)$ is the output signal from the adaptive FIR filter, in this case a bending moment that should be applied to the nodes of the FE-model corresponding to the actuator-boring bar interface position; $e(n)$ is the error transverse displacement at the free end of the FE-model of the active boring bar; $y_C(n)$ is the secondary "anti vibration"; $\hat{C}$ is

the estimate of the forward path; $d(n)$ is the primary disturbance signal (broadband random excitation force modeling the cutting force) and μ is the step size.

To ensure stability of the feedback filtered-x LMS algorithm, a leakage coefficient γ can be introduced in Eq. (3). Thus, the coefficient adjustment algorithm for the leaky filtered-x LMS algorithm may be defined as [9, 10]:

$$\mathbf{w}(n+1) = \gamma \mathbf{w}(n) - \mu \mathbf{x}_{\hat{\mathbf{C}}}(n) e(n), \tag{5}$$

where the leakage factor may be selected in the interval $0 < \gamma < 1$, but is usually selected close to unity.

2.4 Forward Path Estimation

The feedback filtered-x LMS algorithm utilizes the estimate of the forward path $\hat{C}$. The actual forward path C (or the system to be controlled) in the real application is comprised of the following elements: a D/A converter, an actuator amplifier, an actuator and a structural path in the boring bar. However, in the case of the "1-D" finite element model of the active boring bar, the forward path is reduced to the structural path between the bending moment applied to the nodes of the model corresponding to the actuator-boring bar interfaces of the actual active boring bar and the displacement at the node located at the free end of the "1-D" finite element model. The forward path was estimated by means of an LMS algorithm [11]. A block diagram of the forward path estimation using an LMS algorithm is shown in Fig. 4.

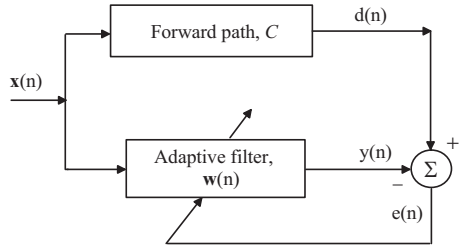

Figure 4: Block diagram describing the forward path estimation.

The LMS algorithm steers the filter coefficients in $\mathbf{w}(n)$ to minimize the error signal $e(n)$ in the mean square sense. The algorithm can be summarized as follows:

$$\begin{aligned} y(n) &= \mathbf{w}^T(n)\mathbf{x}(n), & (6)\\ e(n) &= d(n) - y(n), & (7)\\ \mathbf{w}(n+1) &= \mathbf{w}(n) + \mu e(n)\mathbf{x}(n). & (8) \end{aligned}$$

Here, $\mathbf{x}(n)$ is the reference signal vector, in this case the bending moment applied to the node of the "1-D" FE model corresponding to the actuator-boring bar interface; $y(n)$ is the output of the adaptive filter; $d(n)$ is the desired signal, i.e., the displacement at the node located at the free end of the "1-D" FE model caused by the broadband random excitation force applied to the same node; $e(n)$ is the error signal and μ is the step size.

2.5 System Identification

Non-parametric spectrum estimation has been utilized to produce non-parametric linear least-squares estimates of dynamic systems [11, 12]. For instance, the Welch's method [11] can be used for this purpose.

A dynamic system $H(f_k)$ may be estimated using the estimator as [12]:

$$\hat{H}_1(f_k) = \frac{\hat{P}_{xy}^{PSD}(f_k)}{\hat{P}_{xx}^{PSD}(f_k)}, \tag{9}$$

where $\hat{P}_{xx}^{PSD}(f_k)$ is an estimate of the power spectral density of the input signal and $\hat{P}_{xy}^{PSD}(f_k)$ is an estimate of the cross-power spectral density between the input and output signals. Furthermore, $f_k = \frac{k}{N}F_s$, where N is the block length; $k = 0, 1, \ldots, N-1$, and F_s is the sampling frequency. In the case of power spectral density estimation, the Hanning window is commonly used [11].

The power spectral density estimation parameters used in the production of the forward path frequency response function estimates, as well as in the power spectral density estimates of the controlled displacement, are summarized in Table 1.

Parameter	Value
Excitation force signal	Random noise with the RMS value of 44.455 N
Sampling frequency, F_s	2560 Hz
Number of spectral lines, N	2560
Number of averages	10
Window	Hanning
Overlap	50 %

Table 1: Parameters for power spectral density estimation.

3 Results

The results are presented in the following order: initially, the forward path estimate between the bending moment applied at the node corresponding to the actuator-boring bar interface and the displacement at the node located at the free end is given. Secondly, the results of the simulated active control of the boring bar vibrations are presented as the displacements and power spectral densities of the displacements calculated at the node of the "1-D" FE model, which corresponds to the free end of the boring bar without and with active control.

3.1 Forward Path Estimate

The estimate of the forward path is presented in terms of the frequency response functions between the bending moment applied at the node corresponding to the actuator-boring bar interface and the displacement at the node located at the free end of the active boring bar as well as the output of the adaptive filter, see Fig. 5.

The forward path was estimated using the LMS algorithm with an adaptive FIR filter having 200 coefficients.

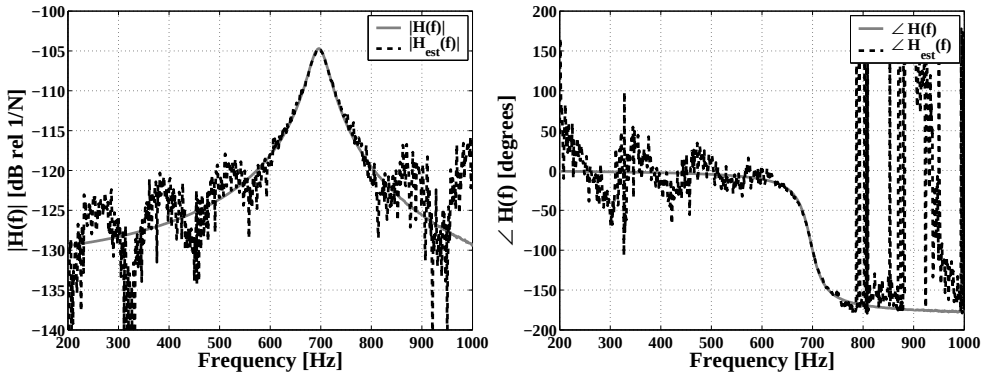

a) b)

Figure 5: Estimates of the a) magnitude and b) phase functions of the forward path frequency response function, produced between the bending moment applied at the node of the "1-D" FE model corresponding to the actuator-boring bar interface and the displacement of the node at the free end of the FE model (in grey color) and between the bending moment and the output of the FIR filter estimate of the forward path (in dashed black color).

3.2 Simulated Active Vibration control of Boring Bar vibration Based on the Filtered-x LMS Algorithm

The results of the simulated vibration control are presented as the displacements calculated at the node corresponding to the free end of the boring bar without and with control, see Fig. 6 a). The results are also presented in terms of the power spectral density estimates of the displacements calculated at the node corresponding to the free end of the boring bar, see Fig. 6 b).

The active control was based on the leaky version of the feedback filtered-x LMS algorithm, where the leakage factor $\gamma = 0.999$ was added to insure the convergence of the algorithm. The length of the adaptive filter was equal to 200 coefficients.

4 Conclusions

In this paper, "1-D" finite element modeling was applied to predict the dynamic response of active boring bars. The Newmark integration scheme was utilized for simulation of the response of the "1-D" finite element model of the active boring bar. As an excitation signal for the estimation of the forward path, as well as for the active suppression simulation of the boring bar vibration, random noise was used. In order to avoid large phase errors in the solution produced by the Newmark integration scheme, the original excitation signal was interpolated with a factor of 10. This resulted in a large filter order for both forward path estimation and active suppression of the vibrations. Thus, at least 200 filter coefficients were necessary to provide sufficient information about the system resulting in the obtained attenuation, see Fig. 5. The utilization of the feedback filtered-x LMS algorithm yielded an attenuation of approximately 26 dB of the simulated vibration level at the frequency related to the fundamental bending mode of the boring bar, see Fig. 6 b). This approach may be

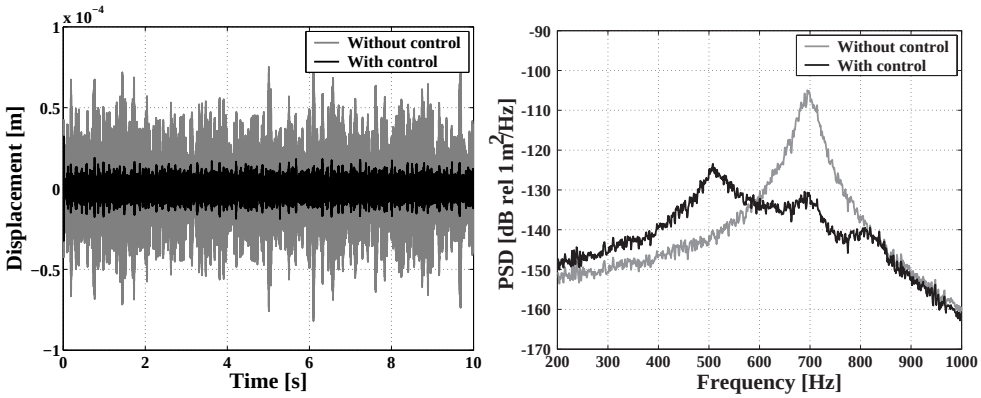

a) b)

Figure 6: a) The displacement versus the time of the simulated boring bar vibration with control (in black color) and without control (in grey color) and b) power spectral density estimates of the simulated boring bar vibration with control (in black color) and without control (in grey color).

utilized for the selection of a "good" actuator position inside the boring bar.

Acknowledgments

The present project is sponsored by the Foundation for Knowledge and Competence Development and the company Acticut International AB.

References

[1] P.-O. H. Sturesson, L. Håkansson, and I. Claesson. Identification of the statistical properties of the cutting tool vibration in a continuous turning operation - correlation to structural properties. *Journal of Mechanical Systems and Signal Processing, Academic Press*, 11(3):459–489, 1997.

[2] E. Marui, S. Ema, and S. Kato. Chatter vibration of lathe tools. part 1: General characteristics of chatter vibration. *Journal of Engineering for Industry*, 105:100–106, May 1983.

[3] G. M. Zhang. Dynamic modeling and analysis of the boring machine system. *Journal of Engineering for Industry*, 109:219–226, 1987.

[4] L. Andrèn, L.Håkansson, A. Brandt, and I. Claesson. Identification of dynamic properties of boring bar vibrations in a continuous boring operation. *Journal of Mechnical Systems & Signal Processing*, 18(4):869–901, 2004.

[5] I. Claesson and L. Håkansson. Adaptive active control of machine-tool vibration in a lathe. *IJAV-International Journal of Acoustics and Vibration*, 3(4):155–162, 1998.

[6] S. G. Tewani, K. E. Rouch, and B. L. Walcott. A study of cutting process stability of a boring bar with active dynamic absorber. *International Journal of Machine Tools & Manufacture*, 35(1):91–108, 1995.

[7] D.J. Inman. *Engineering Vibration*. Prentice-Hall, second edition, 2001.

[8] J.W. Tedesco, W.M. McDougal, and C.A. Ross. *Structural Dynamics: Theory and Application*. Addison-Wesley Longman Inc., 1998.

[9] L. Håkansson, S. Johansson, M. Dahl, P. Sjösten, and I. Claesson. *Chaper 12 - Noise cancelling headsets for speech communication in CRC Press Handbook on Noise Reduction in Speech Applications, Gillian M. Davis (ed.)*. CRC Press, first edition, 2002.

[10] S.J. Elliot. *Signal Processing for Active Control*. Academic Press, London, 2001.

[11] M.H. Hayes. *Statistical Digital Signal Processing and Modeling*. John Wiley & Sons, Inc., 1996.

[12] J.S. Bendat and A.G. Piersol. *Random Data Analysis And Measurement Procedures*. John Wiley & Sons, third edition, 2000.

ABSTRACT

Boring bar vibration in machine tools during internal turning operations is a pronounced problem in the manufacturing industry. Due to the often slender geometry of the boring bar, vibration may easily be induced by the material deformation process. One approach to overcome such vibration problems is to use active control of boring bar vibration. The design time of an active boring bar depends to a great extent on the knowledge of its dynamic properties when clamped in a lathe for different actuator positions and sizes, crucial for its performance. This thesis focuses on the development of accurate dynamic models of active boring bars with the purpose of providing qualitative information on suitable actuator position for a certain boring bar.

The first part of the thesis considers the problem of building an accurate ”3-D” finite element (FE) model of a standard boring bar used in industry. Results from experimental modal analysis of the actual boring bar are the reference. The second and the third parts discuss analytical and experimental methods for modeling the dynamic properties of a boring bar clamped in a machine tool. For this purpose, the Euler-Bernoulli and Timoshenko beam theories are used to produce both distributed-parameter system models and corresponding ”1-D” FE models. A more complete ”3-D” FE model of the system boring bar - clamping house is also developed. Spatial dynamic properties of these models are discussed and compared with adequate experimental modal analysis results from the actual boring bar clamped in a machine tool. The third part also investigates the sensitivity of the spatial dynamic properties of the derived boring bar models to variation in the structural parameters’ values.

The fourth part focuses on the development of a ”3-D” FE model of the system boring bar - actuator - clamping house. Two models are discussed: a linear model and a model enabling variable contact between the clamping house and the boring bar with and without Coulomb friction in the contact surfaces. Based on these FE models fundamental bending modes and control path frequency response functions are discussed in conjunction with the corresponding quantities estimated for the actual active boring bar.

In the fifth part, a method based on FE modeling and artificial neural networks for selecting a suitable actuator position inside an active boring bar is presented. Objective functions for selecting an actuator position are suggested. An active boring bar with an actuator position suggested by the method was manufactured and it displays fairly good correlation with the corresponding FE model.

The final part focuses on modeling of an active boring bar vibration control system. A simple ”1-D” FE model of a boring bar is utilized to simulate the dynamic response and an adaptive digital feedback controller realized by the feedback filtered-x LMS algorithm is used.

ISSN 1653-2090
2010:08
ISBN 978-91-7295-187-7